

Synthesis, Structure and Reactivity of Phosphorus and Arsenic Heterocycles



Darren Michael Charles Ould

A thesis submitted to Cardiff University in
candidature for the degree of Doctor of
Philosophy

March 2020

I. Acknowledgements

To begin with, I would like to extend my thanks and gratitude to my supervisor Dr Rebecca Melen for firstly giving me the opportunity to undertake my PhD in her group and secondly for allowing me to present at a number of conferences both domestically and internationally. Travelling to Canada in the summers of both 2018 and 2019 as part of an exchange program and to present at the Canadian Chemistry Conference and Exhibition 2019 will undoubtedly go down as highlights of my PhD. Thanks must be given to the Melen group both past and present. In particular though to Dr Adam Ruddy, Dr Yashar Soltani and Jamie Carden for their help and suggestions, as well as providing a great working atmosphere. My further thanks to Dr Lewis Wilkins for his help and suggestions, but moreover for teaching me the basics of single crystal X-ray crystallography as well as solving a number of my early structures (compounds **6a**, **7**, **15a–c**, **16a–c**, **17** and **18**). I am grateful for the hard work to the students I have supervised during the course of my PhD, Matthew de Vere-Tucker, Kayla Trafford, Emily Tansley, Dorothea Engl and especially Alex Rigby who helped me develop the initial diazaphosphole and diazarsole work, as well as helping me crystallise a number of complexes (**6a**, **7**, **15a–c**, **16a–c** and **17**). I am grateful to Cardiff University for funding and eight great years as an undergraduate and postgraduate.

I have been fortunate enough to collaborate with a number of people throughout my PhD and wish to express my gratitude to them. Firstly, thanks to Thao Tran and Professor Jeremy Rawson (both at University of Windsor), who established some of the early work of the dithiaphospholes and dithiarsoles. Thao Tran had first synthesised the two paddlewheel structures and intermediates **9**, **10**, **11** and **12**. Professor Jeremy Rawson has solved the crystal structures of **10** and **12**, as well as providing helpful comments for my own structure refinements. Thanks to Dr John Davies (Cambridge University) for solving and refining crystal structures **3**, **4**, **14a** and **14b**. Appreciation must be given to Dr Samuel Adams and Professor Simon Pope for performing the absorption and emission spectroscopy (Chapter 3), Dr Emma Richards for the EPR spectroscopy measurements (Chapter 3) and Dr James Platts for the DFT calculations on the corresponding radical (Chapter 3) as well as teaching me how to perform Fluoride Ion Affinity calculations and generally introducing me to computational chemistry. Although not included in this thesis I would like to show my appreciation to Professor Thomas Wirth, Micol Santi and Dr Jan Wenz for our collaborative work on our paper titled Metal-Free Tandem Rearrangement/Lactonization: Access to 3,3-Disubstituted Benzofuran-2-(3H)-ones, which was published in *Angew. Chem. Int. Ed.* I would like to thank the technical support and professional services staff at Cardiff University, Dr Robert Jenkins,

Simon Waller, Robin Hick, Tom Williams, Evelyn Blake and Jamie Cross. In addition, I would like to recognise Dr Benjamin Ward, Dr Angelo Amoroso and Dr Paul Newman, who although may not have directly contributed to this thesis have greatly helped and supported my time at Cardiff University.

The challenges a PhD as well as life presents at times are difficult and I would like to personally acknowledge the wider inorganic department for always keeping me going by providing numerous amusing and upbeat moments. I would especially like to thank Siôn Edwards for the many lunch time adventures and conversations, which will certainly be sadly missed and Bria Thomas for providing entertaining moments and for proofreading this thesis. I would of course like to thank my family for their continuous support and belief in me, as well my friends from Cornwall (especially Sam Ringrose, Neil Sanders, Chris Lee and Anthony Donaghy) for always providing a welcomed distraction from PhD life. Lastly, I would like to express my upmost gratitude to Ella Carter for our many adventures during the past 3.5 years (and more), support and advice given. Thank you all!

II. List of Publications

Published work included in this thesis:

1. T. T. P. Tran, **D. M. C. Ould**, L. C. Wilkins, D. S. Wright, R. L. Melen and J. M. Rawson, *CrystEngComm*, 2017, **19**, 4696–4699 (Chapters 2 and 3).
2. **D. M. C. Ould**, A. C. Rigby, L. C. Wilkins, S. J. Adams, J. A. Platts, S. J. A. Pope, E. Richards and R. L. Melen, *Organometallics*, 2018, **37**, 712–719 (Chapters 2 and 3).
3. **D. M. C. Ould** and R. L. Melen, *Chem. A Eur. J.*, 2018, **24**, 15201–15204 (Chapter 4)
4. **D. M. C. Ould**, Thao T. P. Tran, J. M. Rawson and R. L. Melen, *Dalton Trans.*, 2019, **48**, 16922–16935 (Chapters 2, 3 and 4).

Published work not included in this thesis:

1. A. J. Ruddy, **D. M. C. Ould**, P. D. Newman and R. L. Melen, *Dalton Trans.*, 2018, **47**, 10377–10381.
2. M. Santi, **D. M. C. Ould**, J. Wenz, Y. Soltani, R. L. Melen and T. Wirth, *Angew. Chem. Int. Ed.*, 2019, **58**, 7861–7865.
3. T. A. Gazis, B. A. Mohajeri, D. Willcox, **D. M. C. Ould**, J. Wenz, J. M. Rawson, M. S. Hill, T. Wirth and R. L. Melen, *Chem Commun.*, 2020, **56**, 3345-3348.
4. Y. Soltani, A. Dasgupta, T. A. Gazis, **D. M. C. Ould**, E. Richards, B. Slater, K. Stefkova, V. Y. Vladimirov, L. C. Wilkins, D. Willcox and R. L. Melen, *Cell Rep. Phys. Sci.*, 2020, 100016.
5. **D. M. C. Ould**, J. L. Carden and R. L. Melen, *Turning the alane key: novel synthesis and reactivity of triarylalanes*, manuscript in revision.
6. **D. M. C. Ould** and R. L. Melen, *Chem. A Eur. J.*, 2020, doi.org/10.1002/chem.202001734

III. Abbreviations

°C	degrees Celcius
Å	Angstrom
AN	acceptor number
BCF	tris(pentafluorophenyl)borane
Bn	benzyl
BSSE	basis set superposition effect
C	concentration
<i>ca.</i>	<i>circa</i> , about
<i>cf.</i>	<i>confer</i> , compared with
CAAC	1-(2,6-diisopropylphenyl)-3,3,5,5-tetramethylpyrrolidin-2-ylidene
COD	1,5-cyclooctadiene
Cp	cyclopentadiene
Cp*	pentamethylcyclopentadiene
CSD	Cambridge structural database
DABCO	1,4-diazabicyclo[2.2.2]octane
DAP	diazaphospholene
DFB	1,2-difluorobenzene
DFT	density functional theory
Dipp	2,6-diisopropylphenyl
Dur	2,3,5,6-tetramethylphenyl
ECP	effective core potential
EI	electron ionisation
EPC	electrophilic fluorophosphonium cation
EPR	electron paramagnetic resonance

ES	electrospray
equiv	equivalent
FIA	fluoride ion affinity
FLP	frustrated Lewis pair
GEI	global electrophilicity index
GIMC	gauge-including magnetically induced current
HBpin	pinacolborane
HMDS	bis(trimethylsilyl)amide
HOMHED	harmonic oscillator model of heterocyclic electron delocalisation
HOMO	highest occupied molecular orbital
HPLC	high performance liquid chromatography
hr	hour
HRMS	high resolution mass spectrometry
LA	Lewis acid
LANL2DZ	Los Alamos National Laboratory 2-double-zeta
LUMO	lowest unoccupied molecular orbital
M	molar, mol dm ⁻³
M06-2X	Minnesota 06
MO	molecular orbital
MP2	Møller–Plesset perturbation theory
NBO	natural bond orbital
NHC	N-heterocyclic carbene
NHP	N-heterocyclic phosphonium
nm	nanometre
NMR	nuclear magnetic resonance

OLED	organic light emitting diode
PCM	polarisable continuum solvation model
Ph	phenyl
PMB	<i>p</i> -methoxybenzyl
ppm	parts per million
RI	Resolution of Identity approximation
r.t.	room temperature
SV(P)	split valence polarization
^t Bu	tert-butyl
TD	time dependent
THF	tetrahydrofuran
TMSOTf	trimethylsilyl trifluoromethanesulfonate
TZP	triple zeta valence polarization
UV	ultraviolet
vs.	versus
VT	variable temperature

IV. Aims

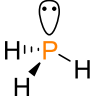
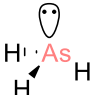
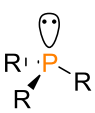

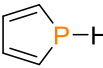
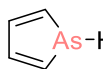
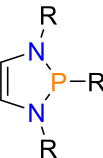
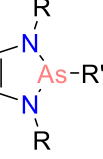
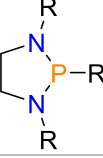

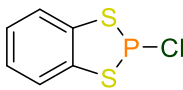
The overriding theme of this thesis is to produce a series of new benzo-fused-phosphole and benzo-fused-arsole derived compounds. By introducing sulfur, nitrogen and oxygen heteroatoms into the pnictole ring core, an interesting comparison and exploration into the fundamental properties and reactivity of this highly interesting but ultimately underexplored class of compound will be achieved. To elaborate further, a multitude of modern-day techniques, including multinuclear NMR spectroscopy, EPR spectroscopy, absorption and emission spectroscopy, single crystal X-ray diffraction and DFT calculations will be employed to bring this class of heterocycle into the 21st century.

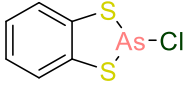
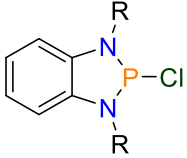
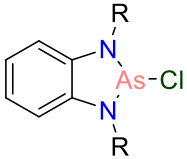
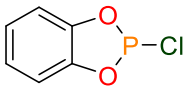
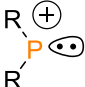
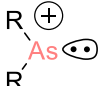


In Chapter 2 the aim is to synthesise a series of novel benzo-fused-phosphole and benzo-fused-arsole derived compounds, which bear a halogen co-ligand. This will create a library of complexes which will be used to explore the structural and electronic properties as well as provide pre-cursors to use in subsequent reactions.

The aims of Chapter 3 are firstly to look at performing substitution of the chloride co-ligand to generate a *N*-centred paddlewheel. Secondly, the compounds from Chapter 2 will be used to synthesise the corresponding phosphonium and arsenium cations, and as they are 10 π aromatic, investigate the optical properties. Lastly, the final objective is to reduce the benzo-fused diaza-chloro-phosphole and benzo-fused diaza-chloro-arsole to form the corresponding dimeric complex.

Chapter 4 is inspired by the recent use of the closely related diazaphospholene complexes as pre-catalysts in hydroboration reduction catalysis. Thus, Chapter 4 has the main aim of using the phosphorus and arsenic compounds from Chapters 2 and 3, as well as producing a benzyloxy-phosphosphole and benzyloxy-arsole, to undergo hydroboration catalysis and give a comparison on the catalytic performance of using phosphorus vs. arsenic.

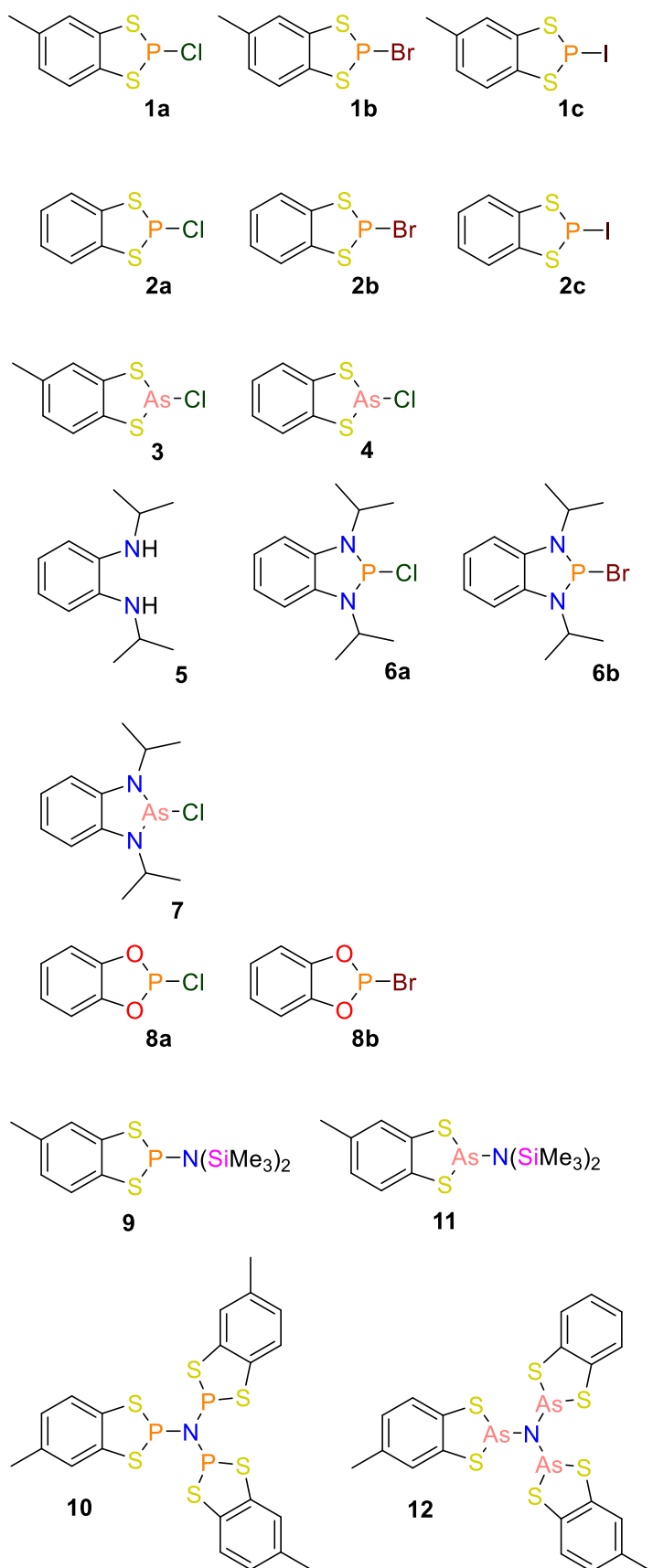
V. Nomenclature

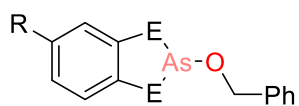
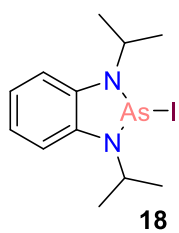
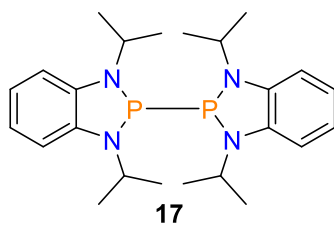
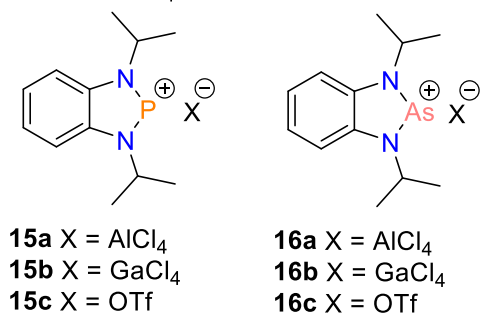
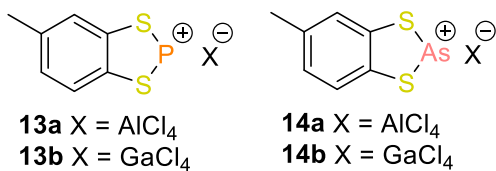
	Phosphane: The saturated hydrides of trivalent phosphorus of the general formula P_nH_{2n+1} . The simplest phosphane is PH_3 .
	Arsane: The saturated hydrides of trivalent arsenic of the general formula As_nH_{2n+1} . The simplest arsane is AsH_3 .
	Phosphine: Organophosphorus compounds derived from PH_3 by replacing one, two or three of the hydrogen atoms. Primary (RPH_2), secondary (R_2PH) and tertiary (R_3P) phosphines respectively ($R \neq H$).
	Arsine: Organoarsenic compounds derived from AsH_3 by replacing one, two or three of the hydrogen atoms. Primary ($RAsH_2$), secondary (R_2AsH) and tertiary (R_3As) arsines respectively ($R \neq H$).
	Phosphole: A five membered ring phosphorus heterocycle with the chemical formula C_4H_4PH .
	Arsole: A five membered ring arsenic heterocycle with the chemical formula C_4H_4AsH .
	Diazaphospholene: N-heterocyclic phosphine contained within a five membered unsaturated ring.
	Diazaarsolene: N-heterocyclic arsine contained within a five membered unsaturated ring.
	Diazaphospholidine: N-heterocyclic phosphine contained within a five membered saturated ring.
	Diazaarsolidine: N-heterocyclic arsine contained within a five membered saturated ring.
	Benzo-fused dithia-chloro-phosphole: Five membered ring phosphorus compound with a benzene ring backbone and the inclusion of sulfur and chloride atoms.

	Benzo-fused dithia-chloro-arsole: Five membered ring arsenic compound with a benzene ring backbone and the inclusion of sulfur and chloride atoms.
	Benzo-fused diaza-chloro-phosphole: Five membered ring phosphorus compound with a benzene ring backbone and the inclusion of nitrogen and chloride atoms.
	Benzo-fused diaza-chloro-arsole: Five membered ring arsenic compound with a benzene ring backbone and the inclusion of nitrogen and chloride atoms.
	Benzo-fused dioxo-chloro-phosphole: Five membered ring phosphorus compound with a benzene ring backbone and the inclusion of oxygen and chloride atoms.
	Phosphonium: Two coordinate phosphorus(III) complex that has a formal positive charge on the phosphorus heteroatom and takes the form $[PR_2]^+$.
	Arsenium: Two coordinate arsenic(III) complex that has a formal positive charge on the arsenic heteroatom and takes the form $[AsR_2]^+$.
	Phosphonium: Phosphorus(V) oxidation state compound with the general formula PR_4^+ .
	Arsonium: Arsenic(V) oxidation state compound with the general formula AsR_4^+ .

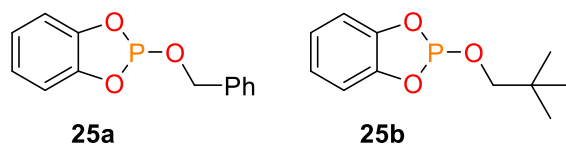
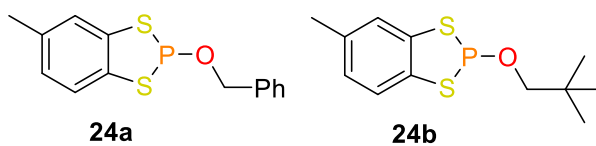
Nomenclature derived from IUPAC: *IUPAC. Compendium of Chemical Terminology, 2nd ed. (the "Gold Book"). Compiled by A. D. McNaught and A. Wilkinson. Blackwell Scientific Publications, Oxford (1997). Online version (2019-) created by S. J. Chalk. ISBN 0-9678550-9-8. <https://doi.org/10.1351/goldbook>.*

VI. Compounds Synthesised in This Thesis





19 E = S, R = Me
20 E = N(ⁱPr), R = H



VII. Table of Contents

Table of Contents

I. Acknowledgements.....	ii
II. List of Publications	iv
III. Abbreviations	v
IV. Aims	viii
V. Nomenclature	ix
VI. Compounds Synthesised in This Thesis	xi
VII. Table of Contents.....	xiii
VIII. Abstract.....	xvii
1: Introduction.....	1
Chapter 1.1 Examples of Group 15 Heterocycles and Cations.....	1
1.1.1 <i>The rise of main group chemistry.....</i>	1
1.1.2 <i>Introduction to phospholes and arsoles.....</i>	2
1.1.3 <i>Optical properties of phospholes and arsoles.....</i>	4
1.1.4 <i>Introduction to diazaphospholenes and diazarsolenes.....</i>	6
1.1.5 <i>Use of diazaphospholenes to make dimers.....</i>	9
Chapter 1.2 Recent Interest in Phosphorus and Arsenic Lewis Acids	11
1.2.1 <i>Introduction to phosphenium and arsenium compounds</i>	11
1.2.2 <i>Lewis acidity of phosphenium and arsenium cations.....</i>	12
1.2.3 <i>Introduction to phosphonium and arsonium compounds.....</i>	13
1.2.4 <i>Phosphorus and arsenic super Lewis acids</i>	16
Chapter 1.3 Heterocyclic Phosphorus(III) Lewis Acid Catalysis	18
1.3.1 <i>Catalysis performed by Kinjo group</i>	18
1.3.2 <i>Catalysis performed by Speed group</i>	22
1.3.3 <i>Catalysis performed by Cramer group</i>	27
Chapter 1.4 Conclusion	30
Chapter 1.5 References	31
Chapter 2: Synthesis of Dithia-, Diaza-, and Dioxa-based Benzophospholes and Benzoarsoles.....	36
Chapter 2.1 Synthesis of Benzo-Fused Dithiaphospholes and Dithiarsoles	36
2.1.1 <i>General synthesis and NMR spectroscopy analysis of benzo-fused dithiaphospholes..</i>	36
2.1.2 <i>Single crystal X-ray diffraction analysis of benzo-fused dithiaphospholes</i>	39
2.1.3 <i>Computational analysis of benzo-fused dithiaphospholes.....</i>	44

2.1.4 General synthesis and NMR spectroscopy analysis of benzo-fused dithia-chloro- arsoles	46
2.1.5 Single crystal X-ray diffraction analysis of benzo-fused dithiarsoles	47
2.1.6 Computational analysis of benzo-fused dithiarsoles	49
Chapter 2.2 Synthesis of Benzo-Fused Diazaphospholes and Diazarsoles	51
2.2.1 General synthesis and NMR spectroscopy analysis of benzo-fused diazaphospholes...	51
2.2.2 Single crystal X-ray diffraction analysis of 2-chloro-1,3-diisopropyl- benzodiazaphosphole	53
2.2.3 Computational analysis of benzo-fused diazaphospholes	54
2.2.4 General synthesis and NMR spectroscopy analysis of benzo-fused diazaphospholes...	55
2.2.5 Single crystal X-ray diffraction analysis of 2-chloro-1,3-diisopropyl-benzodiazarsole.	56
2.2.6 Computational analysis of 2-chloro-1,3-diisopropyl-benzodiazarsole	57
Chapter 2.3 Synthesis of Benzo-Fused Dioxaphospholes	59
2.3.1 General synthesis and NMR spectroscopy analysis of benzo-fused dioxaphospholes ..	59
2.3.2 Computational analysis of benzo-fused dioxaphospholes	61
Chapter 2.4 Conclusion	63
Chapter 2.5 References	67
Chapter 3: Reactivity of Dithiaphospholes, Dithiarsoles, Diazaphospholes and Diazarsoles	68
Chapter 3.1 Paddlewheel Synthesis from Dithiaphosphole and Dithiarsole	68
3.1.1 Synthesis of tris(5-methylbenzo-1,3,2-dithiaphosphol-2-yl)amine: $(\text{MeC}_6\text{H}_3\text{S}_2\text{P})_3\text{N}$	68
3.1.2 Solid-state structure of $(\text{MeC}_6\text{H}_3\text{S}_2\text{P})_3\text{N}$	70
3.1.3 Synthesis of tris(5-methylbenzo-1,3,2-dithiarsole-2-yl)amine: $(\text{MeC}_6\text{H}_3\text{S}_2\text{As})_3\text{N}$	71
3.1.4 Solid-state structure of $(\text{MeC}_6\text{H}_3\text{S}_2\text{As})_3\text{N}$	72
Chapter 3.2 Cation Formation	75
3.2.1 Synthesis of dithiaphospheniums and dithiarseniums	75
3.2.1.1 Synthesis and NMR analysis of dithiaphosphenium cations from dithiaphosphole .	75
3.2.1.2 Solid-state structures of dithiaphospheniums	77
3.2.1.3 Computational analysis of dithiaphosphenium cation	79
3.2.1.4 Synthesis and NMR analysis of dithiarsenium cations from dithiarsole	81
3.2.1.5 Solid-state structures of dithiarseniums	82
3.2.1.6 Computational analysis of dithiarsenium cation	84
3.2.2 Synthesis of diazaphosphenium cations	86
3.2.2.1 Synthesis and NMR analysis of diazaphosphenium cations from diazaphosphole...	86
3.2.2.2 Solid-state structures of diazaphospheniums	89
3.2.2.3 Computational analysis of diazaphosphenium cation	91

3.2.2.4 Synthesis and NMR analysis of diazarsenium cations from diazarsole	93
3.2.2.5 Solid-state structures of diazarseniums	94
3.2.2.6 Computational analysis of diazarsenium cation	96
3.2.3 Attempted Synthesis of dioxarsenium cations from dioxarsole	98
3.2.4 Lewis acidity and aromaticity of phospheniums and arseniums	98
Chapter 3.3 Photophysical Properties of Diazaphosphonium and Diazarsenium Cations	
.....	104
3.3.1 Absorption Properties	104
3.3.2 Emissive Properties	106
Chapter 3.4 Reduction of Diazaphosphole and Diazarsole	109
3.4.1 Synthesis and multinuclear NMR analysis of benzodiazaphosphoryl dimer	109
3.4.2 Solid-state structures of benzodiazaphosphoryl dimer	109
3.4.3 EPR measurements on benzodiazaphosphoryl dimer	111
3.4.5 Attempted synthesis and characterisation of benzodiazarsole dimer	113
3.4.6 Solid-state structure of 2-chloro-1,3-diisopropyl-benzodiazarsole	114
Chapter 3.5 Conclusion	116
Chapter 3.6 References	117
Chapter 4: Aldehyde Reduction Catalysis Using Dithia- and Diaza-Derived Phosphole and Arsole Complexes	119
Chapter 4.1 Hydroboration of Aldehydes Using Benzo-Fused Dithiarsoles and Diazarsoles	
.....	119
4.1.1 Pre-catalyst synthesis and NMR spectroscopy characterisation	119
4.1.2 Solid-state structural analysis of 2-(benzyloxy)-5-methylbenzo-1,3,2-dithiarsole and 2-(benzyloxy)-1,3-diisopropyl-1,3,2-diazarsole	121
4.1.3 Computational analysis of alkoxy derived dithiarsole and diazarsole	124
4.1.4 Homogeneous hydroboration reduction using arsenic pre-catalysts	125
Chapter 4.2 Hydroboration of Aldehydes Using Benzo-Fused Dithiaphospholes and Diazaphospholes	135
4.2.1 Pre-catalyst synthesis and NMR spectroscopy characterisation	135
4.2.2 Solid-state structural analysis of 2-(benzyloxy)-5-methylbenzo-1,3,2-dithiaphosphole	139
4.2.3 Computational analysis of alkoxy derived dithiaphosphole and dioxaphosphole	141
4.2.4 Homogeneous hydroboration reduction using phosphorus pre-catalysts	142
Chapter 4.3 Comparing the Phosphorus and Arsenic Pre-Catalysts	150
Chapter 4.4 Conclusion	153
Chapter 4.5 References	154
Chapter 5: Conclusions and Future Work	155

Chapter 6: Experimental	157
Chapter 6.1 General Experimental	157
Chapter 6.2 Experimental for Synthesis of Dithia-, Diaza-, and Dioxa-based Benzphospholes and Benzarsoles	158
6.2.1 <i>Synthesis of benzo-fused dithiaphospholes and dithiarsoles</i>	158
6.2.2 <i>Synthesis of benzo-fused diazaphospholes and diazarsoles</i>	162
6.2.3 <i>Synthesis of benzo-fused dioxaphospholes</i>	164
Chapter 6.3 Experimental for Reactivity of Dithiaphospholes, Dithiarsoles, Diazaphospholes and Diazarsoles	166
6.3.1 <i>Synthesis of paddlewheel complexes</i>	166
6.3.2 <i>Synthesis of cationic complexes</i>	168
6.3.3 <i>Synthesis of dimeric species</i>	172
6.3.4 <i>Photophysical studies</i>	173
6.3.5 <i>Electron paramagnetic resonance (EPR) studies</i>	173
6.3.6 <i>Computational studies</i>	173
6.3.7 <i>Gutmann-Beckett Lewis Acidity Measurements</i>	174
6.3.8 <i>HOHMED aromaticity calculations</i>	175
Chapter 6.4 Experimental for Aldehyde Reduction Catalysis Using Dithia- and Diaza-Derived Arsole Complexes	178
6.4.1 <i>Synthesis of arsenic pre-catalyst complexes</i>	178
6.4.2 <i>General experimental for hydroboration catalysis</i>	179
6.4.3 <i>Characterisation of hydroboration products</i>	179
Chapter 6.5 Experimental for Aldehyde Reduction Catalysis Using Dithia-, Diaza- and Dioxa-Derived Phosphole Complexes	186
6.5.1 <i>Synthesis of phosphorus pre-catalyst complexes</i>	186
6.5.2 <i>General experimental for hydroboration catalysis</i>	188
6.5.3 <i>Characterisation of hydroboration products</i>	188
Chapter 6.6 X-ray Crystallography	190
6.6.1 <i>General X-ray experimental</i>	190
6.6.2 <i>X-ray refinement data</i>	192
Chapter 6.7 General Computational Experimental	202
Chapter 6.8 References	203

VIII. Abstract

The work described in this thesis relates to the synthesis and exploration of benzo-fused phosphole and benzo-fused arsole complexes, which have been modified by the inclusion of sulfur, nitrogen and oxygen heteroatoms in the pnictole ring, along with the inclusion of a halogen co-ligand. Chapter 2 synthesised the dithiaphospholes, dithiarsoles, diazaphospholes, diazarsoles and dioxaphospholes by adding the appropriate ligand to phosphorus trihalides (PCl_3 , PBr_3 or PI_3) or arsenic trichloride. Structural determination found that these compounds have an envelope geometry and an exocyclic halogen co-ligand. Chapter 3 then made use of these compounds to firstly synthesise an intriguing looking *N*-centred paddlewheel complex. After this, halide abstraction was performed to acquire phosphonium and arsenium cations. UV-visible spectroscopy performed on the diazaphospheniums and diazarseniums revealed the shape and positioning of the absorption bands is highly dependent on the choice of cation (P or As) and counterion (AlCl_4^- , GaCl_4^- or OTf^-). Lastly, Chapter 3 synthesised a P–P dimer from the diazaphosphole, which by using EPR spectroscopy underwent homolytic cleavage at 350 K in toluene solvent. Interestingly, the corresponding As–As dimer had formed but underwent oxidative addition to form 2-iodo-1,3-diisopropyl-benzodiazarsole. Having established fundamental insight into the structure and reactivity of these heterocycles, Chapter 4 used these compounds as pre-catalysts for hydroboration reduction catalysis of aldehydes. The benzyloxy-diazarsole was found to be highly effective for this, as using 5 mol% pre-catalyst loading effectively hydroborated a wide variety of electron donating and electron withdrawing substrates, as well as more sterically demanding ones. When using the phosphole and phosphonium compounds as pre-catalysts, the diazaphosphenium triflate proved to be the most effective for the catalysis, but required higher catalytic loading (10 mol%) and longer reaction times for quantitative conversion to occur. Comparing the arsenic and phosphorus pre-catalysts found that the benzyloxy-diazarsole was superior to the diazaphosphenium triflate.

1: Introduction

Chapter 1.1 Examples of Group 15 Heterocycles and Cations

1.1.1 The rise of main group chemistry

Over the past 50 years the field of main group chemistry has garnered ever more attention, driven principally by the growing need to move away from the use of rare, expensive and in some cases toxic transition metals, but additionally by scientific curiosity. It has been 10 years since Philip Power's review titled 'Main-Group Elements as Transition Metals', which compared how heavier main group elements bear similarities with transition metals and highlighted a number of key discoveries in the field.¹ One particular field to have emerged in main group chemistry since the start of the millennium is frustrated Lewis pairs (FLPs); reported by Stephan and workers it uses the concept of increasing steric bulk between the Lewis acid and Lewis base, which in turn prevents the formation of a classic adduct.² Initially observed by the work of Piers,³ FLPs have been utilised in a wide plethora of reactions.^{4,5} Another key area to have grown is the discovery of multiple bonding in the heavier main group elements, with Lappert's stannylene^{6,7} and West's disilene.⁸

Since Powers' review, the last 10 years has seen a number of key findings. A recent review by Weetman and Inoue on this very topic discussed the rise of biradicaloid complexes, which have been used for small molecule activation, as well as the growth of *s*-block chemistry.⁹ Perhaps though the biggest advance in the past ten years was the progress made in dinitrogen activation, a feature that was previously exclusive to transition metals.¹⁰ This challenging feat was finally achieved in 2018 by the group of Braunschweig, who reacted the complex $[(\text{Dur})\text{B}(\text{CAAC})\text{Br}_2]$ (Dur = 2,3,5,6-tetramethylphenyl, CAAC = 1-(2,6-diisopropylphenyl)-3,3,5,5-tetramethylpyrrolidin-2-ylidene) with excess $\text{K}^+\text{C}_8\text{H}_8^-$ to form the dicoordinate borylene complex, which when exposed to an N_2 atmosphere at -80°C gave the N_2 activated product (Figure 1.1).¹¹

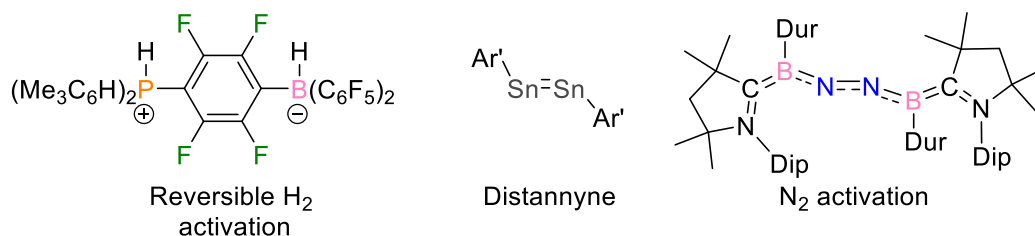


Figure 1.1: Examples of the advancements in main group chemistry.

These recent discoveries show that main group chemistry is thriving and ever evolving. Despite this though many areas are still underexplored and underexploited, and one such field is the use of heavier group 15 (pnictogen) heterocycles; phospholes and arsoles.

1.1.2 Introduction to phospholes and arsoles

Heterocycles form the largest and arguably most interesting class of compound in organic chemistry, with their uses widespread in the pharmaceutical sector.¹² Moreover, the five membered ring heterole class form a very common class of heterocycles, with compounds including pyrrole, furan and thiophene, which have the inclusion of nitrogen, oxygen and sulfur respectively. These compounds are well-known and as a result have been extensively studied for their fundamental properties and reactivity.^{13–15} However, although the inclusion of a nitrogen heteroatom is well-understood, exchanging this for the heavier group 15 elements phosphorus or arsenic leads to the much less explored phosphole and arsole compounds.

Phosphole is formally defined as a five membered ring heterocycle with the chemical formula C_4H_4PH ; it is the phosphorus analogue of pyrrole. Likewise, arsole is a five membered ring heterocycle with the chemical formula C_4H_4AsH . Although these compounds are not as familiar as pyrrole, 1,2,3,4,5-pentaphenylphosphole was first discovered in 1959 by two independent groups¹⁶ and the parent 1*H*-phosphole was first described by the group of Mathey in 1983 by low temperature protonation of phospholyl anions.¹⁷ Meanwhile, the history of arsoles is more extensive, with the first potential arsole reported in the early 1920's by Turner and Burrows while working at the University of Sydney. However, when it came to publication the editor of Journal and Proceedings of the Royal Society of New South Wales rejected the name arsole given the structure was the arsenic version of indole.¹⁸ Unlike the 1*H*-phosphole, the 1*H*-arsole has not been synthesised, but the arsole moiety was produced by Braye, Hübel and Caplier in 1961 when they synthesised 1,2,3,4,5-pentaphenylarsole (Figure 1.2).¹⁹ Further synthesis involving the arsole ring was continued by the work of Märkl and Hauptmann.^{20,21}

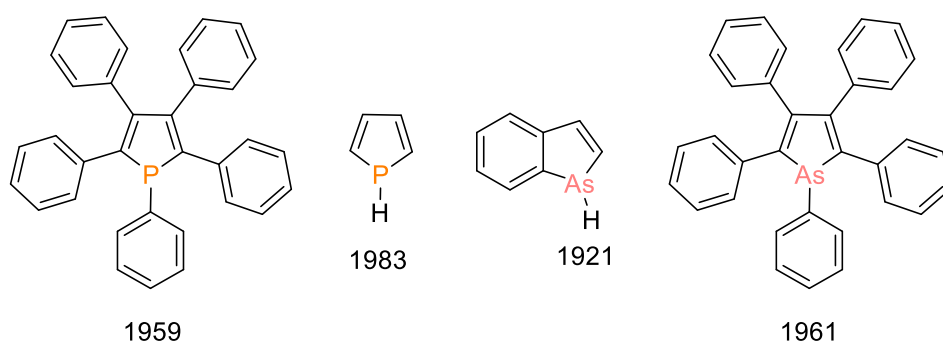


Figure 1.2: Early examples of phosphole and arsole compounds.

Given that phospholes and arsoles are the heavier analogues to pyrroles, questions started to be raised over the extent of aromaticity these compounds possess, if any. At first it may appear that phospholes and arsoles would be non-aromatic, given the phosphorus and

arsenic centre preferably adopt a trigonal pyramidal geometry as opposed to lying planar (Figure 1.3).¹⁶ This is a consequence of the lack of efficient overlap between the phosphorus/arsenic lone pair and the rest of the phosphole/arsole core; an effect which is more prominent in arsoles.²²

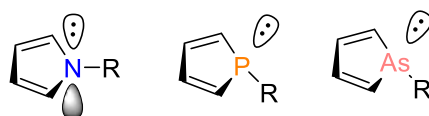


Figure 1.3: Pyrrole (left), phosphole (middle) and arsole (right) showing lone pair.

Early reactivity studies of arsoles showed them to react in a way of non-aromatic compounds¹⁹ and early reports in 1973 by Mathey and colleagues claimed results from photoelectron spectroscopy gave “direct proof of the non-aromaticity of phospholes and arsoles”.²³ These observations support the initial assessment that these compounds are not aromatic. However, this “direct proof” was later discredited by the work of Epiotis who used one electron molecular orbital (MO) analysis to prove phospholes and arsoles have a degree of aromaticity.²⁴ Further work into the aromaticity was performed,^{25,26} but it was not until recently when Johansson and Juselius used the computational method gauge-including magnetically induced currents (GIMIC) method that a widely accepted answer was given.²⁷ In this method, which computationally models the paramagnetic and diamagnetic current within the heterocycle, Johansson and Juselius found that the 1*H*-phosphole has approximately 60% the induced ring current strength of pyrrole, whereas 1*H*-arsole is a little lower at 47%, when calculated at BP86 level of theory. Therefore, applying a magnetic aromaticity criterion suggests that phospholes and arsoles are to a certain point aromatic, although it should be noted that this result directly contradicts additional work which uses an energetic criterion for aromaticity.^{28,29}

Indeed, it seems that the aromaticity of these compounds is far from simple and highly depends on how one defines aromaticity. The group of Heeney have recently synthesised a luminescent phosphole and arsole derived complex and applied the harmonic oscillator model of heterocyclic electron delocalisation (HOMHED) to determine experimentally the aromaticity (Figure 1.4). This approach uses experimentally determined bond lengths from X-ray crystallography and compares them to “optimal” bond lengths. This then gives a HOMHED value, which lies between 1 and 0 (fixed at the aromaticity of benzene and its theoretical Kekulé form accordingly), where a value >0.5 is considered aromatic. Using HOMHED Heeney and colleagues found that phospholes and arsoles are aromatic, with

HOMHED values of 0.8015 and 0.6863 respectively,³⁰ a result that agrees with the work of Johansson and Juselius that phospholes are more aromatic than arsoles.

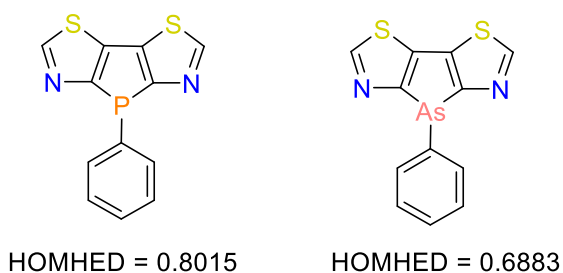


Figure 1.4: Luminescent phosphole and arsole used for HOMHED calculations.

1.1.3 Optical properties of phospholes and arsoles

Given its aromatic nature, pyrrole has been extensively studied with regards to its optical applications.^{31–34} However, the fundamental properties of phospholes are vastly different to that of pyrrole, which allows for different material characteristics. As just discussed, the aromaticity of the phosphole ring is controversial but it is at least significantly reduced compared to pyrrole; the phosphorus centre adopts a trigonal pyramidal geometry as opposed to planar (due to insufficient n- π orbital interaction) and the LUMO energy level lies at a lower energy level, which is a result of the effective $\sigma^*(\text{P-R})-\pi^*(1,3\text{-diene})$ interaction. These differences along with the ability to tune the electronics by modifying the phosphorus centre, such as through oxidation, alkylation or coordination to metals, mean that phospholes offer an intriguing moiety for materials design. Matano and Imahori,³⁵ and more recently Hissler and colleagues¹⁶ have produced reviews discussing the application of phospholes in solid-state devices and discuss the matter at great length.

Organic light emitting diodes (OLEDs) have received great attention in recent times due to their use in screen technology,³⁶ and the first example of a phosphole incorporated into one was from Réau, Wu and colleagues.³⁷ They prepared three different fluorophores based on the phosphole moiety, the first with a free lone pair on phosphorus, the second with a P(V) bound sulfur and the third coordinated to gold(I). Since then a number of reports have been produced using phospholes in OLEDs.¹⁶ Another important emerging solid-state device is dye-sensitised solar cells (DSSCs), which are a promising alternative to traditional silicon solar cells. Again phospholes have been used in the design of these, with their first use from the group of Imahori and workers who showed that 1-hydroxy-1-oxodithieno-phospholes could be used as anchoring groups to the TiO₂ electrode.³⁸ Furthermore, in 2014 Mantano synthesised copolymers that incorporated π -conjugated phospholes that were used in a bulk heterojunction organic solar cell (Figure 1.5).³⁹

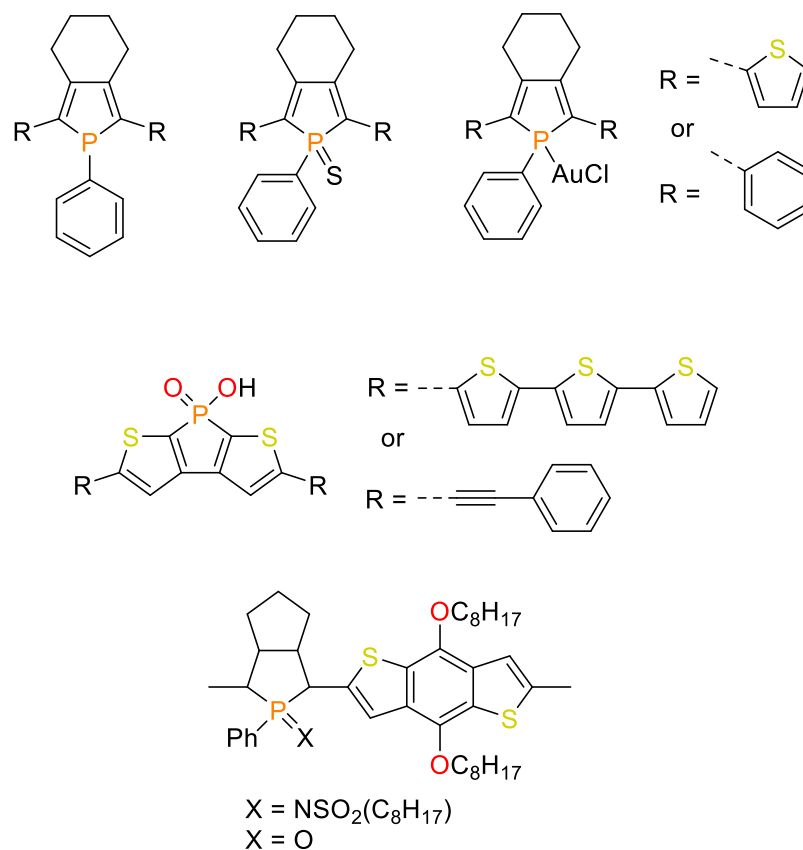


Figure 1.5: Examples of phosphole compounds used in optical devices.

In contrast to phospholes, the photophysical properties of arsoles are significantly underexplored, a consequence perhaps of their toxicity. Nevertheless, the use of arsoles in such solid-state devices could be advantageous over their phosphorus analogues given their greater oxygen tolerance⁴⁰ and high inversion barrier of the trigonal pyramidal coordination geometry.²² The Naka group in 2015 published the synthesis of 2,5-diarylarsoles which showed intense emission in both solution and solid-state. The diarylarsole (where R = H) in solution showed an absorption band at 374 nm in chloroform solvent and an emission maximum at 458 nm, with accompanying quantum yield of 59%. Meanwhile, solid-state measurements gave emission at 482 nm and a reduced quantum yield of 21%. The diarylarsole with R = *o*-OMe had absorption and emission maxima that were red-shifted from the former unsubstituted 2,5-diarylarsoles. The diarylphosphole (where R = H) was also synthesised to act as a comparison, and it was found that the absorption and photoluminescent values were very similar to diarylarsole. In addition to this, Naka and colleagues controlled the optical properties of the diarylarsole by coordinating it to Au(I)Cl, which after coordination the quantum yield in solution increased to 86%, although it was only 17% in the solid-state.⁴¹ Later in 2016 Naka followed up on this work by showing that

these 2,5-diarylarsoles can undergo mechanochromism because of their molecular packing in the crystalline state, which showed only weak intermolecular interactions exist. Crystals of the diarylarsoles were ground in a mortar, and measurements of these now ground crystals displayed a hypsochromic shift (blue shift) compared to the starting crystals (Figure 1.6).⁴²

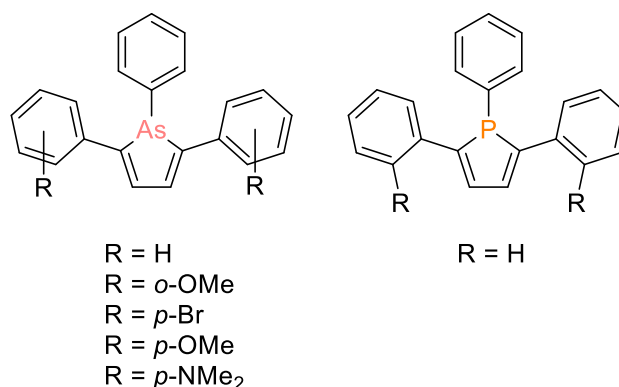


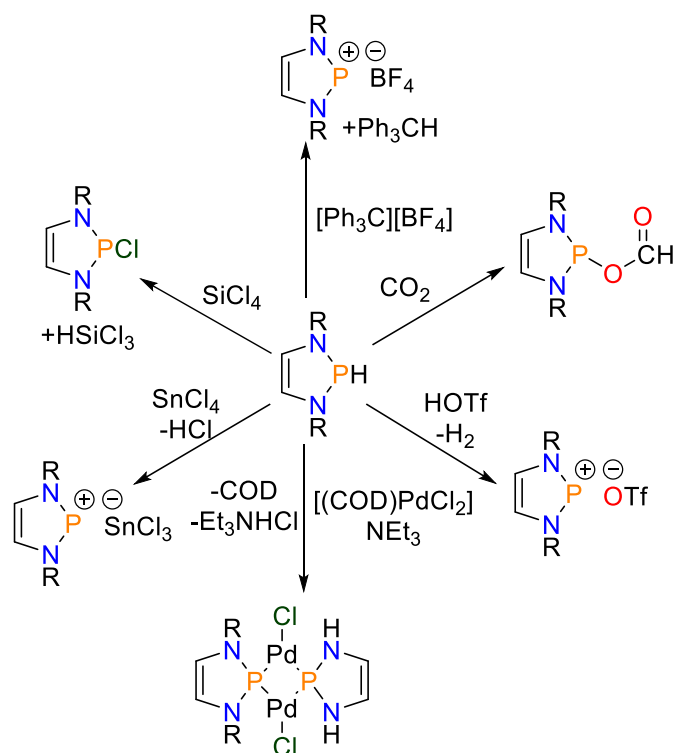
Figure 1.6: Examples of arsole and phosphole compounds used by the Naka group.

1.1.4 Introduction to diazaphospholenes and diazarsolenes

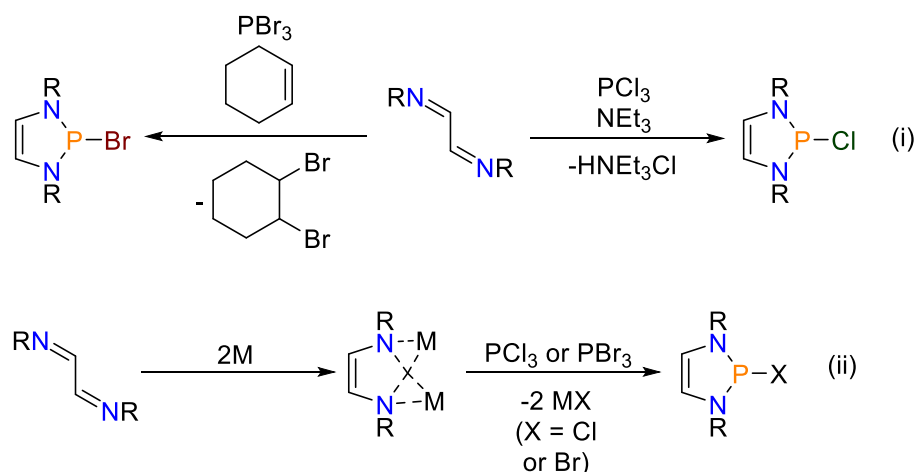
Heterocyclic phosphorus and arsenic chemistry certainly expands beyond the traditional phosphole and arsole ring. Another class of group 15 heterocycle that is closely related to phospholes are diazaphospholenes (DAPs), which are N-heterocyclic phosphines contained within a five membered unsaturated ring. Gudat has recently written an excellent review into this topic and so their chemistry will not be exhaustively discussed, with just the key features mentioned.⁴³ Initial interest in diazaphospholenes intensified in the 1990s when it was discovered that they could act as precursors to phosphonium cations (which are isoelectronic to NHCs; *vide infra*),⁴⁴ resulting in their structure, bonding and reactivity to be more closely examined. From these studies an interesting feature to emerge was the possibility of 6π -delocalisation in the five-membered ring unit, however to achieve this the $\sigma^*(\text{P-X})$ -antibonding orbital is required. This in turn reduces the bond order of the P-X bond and transfers additional negative charge on the X atom. Thus, a compromise is reached where greater energetic stabilisation in the DAP ring is achieved but at the cost of a loss of the degree of covalency in the P-X bond. The extent of this hyperconjugation was found to be highly dependent on the nature of the exocyclic X atom.⁴⁵ Expanding on this theme further, Gudat and colleagues looked to synthesise a diazaphospholene where X = H to look at what effect this would have on the electronics. The result was ground breaking as it was found that unlike classical systems where the reactivity of P-H bonds is governed by the protic character of the hydrogen atom, in diazaphospholenes because of donation of π -electron density into the $\sigma^*(\text{P-H})$ orbital the P-H bond is hydridic.⁴⁶ This finding would prove

pivotal later when these compounds would be used in catalysis (see section 1.3). Scheme 1.1 below highlights a number of reactions where the umpolung reactivity of the P–H bond has been exploited, including in phosphonium generation,^{46,47} reduction of SiCl_4 ⁴⁷ and stabilisation of metal(0) complexes.⁴⁸

Synthetically diazaphospholene compounds are straight forward to produce and commonly involve a one-pot synthesis from the appropriate diazadiene and phosphorus trihalide in the presence of auxiliary reagents. When using PCl_3 as the phosphorus trihalide triethylamine is also used, giving the salt HNEt_3Cl as a by-product, whereas cyclohexene is used with PBr_3 , giving 1,2-dibromocyclohexane. Alternatively, DAPs may be synthesised in a two-step procedure starting by reducing the diazadiene to its dianion (such as by using lithium or sodium metal) and then undergoing metathetic ring closure.⁴³ Both procedures are displayed below in Scheme 1.2.



Scheme 1.1: Selected stoichiometric reactions involving the use of diazaphospholenes (COD = 1,5-cyclooctadiene). Scheme adapted from Gudat review.⁴³



Scheme 1.2: Synthesis of diazaphospholene. (i) One pot synthesis from diazadienes and PX_3 . (ii) Two step procedure, $M = \text{metal (Li or Na)}$. Scheme adapted from Gudat review.⁴³

The arsenic analogue of the diazaphospholene is termed diazarsolene. Early examples of diazarsolidines (five membered ring heterocycle containing arsenic but a saturated backbone) were reported by Wolf⁴⁹ and Cowley,⁵⁰ but a literature search into diazarsolenes gave few results. Minkin and colleagues computationally looked at the energy barrier of pyramidal inversion in diazarsolenes,⁵¹ but synthetic work is rare. However, Nieger *et al.* previously reported the synthesis of 2-halogeno-1,3,2-diazarsolenes (Figure 1.7). In this work the diazarsolene was prepared from α -amino-aldimine *via* base-induced dehydrohalogenation with $AsCl_3$, with tert-butyl or mesityl groups on the nitrogen atoms. Single crystal X-ray diffraction and spectroscopic analyses showed that as is the case in diazaphospholenes, diazarsolenes are stabilised by π -delocalisation effects, leading to elongation in the $As-X$ bond.⁵² As is shown below in Scheme 1.5, the diazarsolene with mesityl groups was then used by Gudat to synthesise the corresponding arsenium cation and coordinate it to a transition metal.⁵³ Note that later work by Ragona used a diazarsolene moiety with a conjugated bithiophene backbone to act as precursors for cation synthesis. This was achieved by abstracting the chloride using trimethylsilyl trifluoromethanesulfonate (TMS triflate), after which the cation was coordinated to $Pt(PPh_3)_4$.⁵⁴

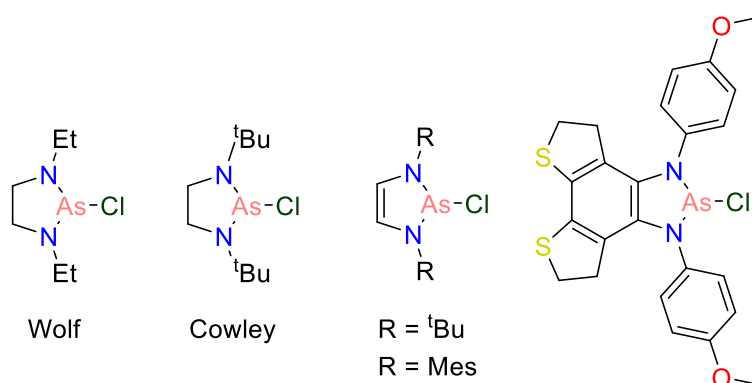
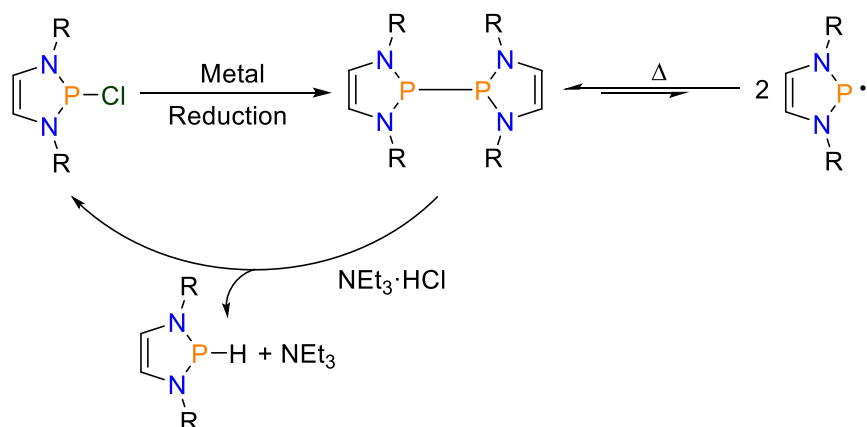


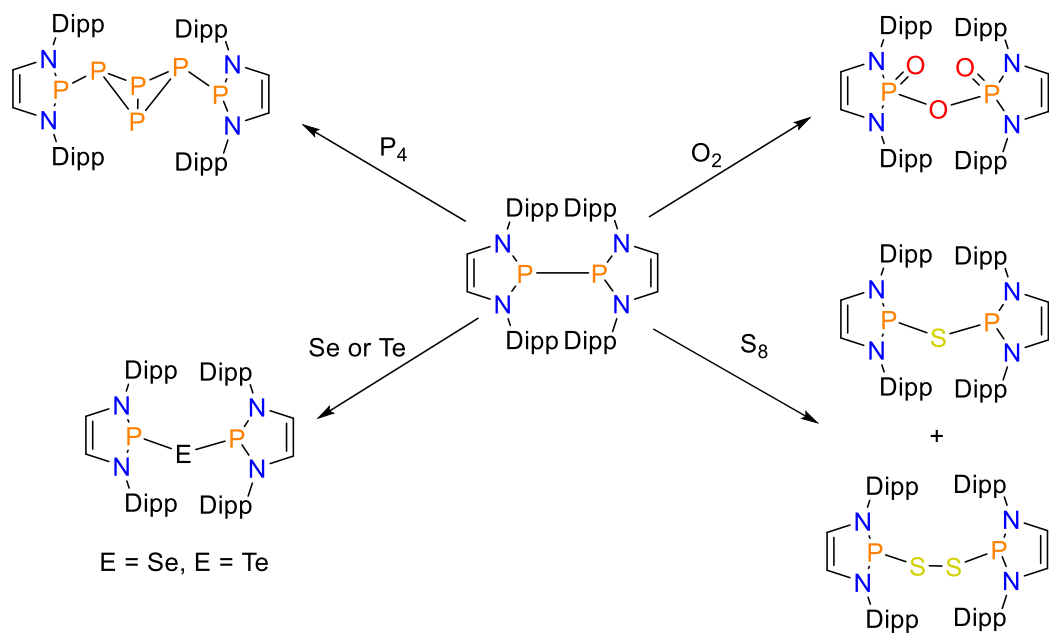
Figure 1.7: Examples of diazarsolidines and diazarsolenes.

1.1.5 Use of diazaphospholenes to make dimers.

One use diazaphospholene compounds have seen is in the formation of P–P dimers, which are synthesised by their reduction with metals (typically Mg, Na or Li). The possibility that these compounds can undergo homolytic cleavage when heated and form radicals has been a major driving force for their research interest, with the groups of Gudat,^{55–57} Masuda⁵⁸ and Wright⁵⁹ all having reported examples of these dimers. Gudat and colleagues have previously synthesised the 1,1'-3,3'-tetrahydro-2,2'-bi-1,3,2-diazaphosphole dimer and by using variable-temperature electron paramagnetic resonance (VT-EPR) studies found that the bond dissociation energy is 79 KJ mol⁻¹.⁵⁶ Gudat also found that the corresponding radical that is formed may be reacted with ammonium salts to form a mixture of secondary phosphanes and chlorophosphanes (Scheme 1.3).⁵⁷ Meanwhile, Masuda has showed that the P–P bond may be oxidatively cleaved by reacting it with chalcogens and P₄ to yield the related phosphinic acid anhydride, sulphide/disulphide, selenide, telluride and a perphospha-bicyclo-butadiene structure with *trans,trans*-geometry (Scheme 1.4). Although the As–As dimer is known, which was prepared from AsCl(CH(SiMe₃)₂)₂, literature examples from diazarsolene compounds is not.⁶⁰



Scheme 1.3: General synthesis for forming the P-P dimer, subsequent radical formation and reactivity with ammonium salt.



Scheme 1.4: Oxidative addition of P-P dimer using chalcogens and P₄.
Dipp = 2,6-diisopropylphenyl.

Chapter 1.2 Recent Interest in Phosphorus and Arsenic Lewis Acids

1.2.1 Introduction to phosphonium and arsenium compounds

If the heterocycles described above contain a halogen atom adjoining the phosphorus/arsenic centre they may undergo halide abstraction using simple Lewis acids, such as AlCl_3 or GaCl_3 , or by salt metathesis, for example with triflate salts, to form the corresponding phosphonium or arsenium cations.^{61,62} First reported by Dimroth and Hoffmann in 1964,⁶³ a phosphonium cation is defined as a two coordinate phosphorus complex that has a formal positive charge on the phosphorus heteroatom and takes the form $[\text{PR}_2]^+$. Phosphonium cations possess a lone pair of electrons and a vacant p -orbital, which means they have ambiphilic properties of both a Lewis acid and Lewis base. N-heterocyclic phosphoniums (NHPs) with their divalent nature and similar frontier orbital layout (Figure 1.8) means comparisons can be made with the familiar Arduengo N-heterocyclic carbenes (NHCs). NHCs and NHPs are isolobal with each other, but the latter has inverse electronic properties of being a weaker σ -donor but much stronger π -acceptor; a consequence of the formal positive charge and +3 oxidation state at phosphorus.^{64,65}

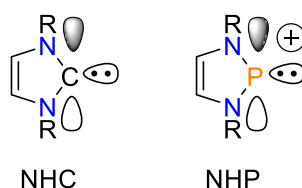


Figure 1.8: Comparison of the frontier orbitals shown in an NHC and NHP.

As a result of their inherent properties, traditionally phosphonium cations have been utilised as ligands for low valent late transition metals,⁶⁵⁻⁷⁰ with theoretical calculations suggesting that the bonding is dominated by their acceptor properties.^{45,71} An interesting feature with using NHPs as ligands in coordination chemistry is that they closely resemble the nitrosyl ligand NO^+ , not only with regards to the cationic charge but also as they are able to adopt two different binding modes (Figure 1.9). When coordinated to an electron rich metal, the NHP adopts a pyramidal geometry to the metal centre, suggesting the lone pair is not involved in the bonding, such as that seen in $\text{Cp}^*(\text{CO})_2\text{Fe}-(\text{NHP}^{\text{Me}})$.⁷² On the other hand, when coordinated to an electron poor metal a planar geometry at phosphorus of the NHP is preferred, where it acts as both a σ -donor and π -acceptor. A resulting double bond is formed between the NHP and metal centre, an example of which is seen in $\text{Cp}-(\text{CO})_2\text{Mo}(\text{NHP}^{\text{Me}})$.⁷³ The use of a phosphonium cation offers potential benefits as a ligand when compared to NO^+ as the former may be tailored to have certain electronic properties

through changing the ligand scaffold, which in turn can also change the steric properties of the NHP.

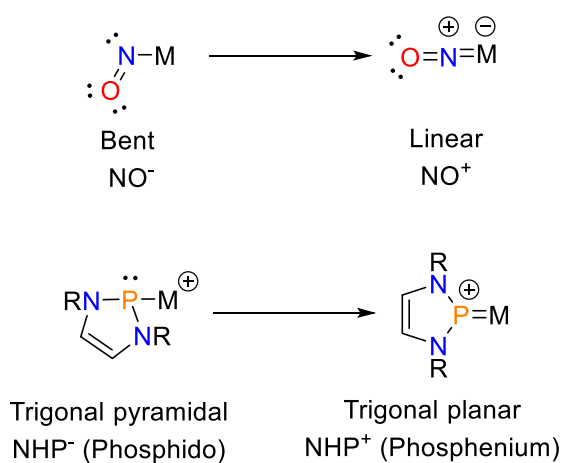
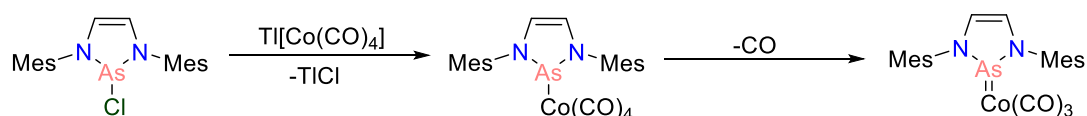


Figure 1.9: Bonding modes of the NO^+ and NHP ligands to a transition metal (M). Note the use of the lone pair in the bonding model for the right hand side structures.

Much of what was described for phosphenium cations is true for the heavier arsenium cations, in that they are divalent arsenic compounds with a positive charge. Synthesised first by Burford in the 1990's,⁷⁴ unlike their phosphorus counterpart these cations are much rarer, though examples are known.^{50,54,75,76} Although a lone pair and a vacant p -orbital still are present, their bonding to transition metals is typically confined to Lewis acid chemistry, where there is little to no σ -donation from the lone pair.^{62,77} This is due to the heavier pnictogen elements having a greater reluctance to form a trigonal planar geometry and so the lone pair adopts more s -orbital character.⁵³ Consequently, well characterised double bonded carbene analogues to the transition metal centre are not common. Indeed, although the complex $[\text{CpMo}(\text{CO})_2=\text{EMe}_2]$ ($\text{E} = \text{As}, \text{Sb}$) was observed from matrix isolation techniques,⁷⁸ the first formal double bond arsenium–metal complex was not reported until Gudat and colleagues prepared $[\text{Co}(\text{AsR}_2)(\text{CO})_3]$ from the reaction of 2-chloro-1,3,2-diazarsolenes with $\text{Tl}[\text{Co}(\text{CO})_4]$ in 2005 (Scheme 1.5).⁵³



Scheme 1.5: Formation of $[\text{Co}(\text{AsR}_2)(\text{CO})_3]$ with an $\text{As}=\text{Co}$ double bond.

1.2.2 Lewis acidity of phosphenium and arsenium cations

The reactivity of phosphenium and arsenium cations is dominated by their formal positive charge, empty $3p/4p$ -orbital and lone pair of electrons. The Lewis acidity of phosphenium

cations can be clearly observed by their formation of classic Lewis acid-base adducts, such as with phosphines,⁶⁵ carbenes,⁷⁹ amines⁸⁰ and imines,⁸¹ whereas arsenium cations have been known to form Lewis acid-base type dimeric structures with sulfur atoms interacting with arsenic in solution.⁷⁴ One of the first attempts to measure quantitatively the Lewis acidity of phosphonium and arsenium cations though was by Wolf *et al.* who measured their Lewis acidity based on their ability to coordinate pyridine. By looking at the change in the chemical shift of the C-4 carbon in pyridine by ¹³C{¹H} NMR spectroscopy the equilibrium constant K_c was determined, which in turn was used to measure the Lewis acidity. This study found that the trend in Lewis acidity was cyclic<acyclic, diamino<dithia and rather interestingly arsenium<phosphonium.⁸²

The Lewis acidity of phosphonium cations has more recently been explored by Slattery and Hussein using the computationally determined Fluoride Ion Affinity (FIA). In this method the attraction the Lewis acidic phosphonium has for the Lewis basic fluoride is measured and the negative enthalpy of reaction is the FIA; a greater enthalpy signifies greater Lewis acidity. These FIA calculations found that the inclusion of π -donor substituents help stabilise the phosphonium cation, which in turn reduces the Lewis acidity, a feature seen by Wolf.⁸² Further reductions in Lewis acidity were caused by inductive as well as steric effects, where it was found the use of very bulky ligands significantly reduce the FIA. Some of the FIA values calculated are shown in Figure 1.10.⁸³

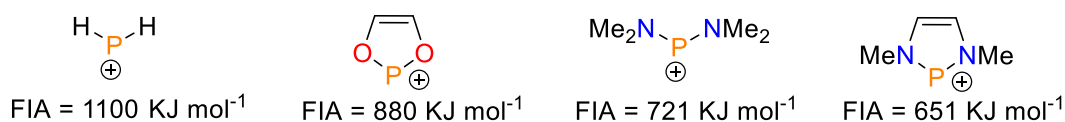


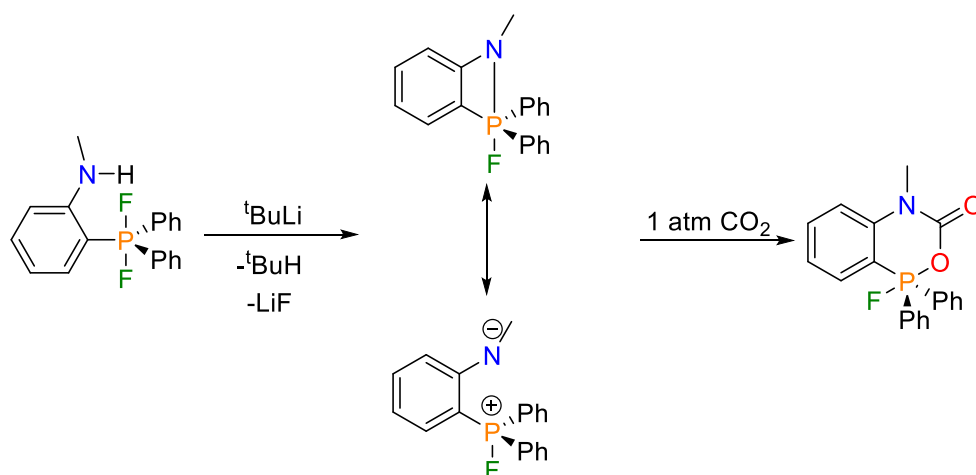
Figure 1.10: Example FIA values of phosphonium cations, theory MP2 (RI-)BP86/SV(P).

1.2.3 Introduction to phosphonium and arsonium compounds

Although not necessarily heterocyclic compounds, it is worth briefly discussing phosphonium and arsonium compounds when discussing group 15 Lewis acids. Unlike phosphonium and arsenium compounds, which are formally in a +3 oxidation state, phosphonium and arsonium complexes are in a +5 oxidation state. They have the general formula PR_4^+/AsR_4^+ where R = alkyl, aryl, halide or H. Pentacoordinate phosphorus/arsenic compounds with electron withdrawing substituents have been known for some time to be Lewis acidic due to the presence of a low lying σ^* -orbital and these complexes are known to form traditional Lewis acid and Lewis base adducts.⁸⁴ The formation of a phosphonium or arsonium cation can proceed by a number of routes, but perhaps the most recognised is by the alkylation of organophosphines, such as the reaction of triphenylphosphine with methyl

iodide to give methyltriphenylphosphonium iodide. This is the precursor to a Wittig reagent.⁸⁵ Historically this is the biggest use of phosphonium compounds; their use in the Wittig reaction which transforms aldehydes and ketones to alkenes.⁸⁶

More recently the phosphonium cation has received significant attention from the group of Stephan as part of their FLP work. They have also written an extensive review on the subject.⁸⁷ Stephan and co-workers have previously reported the irreversible sequestration of CO₂ using an aminophosphonium salt, which was prepared by the reaction of *o*-phosphinoaniline with XeF₂. Subsequent addition of ^tBuLi and fluoride abstraction generated the amidophosphorane Ph₂PF(*o*-C₆H₄NMe). Exposure of the amidophosphorane to 1 atm of CO₂ at room temperature gave insertion into the P–N bond, giving the product Ph₂PF(*o*-C₆H₄NMe)(CO₂) (Scheme 1.6). This reactivity is believed to stem from the P–N FLP behaviour.⁸⁸

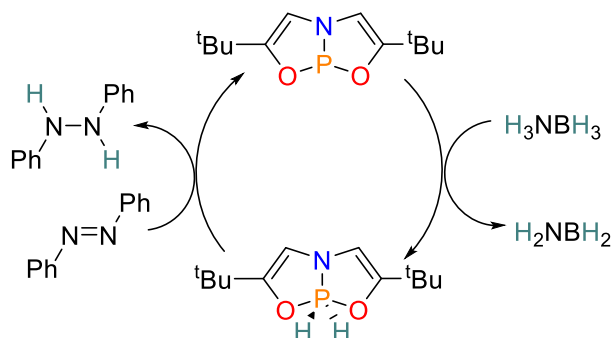


Scheme 1.6: Use of phosphonium in CO₂ sequestration.

The growing use of highly electrophilic fluorophosphonium cations (EPCs) led to a number of studies to try and quantify how Lewis acidic these compounds are. Deriving their Lewis acidity from low lying P–F σ*-orbital, attempts to perform the experimentally well-known Gutmann-Beckett (coordination with triethylphosphine oxide) or Childs methods (coordination to crotonaldehyde) are plagued with difficulty, so in 2015 Stephan and colleagues synthesised an array of these EPCs and computationally measured the Lewis acidity using Fluoride Ion Affinity (FIA) calculations. FIA is defined as the negative of the reaction enthalpy of adding a fluoride to the phosphonium. As expected, the electrophilicity of the phosphonium species were found to increase with more electron withdrawing substituents added, and in fact when two -C₆F₅ groups were added, the Lewis acid B(C₆F₅)₃ was not able to abstract the fluoride. Using the theory level WB97XD/def2TZV, the phosphonium [^tBu₃PF]⁺ was found to have an FIA of 163 KJ mol⁻¹, [Ph₃PF]⁺ 200 KJ mol⁻¹ and

$[(C_6F_5)_3PF]^+$ 311 KJ mol^{-1} . For reference, using this theory level $B(C_6F_5)_3$ has an FIA of 260 KJ mol^{-1} .⁸⁹ Another computational method for determining Lewis acidity is the Global Electrophilicity Index (GEI), which simply put is a measure of the ability of molecules to take up electrons. It is often denoted as ω . In 2018 Stephan applied this to phosphonium compounds, which generally speaking follow the same trend as the FIA calculations.⁸⁹ To try to make EPCs more accessible, a range of phenoxy-substituted phosphonium cations were prepared, and whereas their GEI was lower than $[(C_6F_5)_3PF]^+$, the addition of fluorine atoms to the phenoxy ring does increase their Lewis acidity.⁹⁰

A nice example that ties together P(III) and P(V) chemistry (which would help inspire Kinjo to catalytically use diazaphospholenes for catalysis; see Chapter 1.3) is the work by Radosevich, who first reported the reversible two-electron redox cycling of P(III)/P(V), which enabled it to be used for transfer hydrogenation reactions. This was achieved by using a three-coordinate phosphorus species with an NO_2 type pincer ligand that forced a strained, planar T-shaped geometry. The reaction of catalytic (10 mol%) trivalent phosphorus species with ammonia-borane gives the dihydridophosphorane intermediate, which transfers hydrogen to azobenzene. It was proposed that this occurs by the ammonia-borane firstly protonating the trivalent phosphorus species, generating a phosphonium intermediate, which then abstracts a hydride from the aminoborane. The transfer of hydrogen to azobenzene gives the product diphenylhydrazine and regenerates the catalyst (Scheme 1.7).⁹¹



Scheme 1.7: Transfer hydrogenation and redox cycling between P(III) and P(V).

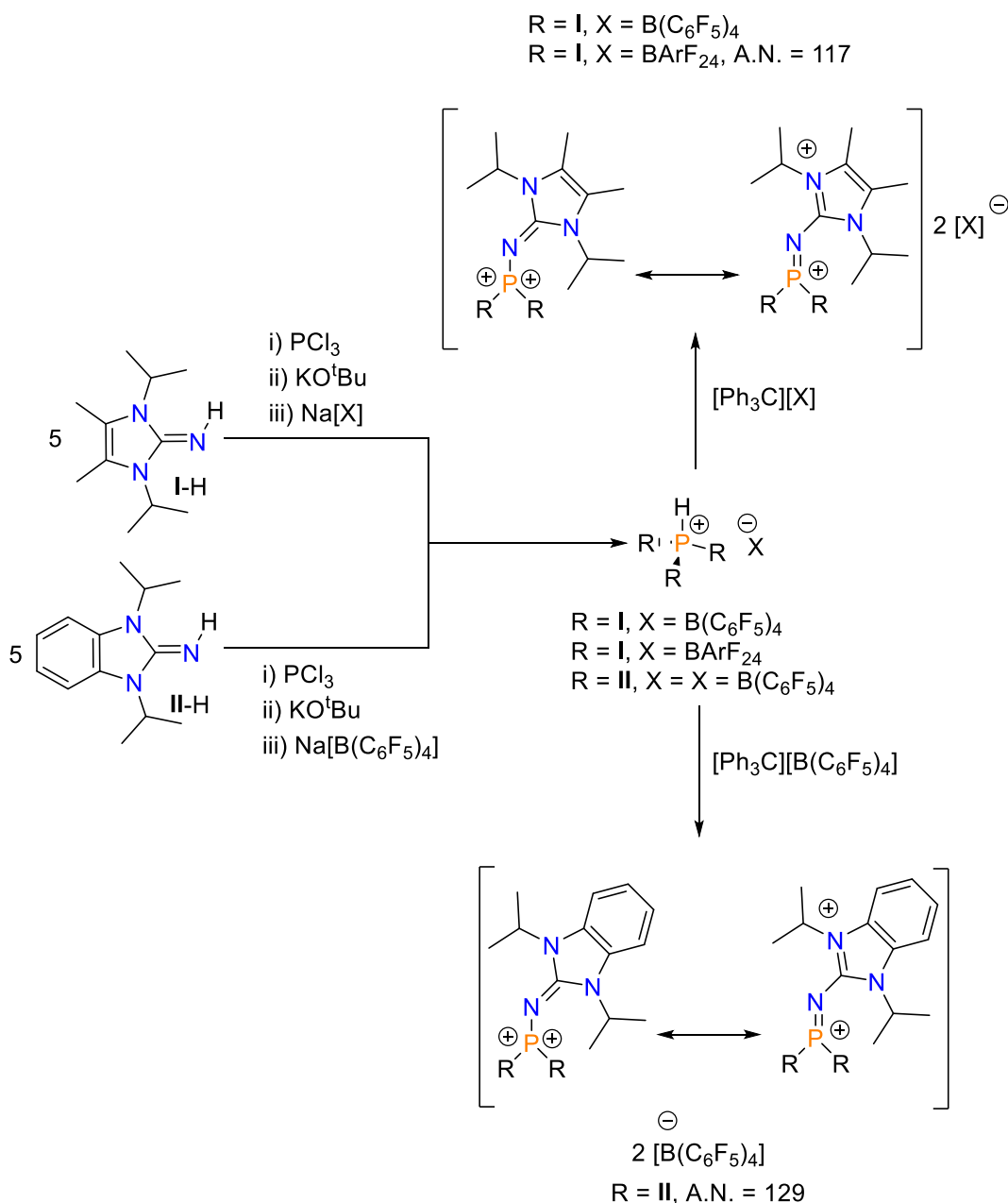
As is the theme of this introduction, there is much less reported on arsonium cations than their phosphorus counterpart. The rise of the Wittig phosphonium ylide led to the arsonium ylide, driven principally by the fact that phosphonium ylides are relatively unreactive towards certain substrates, such as ketones. These ylides are typically prepared in an analogous fashion to their phosphonium counterparts.⁹² The chemistry of arsonium ylides has previously been reviewed.^{92,93} However, unlike growth in EPCs, examples of highly

electrophilic fluoroarsonium cations are not known, despite fluorinated stibonium⁹⁴ and bismuthonium⁹⁵ salts being reported.

1.2.4 Phosphorus and arsenic super Lewis acids

On the theme of Lewis acids, it is worth touching on the rise of group 15 strong Lewis acids, which have been used in FLP chemistry as well as catalysis.^{87,96} Given the Stephan group's interest in Lewis acids, they have recently reported a η^5 -pentamethylcyclopentadienyl phosphorus dication that is a super Lewis acid. Here a super Lewis acid is defined as a species that can abstract a fluoride from the anion $[\text{SbF}_6]^-$, which would correspond to an acceptor number greater than 100 using the Gutmann-Beckett method determination of Lewis acidity.⁹⁷ This super Lewis acid was first prepared by abstracting a fluoride from Cp^*PF_2 with two equivalents of the silylium salt $[\text{Et}_3\text{Si}][\text{B}(\text{C}_6\text{F}_5)_4]$, giving $[(\eta^5\text{-Cp}^*)\text{P}][\text{B}(\text{C}_6\text{F}_5)_4]_2$. This was then shown to be able to abstract a fluoride from $[\text{SbF}_6]^-$, giving the product $[(\eta^5\text{-Cp}^*)\text{PF}][\text{B}(\text{C}_6\text{F}_5)_4]$, as well as meeting the criteria for super Lewis acidity. In probing the source of this enhanced Lewis acidity, DFT calculations suggested that the LUMO and LUMO+1 energy levels are degenerate in energy and comprise of the vacant p -orbitals on the phosphorus atom. Furthermore, NBO analyses found a highly positively charged phosphorus atom (+1.08 a.u.).⁹⁸

Another example of a phosphorus super Lewis acid is from Dielmann and colleagues, who reported a phosphorus dication isoelectronic to silylium cations. This dication was prepared by first synthesising the phosphonium salt with $\text{B}(\text{C}_6\text{F}_5)_4^-$ and BArF_{24}^- counterions, which involved the addition of phosphorus(III) chloride to excess N-heterocyclic imine, followed by exchange of the chloride with weakly coordinating anions. Hydride abstraction of the phosphonium salts with trityl salt gave the desired phosphorandiylum ions, and when using the Gutmann-Beckett method an acceptor number (A.N.) of 117 was obtained ($X = \text{BArF}_{24}^-$), thus confirming super Lewis acidity. Developing this, Dielmann *et al.* realised that the electronic properties of the phosphorus atom could be modified by manipulating the imidazoline backbone. With a new N-heterocyclic imine bearing a benzene ring, the same synthetic procedure to produce was followed. Remarkably, the Gutmann-Beckett method gave an acceptor number of 129 for this phosphorandiylum ions. The enhanced Lewis acidity was rationalised by the reduced π -electron donating ability of the latter N-heterocyclic imine. DFT methodology suggested the Lewis acidity is a result of the low energy level of the LUMO (-6.81 eV).⁹⁹ The synthesis is shown below in Scheme 1.8.



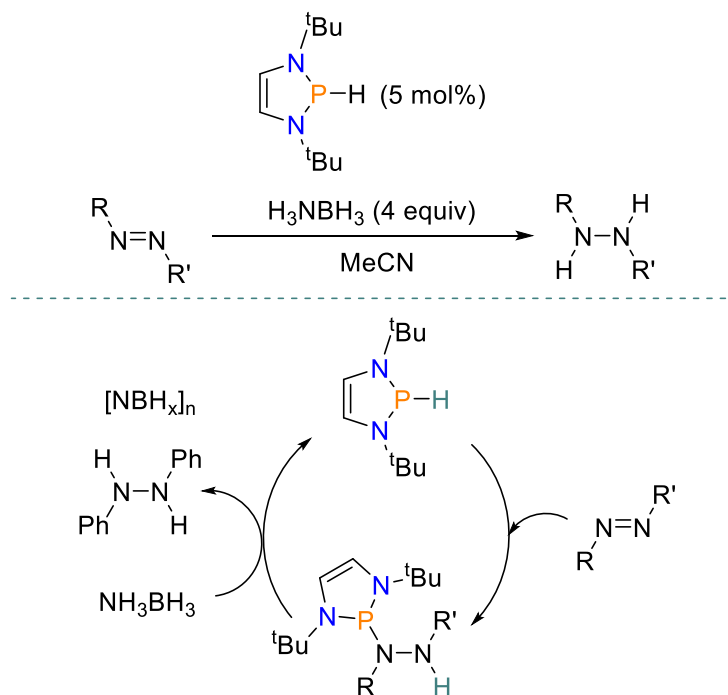
Scheme 1.8: Synthesis of super Lewis acidic phosphorandiyl cations.

As well as phosphorus, an arsenic super Lewis acid has recently been published, again from the group of Stephan. Its synthesis was similar to that of their phosphorus super Lewis acid $[(\eta^5\text{-Cp}^*)\text{PF}][\text{B}(\text{C}_6\text{F}_5)_4]$, where double chloride abstraction of Cp^*AsCl_2 gave the dicationic arsenic species $[\eta^5\text{-Cp}^*)\text{As}(\text{tol})][\text{B}(\text{C}_6\text{F}_5)_4]_2$. Again, super Lewis acidity was confirmed by its ability to abstract a fluoride from $[\text{SbF}_6]^-$, giving the product $[(\eta^5\text{-Cp}^*)\text{AsF}][\text{B}(\text{C}_6\text{F}_5)_4]$. On account of its strong Lewis acidity, it was found to react with the Lewis base 2,2'-bipyridine (bipy) in 1,2-difluorobenzene (DFB) at -35°C , giving the product $[(\eta^1\text{-Cp}^*)\text{As}(\text{bipy})][\text{B}(\text{C}_6\text{F}_5)_4]_2$. Furthermore, the super Lewis acid was found to participate in the activation of THF, giving the product $[(\eta^2\text{-Cp}^*)\text{AsO}(\text{CH}_2)_4(\text{THF})][\text{B}(\text{C}_6\text{F}_5)_4]_2$.¹⁰⁰

Chapter 1.3 Heterocyclic Phosphorus(III) Lewis Acid Catalysis

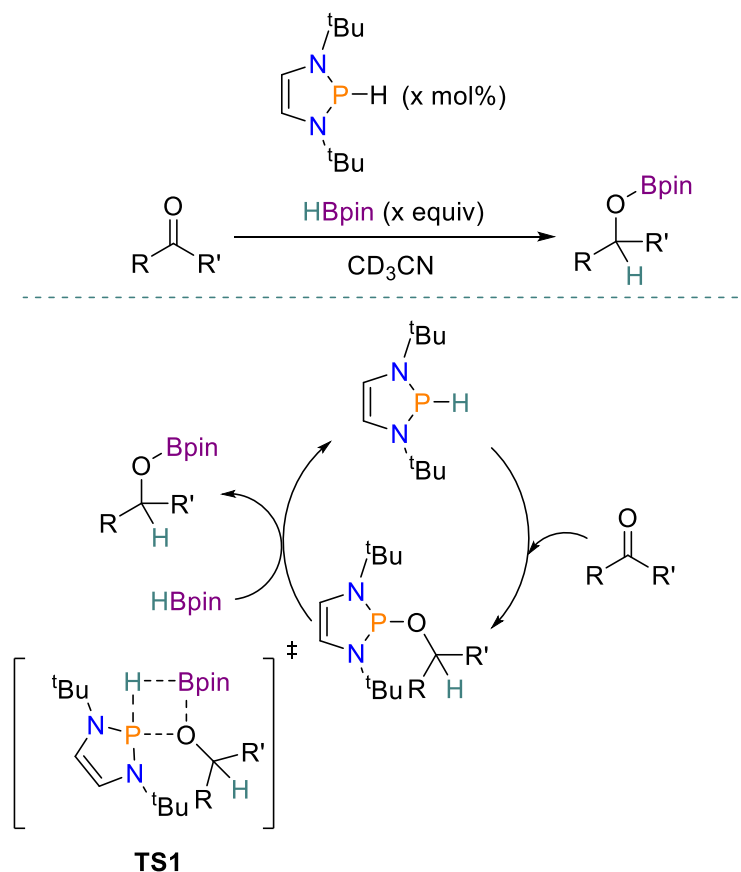
1.3.1 Catalysis performed by Kinjo group

Much has already been described of the fundamental chemistry of an array of heterocyclic pnictole compounds, but recently these compounds have received attention as pre-catalysts for a variety of reductions. Gudat first described the hydridic nature of the P–H bond in diazaphospholene compounds and showed using stoichiometric quantities that it could reduce benzaldehyde.⁴⁶ Then, Radosevich and co-workers reported the catalytic reduction of azobenzene using P(III)↔P(V) redox cycling (Scheme 1.7).⁹¹ These two observations led to the Kinjo group in 2014 to use 2-*H*-1,3,2-diazaphospholene as a catalyst for reduction of azobenzenes using ammonia-borane. After optimisation, 5 mol% of diazaphospholene with four equivalents of ammonia-borane were used for the reduction of a range of (*E*)-azo-compounds, giving the corresponding hydrazine product. Unlike in Radosevich's case, mechanistically this catalysis proceeded firstly by the addition of the P–H bond to the N=N bond to give phosphinohydrazine intermediate, then hydrogenolysis of the exocyclic P–N bond by hydrogen transfer from ammonia-borane occurs to give the product and regenerate the diazaphospholene catalyst (Scheme 1.9).¹⁰¹



Scheme 1.9: Reduction of azobenzenes with ammonia-borane using 2-*H*-1,3,2-diazaphospholene as a catalyst.

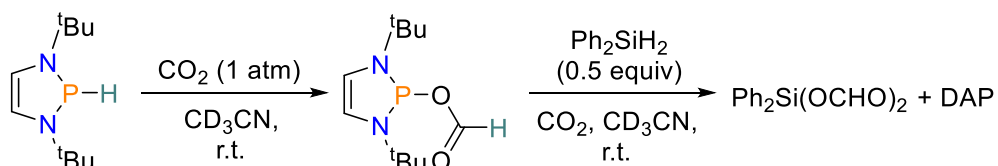
The Kinjo group continued to use 1,3,2-diazaphospholene compounds in catalysis and followed this work by reporting the hydroboration reduction catalysis of carbonyl compounds with pinacolborane (HBpin). Here catalytic amount of the diazaphospholene catalyst was able to reduce aldehydes (using 0.5 mol% cat.) and ketones (using 10 mol% cat.) with HBpin (1 equiv and 1.3 equiv respectively). A wide substrate scope was performed and the diazaphospholene was found to be tolerant to both aliphatic and aromatic aldehydes as well as a variety of ketones. Mechanistically this catalysis proceeds by the formation of an alkoxyphosphine intermediate from the addition of diazaphospholene to the carbonyl substrate, where subsequent cleavage of the P–O bond and the B–H bond in HBpin gives the hydroborated product and regenerates the catalyst. Kinetic studies along with DFT calculations found that the bond dissociation is involved in the rate-determining step in the transition state **TS1** and that the process is stepwise, albeit almost concerted (Scheme 1.10).¹⁰²



Scheme 1.10: General scheme for carbonyl reduction. 0.5 mol% cat. for aldehyde reduction and 1 equiv HBpin; 10 mol% cat. for ketone reduction and 1.3 equiv HBpin.

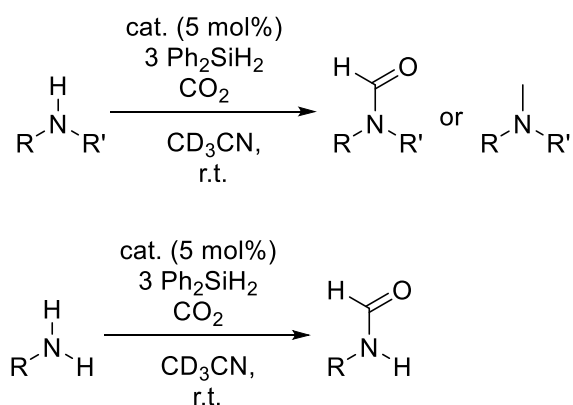
The use of CO₂ as a C1 source is potentially very powerful as it offers a non-toxic way to build more synthetically useful products in a cheap manner, but also gives a use for this harmful

greenhouse gas.¹⁰³ Because of this in 2015 Kinjo performed hydrophosphination of CO₂ with 2-*H*-1,3,2-diazaphospholene to give the phosphorus formate product. The formate group could then be transferred to Ph₂SiH₂, which formed Ph₂Si(OCHO)₂ (Scheme 1.11). Interestingly, the use of 5 mol% diazaphospholene was found to catalyse the formate transfer step, and as a result of these two reactions, Kinjo *et al.* undertook the catalytic *N*-formylation of amine compounds with CO₂ in a one pot reaction (Scheme 1.12).



Scheme 1.11: Reaction of DAP with CO₂ and subsequent formate transfer to Ph₂SiH₂. Where DAP = diazaphospholene.

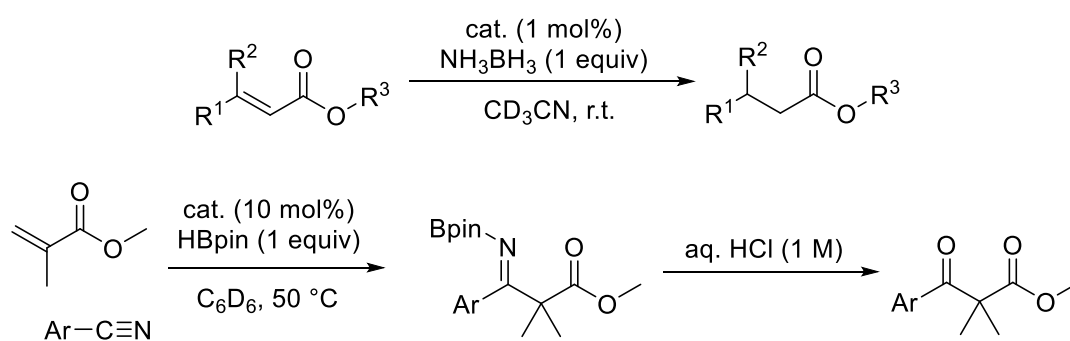
For the catalysis, a wide substrate scope of both primary and secondary amines was used. For the secondary amines, less-hindered aliphatic amines gave the *N*-formylamine in excellent yields of >90%, but an increase in sterics afforded *N*-methylated amines. Secondary amines containing aryl substituents were found to be tolerated. Expanding the scope, all aliphatic and aromatic primary amines tested were found to work well, with yields in the range of 72% to 99%.¹⁰⁴



Scheme 1.12: Catalytic *N*-formylation of secondary (top) and primary (bottom) amines with CO₂ using 2-*H*-1,3,2-diazaphospholene as a catalyst.

In 2017 Kinjo continued to use 2-*H*-1,3,2-diazaphospholene as a catalyst, this time for the reduction of α,β -unsaturated esters and subsequent C–C coupling with nitriles. Using 1 mol% catalyst, conjugate transfer hydrogenation from ammonia-borane was found to give reduction of the alkene moiety. In addition to this, the diazaphospholene was used to catalyse the 1,4-hydroboration of these α,β -unsaturated esters. The hydroborated product

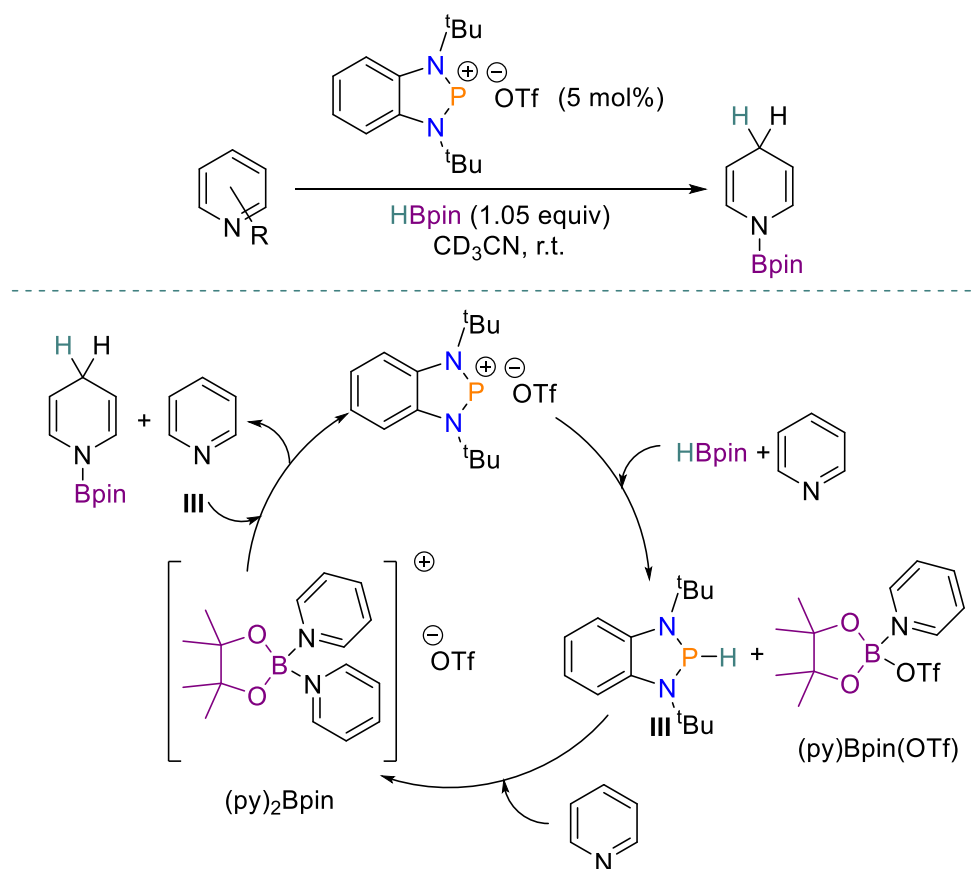
could then be coupled with nitriles to generate substituted amino diesters or 1,3-imino esters, depending on the nature of the α,β -unsaturated ester. Mechanistically the transfer hydrogenation and hydroboration is similar and involves a 1,4-hydrophosphination of the α,β -unsaturated ester to give a phosphinyl enol ether. Cleavage of the P–O bond in this ether by ammonia-borane gives an enol intermediate, which after tautomerisation gives the saturated ester. Meanwhile, cleavage of the P–O bond by HBpin by σ -bond metathesis produces a boryl enolate intermediate, which is then able to undergo the coupling reaction with nitriles. The general reactions are given below in Scheme 1.13.¹⁰⁵



Scheme 1.13: Conjugate transfer hydrogenation and 1,4-hydroboration of α,β -unsaturated esters.

Having successfully showed the diversity of reactions 2-*H*-1,3,2-diazaphospholene can catalyse, in 2018 Kinjo looked at using phosphonium cations as pre-catalysts. For this, a wide range of phosphonium triflate complexes were synthesised and then used as potential pre-catalysts for the hydroboration of pyridines with HBpin. Screening results showed that using 5 mol% phosphonium triflate was highly efficient for this catalysis, giving both regio- and chemoselectivity to the hydroborated product. A substrate scope showed that the phosphonium cation had good functional group tolerance when the pyridine ring was substituted in the *meta*-position, however when in the *ortho*- and *para*-position these substrates proved challenging. Mechanistically this catalysis proceeds in a different way to the hydroboration of carbonyl compounds using 2-*H*-1,3,2-diazaphospholene, given the cationic nature of the phosphonium. Investigating the mechanism, Kinjo and colleagues found that the first step involves hydride transfer from HBpin to the phosphonium, generating 1,3-di-*tert*-butyl-2,3-dihydro-1*H*-benzo-1,3,2-diazaphosphole (**III**) and the

boronium salt [(py)₂Bpin]OTf. The second step is then reduction of the activated pyridine using the diazaphosphole intermediate I (Scheme 1.14).¹⁰⁶



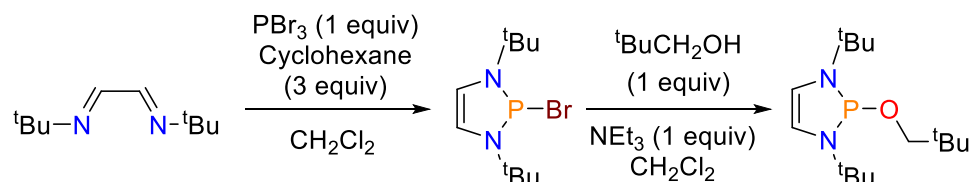
Scheme 1.14: General scheme and catalytic cycle for pyridine reduction.

1.3.2 Catalysis performed by Speed group

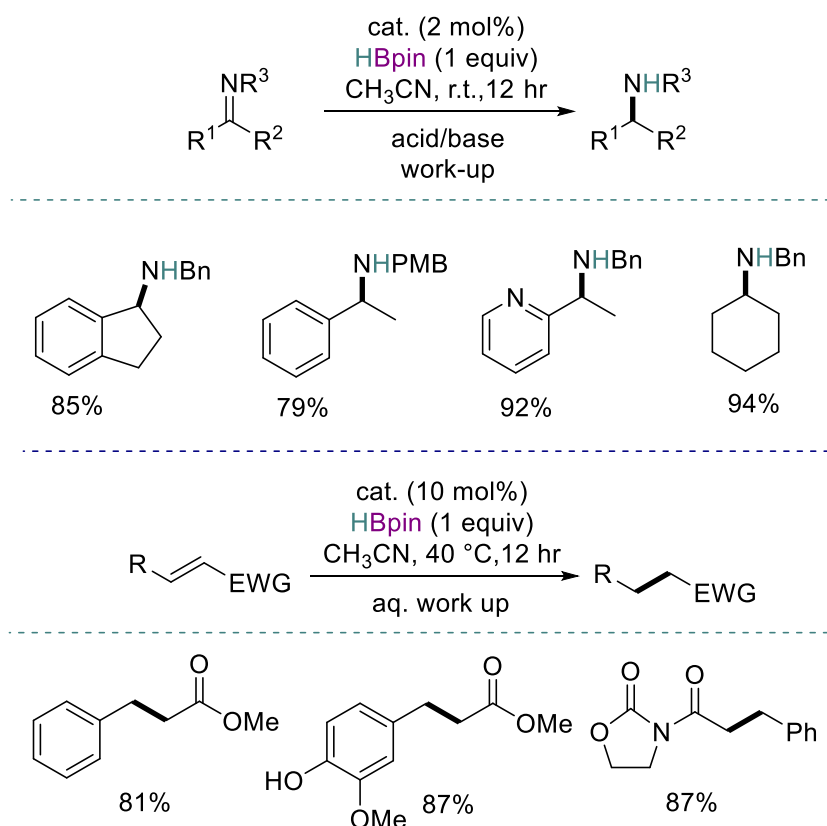
During the time the Kinjo group were performing this reduction catalysis, the Speed group were also interested in exploiting the inherent reactivity of diazaphospholene compounds. In 2017 Speed and workers reported the use of a diazaphospholene pre-catalyst that efficiently reduces imines with HBpin. Unlike Kinjo who used the diazaphospholene hydride, Speed used a neopentyloxy-diazaphospholene pre-catalyst that could be handled in air and would form the highly air and moisture sensitive 2-*H*-1,3,2-diazaphospholene catalyst upon addition with HBpin *via* σ -bond metathesis. Mechanistically after this the catalysis proceeds in an analogous way to the carbonyl reduction shown by Kinjo (Scheme 1.10).¹⁰² To synthesise the pre-catalyst, the appropriate diimine was added to stoichiometric phosphorus(III) bromide and three equivalents of cyclohexane to form the bromodiazaphospholene, which was then added to stoichiometric neopentyl alcohol to give the neopentyloxy-diazaphospholene (Scheme 1.15).

Optimisation reactions for the imine reduction found that the optimal conditions to use for the catalysis were 2 mol% pre-catalyst and one equivalent of HBpin at room temperature. A

host of amines were used in the substrate scope, with sterically hindered indanone-derived imine and aldimines with different steric demand tolerated. A Lewis basic pyridyl ring was found to give no detrimental effect and, using a *p*-methoxybenzyl (PMB) protecting group gave the expected reduced product. Having successfully reduced imines, Speed *et al.* looked to investigate the potential of the pre-catalyst and perform conjugate reduction with HBpin. Increasing the catalytic loading to 10 mol%, it was able to reduce conjugated ketones and esters (Scheme 1.16).¹⁰⁷



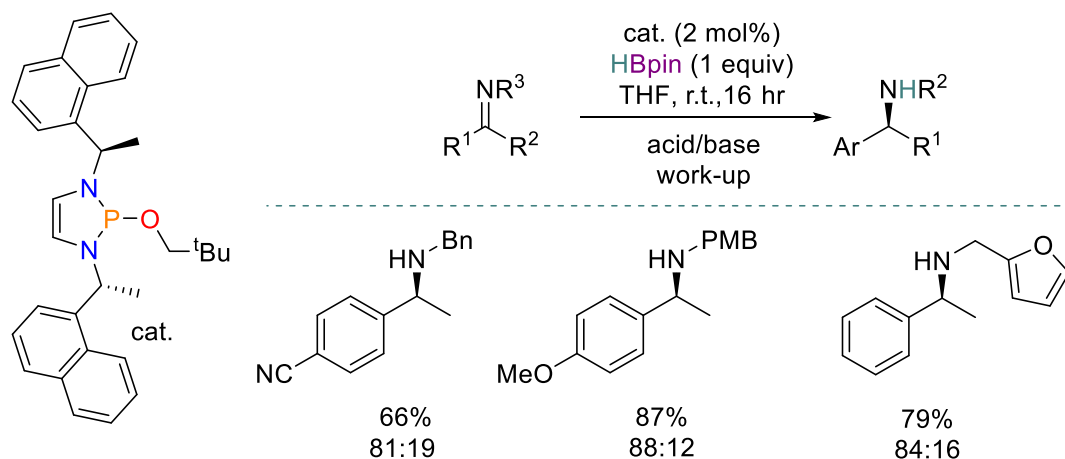
Scheme 1.15: Formation of neopentyloxy-diazaphospholene pre-catalyst from a diimine.



Scheme 1.16: Imine (top) and conjugate (bottom) reduction using neopentyloxy-diazaphospholene as a pre-catalyst, including selected substrate scope results. Bonds in bold indicate previous imine or alkene. Isolated yields after work-up.

The Speed group quickly followed up this result by reporting the first example of chiral diazaphospholene assisted catalysis, with asymmetric imine reduction with HBpin

(Scheme 1.17). Needing a source of chirality, a chiral diimine was used and the synthesis route of the chiral pre-catalyst followed that of the achiral neopentyloxy-diazaphospholene. Using the same optimised conditions as before, albeit with THF not CH₃CN, a substrate scope of imines flanked by aromatic groups revealed high enantiometric ratios of up to 88:12, with these results at the time being the best reported for alkyl imine hydroboration with HBpin.¹⁰⁸

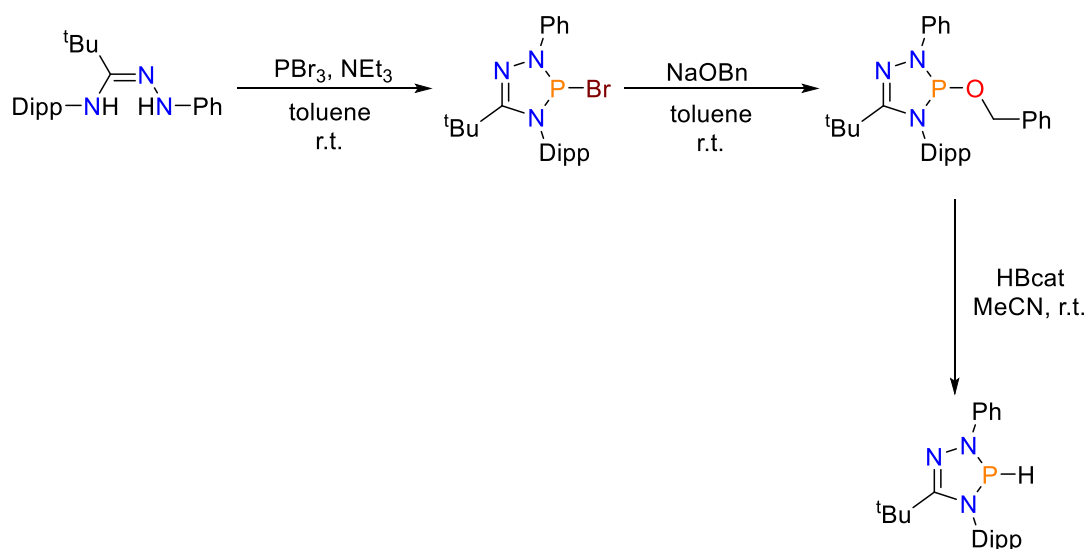


Scheme 1.17: Chiral diazaphosphole and selected substrate scope for chiral hydroboration of imines. Isolated yields after work-up. Enantiomeric ratio determined by HPLC analysis of the amine on a chiral stationary phase.

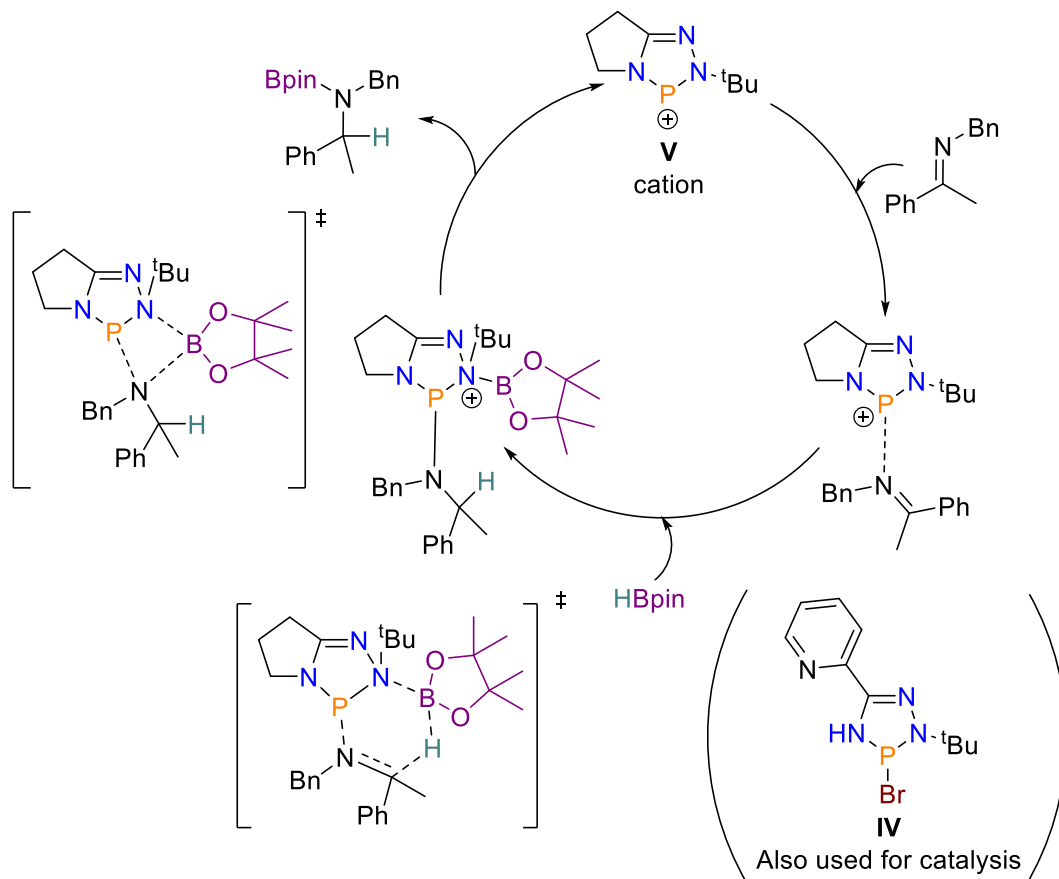
Continuing this theme, the Speed group in 2017 again published another example of imine reduction, but this time using a 1,2,4,3-triazaphospholene, which is believed to be the first example of this heterocycle partaking in catalysis. The triazaphospholene ring is similar to that of a diazaphospholene, except it contains three nitrogen atoms instead of two. Initial work led to triazaphospholene being synthesised by firstly reacting a bulky amidrazone with phosphorus(III) bromide and triethylamine, giving the triazaphospholene bromide. Treating the bromide intermediate with sodium benzyloxide substituted the bromide for an alkoxy group, which when added to catecholborane (HBcat) gave the triazaphospholene hydride, although it was not isolated (Scheme 1.18).

A series of less hindered triazaphospholene compounds were then made, and screening results found that the triazaphospholenes **IV** and **V** (Scheme 1.19) were the most suitable to proceed with a substrate scope. Using 10 mol% catalyst, a variety of imines were found to readily undergo hydroboration, but more interestingly imines derived from aniline were also readily reduced. Note this is of interest as these substrates do not undergo reduction using diazaphospholene catalysts. Mechanistically this catalysis is intriguing as unlike the other catalytic examples discussed so far, Speed found no evidence of P–H bond formation. Instead, **V** is ionised in MeCN, giving the cation, leading to an interaction between the

positively charged phosphorus on **V** and N atom from the imine. Hydride transfer *via* a six-membered transition state then occurs, after which the active catalyst is regenerated by releasing the borylated amine. The catalytic cycle is given below in Scheme 1.19.¹⁰⁹

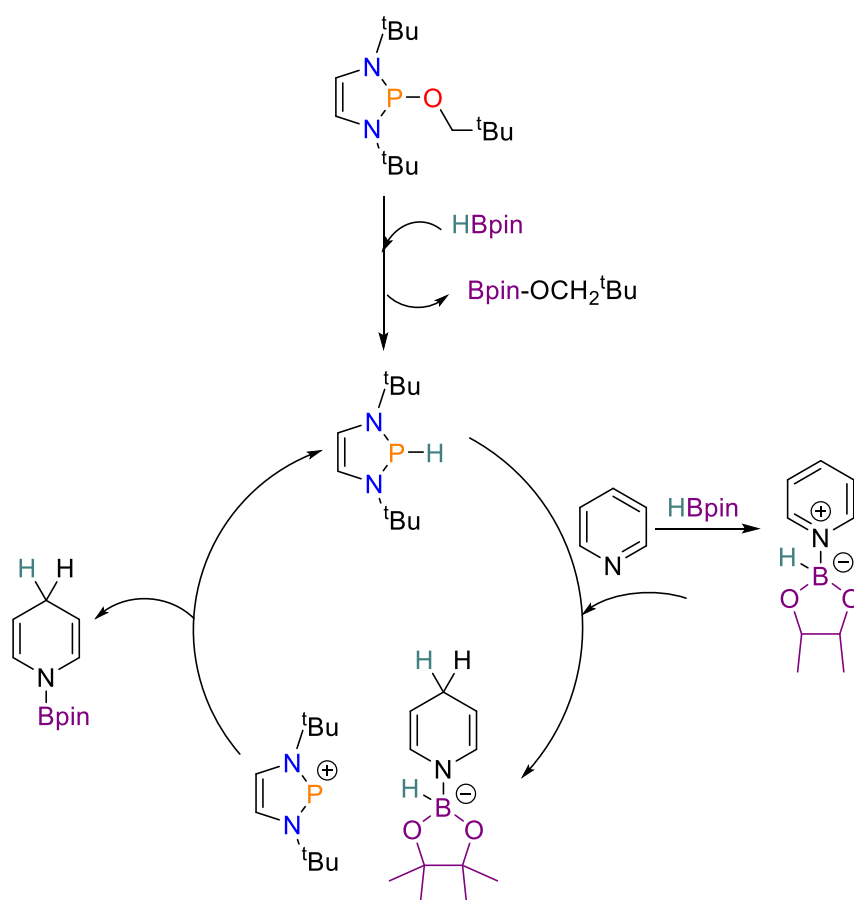


Scheme 1.18: Reaction scheme for synthesising triazaphospholenes. Dipp = 2,6-diisopropylphenyl.



Scheme 1.19: Catalytic cycle for imine reduction with HBpin, using triazaphospholene **V** as a pre-catalyst. Anion = Cl⁻ and is omitted for clarity.

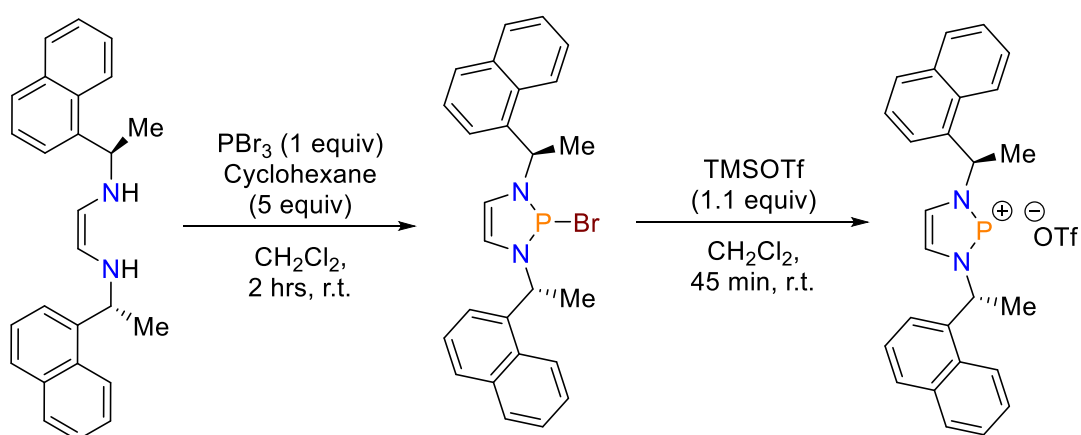
Returning to the neopentyloxy-diazaphospholene pre-catalyst in 2018, Speed looked at its further potential and investigated the hydroboration of pyridines with HBpin, similar to the work of Kinjo with a phosphonium cation.¹⁰⁶ In this work, using 2.5 mol% catalyst proved effective for the catalysis, with a range of *meta*-substituted pyridines efficiently being hydroborated, although regioselectivity in some case was problematic. As in the case of Kinjo, the use of *ortho*- and *para*-position substituents proved challenging. Mechanistically the catalysis proceeds differently to phosphonium catalysed pyridine reduction, with the formation of the diazaphospholene hydride being the first step. After this, pyridine reduction occurs from hydride delivery and then B–P hydride transfer gives the desired hydroborated pyridine product and regenerates the catalyst (Scheme 1.20).¹¹⁰



Scheme 1.20: Proposed catalytic cycle for the hydroboration of pyridines using neopentyloxy-diazaphospholene pre-catalyst.

Lastly, the Speed group in 2019 presented the first example of chiral phosphonium catalysis with enantioselective reduction of imines using HBpin. Using the same ligand scaffold as their chiral diazaphospholene, the diimine was added to phosphorus(III) bromide, giving the diazaphospholene bromide, after which the bromide was abstracted using TMS triflate to

give the chiral phosphonium (Scheme 1.21). Proceeding with this, 1 mol% pre-catalyst and 1.2 equivalents of HBpin were used in the substrate scope of cyclic imines, giving aryl pyrrolidines as products, where enantiomeric ratios of up to 97:3 were obtained. Moreover, imines incorporating functional groups such as pyridyl rings and thiophenes which are traditionally challenging for transition metal catalysts were reduced using the phosphonium cation. Mechanistically this catalysis is believed to proceed in a similar fashion to that reported by Kinjo,¹⁰⁶ where the phosphonium cation abstracts a hydride from HBpin and delivers it to the subsequent imine-borenium complex. In addition to this, screening of other reductants found that phosphonium can promote the asymmetric hydrosilylation of imines.¹¹¹

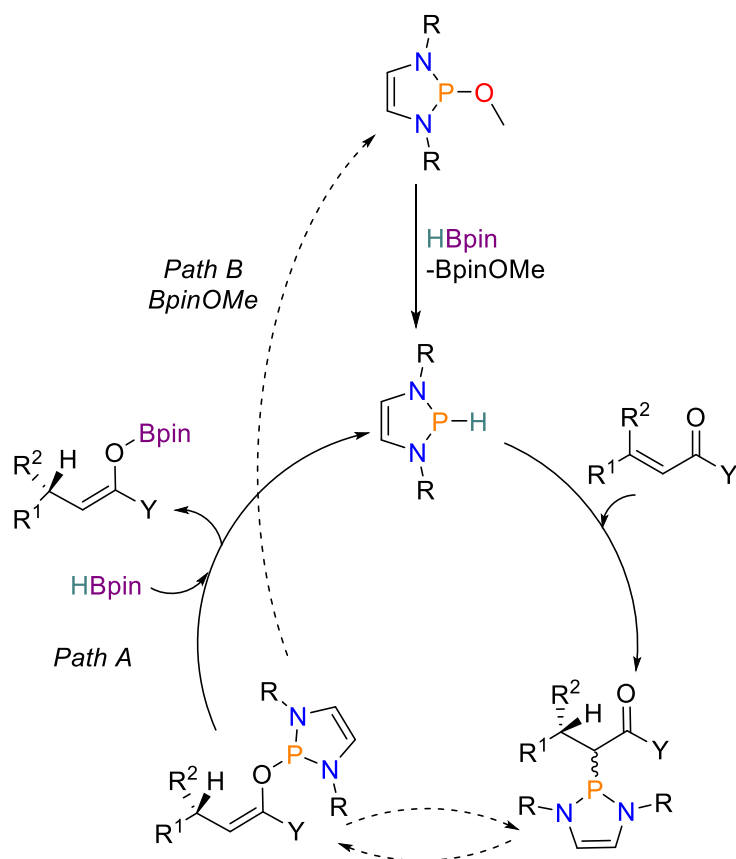


Scheme 1.21: Synthesis of chiral phosphonium triflate.

1.3.3 Catalysis performed by Cramer group

Given the groups interest in chiral ligand design, Cramer and colleagues in 2018 reported enantioselective conjugate reduction using a chiral 1,3,2-diazaphospholene bearing a methoxy group as a pre-catalyst. To begin with, a number of chiral pre-catalysts were synthesised, but screening results found that the diazaphospholene pre-catalyst, which contains 3,5-xyllyl substituents, gave the best performance for the conjugate reduction of acyl pyrrole. A substrate scope of a variety of α,β -unsaturated acyl pyrroles using the conditions 5 mol% pre-catalyst and 1.5 equivalents of HBpin in toluene solvent gave reduced products in yields and enantiomeric ratios of up to 97% and 93.5:6.5 respectively. In addition, chalcones were found to reduce smoothly to the corresponding ketone and more challenging α,β -unsaturated amides were tolerated, with an enantiomeric ratio of up to 86:14. Upon explaining the origin of enantioselectivity, knowing that the P–H bond in the active catalyst is in a perpendicular position as a result of the pyramidal geometry, two accessible quadrants are available away from the bulky aromatic backbone. This led to Cramer proposing the depicted stereoselectivity shown in Figure 1.11. Mechanistically

Cramer proposed two potential catalytic cycles for the catalysis; Path A and Path B. In Path A, the diazaphospholene hydride is the active catalyst, where the hydride is delivered upon addition of the conjugated substrate, after which regeneration of the active catalyst occurs *via* addition of HBpin; in turn giving a boron enolate. After hydrolytic work-up the final product is given. Alternatively, in Path B the first part of the catalytic cycle is the same, but the coordinated intermediate undergoes σ -bond metathesis with pinBOMe, regenerating the pre-catalyst and giving the boron enolate (Scheme 1.22).¹¹²



Scheme 1.22: Proposed catalytic cycle for conjugate reduction.

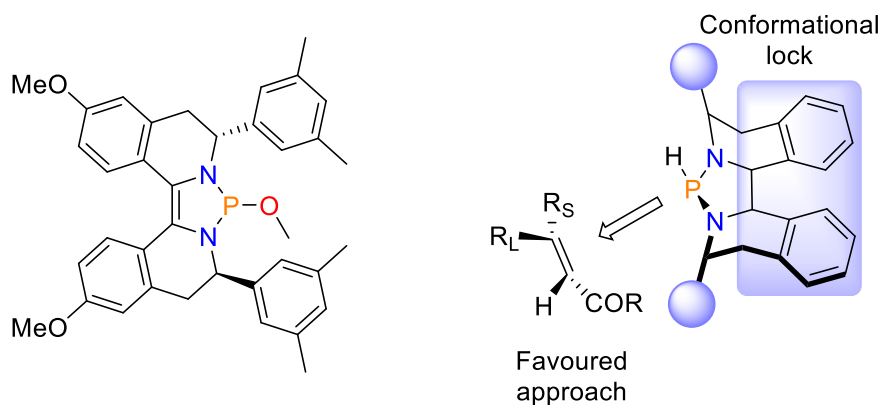
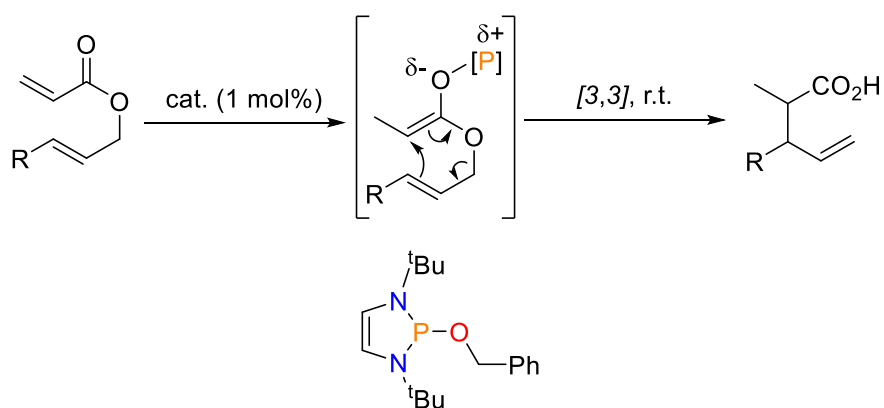


Figure 1.11: Chiral pre-catalyst and selectivity model for the asymmetric reduction.

This work was followed up by the Cramer group in 2019 by using a diazaphospholene as a pre-catalyst to perform a reductive Claisen rearrangement (Scheme 1.23). Using 1 mol% of the benzyloxy-diazaphospholene pre-catalyst and 2.5 equivalents of HBpin at ambient temperature, a wide array of allylic acrylates bearing various functional groups were found to be tolerated for the rearrangement, which was also enantiospecific for substrates with existing stereogenic centres. Investigations into the diastereoselectivity found it could be tuned by varying the solvent as well as changing the diazaphospholene catalyst. Mechanistic studies found that a number of pathways exist depending on the nature of the pre-catalyst and substrate.¹¹³



Scheme 1.23: Claisen rearrangement catalysed by a diazaphospholene pre-catalyst.

Chapter 1.4 Conclusion

In this chapter the heterocycles phosphole and arsole have been introduced, which have been defined as being the phosphorus and arsenic analogues of pyrrole respectively. A discussion has been presented about their aromaticity, which found using both experimental and computational methodology that phospholes are more aromatic than arsoles; but both are significantly less aromatic than pyrrole. This is a consequence of their non-planar nature due to insufficient n- π orbital interaction. However, the differences between phospholes and arsoles vs. pyrrole can be advantageous for optical applications, where greater tunability may be achieved through modification of the electronics of the phosphorus or arsenic centre. The phosphole/arsole ring may be modified to by including nitrogen heteroatoms, which produces the heterocycle diazaphospholene or diazarsolene accordingly. Diazaphospholenes act as precursors to N-heterocyclic phosphonium cations, which are divalent phosphorus species that have a formal positive charge; $[\text{PR}_2]^+$. Diazaphospholene compounds have also recently been used for catalysis in a number of organic transformations, with the groups of Kinjo, Speed and Cramer all presenting examples. Generally speaking, the catalysis mechanistically proceeds *via* the formation of a diazaphospholene-hydride species, which then transfers the hydride and reduces the organic substrate.

Chapter 1.5 References

- 1 P. P. Power, *Nature*, 2010, **463**, 171–177.
- 2 G. C. Welch, R. R. S. Juan, J. D. Masuda and D. W. Stephan, *Science*, 2006, **314**, 1124–1127.
- 3 D. J. Parks and W. E. Piers, *J. Am. Chem. Soc.*, 1996, **7863**, 9440–9441.
- 4 F.-G. Fontaine and D. W. Stephan, *Phil. Trans. R. Soc. A*, 2017, **375**, 20170004.
- 5 J. Lam, K. M. Szkop, E. Mosaferi and D. W. Stephan, *Chem. Soc. Rev.*, 2019, **48**, 3592–3612.
- 6 P. J. Davidson and M. F. Lappert, *J. C. S. Chem. Comm.*, 1973, 317a–317a.
- 7 D. E. Goldberg, D. H. Harris, M. F. Lappert and K. M. Thomas, *J. C. S. Chem. Comm.*, 1976, 261–262.
- 8 C. J. Orth, J. S. Gilmore, J. D. Knight, C. L. Pilmore, R. H. Tschudy and J. E. Fassett, *Science*, 1981, **214**, 1343–1345.
- 9 C. Weetman and S. Inoue, *ChemCatChem*, 2018, **10**, 4213–4228.
- 10 A. J. Ruddy, D. M. C. Ould, P. D. Newman and R. L. Melen, *Dalton Trans.*, 2018, **47**, 10377–10381.
- 11 M.-A. Légare, G. Bélanger-Chabot, R. D. Dewhurst, E. Welz, I. Krummenacher, B. Engels and H. Braunschweig, *Science*, **359**, 896–900.
- 12 P. Arora, V. Arora, H.S. Lamba and D. Wadhwa, *IJPSR*, 2012, **3**, 2947–2954.
- 13 R. E. Bunrock, *Review of Heterocyclic Chemistry*, 5th Edition, 2012, 1349–1350.
- 14 V. Estévez, M. Villacampa and J. C. Menéndez, *Chem. Soc. Rev.*, 2014, **43**, 4633–4657.
- 15 R. Shah and P. K. Verma, *Chem. Cent. J.*, 2018, **12**, 1–22.
- 16 M. P. Duffy, W. Delaunay, P.-A. Bouit and M. Hissler, *Chem. Soc. Rev.*, 2016, **45**, 5296–5310.
- 17 C. Charrier, H. Bonnard, G. De Lauzon and F. Mathey, *J. Am. Chem. Soc.*, 1983, **105**, 6871–6877.
- 18 A. Maccoll, *Ambix*, 1989, **36**, 82–90.
- 19 E. H. Braye, W. Hübel and I. Caplier, *J. Am. Chem. Soc.*, 1961, **83**, 4406–4413.
- 20 G. Märkl and H. Hauptmann, *J. Organomet. Chem.*, 1983, **248**, 269–285.
- 21 G. Märkl and H. Hauptmann, *Angew. Chem. Int. Ed.*, 1972, **11**, 441–441.
- 22 A. Alparone, H. Reis and M. G. Papadopoulos, *J. Phys. Chem. A*, 2006, **110**, 5909–5918.
- 23 W. Schafer, A. Schweig, G. Märkl, H. Hauptmann and F. Mathey, *Angew. Chem. Int. Ed.*, 1973, **12**, 145–146.
- 24 N. D. Epiotis and W. Cherry, *J. Am. Chem. Soc.*, 1975, **98**, 4365–4370.

- 25 M. Cyraliski, *Tetrahedron*, 1996, **52**, 10255–10264.
- 26 P. Von Ragué, C. Maerker, A. Dransfeld, H. Jiao and N. J. R. van Eikema Hommes, *J. Am. Chem. Soc.*, 1996, **118**, 6317–6318.
- 27 M. P. Johansson and J. Juselius, *Lett. Org. Chem.*, 2005, **2**, 469–474.
- 28 M. K. Cyranski, T. M. Krygowski, A. R. Katritzky and P. von Ragué Schleyer, *J. Org. Chem.*, 2002, **67**, 1333–1338.
- 29 M. K. Cyranski, P. von Ragué Schleyer, T. M. Krygowski, H. Jiao and G. Hohlneicher, *Tetrahedron*, 2003, **59**, 1657–1665.
- 30 J. P. Green, S. J. Cryer, J. Marafie, A. J. P. White and M. Heeney, *Organometallics*, 2017, **36**, 2632–2636.
- 31 Y. M. Poronik, L. M. Mazur, M. Samoc', D. Jacquemin and D. T. Gryko, *J. Mater. Chem. C*, 2017, **5**, 2620–2628.
- 32 J. Chen, X. Zhu, C. Luo and Y. Dai, *Int. J. Quantum Chem.*, 2017, **117**, <https://doi.org/10.1002/qua.25453>.
- 33 B. Li, E. Peng, L. Ye and Z. Wu, *Front. Optoelectron.*, 2016, **9**, 99–105.
- 34 M. Kirkus, S. Knippenberg, D. Beljonne, J. Cornil, R. A. J. Janssen and S. C. J. Meskers, *J. Phys. Chem. A*, 2013, **117**, 2782–2789.
- 35 Y. Matano and H. Imahori, *Org. Biomol. Chem.*, 2009, **7**, 1258–1271.
- 36 G. M. Farinola and R. Ragni, *Chem. Soc. Rev.*, 2011, **40**, 3467–3482.
- 37 C. Fave, T.-Y. Cho, M. Hissler, C.-W. Chen, T.-Y. Luh, C.-C. Wu and R. Réau, *J. Am. Chem. Soc.*, 2003, **125**, 9254–9255.
- 38 A. Kira, Y. Shibano, S. Kang, H. Hayashi, T. Umeyama, Y. Matano and H. Imahori, *Chem. Lett.* 2010, **39**, 448–450.
- 39 Y. Matano, H. Ohkubo, T. Miyata, Y. Watanabe, Y. Hayashi, T. Umeyama and H. Imahori, 2014, *Eur. J. Inorg. Chem.*, 2014, 1620–1624.
- 40 H. A. van Kalker, S. H. A. M. Leenders, C. R. A. Hommersom, F. P. J. T. Rutjes and F. L. Van Delft, *Chem. Eur. J.*, 2011, **17**, 11290–11295.
- 41 M. Ishidoshiro, Y. Matsumura, H. Imoto, Y. Irie, T. Kato, S. Watase, K. Matsukawa, S. Inagi, I. Tomita and K. Naka, *Org. Lett.* 2015, **17**, 4854–4857.
- 42 M. Ishidoshiro, H. Imoto, S. Tanaka and K. Naka, *Dalton Trans.*, 2016, **45**, 8717–8723.
- 43 D. Gudat, *Dalton Trans.*, 2016, **45**, 5896–5907.
- 44 M. K. Denk, S. Gupta and A. J. Lough, *Eur. J. Inorg. Chem.*, 1999, 41–49.
- 45 D. Gudat, A. Haghverdi, H. Hupfer and M. Nieger, *Chem. Eur. J.*, 2000, **6**, 3414–3425.
- 46 D. Gudat, A. Haghverdi and M. Nieger, *Angew. Chem. Int. Ed.*, 2000, **39**, 3084–3086.
- 47 S. Burck, D. Gudat, M. Nieger and W.-W. Du Mont, *J. Am. Chem. Soc.*, 2006, **128**, 3946–3955.
- 48 D. Förster, J. Nickolaus, M. Nieger, Z. Benko, A. W. Ehlers and D. Gudat, *Inorg. Chem.*, 2013, **52**, 7699–7708.

- 49 C. Payraastre, Y. Madaule and J. G. Wolf, *Tetrahedron Lett.*, 1990, **31**, 1145–1146.
- 50 C. J. Carmalt, V. Lomeli, B. G. McBurnett and A. H. Cowley, *Chem. Commun.*, 1997, 2095–2096.
- 51 E. G. Nesterova, R. M. Minyaev and V. I. Minkin, *Russ. J. Org. Chem.*, 2003, **39**, 1167–1173.
- 52 T. Gans-Eichler, D. Gudat and M. Nieger, *Heteroat. Chem.*, 2005, **16**, 327–338.
- 53 S. Burck, J. Daniels, T. Gans-Eichler, D. Gudat, K. Nättinen and M. Nieger, *Z. Anorg. Allg. Chem.*, 2005, **631**, 1403–1412.
- 54 J. T. Price, M. Lui, N. D. Jones and P. J. Ragogna, *Inorg. Chem.*, 2011, **50**, 12810–12817.
- 55 O. Puntigam, I. Hajdók, M. Nieger, M. Niemeyer, S. Strobel and D. Gudat, *Z. Anorg. Allg. Chem.*, 2011, **637**, 988–994.
- 56 D. Förster, H. Dilger, F. Ehret, M. Nieger and D. Gudat, *Eur. J. Inorg. Chem.*, 2012, 3989–3994.
- 57 O. Puntigam, D. Förster, N. A. Giffin, S. Burck, J. Bender, F. Ehret, A. D. Hendsbee, M. Nieger, J. D. Masuda and D. Gudat, *Eur. J. Inorg. Chem.*, 2013, 2041–2050.
- 58 N. A. Gi, A. D. Hendsbee, T. L. Roemmele, M. D. Lumsden, C. C. Pye and J. D. Masuda, *Inorg. Chem.* 2012, **51**, 11837–11850.
- 59 R. Edge, R. J. Less, E. J. L. McInnes, K. Müther, V. Naseri, J. M. Rawson and D. S. Wright, *Chem. Commun.*, 2009, 1691–1693.
- 60 S. L. Hinchley, C. A. Morrison, D. W. H. Rankin, C. L. B. Macdonald, R. J. Wiacek, A. Voigt, A. H. Cowley, M. F. Lappert, G. Gundersen, J. A. C. Clyburne and P. P. Power, *J. Am. Chem. Soc.*, 2001, **123**, 9045–9053.
- 61 A. H. Cowley and R. A. Kemp, *Chem. Rev.*, 1985, **85**, 367–382.
- 62 K. A. Porter, A. C. Willis, J. Zank and S. B. Wild, *Inorg. Chem.*, 2002, **41**, 6380–6386.
- 63 K. Dimroth and K. J. Kraft, *Angew. Chem. Int. Ed.*, 1964, **3**, 384.
- 64 S. Volodarsky and R. Dobrovetsky, *Chem. Commun.*, 2018, **54**, 6931–6934.
- 65 M. B. Abrams, B. L. Scott and R. T. Baker, *Organometallics*, 2000, **19**, 4944–4956.
- 66 H. Nakazawa, Y. Yamaguchi, T. Mizuta and K. Miyoshi, *Organometallics*, 1995, **14**, 4173–4182.
- 67 B. Pan, Z. Xu, M. W. Bezpalko, B. M. Foxman and C. M. Thomas, *Inorg. Chem.*, 2012, **51**, 4170–4179 .
- 68 C. A. Caputo, M. C. Jennings, H. M. Tuononen and N. D. Jones, *Organometallics*, 2009, **28**, 990–1000.
- 69 J. Petušková, H. Bruns and M. Alcarazo, *Angew. Chem. Int. Ed.*, 2011, **50**, 3799–3802.
- 70 A. Kozma, T. Deden, J. Carreras, C. Wille, J. Petušková, J. Rust and M. Alcarazo, *Chem. Eur. J.*, 2014, **20**, 2208–2214.
- 71 K. Takano, H. Tsumura, H. Nakazawa, M. Kurakata and T. Hirano, *Organometallics*, 2000, **19**, 3323–3331.

- 72 L. D. Hutchins, E. N. Duesler and R. T. Paine, *Organometallics*, **1**, 1982, 1254–1256.
- 73 L. D. Hutchins, R. T. Paine and C. F. Campana, *J. Am. Chem. Soc.*, 1980, **102**, 4521–4523.
- 74 N. Burford, T. M. Parks, B. W. Royan, B. Borecka, T. S. Cameron, J. F. Richardson, E. J. Gabe and R. Hynes, *J. Am. Chem. Soc.*, 1992, **114**, 8147–8153.
- 75 N. Burford, T. M. Parks, P. K. Bakshi and T. S. Cameron, *Angew. Chem. Int. Ed.*, 1994, **33**, 32–33.
- 76 K. Izod, P. Evans and P. G. Waddell, *Angew. Chem. Int. Ed.*, 2019, **58**, 11007–11012.
- 77 N. Burford, J. A. C. Clyburne, P. Losier, T. M. Parks and T. S. Cameron, *Phosphorus, Sulfur and Silicon*, 1994, **93–94**, 301–304.
- 78 T. D. Tilley, R. H. Grubbs and J. E. Bercaw, *Organometallics*, 1984, **3**, 274–278.
- 79 K. A. Mahmoud, A. J. Rest, M. Lukza, K. Jörg and W. Malisch, *Organometallics*, 1984, **3**, 501–503.
- 80 T. Kaukorat, I. Neda and R. Schmutzler, *Coord. Chem. Rev.*, 1994, **137**, 53–107.
- 81 R. Reed, R. Réau, F. Cahn and Guy Bertrand, *Angew. Chem. Int. Ed.*, **32**, 1993, 399–401.
- 82 C. Payraastre, Y. Madaule, J. G. Wolf, T. C. Kim, M.-R. Mazières, R. Wolf and M. Sanchez, *Heteroat. Chem.*, 1992, **3**, 157–162.
- 83 J. M. Slattery and S. Hussein, *Dalton Trans.*, **41**, 2012, 1808–1815.
- 84 C. Y. Wong, D. K. Kennepohl and R. G. Cavell, *Chem. Rev.*, 1996, **96**, 1917–1952.
- 85 G. Wittig and U. Schoellkopf, *Org. Synth.*, 1960, **40**, 66.
- 86 H. J. Cristau, *Chem. Rev.*, 1994, **94**, 1299–1313.
- 87 J. M. Bayne and D. W. Stephan, *Chem. Soc. Rev.*, 2016, **45**, 765–774.
- 88 L. J. Hounjet, C. B. Caputo and D. W. Stephan, *Angew. Chem. Int. Ed.*, 2012, **51**, 4714–4717.
- 89 C. B. Caputo, D. Winkelhaus, R. Dobrovetsky, L. J. Hounjet and D. W. Stephan, *Dalton Trans.*, 2015, **44**, 12256–12264.
- 90 A. R. Jupp, T. C. Johnstone and D. W. Stephan, *Dalton Trans.*, 2018, **47**, 7029–7035.
- 91 N. L. Dunn, M. Ha and A. T. Radosevich, *J. Am. Chem. Soc.*, 2012, **134**, 11330–11333.
- 92 Y. Z. Huang and Y. C. Shen, *Adv. Organomet. Chem.*, 1982, **20**, 115–157.
- 93 D. Lloyd, I. Gosney and R. A. Ormiston, *Chem. Soc. Rev.*, 1987, **16**, 45–74.
- 94 B. Pan and F. P. Gabbai, *J. Am. Chem. Soc.*, 2014, **136**, 9564–9567.
- 95 S. Solyntjes, B. Neumann, H.-G. Stammler, N. Ignat'ev and B. Hoge, *Eur. J. Inorg. Chem.*, 2016, 3999–4010.
- 96 C. B. Caputo, L. J. Hounjet, R. Dobrovetsky and D. W. Stephan, *Science*, 2013, **341**, 1374–1377.
- 97 L. O. Müller, D. Himmel, J. Stauffer, G. Steinfeld, J. Slattery, G. Santiso-Quiñones, V.

- Brecht and I. Krossing, *Angew. Chem. Int. Ed.*, 2008, **47**, 7659–7663.
- 98 J. Zhou, L. L. Liu, L. L. Cao and D. W. Stephan, *Chem*, 2018, **4**, 2699–2708.
- 99 P. Mehlmann, T. Witteler, L. F. B. Wilm and F. Dielmann, *Nat. Chem.*, 2019, **11**, 1139–1143.
- 100 J. Zhou, L. L. Liu, L. L. Cao and D. W. Stephan, *Angew. Chem. Int. Ed.*, 2019, **58**, 5407–5412.
- 101 C. C. Chong, H. Hirao and R. Kinjo, *Angew. Chem. Int. Ed.*, 2014, **53**, 3342–3346.
- 102 C. C. Chong, H. Hirao and R. Kinjo, *Angew. Chem. Int. Ed.*, 2015, **54**, 190–194.
- 103 D. M. D’Alessandro, B. Smit and J. R. Long, *Angew. Chem. Int. Ed.*, 2010, **49**, 6058–6082.
- 104 C. C. Chong and R. Kinjo, *Angew. Chem. Int. Ed.*, 2015, **54**, 12116–12120.
- 105 C. C. Chong, B. Rao and R. Kinjo, *ACS Catal.*, 2017, **7**, 5814–5819.
- 106 B. Rao, C. C. Chong and R. Kinjo, *J. Am. Chem. Soc.*, 2018, **140**, 652–656.
- 107 M. R. Adams, C.-H. Tien, B. S. N. Huchenski, M. J. Ferguson and A. W. H. Speed, *Angew. Chem. Int. Ed.*, 2017, **56**, 6268–6271.
- 108 M. R. Adams, C.-H. Tien, R. McDonald and A. W. H. Speed, *Angew. Chem*, 2017, **56**, 16660–16663.
- 109 C. H. Tien, M. R. Adams, M. J. Ferguson, E. R. Johnson and A. W. H. Speed, *Org. Lett.*, 2017, **19**, 5565–5568.
- 110 T. Hynes, E. N. Welsh, R. McDonald, M. J. Ferguson and A. W. H. Speed, *Organometallics*, 2018, **37**, 841–844.
- 111 T. Lundrigan, E. N. Welsh, T. Hynes, C.-H. Tien, M. R. Adams, K. R. Roy, K. N. Robertson and A. W. H. Speed, *J. Am. Chem. Soc.*, **141**, 2019, 14083–14088.
- 112 S. Miaskiewicz, J. H. Reed, P. A. Donets, C. C. Oliveira and N. Cramer, *Angew. Chem. Int. Ed.*, 2018, **57**, 4039–4042.
- 113 J. H. Reed, P. A. Donets, S. Miaskiewicz and N. Cramer, *Angew. Chem. Int. Ed.*, 2019, **58**, 8893–8897.

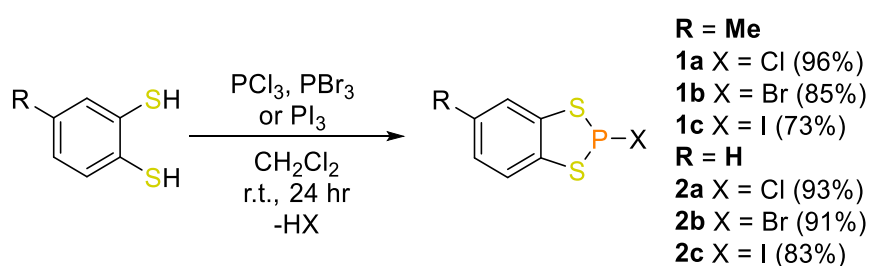
Chapter 2: Synthesis of Dithia-, Diaza-, and Dioxa-based Benzophospholes and Benzoarsoles

Chapter 2.1 Synthesis of Benzo-Fused Dithiaphospholes and Dithiarsoles

In advance of any structural or reactivity analyses of phosphole and arsole derived compounds, a series of them firstly needed to be synthesised. To begin with, either commercially available toluene-3,4-dithiol or benzene-1,2-dithiol was used as the starting ligand, which when reacted with a phosphorus trihalide would generate the first phosphole derived species to investigate. The synthesis of the dithiaphospholes and their structural scrutiny is described below.

2.1.1 General synthesis and NMR spectroscopy analysis of benzo-fused dithiaphospholes

The synthesis of the benzo-fused dithiaphospholes (shortened herein to dithiaphospholes) proceeded in a similar fashion to that first described by Baudler.¹ This involved the addition of either toluene-3,4-dithiol or benzene-1,2-dithiol to the phosphorus trihalide, PX_3 , in CH_2Cl_2 solvent and stirring at room temperature for 24 hours (Scheme 2.1). The liberation of HX gas proceeded during this time. Upon the removal of volatiles and subsequent pentane washings, the dithiaphosphole compounds were isolated in good to excellent yields of 73–96%. The products 2-chloro-5-methylbenzo-1,3,2-dithiaphosphole (**1a**), 2-bromo-5-methylbenzo-1,3,2-dithiaphosphole (**1b**), 2-chlorobenzo-1,3,2-dithiaphosphole (**2a**) and 2-bromobenzo-1,3,2-dithiaphosphole (**2b**) were obtained as white powders, whereas 2-iodo-5-methylbenzo-1,3,2-dithiaphosphole (**1c**) and 2-iodobenzo-1,3,2-dithiaphosphole (**2c**) are orange and red powders respectively.²



Scheme 2.1: Synthesis of dithiaphosphole compounds **1a–2c**.

For the reactions of toluene-3,4-dithiol with phosphorus trihalide (phosphorus trichloride, phosphorus tribromide or phosphorus triiodide), giving products **1a–1c**, $^{31}P\{^1H\}$ NMR spectroscopy was first employed to confirm product formation. ^{31}P NMR spectroscopy is a very powerful and highly useful characterisation technique for diamagnetic complexes that contain phosphorus. The ^{31}P nuclei is NMR active with a nuclear spin of $I = \frac{1}{2}$, 100% isotopic abundance and has a relatively high gyromagnetic ratio ($\gamma = 108 \times 10^6 \text{ rad s}^{-1}T^{-1}$, cf. 1H where

$\gamma = 268 \times 10^6 \text{ rad s}^{-1} \text{ T}^{-1}$). Unlike in a typical ^1H NMR spectrum, which is performed over a spectral width that covers $\delta = 13\text{--}0$ ppm, a ^{31}P NMR spectrum will usually cover a chemical shift range from $\delta = +250$ to -250 ppm with respect to 85% H_3PO_4 ; a spectral width of several hundred ppm and much wider than a ^1H NMR spectrum. Moreover, the characteristics of ^{31}P NMR spectroscopy are different to ^1H NMR spectroscopy, in that the ^1H NMR spectrum is dominated by the magnitude of the diamagnetic shielding tensor (σ_d), meaning that the nuclei are sensitive to the electron donating and withdrawing nature of the bound substituent. On the other hand, the ^{31}P NMR spectrum (and any nuclei heavier than ^1H) is governed by the paramagnetic shielding tensor (σ_p). σ_p involves interactions between the circulation of electrons in the ground state and higher energy excited states caused by the external magnetic field. The results of the magnitude of σ_p give rise to the large spectral width seen in the ^{31}P NMR spectrum.³

As the paramagnetic shielding tensor, which as just described is the mixing of the ground state and excited state wavefunctions, is largely responsible for the chemical shift in the ^{31}P NMR spectrum, the oxidation state and coordination geometry are vastly important in chemical shift determination. For example, triethylphosphine has a chemical shift of $\delta = -20.0$ ppm in the ^{31}P NMR spectrum, whereas the chemical shift for triethylphosphine oxide is shifted downfield to $\delta = +48.3$ ppm. It is important to stress though that the ^{31}P chemical shift is independent of the formal oxidation state but instead is dependent on the electron density on the phosphorus atom, as well as the geometry and degree of π -bonding present.³

$^{31}\text{P}\{^1\text{H}\}$ NMR spectroscopic analysis of **1a–1c** revealed loss of the starting phosphorus trihalide, *cf.* $\delta = 218, 227$ and 178 ppm for PCl_3 , PBr_3 and PI_3 respectively, and an upfield singlet resonance at $\delta = 160.4$ ($X = \text{Cl}$), $\delta = 163.3$ ($X = \text{Br}$) and $\delta = 155.0$ ($X = \text{I}$) ppm corresponding to the product (Figure 2.1). $^{31}\text{P}\{^1\text{H}\}$ NMR chemical shifts of **1a–1c** are interesting as they do not correlate to a simple trend based on electronegativity arguments alone. That is, it would be expected to observe an upfield shift from **1a** ($X = \text{Cl}$) to **1c** ($X = \text{I}$). However, **1b** is found to be slightly downfield (by *ca.* 3 ppm) to **1a**, which is also seen in the PCl_3 vs. PBr_3 ^{31}P NMR chemical shifts in the starting trihalides.

Given the nature of the structure in the dithiaphosphole the ^1H and $^{13}\text{C}\{^1\text{H}\}$ NMR spectra of **1a–1c** showed little change when compared to the toluene-3,4-dithiol starting material, although the ^1H NMR spectrum showed loss of the two dithiol signals at *cf.* $\delta = 3.70$ and 3.60 ppm. Using **1a** as an example, the ^1H NMR spectrum shows three aromatic signals,

corresponding to the three aromatic protons at $\delta = 7.55$, 7.50 and 7.12 ppm. Given the NMR active nature of the ^{31}P nuclei (*vide supra*), coupling to the phosphorus heteroatom is seen in the splitting pattern of the aromatic protons, with $^4J_{\text{PH}} = 1.2$ Hz and even $^5J_{\text{PH}} = 0.6$ Hz observed (see experimental chapter). The methyl group from the ligand backbone is a singlet at $\delta = 2.39$ ppm.

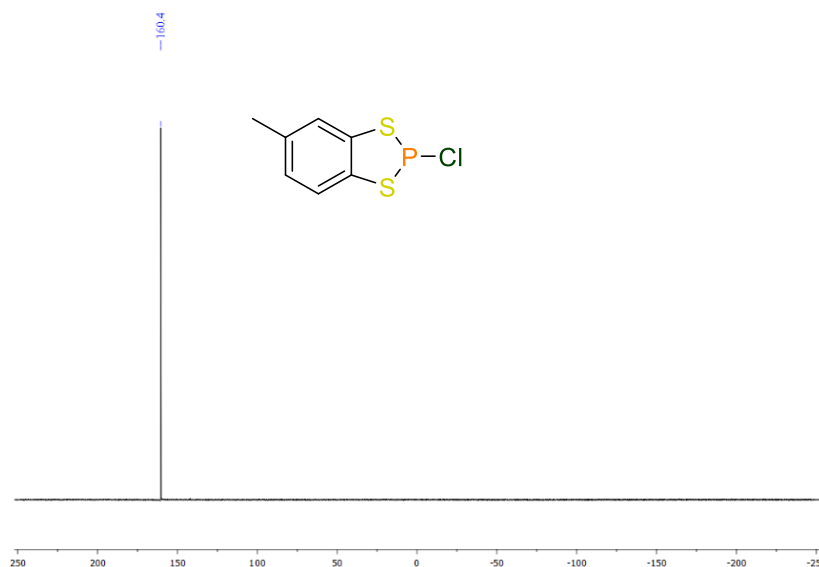


Figure 2.1: $^{31}\text{P}\{^1\text{H}\}$ NMR (202 MHz, CDCl_3 , 295 K) spectrum of the dithiaphosphole **1a**.

Similar observations to those discussed above were found for the reactions of benzene-1,2-dithiol with phosphorus trihalides (phosphorus trichloride, phosphorus tribromide or phosphorus triiodide), giving products **2a–2c** (Scheme 2.1). $^{31}\text{P}\{^1\text{H}\}$ NMR spectroscopy of the products showed loss of starting phosphorus trihalide and singlet signals at $\delta = 158.3$ (X = Cl), $\delta = 160.9$ (X = Br) and $\delta = 152.4$ (X = I) ppm, which are comparable to their counterparts **1a–1c** ($\delta = 160.4$, 163.3 and 155.0 ppm respectively). The highly symmetric nature of **2a–2c** resulting from the C_2 axis present results in chemically equivalent aromatic protons in the ^1H NMR spectrum, meaning that only two aromatic proton signals are seen (*cf.* three in **1a–1c**). Using **2a** as an example, the first aromatic chemical shift splits into a doublet of doublet of doublets centred at $\delta = 7.69$ ppm ($^3J_{\text{HH}} = 5.9$ Hz, $^4J_{\text{HH}} = 3.3$ Hz, $^4J_{\text{PH}} = 1.3$ Hz). This coupling pattern arises due to the fact that both chemically and magnetically inequivalent protons are present. The second aromatic signal is a doublet of doublets positioned at $\delta = 7.32$ ppm, with $^3J_{\text{HH}} = 5.9$ Hz and $^4J_{\text{HH}} = 3.3$ Hz coupling constant values (Figure 2.2).

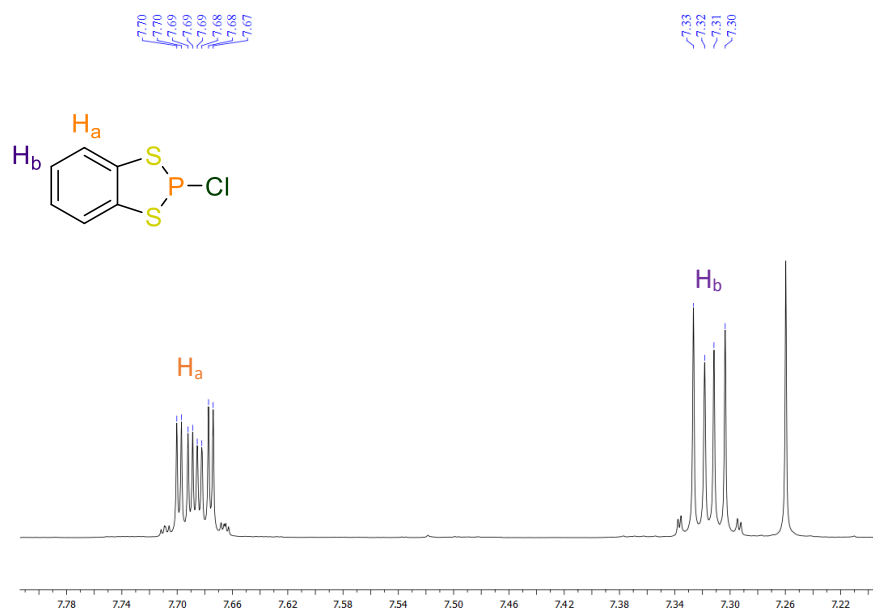


Figure 2.2: ^1H NMR (400 MHz, CDCl_3 , 295 K) spectrum showing aromatic resonances of the dithiaphosphole **2a**.

2.1.2 Single crystal X-ray diffraction analysis of benzo-fused dithiaphospholes

As one of the aims of this thesis is to understand better the fundamental bonding and structure of this class of heterocycle, single crystal X-ray diffraction was used to visualise and examine their geometry. Single crystal X-ray diffraction would prove to be an invaluable method throughout this thesis for compound characterisation and analysis. Crystals of **1a–1c** suitable for single crystal X-ray diffraction were grown from saturated solutions of CH_2Cl_2 with a few drops of pentane and cooled to $-40\text{ }^\circ\text{C}$ (Figure 2.3). Upon data collection and refinement, the solid-state structures of **1a–1c** were found to crystallise in the monoclinic space group $P2_1/c$ with one molecule in the asymmetric unit (Z'); increasing to four molecules in the unit cell (Z). Structure solution revealed the anticipated three-coordinate phosphorus centre, in which the halogen co-ligand ($X = \text{Cl}, \text{Br}$ or I) is exocyclic to the fused rings. The dithiaphosphole ring itself is not planar but instead adopts an envelope-type geometry, as seen in the structure of cyclopentane, in which there is a fold angle about the $\text{S}\cdots\text{S}$ vector (Figure 2.4). The fold angle for **1a** was calculated to be $26.07(6)^\circ$, whereas for **1b** this fold angle is $24.19(10)^\circ$ and $19.45(14)^\circ$ for **1c**. That is, upon descending down group 17 for the co-ligand, the fold angle decreases and the structure tends towards molecular planarity. An explanation for this is that due to the larger steric hinderance caused by the bromide and iodide co-ligand, the lone pair on the phosphorus heteroatom is forced to donate into the dithia pnictole ring and better $n-\pi$ orbital overlap takes place; hence planarity. A similar feature is observed with phospholes where an increase in bulky

substituents around phosphorus promotes planarity by increasing the barrier of pyramidal inversion.⁴ Although the P–S bond lengths and S–P–S interior bond angles remain similar in **1a–1c**, the bond length of the P–X bond appreciably changes and increases upon descending group 17. The P–X bond lengths are 2.1134(7) Å (**1a**), 2.3153(9) Å (**1b**), and 2.5730(12) Å (**1c**) (Table 2.1). Furthermore, the P–X bond lengths show slight elongation compared to typical values, with standard P–X bond lengths of 2.008 Å (P–Cl), 2.206 Å (P–Br) and 2.490–2.493 Å (P–I).⁵

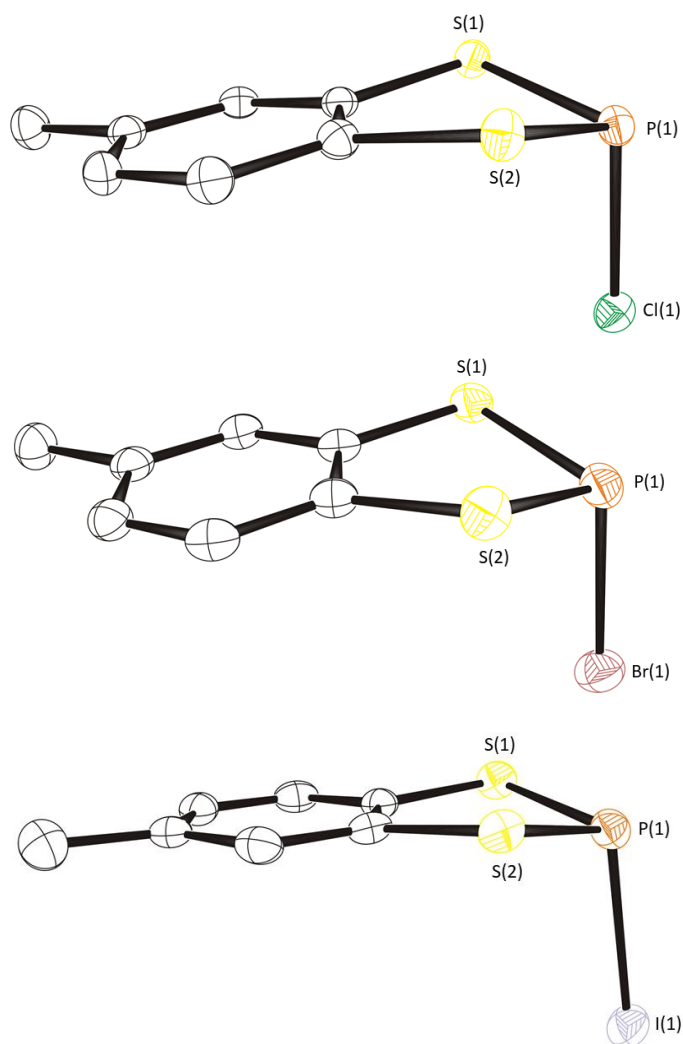


Figure 2.3: Solid-state structures of dithiaphospholes **1a–1c** (top: 2-chloro-5-methylbenzo-1,3,2-dithiaphosphole (**1a**), middle: 2-bromo-5-methylbenzo-1,3,2-dithiaphosphole (**1b**), bottom: 2-iodo-5-methylbenzo-1,3,2-dithiaphosphole (**1c**)). Thermal ellipsoids drawn at 50% probability and H-atoms removed for clarity.

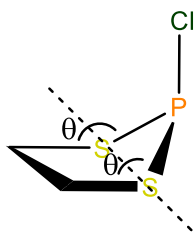


Figure 2.4: Figure of the dithia C_2S_2P 5-membered ring which shows the envelope geometry. The C_2S_2 atoms lie in the plane, whereas the phosphorus atom (and by proxy the chloride) are above the plane at an angle θ . This angle θ is what is meant by the term fold angle.

Table 2.1: Selected bond lengths and interior bond angles for compounds **1a–1c**.

Selected bond	1a / Å (X = Cl)	1b / Å (X = Br)	1c / Å (X = I)
P(1)–S(1)	2.0936(7)	2.0791(12)	2.0941(15)
P(1)–S(2)	2.0954(7)	2.0853(12)	2.0898(14)
S(1)–C(1)	1.769(2)	1.766(3)	1.767(4)
S(2)–C(2)	1.7714(17)	1.763(3)	1.761(4)
P(1)–X	2.1134(7)	2.3154(9)	2.5730(12)
Selected angle	1a / °	1b / °	1c / °
S(1)–P(1)–S(2)	95.43(3)	96.00(5)	96.13(6)

The presence of the methyl group on the benzene backbone in theory could give rise to enantiomers, with chirality being centred on the phosphorus heteroatom. However, the space group $P2_1/c$, which **1a–1c** crystallise in, is centrosymmetric and consequently contains an inversion centre. The presence of this inversion centre means that a 50:50 mixture of both enantiomers is observed.

When looking at the packing arrangement of the dithiaphosphole **1a**, the phosphorus and sulfur atoms display short contacts with the chloride of the neighbouring dithiaphosphole, with contacts measuring 3.47378(8) Å and 3.42797(9) Å for the $P\cdots Cl$ and $S\cdots Cl$ contacts respectively (Figure 2.5). These values are within the van der Waals radii distances of 355 ppm for both $P\cdots Cl$ and for $S\cdots Cl$. Interestingly such close contacts do not exist for compounds **1b** and **1c** and no meaningful close contacts are found.

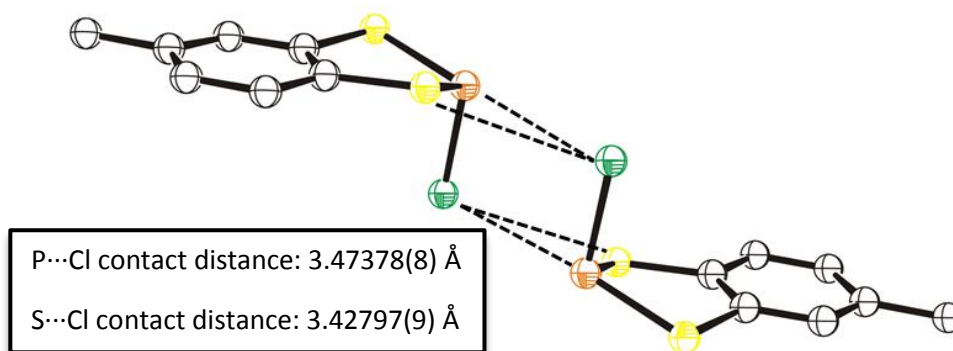


Figure 2.5: Close contacts that exist in the unit-cell in compound **1a**. Dashed lines show the close contacts between phosphorus, sulfur and chloride atoms. Orange: phosphorus, yellow: sulfur, green: chlorine.

Crystals of **2a–2c** suitable for single crystal X-ray diffraction were grown as described above. **2a** crystallises in the monoclinic space group $P2_1/n$ with one molecule in the asymmetric unit; increasing to four in the unit cell. On the other hand, compounds **2b** and **2c** crystallised in the reduced symmetry lattice triclinic space group $P-1$, with two molecules in the asymmetric unit but four molecules in the unit cell (Figure 2.6). A fold angle about the $S\cdots S$ vector is again observed, with molecular planarity arising upon descending group 17 in the co-ligand. The fold angle is $28.65(6)^\circ$ for **2a**, $26.45(9)^\circ$ and $26.57(9)^\circ$ for the two crystallographically independent molecules in **2b** and $28.38(14)^\circ$ and $23.93(11)^\circ$ for the two crystallographically independent molecules in **2c**. Interestingly, despite the only structural difference in **2a–2c** compared to **1a–1c** being the lack of methyl group on the benzene backbone, the fold angles present in **2a–2c** are consistently lower than the analogous complex in **1a–1c**. For comparison the fold angles present in **1a–1c** were $26.07(6)^\circ$, $24.19(10)^\circ$ and $19.45(14)^\circ$ respectively. Further structural features mirror that of **1a–1c**, with the $P-X$ bond lengths approximately the same, although the internal $S(1)-P(1)-S(2)$ for **2b** and **2c** do show a small contraction compared to the analogous **1b** and **1c**. These metrics are given in Table 2.2 below.

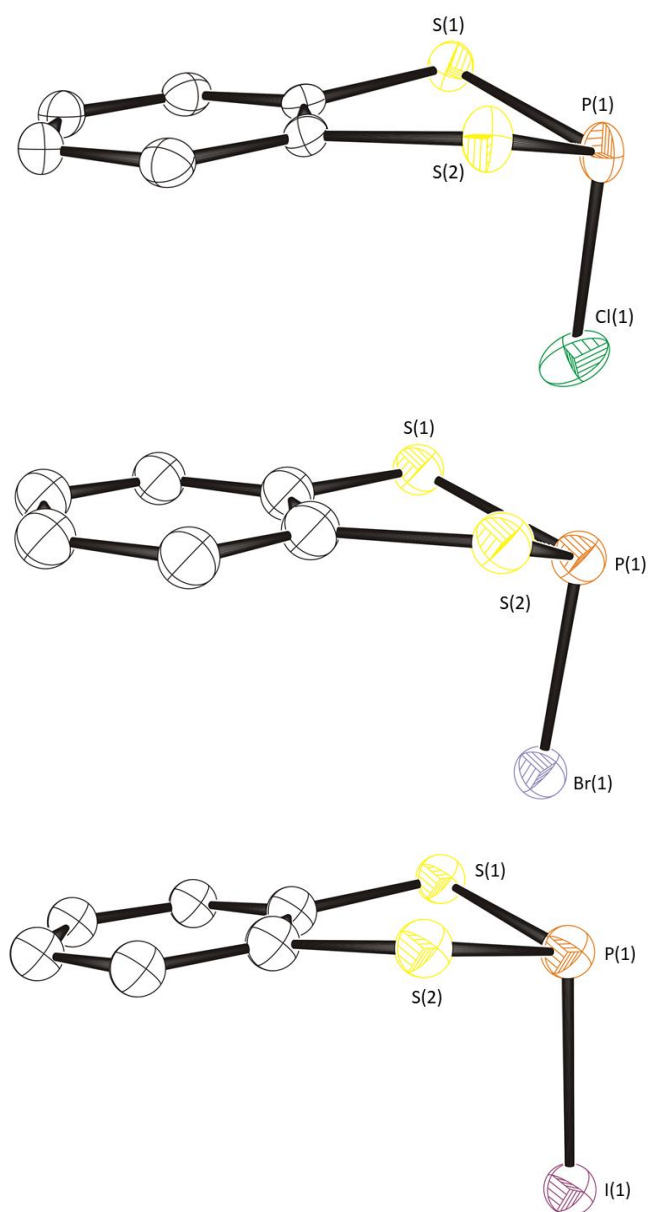


Figure 2.6: Solid-state structures of dithiaphospholes **2a–2c** (Top: 2-chlorobenzo-1,3,2-dithiaphosphole (**2a**), middle: 2-bromobenzo-1,3,2-dithiaphosphole (**2b**), bottom: 2-iodobenzo-1,3,2-dithiaphosphole (**2c**)). Thermal ellipsoids drawn at 50% probability and H-atoms removed for clarity.

Inspection of the unit cell packing of **2a** does not show the P \cdots Cl and S \cdots Cl short contacts as seen in the analogous **1a**, instead close contacts between pairs of neighbouring sulfur atoms are present, that are within 0.112 Å of the van der Waals radii. Structures **2b** and **2c** do not show any significant short contacts within the unit cell.

Table 2.2: Selected bond lengths and interior bond angles for compounds **2a–2c**.

Selected bond	2a / Å (X = Cl)	2b / Å (X = Br)	2c / Å (X = I)
P(1)–S(1)	2.08668(8)	2.0898(11)– 2.0907(11)	2.0842(19)– 2.0947(16)
P(1)–S(2)	2.0863(8)	2.0789(15)– 2.0886(12)	2.0873(16)– 2.0940(17)
S(1)–C(1)	1.7625(17)	1.763(4)–1.770(3)	1.760(5)–1.761(4)
S(2)–C(2)	1.7654(19)	1.755(4)–1.759(3)	1.761(5)–1.771(4)
P(1)–X	2.1038(9)	2.2908(7)– 2.2981(9)	2.5188(11)– 2.5295(13)
Selected angle	2a / °	2b / °	2c / °
S(1)–P(1)–S(2)	95.40(3)	95.33(5)– 95.67(5)	95.22(7)– 95.58(7)

2.1.3 Computational analysis of benzo-fused dithiaphospholes

To understand better the structural features of these compounds, density functional calculations (DFT) were performed on the complexes **1a–2c**. Initially a series of different functionals and basis sets were screened to determine the most appropriate combination that gave the closest fit to the single crystal data. With that, for the chloro- and bromo-dithiaphospholes (**1a**, **1b**, **2a** and **2b**) the Minnesota 06-2X⁶ (commonly abbreviated to M06-2X) was chosen with the Pople basis set 6-311+G(2d,p).⁷ However, given the heavier nature of the iodide co-ligand, the 6-311+G(2d,p) basis set is inappropriate to use. This is firstly because of the increased computational time required due to the increased number of electrons, but secondly and arguably more importantly, the need to describe relativistic effects of core electrons of heavier atoms. Consequently, effective core potentials (ECPs) are commonly used for heavier atoms and the Karlsruhe basis set Def2-TZVP⁸ (triple zeta valence polarisation) was employed for the iodine atom of **1c** and **2c**. Again M06-2X was used as the functional and the 6-311+G(2d,p) basis set was used for the remaining atoms.

Geometry optimisation and vibrational frequency calculations on **1a–2c** were initially performed, ensuring that each structure was a true minimum on the potential energy curve, after which natural bond orbital (NBO) calculations were undertaken.⁹ NBO calculations are a powerful tool as they allow the fundamental bonding model of a molecule to be probed

and provide great structural detail which can complement the results of the crystallography. When performed on **1a**, NBO calculations revealed a high level of polarisation in the P–Cl bond, with natural charges of +0.53 and –0.32 on the phosphorus and chloride atoms respectively. Further to this, the P–Cl bond exhibits a small reduction in single bond character, with a Wiberg bond order of 0.86. Given the interesting result of this reduced bond order, it was investigated further by looking at the orbital interactions that exist in **1a**. This was done by analysis of the second-order perturbative estimates of donor-acceptor interactions, which in short looks at any donations of electron density from filled bonding orbitals into vacant (or partially filled) orbitals. This analysis showed there was π -electron density from the bonding orbitals of the P–S bonds and donation from the lone pairs on the sulfur atoms both donating into the σ^* -antibonding orbital of the P–Cl bond. The lone pair donation from the sulfur atoms contribute much more to the stabilisation energy gained, at 58 KJ mol⁻¹ for each sulfur atoms compared to 6 KJ mol⁻¹ from each P–S bond. That is to say dithiaphosphole **1a** gains approximately 128 KJ mol⁻¹ in stabilisation energy than if these donations did not take place. This donor-acceptor analysis therefore explains the reason behind why the P–Cl bond length is elongated, as it is the donation of electron density into the σ^* P–Cl orbital which reduces the bond order and thus elongates it.

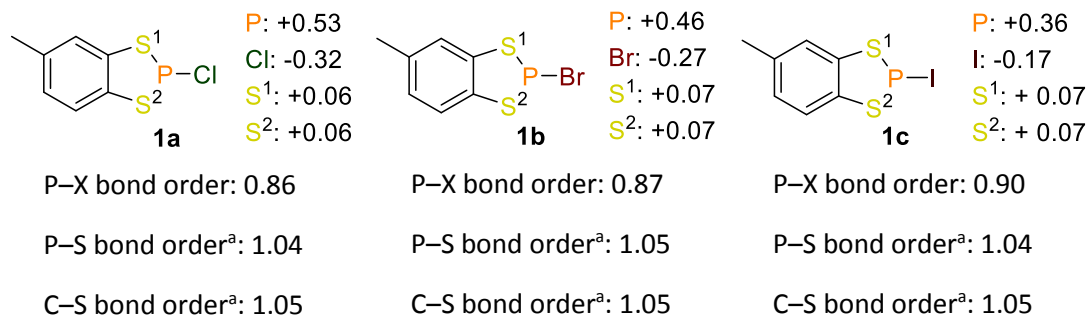


Figure 2.7: NBO analysis of dithiaphosphole compounds **1a–1c**. All atoms treated with M06-2X functional and 6-311G+(2d,p) basis set, with the exception of **1c**, which used Def2-TZVP for the I atom. ^aAverage values taken.

NBO analysis was then used to compare the series of the three dithiaphospholes **1a–1c**, to see what effect, if any, the change in co-ligand has on the electronic properties. Upon moving from chloride to bromide to iodide as the co-ligand, a reduction in the polarisation of the bond was calculated (Figure 2.7). That is the phosphorus heteroatom has less positive charge build-up (+0.46 in **1b** and +0.36 in **1c**) and the bromide and iodide co-ligand have less negative charge (–0.27 in **1b** and –0.17 in **1c**). The Wiberg bond order remained approximately constant when changing the co-ligand to bromide and iodide; 0.87 for **1b** and

0.90 for **1c**. Meanwhile the partial charges on the sulfur atoms were found to remain largely unchanged. It should be noted that NBO analysis on **2a–2c** showed comparative results to their analogues **1a–1c** as expected. Their results are also summarised in Figure 2.8.

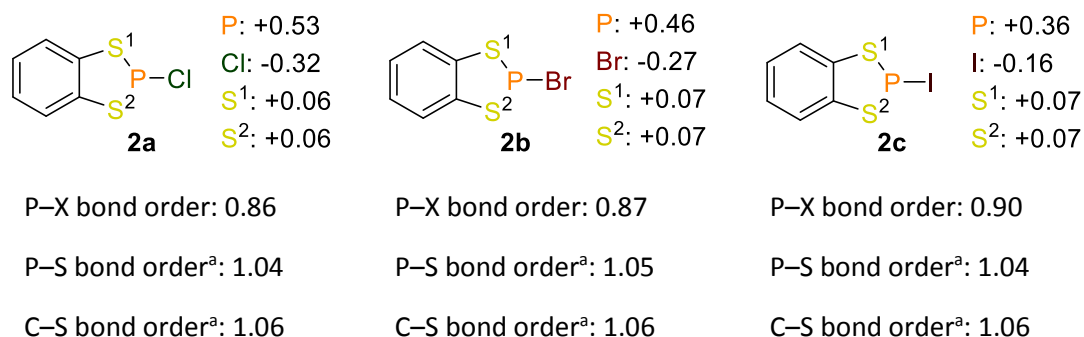
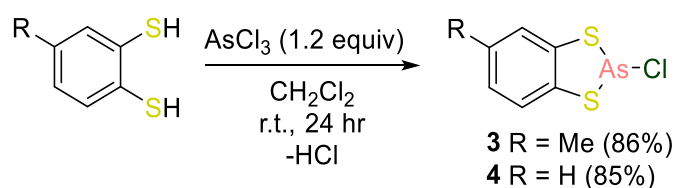


Figure 2.8: NBO analysis of dithiaphosphole compounds **2a–2c**. All atoms treated with M06-2X functional and 6-311G+(2d,p) basis set, with the exception of **1c**, which used Def2-TZVP for the I atom. ^aAverage values taken.

2.1.4 General synthesis and NMR spectroscopy analysis of benzo-fused dithia-chloro-arsoles
 In a similar fashion to the synthesis of the dithiaphospholes, the synthesis of the benzo-fused dithia-chloro-arsoles (shortened herein to dithiarsoles) involved the addition of either toluene-3,4-dithiol or benzene-1,2-dithiol to arsenic trichloride in CH₂Cl₂ solvent and stirred at room temperature for 24 hours (Scheme 2.2). Vigorous effervescence was immediately observed and the solution turned yellow. When using toluene-3,4-dithiol as the starting ligand the product 2-chloro-5-methylbenzo-1,3,2-dithiarsole (**3**) was obtained as a yellow powder in an 86% yield, whereas using benzene-1,2-dithiol produced the product 2-chlorobenzo-1,3,2-dithiarsole (**4**), again as a yellow powder and in 85% yield.¹⁰



Scheme 2.2: Synthesis of dithiarsole compounds **3** and **4**.

In contrast to the dithiaphosphole synthesis, NMR spectroscopy analysis is less useful as a characterisation technique. The ⁷⁵As nucleus, which is the only active arsenic NMR nucleus, has 100% natural abundance and is quadrupolar with I = 3/2. Despite its moderately high gyromagnetic ratio ($\gamma = 45.6 \times 10^6 \text{ rad s}^{-1} \text{ T}^{-1}$), solution-phase ⁷⁵As NMR spectroscopy is not routinely performed. This is principally because the large quadrupole moment ($Q = 0.3 \times 10^{-24} \text{ cm}^2$) leads to shorter relaxation times due to the subsequent quadrupole

relaxation mechanisms, which in turn leads to line broadening. This line broadening is often so severe that even in small molecules with symmetrical environments, resonances may cover several ppm.^{11,12} Although ⁷⁵As NMR spectroscopy cannot practically be used, ¹H and ¹³C{¹H} NMR spectroscopy is unaffected by the quadrupolar ⁷⁵As nuclei and proceeds as normal. ¹H NMR spectroscopy shows loss of the two dithiol protons, at *cf.* 3.70 and 3.60 ppm, and the expected three aromatic signals for **3** and two for **4**. The dithiarsole **3** also shows the methyl group with a singlet resonance centred at $\delta = 2.37$ ppm. With that, other characterisation methods were more heavily relied on for characterisation. High resolution mass spectrometry (HRMS), using the electron ionisation (EI) method, helped further confirm the synthesis of **3** and **4**, with [M]⁺ [C₇H₆AsClS₂]⁺ for **3** at 263.8810 (theoretical: 263.88099) and [M]⁺ [C₆H₄AsClS₂]⁺ for **4** at 249.8655 (theoretical: 249.86534).

2.1.5 Single crystal X-ray diffraction analysis of benzo-fused dithiarsoles

Needing further confirmation of the formation of the two dithiarsoles **3** and **4**, attention turned to X-ray crystallography. Crystals of **3**, solved by Dr John Davies, suitable for single crystal X-ray diffraction were grown by Dr Rebecca Melen from either MeOH (**3 α**) or MeCN (**3 β**) (Figure 2.9), giving two separate polymorphs, whereas crystals of **4** were grown from a saturated solution of THF (Figure 2.10), again by Dr Rebecca Melen. When recrystallised from MeOH, the structure of **3 α** was the same as previously reported (CSD identifier code: DAXLOD) and crystallised in the *P2₁/c* space group. On the other hand, recrystallisation from MeCN produced a new polymorph, **3 β** , which crystallised in the triclinic space group *P*-1. This new polymorph **3 β** has two molecules in the asymmetric unit, which increases to four molecules in the unit cell. For reference, **3 α** has one molecule in the asymmetric unit and four molecules in the unit cell. Similarly to **3 β** , **4** crystallised in the triclinic space group *P*-1. However, unlike **3 β** , **4** possesses 17 molecules in the asymmetric unit, which increases to 34 in the unit cell. Having 17 molecules in the asymmetric unit is crystallographically unusual, as excluding this structure there are only 10 other structures with $Z' \geq 17$ in the Cambridge Structural Database (CSD).¹³

Looking at the structural features of the dithiarsoles **3 α** and **3 β** , they are in essence equivalent and show similarities to the dithiaphospholes described above. That is the arsenic heteroatom is three-coordinate with an exocyclic chloride to the fused benzarsole ring. The As–Cl bond length was found to measure 2.2498(5) Å in **3 α** and 2.2582(7) Å and 2.2540(8) Å (Table 2.3) for the two crystallographically independent molecules in **3 β** (*cf.* standard As–Cl bond length 2.268 Å).⁵ In addition, a fold angle about the S...S vector is observed, which for **3 α** is 23.60(4)° and for **3 β** 19.44(8)° and 21.51(8)° for the two

crystallographically independent molecules. These fold angles are lower than that found in the dithiaphosphole analogue **1a**, which was $26.07(6)^\circ$ (*vide supra*), suggesting that the dithiarsole tends more to molecular planarity than the dithiaphosphole analogue (Table 2.3).

Analysis of the packing of the unit cell of **3a** shows no significant close contacts and instead appears to be directed by $\text{As}\cdots\pi$ interactions between the arsenic heteroatom and the fused benzene ring. In contrast, the packing in **3b** shows interactions between the arsenic atom and chloride on the neighbouring dithiarsole; similar to that observed in **1a**. However, unlike **1a** these contacts do not fall in the range of the sum of the van der Waals radii.

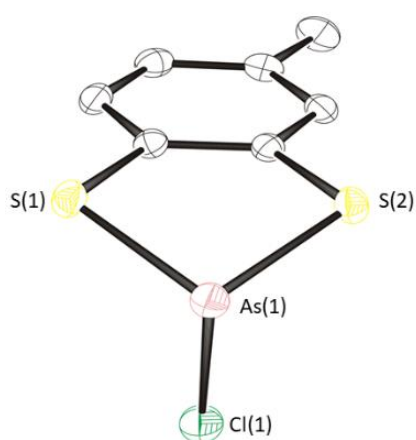


Figure 2.9: Solid-state structure of **3b**. Thermal ellipsoids drawn at 50% probability and H-atoms removed for clarity.

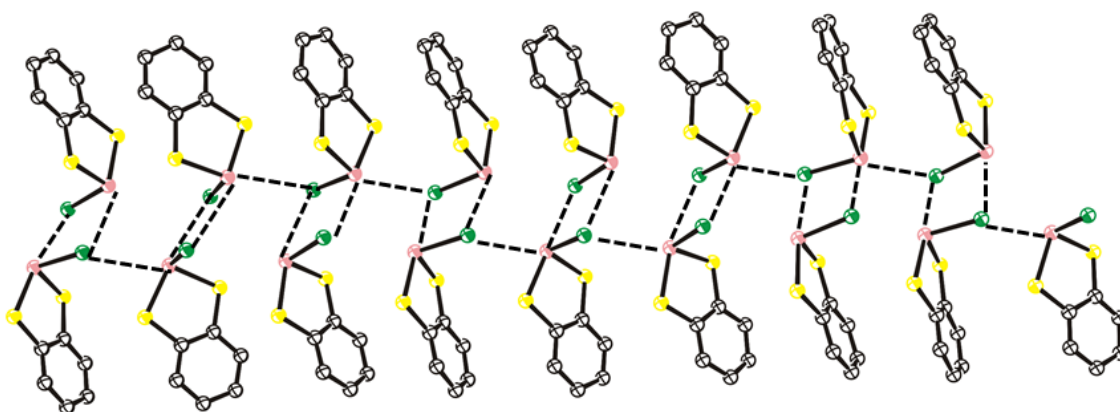


Figure 2.10: Solid-state structure of **4** showing the 17 molecules in the asymmetric unit. Dashed lines show the close contacts between arsenic and chloride atoms. Pink: arsenic, yellow: sulfur, green: chlorine.

Similar structural analysis of **4** shows comparable results to that just described for **3**. The As–Cl bond length ranges from 2.27436(4) Å to 2.31361(4) Å and the fold angle has a mean value of 14.28°. The packing of the 17 molecules in **4** in the asymmetric unit is highly interesting as it is found that all 17 molecules participate in forming dimers between the arsenic heteroatom and the neighbouring chloride. This is similar to what occurs in **3β** but these As⋯Cl contacts in **4** are shorter than the sum of the van der Waals radii. These close contacts are made up of 8 distinct crystallographic dimers and one dimer which is situated about an inversion centre (Figure 2.10).

Table 2.3: Selected bond lengths and interior bond angles for compounds **3β** and **4**.

Selected bond	3β / Å (R = Me)	4 / Å (R = H)
As(1)–S(1)	2.2180(9)–2.2212(9)	2.188(7)–2.227(7)
As(1)–S(2)	2.2099(8)–2.2147(7)	2.196(7)–2.224(7)
S(1)–C(1)	1.765(2)–1.773(2)	1.75(2)–1.773(11)
S(2)–C(2)	1.760(3)–1.766(3)	1.748(14)–1.776(13)
As(1)–Cl(1)	2.2540(8)–2.2582(7)	2.27436(4)–2.31361(4)
Selected angle	3β / °	4 / °
S(1)–As(1)–S(2)	92.77(3)–93.08(3)	92.2(2)–93.9(3)

2.1.6 Computational analysis of benzo-fused dithiarsoles

As was done for the dithiaphospholes, DFT calculations were performed on the dithiarsoles to understand the structural features of **3** and **4** as well as to compare to their phosphorus analogues **1a** and **2a** respectively. The M06-2X functional and 6-311+G(2d,p) basis set were again employed on all atoms, except for the arsenic heteroatom. Due to the relatively heavy nature of arsenic, the ECP Los Alamos National Laboratory 2-double-zeta^{14–16} (commonly abbreviated to LANL2DZ) basis set was used in conjunction with M06-2X. NBO analysis on **3** shows the As–Cl bond is polarised, with natural charges of +0.81 and –0.42 for the arsenic and chloride atoms respectively. Furthermore, the As–Cl bond possesses reduced single bond character, with a Wiberg bond index of 0.76. As was the case with the dithiaphospholes, this reduction in bond length is explained by the donation of electron density from the C₂S₂ unit into the σ*-antibonding orbital of the As–Cl bond. The lone pairs on the sulfur atom again each attribute 60 KJ mol⁻¹ in stabilisation energy, whereas electron density from each As–S bond contributes 4 KJ mol⁻¹. Unsurprisingly, given the structural

similarities to **3**, NBO results of **4** were largely similar. There is again the same build-up of positive charge on the arsenic heteroatom (+0.81) and negative charge on the chloride co-ligand (-0.42). The sulfur heteroatoms in both **3** and **4** are mostly neutral, with natural charges of -0.03 and -0.02 respectively (Figure 2.11). This is a similar feature as was seen with the dithiaphospholes.

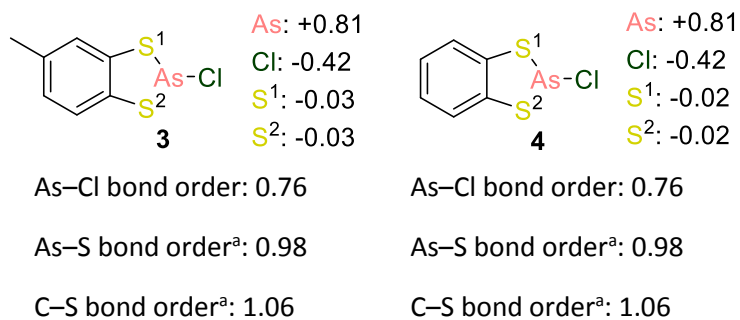


Figure 2.11: NBO analysis of dithiarsole compounds **3** and **4**. All atoms treated with M06-2X functional and 6-311G+(2d,p) basis set, with the exception of As, which used LANL2DZ.

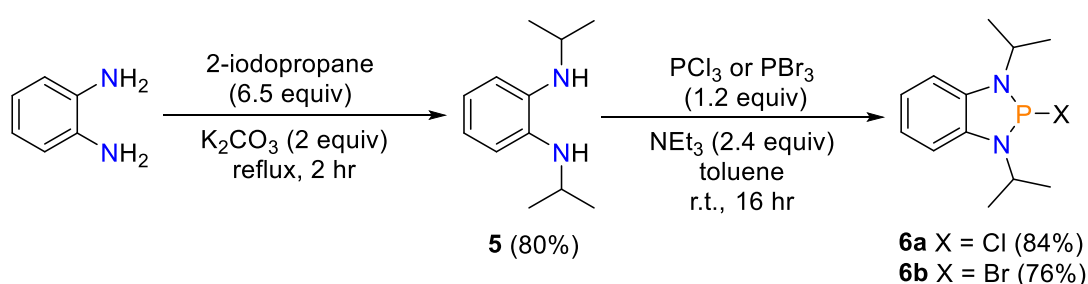
^aAverage values taken.

Chapter 2.2 Synthesis of Benzo-Fused Diazaphospholes and Diazarsoles

Having synthesised and explored the structural and electronic properties of the dithiaphosphole and dithiarsole complexes, attention then turned to using a new class of starting ligand which would presumably offer a different variation on these fundamental characteristics. Swapping the sulfur for nitrogen heteroatoms in the five-membered ring would give rise to diazaphosphole and diazarsole structures, which given the electronegativity differences between sulfur and nitrogen ($S = 2.58$, $N = 3.04$ by Pauling scale) was expected to offer significant changes, which would then be exploited later with regards to their reactivity.

2.2.1 General synthesis and NMR spectroscopy analysis of benzo-fused diazaphospholes

Synthesis of the benzo-fused diazaphospholes (shortened herein to diazaphospholes) first required an appropriate diamine starting ligand. The ligand *N,N'*-diisopropylbenzene-1,2-diamine (**5**) was chosen, in part due to its relatively simple synthesis, and was produced as described by Weber and Fox,¹⁷ which in short involved reacting *o*-phenylenediamine with excess 2-iodopropane and potassium carbonate (Scheme 2.3). After heating under reflux for two hours, the product was extracted in hexane solvent which gave the crude product as a brown oil. This oil was then purified using a Kugelröhr short-path distillation (180 °C, 5 mbar) to yield a colourless oil. The formation of ligand **5** was confirmed by NMR spectroscopy as analysis of the ¹H NMR spectrum showed a septet centred at $\delta = 3.65$ ppm ($^3J_{\text{HH}} = 6.3$ Hz) and a doublet centred $\delta = 1.32$ ppm ($^3J_{\text{HH}} = 6.3$ Hz), which are assigned to the isopropyl groups. A broad singlet signal at $\delta = 3.23$ ppm with an integral of two was also observed which could be assigned to the NH group present.



Scheme 2.3: Synthesis of diamine ligand and diazaphospholes.

Formation of the diazaphospholes proceeded *via* the addition of the diamine ligand to either phosphorus trichloride or phosphorus tribromide, with triethylamine acting as a base. The ammonium salt by-product was removed by filtration (using a cannula filter) of the resulting solution, followed by removal of the solvent *in vacuo*. Subsequent pentane washings and drying *in vacuo* yielded the product 2-chloro-1,3-diisopropyl-benzodiazaphosphole (**6a**) or

2-bromo-1,3-diisopropyl-benzodiazaphosphole (**6b**) respectively in high yields of 84% and 76% respectively (Scheme 2.3).¹⁸ Again, multinuclear NMR spectroscopy confirmed the formation of **6a** and **6b**. In the case of **6a**, ³¹P{¹H} NMR spectroscopy showed a singlet resonance at $\delta = 147.2$ ppm, which is similar but more upfield to that of **1a** ($\delta = 160.4$), and full consumption of the phosphorus trichloride starting material. The ¹H NMR spectrum of **6a** showed loss of the broad NH signal seen in **5**. More interestingly though, it only showed one singlet resonance for the aromatic signals, appearing at $\delta = 7.08$ ppm, suggesting rapid molecular rotation in solution causing these protons to become equivalent on the NMR timescale (Figure 2.12). Note this was not seen for the dithiaphospholes. The isopropyl groups are shifted slightly downfield compared to the free ligand and have chemical shifts of $\delta = 4.32$ and 1.69 ppm, with ³J_{HH} = 6.6 Hz.

The synthesis of **6b** was analogous to that as described for **6a** and made use of phosphorus tribromide as the starting phosphorus trihalide. ³¹P{¹H} NMR spectroscopy showed formation of **6b** with a singlet resonance at $\delta = 169.2$ ppm (appreciably more downfield than **6a**) and complete loss of phosphorus tribromide precursor. The ¹H NMR spectrum shares the same features as **6a** with the exception that the aromatic resonances are not a well-defined singlet but instead appear as a multiplet.

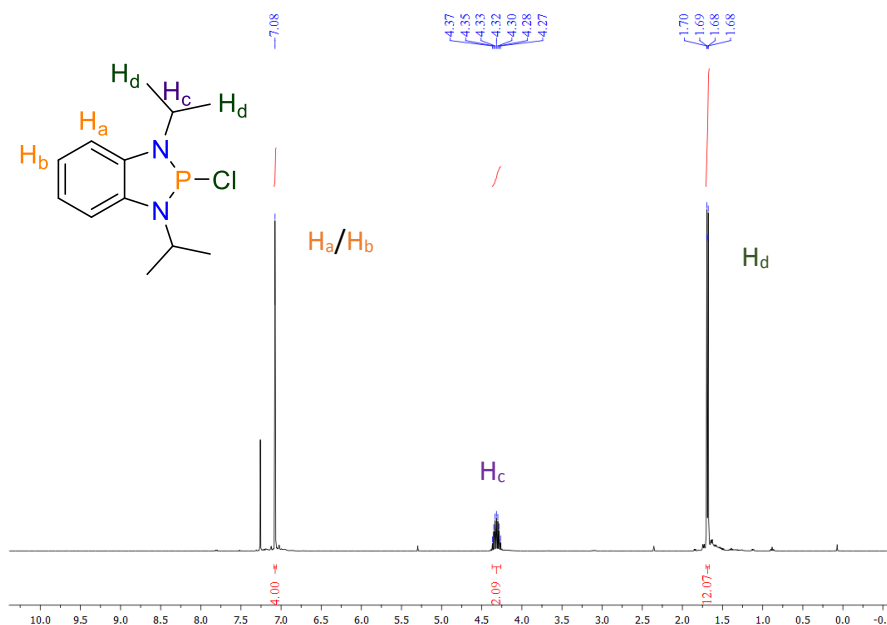


Figure 2.12: ¹H NMR (400 MHz, CDCl₃, 295 K) spectrum of the diazaphosphole **6a**.

2.2.2 Single crystal X-ray diffraction analysis of 2-chloro-1,3-diisopropylbenzodiazaphosphole

Crystals of **6a** suitable for single crystal X-ray diffraction were grown in collaboration with Alex Rigby from a saturated solution of CH₂Cl₂ with a few drops of pentane added and cooled to -40 °C (Figure 2.13). Upon structure refinement by Dr Lewis Wilkins, **6a** was found to crystallise in the triclinic space group *P*-1 and contain two molecules in the asymmetric unit. This increases to four molecules in the unit cell. As was observed in the dithiaphospholes, the solid-state structure of **6a** shows that the phosphorus is three-coordinate with an exocyclic chloride. Structurally it possesses an envelope-type geometry, with a fold angle about the N...N vector of 8.82(11)° and 11.2(2)° for the two crystallographically independent molecules. These diazaphospholes therefore tend much more towards molecularly planarity than their dithiaphosphole counterparts, which have a significantly increased fold angle (*cf.* **1a** fold angle = 26.07(6)° and **2a** fold angle = 28.65(6)°).

6a shows significant elongation in the P(1)–Cl(1) bond, with a bond length of 2.3240(7) Å and 2.3377(7) Å (Table 2.4), which was a similar feature to the dithiaphospholes and is explained further using DFT calculations; *vide infra*. For reference a typical P–Cl bond length is 2.008 Å and the P–Cl bond length observed in **1a** was 2.1134(7) Å.⁵ Further to this, the C–N bond lengths are slightly shorter than typical values (1.47 Å), measuring 1.403(2)–1.405(2) Å. The N(1)–P(1)–N(2) internal bond angle is 90.95(8)° and 91.04(8)°, which is notably contracted compared to **1a**. Analysis of the packing in the unit cell of **6a** did not show any short interactions between the chloride and phosphorus atom, such as that seen in **1a** and no meaningful close contacts were found.

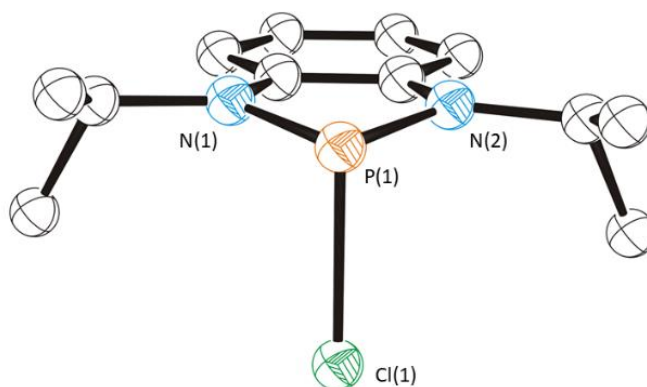


Figure 2.13: Solid-state structure of **6a**. Thermal ellipsoids drawn at 50% probability and H-atoms removed for clarity.

Table 2.4: Selected bond lengths and interior bond angles for compounds **6a**.

Selected bond	6a / Å
P(1)–N(1)	1.6713(16)–1.6733(18)
P(1)–N(2)	1.6728(17)–1.6740(15)
N(1)–C(1)	1.403(2)–1.403(3)
N(2)–C(2)	1.403(3)–1.405(3)
P(1)–Cl(1)	2.3240(7)–2.3377(7)
<hr/>	
Selected angle	6a / °
N(1)–P(1)–N(2)	90.95(8)–91.04(8)

2.2.3 Computational analysis of benzo-fused diazaphospholes

DFT calculations were performed on the diazaphospholes to obtain a better understanding of the fundamental structure and bonding that is exhibited, which could also then be compared against the dithiaphospholes. Geometry optimisation and vibrational frequency calculations of both **6a** and **6b** were initially performed, using the functional and basis set M06-2X and 6-311+G(2d,p) respectively, after which NBO analysis was undertaken (results are summarised in Figure 2.14). The solid-state structure of **6a** showed substantial elongation in the P–Cl bond length, which was a similar observation to that found in the dithiaphospholes. This elongation is more extreme in the diazaphosphole case though, with a Wiberg P–Cl bond order of just 0.67. This compares to a Wiberg P–Cl bond order of 0.86 for the dithiaphosphole **1a**. The reasoning for this bond elongation is the same as for **1a**, in that electron density from the C₂N₂ unit donates into the σ^* -antibonding orbital of the P–Cl bond. Examination of the second-order perturbative estimates of donor-acceptor interactions shows how significant this donation is, with a stabilisation energy gain of 139 KJ mol⁻¹ from electron density from each C–N bond to P–Cl σ^* -antibonding orbital.

Further to this, the P–Cl bond is polarised, with natural charges of +1.29 and –0.49 for the phosphorus and chloride atoms accordingly. Again, comparing to the dithiaphosphole **1a** this polarisation is more extreme in **6a**, with **1a** having natural charges of +0.53 and –0.32 for phosphorus and chloride atoms respectively. The nitrogen heteroatoms both have natural charges of –0.82. Interestingly, the P–N bond order in **6a** is also low; calculated at just 0.84. Once more this can be explained by the donation of π electron density from the

fused benzene ring into the P–N antibonding orbital, as second-order perturbative estimates of donor-acceptor interactions finds a 46.3 KJ mol⁻¹ stabilisation gain from this donation.

NBO analysis on **6b** showed similar results as seen in **6a**. The P–Br bond is highly polarised, with natural charges of +1.25 and –0.49 for the phosphorus and bromide atoms respectively. For comparison, in the dithiaphosphole **1b**, natural charges of +0.46 and –0.27 for the phosphorus and bromide atoms respectively were observed. Like **6a**, the P–Br bond also exhibits significant reduced single bond character, with a Wiberg P–Br bond order of 0.63. The reasoning for this is the same as **6a**. The nitrogen heteroatoms both have natural charges of –0.81.

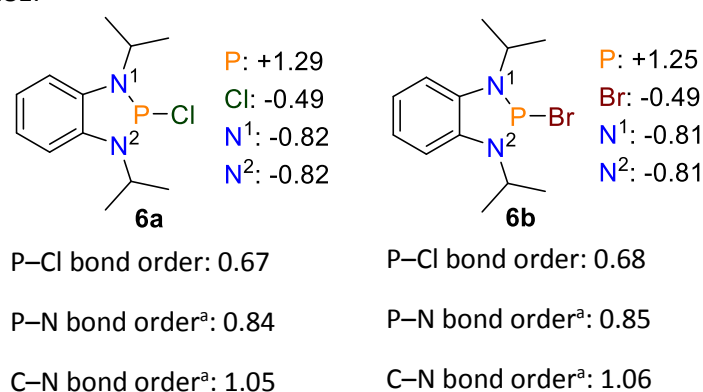
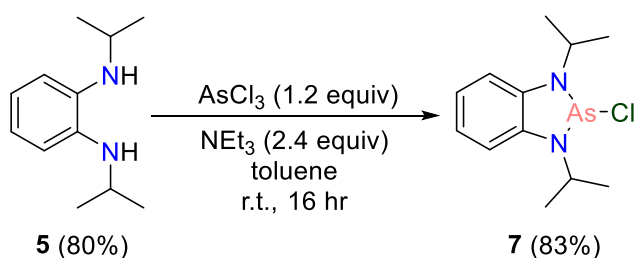


Figure 2.14: NBO analysis of compounds **6a** and **6b**. All atoms treated with M06-2X functional and 6-311G+(2d,p) basis set. ^aAverage values taken.

2.2.4 General synthesis and NMR spectroscopy analysis of benzo-fused diazaphospholes

The synthesis of the benzo-fused diaza-chloro-arsole (shortened herein to diazarsoles), originally undertaken with Alex Rigby, followed the same procedure as described above for the diazaphospholes; reacting arsenic trichloride with the ligand *N,N'*-diisopropylbenzene-1,2-diamine (**5**) and excess triethylamine (Scheme 2.4). Again, after filtering to remove the ammonium salt by-product, the solvent was removed *in vacuo* and the product was washed with pentane and further dried *in vacuo*. 2-chloro-1,3-diisopropyl-benzodiazarsole (**7**) was obtained as a yellow solid in high yield of 83%.¹⁸



Scheme 2.4: Synthesis of 2-chloro-1,3-diisopropyl-benzodiazarsole.

As was encountered with the dithiarsoles, NMR spectroscopy analysis is less useful than for the diazaphospholes, given the difficulties of performing ^{75}As NMR spectroscopy. ^1H NMR spectroscopy is still useful however as the ^1H NMR spectrum of **7** showed loss of the broad signal at $\delta = 3.23$ ppm, corresponding to the NH group, indicating coordination to arsenic. In addition, the septet resonance that is observed at $\delta = 3.65$ ppm in the free ligand is shifted appreciably downfield to $\delta = 4.46$ ppm in **7**. Likewise, the doublet resonance of the isopropyl group is shifted downfield from $\delta = 1.32$ ppm to $\delta = 1.70$ ppm upon coordination to arsenic. Moreover, as was seen in the diazaphosphole **6a**, the aromatic signals appear as a singlet, with a resonance centred at $\delta = 7.04$ ppm. Like the dithiarsoles, mass spectrometry was highly informative in the characterisation, with a $[\text{M}]^+$ $[\text{C}_{12}\text{H}_{18}\text{AsN}_2\text{Cl}]^+$ peak found at 300.0376 (theoretical: 300.0374) using ES^+ .

2.2.5 Single crystal X-ray diffraction analysis of 2-chloro-1,3-diisopropyl-benzodiazarsole

As before, crystals of **7** suitable for single crystal X-ray diffraction were grown in collaboration with Alex Rigby from a saturated solution of CH_2Cl_2 with a few drops of pentane added and cooled to -40 °C (Figure 2.15). From structure solution and refinement by Dr Lewis Wilkins, diazarsole **7** crystallises in the monoclinic space group Cc , with one molecule in the asymmetric unit and four molecules in the unit cell. Structurally the diazarsole shows the expected three coordinate arsenic centre with an exocyclic chloride; an envelope type geometry is also present. The fold angle about the $\text{N}\cdots\text{N}$ vector measures $6.4(2)^\circ$, which is lower than that seen in **6a** (*cf.* $8.82(11)^\circ$ and $11.2(2)^\circ$) and therefore tends even more to molecular planarity. This trend of the diazarsole having a reduced fold angle compared to the diazaphosphole is the same as the dithiarsole and dithiaphosphole (*vide supra*). Elongation in the $\text{As}(1)\text{--Cl}(1)$ bond length is found, measuring $2.4440(13)$ Å (*cf.* standard As--Cl bond length of 2.268 Å)⁵ (Table 2.5).

The As--N bond lengths were found to be $1.812(3)$ Å and $1.809(3)$ Å, whereas the C--N bond lengths measure $1.394(5)$ Å and $1.390(5)$ Å. These are just shorter than a standard C--N bond length (1.47 Å). Lastly, the $\text{N}(1)\text{--As}(1)\text{--N}(2)$ internal bond angle is $86.45(14)^\circ$, which is considerably less than that seen in **6a**, where the $\text{N}(1)\text{--P}(1)\text{--N}(2)$ internal bond angle measured $90.95(8)^\circ$ and $91.04(8)^\circ$. Upon investigating the packing of **7**, no short contacts exist between the chloride and arsenic atom, such as that seen in **4**. Indeed, no meaningful short contacts exist in the packing structure of **7**.

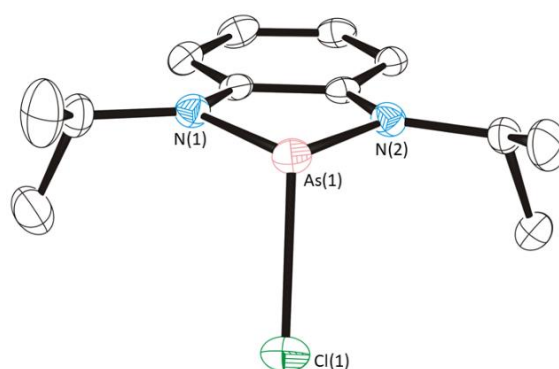


Figure 2.15: Solid-state structure of **7**. Thermal ellipsoids drawn at 50% probability and H-atoms removed for clarity.

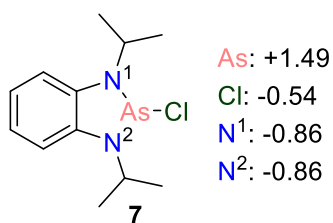
Table 2.5: Selected bond lengths and interior bond angles for compounds **7**.

Selected bond	7 / Å
As(1)–N(1)	1.812(3)
As(1)–N(2)	1.809(3)
N(1)–C(1)	1.394(5)
N(2)–C(2)	1.390(5)
As(1)–Cl(1)	2.440(13)
Selected angle	7 / °
N(1)–As(1)–N(2)	86.45(14)

2.2.6 Computational analysis of 2-chloro-1,3-diisopropyl-benzodiazarsole

In an analogous fashion to the diazaphospholes **6a** and **6b**, the diazarsole **7** was first geometry optimised, after which a vibrational frequency calculation was performed. The M06-2X functional and 6-311+G(2d,p) basis set was employed on all atoms with the exception of the arsenic heteroatom. As was the case for the dithiarsoles **3** and **4**, the ECP LANL2DZ basis set was used along with M06-2X for arsenic. Following this optimisation, NBO calculations were performed on **7**, which allowed for a comparison to the diazaphosphole **6a** and the dithiarsoles. As has been well established now, these heterocycles possess a polarised E–X bond (where E = P/As and X = halogen), and indeed this is true for **7** as well. The arsenic heteroatom has a natural charge of +1.49 and the chloride –0.54, which is comparable to the diazaphosphole, albeit slightly more polarised, but the arsenic atom has

much more positive charge build-up than in the dithiarsoles **3** and **4** (+0.81 for both). As was the case with the P–Cl bond in **6a**, the As–Cl bond exhibits a very low Wiberg bond order of just 0.60; much lower than the 0.76 bond order in the dithiarsoles **3** and **4**. The reasoning for this is the same as was discussed for **6a**. The nitrogen atoms have a natural charge of –0.86 each (Figure 2.16).



As–Cl bond order: 0.60

As–N bond order^a: 0.74

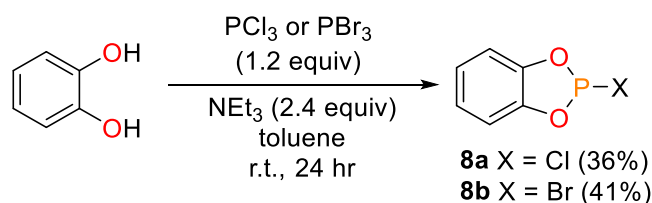
C–N bond order^a: 1.08

Figure 2.16: NBO analysis of compounds **7**. All atoms treated with M06-2X functional and 6-311G+(2d,p) basis set, with the exception of As, which used LANL2DZ. ^aAverage values taken.

Chapter 2.3 Synthesis of Benzo-Fused Dioxaphospholes

2.3.1 General synthesis and NMR spectroscopy analysis of benzo-fused dioxaphospholes

The synthesis of the benzo-fused dioxaphospholes (shortened herein to dioxaphospholes) proceeded by the addition of catechol to the phosphorus trihalide in the presence of triethylamine, using toluene as a solvent. After stirring at ambient temperature for 24 hours, the solution was filtered to remove the ammonium salt by-product and the solvent was removed *in vacuo*. At this point $^{31}\text{P}\{^1\text{H}\}$ NMR spectroscopy revealed that two products existed in the resulting yellow coloured oil, with chemical shifts of $\delta = 173.6$ and 129.2 ppm for 2-chlorobenzo-1,3,2-dioxaphosphole (**8a**) and $\delta = 195.3$ and 129.2 ppm for 2-bromobenzo-1,3,2-dioxaphosphole (**8b**) (Figure 2.17). In order to purify the dioxaphospholes, an air-sensitive distillation was performed on both **8a** and **8b**, with **8a** distilling at 44–52 °C under 5 mbar vacuum and **8b** distilling at 60–62 °C under the same vacuum pressure. These distillations yielded the desired dioxaphospholes as colourless oils in moderate yields of 36% for **8a** and 41% for **8b** (Scheme 2.5).² The moderate yields can be explained as a combination of both loss of product from the distillation and formation of undesired side product.



Scheme 2.5: Synthesis of the dioxaphospholes compounds **8a** and **8b**.

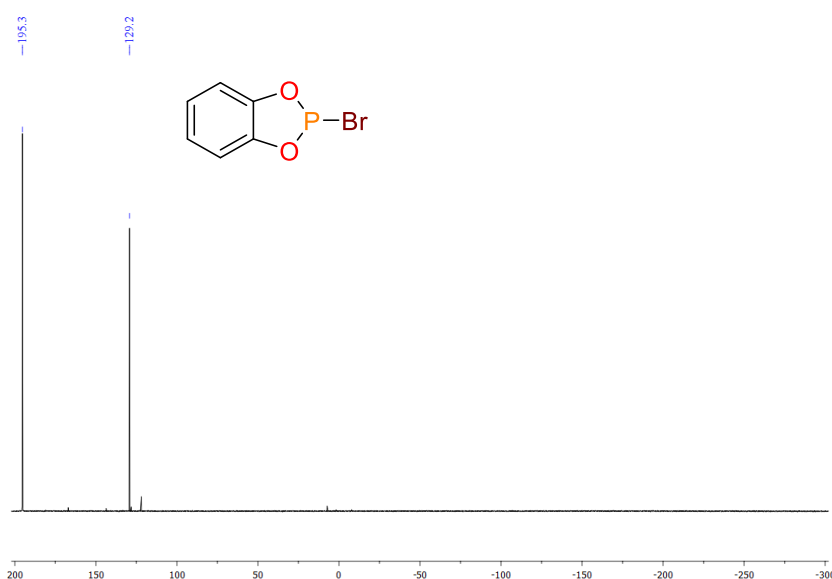


Figure 2.17: $^{31}\text{P}\{^1\text{H}\}$ NMR spectrum (202 MHz, CDCl_3 , 295 K) of **8b** before distillation.

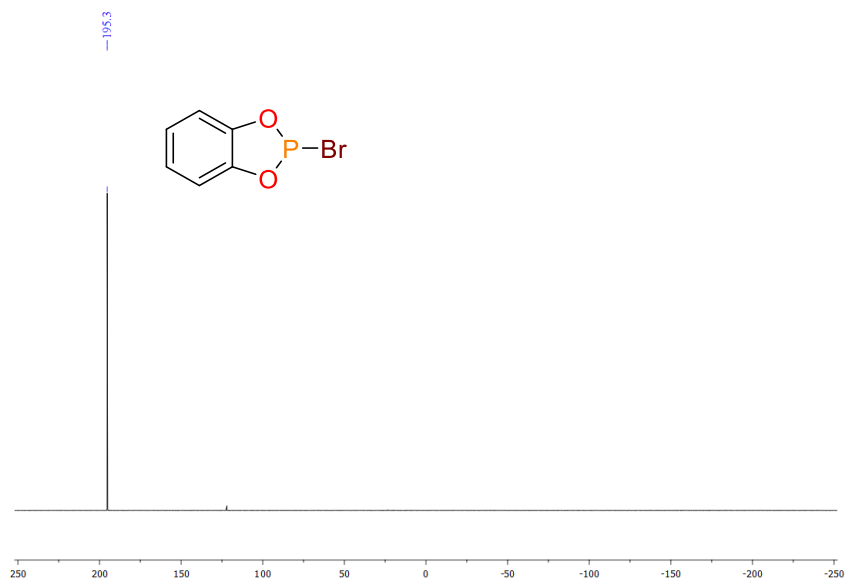


Figure 2.18: $^{31}\text{P}\{^1\text{H}\}$ NMR spectrum (202 MHz, CDCl_3 295 K) of **8b** after distillation.

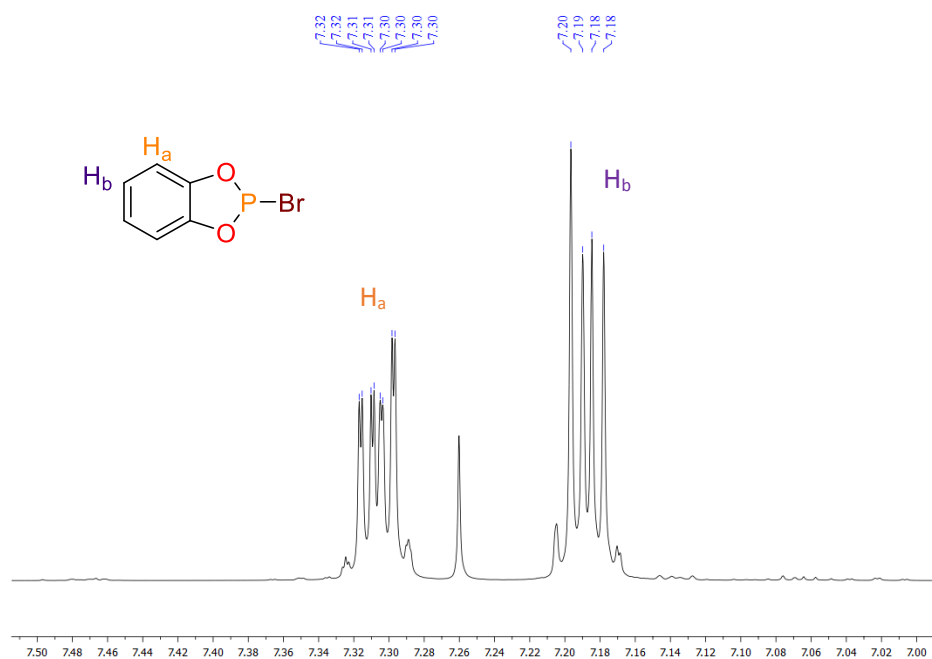


Figure 2.19: ^1H NMR spectrum (500 MHz, 295 K, CDCl_3) of **8b** after distillation.

$^{31}\text{P}\{^1\text{H}\}$ NMR spectroscopy was performed on the dioxaphospholes after the air-sensitive distillation, which showed only one phosphorus containing species at $\delta = 173.6$ ppm for **8a** and $\delta = 195.3$ ppm for **8b** (Figure 2.18). It is unclear the identity of the impurity at $\delta = 129.2$ ppm. These ^{31}P NMR values for **8a** and **8b** match those previously reported in the literature.^{19,20} The positioning of the chemical shift for **8a** is more downfield than for the dithiaphosphole and diazaphosphole analogues **1a**, **2a** and **6a** previously discussed, which

have $^{31}\text{P}\{^1\text{H}\}$ NMR chemical shifts of $\delta = 160.4$, $\delta = 158.3$ and $\delta = 147.2$ ppm respectively. Inspection of the ^1H NMR spectra for **8a** displayed the expected two aromatic signals, but the coupling could not be resolved, thus two multiplets were reported at $\delta = 7.19\text{--}7.17$ and $\delta = 7.07\text{--}7.05$ ppm. **8b** also showed the expected two aromatic signals, however the coupling was resolved (Figure 2.19). Both chemical and magnetic inequivalence was observed, with the first aromatic signal centred at $\delta = 7.31$ ppm splitting into a doublet of doublets; coupling constant values of $^3J_{\text{HH}} = 5.9$ Hz, $^4J_{\text{HH}} = 3.4$ Hz, $^4J_{\text{PH}} = 0.8$ Hz. The second aromatic signal does not show $^5J_{\text{PH}}$ coupling and splits into a doublet of doublets, with coupling constant values of $^3J_{\text{HH}} = 5.9$ Hz, $^4J_{\text{HH}} = 3.4$ Hz.

2.3.2 Computational analysis of benzo-fused dioxaphospholes

In a similar vein to both the dithiaphospholes and diazaphospholes, computational studies were performed on the dioxaphospholes to better understand compounds **8a** and **8b**. Geometry optimisation and vibrational frequency calculations of both **8a** and **8b** were initially performed, using the functional and basis set M06-2X and 6-311+G(2d,p) respectively, after which NBO analysis was undertaken. The results of the NBO calculations follow a similar pattern to before, with a P–X bond that is reduced from single bond character. Both **8a** and **8b** have a Wiberg bond index of 0.87. The explanation of the P–X single bond character reduction is similar to that as described before, *vide supra*, with this time the lone pairs on the oxygen responsible for donation into the P–X σ^* -antibonding orbital. For **8a** this stabilisation energy gain is worth 56 kJ mol^{-1} per oxygen atom; which is substantially less than the 139 kJ mol^{-1} stabilisation energy gain found in **6a** but much more comparable to the 58 kJ mol^{-1} gain seen in **1a** from the lone pairs on the sulfur atom. The donation of bonding electrons from the C–O bond make up an insignificant 2 kJ mol^{-1} stabilisation energy gain. For **8b** the stabilisation from oxygen lone pair donation is similar to **8a**, at 61 kJ mol^{-1} .

The P–X bond in both **8a** and **8b** is polarised as well as elongated, with natural charges $+1.40$ and $+1.36$ for the phosphorus atoms and -0.36 and -0.33 for the chloride and bromide atoms in **8a** and **8b** respectively. This build-up of positive charge is greater than that seen in either the dithiaphospholes or diazaphospholes, although the halogen atom receives more negative charge in the diazaphospholes. The oxygen atoms have a natural charge of -0.79 in both **8a** and **8b**, which is comparable to the natural charges of -0.82 and -0.81 observed in **6a** and **6b** accordingly (Figure 2.20).

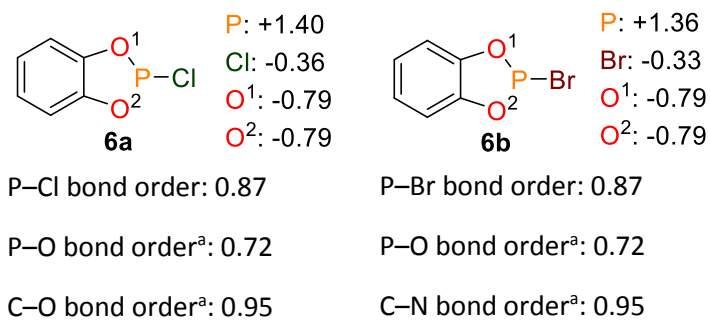


Figure 2.20: NBO analysis of dioxaphosphole compounds **8a** and **8b**. All atoms treated with M06-2X functional and 6-311G+(2d,p) basis set. ^aAverage values taken.

Chapter 2.4 Conclusion

In this chapter the synthesis of a range of novel benzophosphole and benzoarsole compounds has been presented (Figure 2.21). Initially, commercially available toluene-3,4-dithiol or benzene-1,2-dithiol was used as a starting ligand and reacted with both phosphorus and arsenic trihalides to yield the desired dithiaphosphole and dithiarsole. From here the *N,N'*-diisopropylbenzene-1,2-diamine ligand was synthesised and when reacted with phosphorus and arsenic trihalides and triethylamine gave the corresponding diazaphospholes and diazarsoles. The last class of heterocycles produced were the dioxaphospholes. These were produced in a similar vein to the diazaphospholes, with the phosphorus trihalide reacting with catechol and excess triethylamine. However, the dioxaphospholes required an air-sensitive distillation due to the formation of an impurity as detected by $^{31}\text{P}\{^1\text{H}\}$ NMR spectroscopy.

The solid-state structures of the dithia and diaza pnictoles were obtained which showed that these complexes possess an envelope-type geometry, with fold angles about the S...S and N...N vector. Generally speaking, the arsenic species had lower fold angles than their phosphorus counterparts, a result of their high inversion barrier of the trigonal pyramidal coordination geometry.²¹ The dithia pnictoles also had a greater fold angle than the diaza pnictoles, which can be explained by the greater aromaticity, and therefore planarity, in the latter (see Chapter 3). DFT calculations found that the P/As-X (X = Cl, Br or I) bond has reduced single bond character due to donation of electron density into the σ^* -antibonding orbital of the P/As-X bond and that the electronic structure of the pnictole greatly differs depending on the inclusion of S, N or O in the five membered ring. A summary of these results is given in Figure 2.21 and Tables 2.6 and 2.7 below.

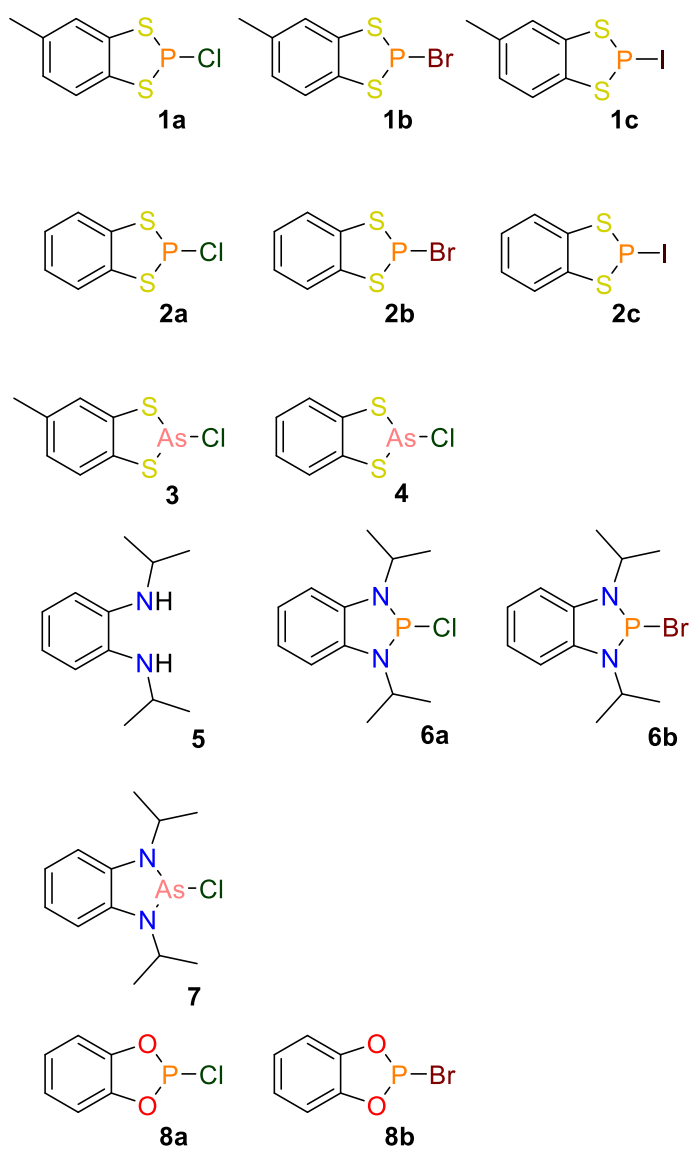


Figure 2.21: Summary of the complexes synthesised in Chapter 1.

Table 2.6: Summary of characteristics of phosphole derived compounds synthesised.

	1a	1b	1c	2a	2b
³¹ P NMR chemical shift/ppm	160.4	163.3	155.0	158.3	160.9
Fold angle/ °	26.07(6)	24.19(10)	19.45(14)	28.65(6)	26.45(9)– 26.57(9)
P–X bond length/ Å	2.1134(7)	2.3154(9)	2.5730(12)	2.1038(9)	2.2908(7)– 2.2981(9)
P–X bond order ^a	0.86	0.87	0.90	0.86	0.87
P natural charge ^b	+0.53	+0.46	+0.36	+0.53	+0.46
X natural charge ^b	–0.32	–0.27	–0.17	–0.32	–0.27
S/ N/ O natural charge ^b	+0.06	+0.07	+0.07	+0.06	+0.07
	2c	6a	6b	8a	8b
³¹ P NMR chemical shift/ppm	152.4	147.2	169.2	173.6	195.3
Fold angle/ °	23.93(11)– 28.38(14)	8.8(2)– 11.2(2)	N/A	N/A	N/A
P–X bond length/ Å	2.5188(11)– 2.5295(13)	2.3240(7)– 2.3377(7)	N/A	N/A	N/A
P–X bond order ^a	0.90	0.67	0.68	0.87	0.87
P natural charge ^b	+0.36	+1.29	+1.25	+1.40	+1.36
X natural charge ^b	–0.16	–0.49	–0.49	–0.36	–0.33
S/ N/ O natural charge ^b	+0.07	–0.82	–0.81	–0.79	–0.79

^aCalculated Wiberg bond order from NBO analysis. ^bCalculated from NBO analysis.

Table 2.7: Overview of characteristics of arsole derived compounds synthesised.

	3β	4	7
Fold angle/ °	19.44(8)–21.51(8)	14.28	6.4(2)
As–Cl bond length/ Å	2.2540(8)– 2.2582(7)	2.27436(4) – 2.31361(4)	2.440(13)
As–Cl bond order ^a	0.76	0.76	0.60
As natural charge ^b	+0.81	+0.81	+1.49
Cl natural charge ^b	–0.42	–0.42	–0.54
S/ N natural charge ^b	–0.03	–0.02	–0.87

^aCalculated Wiberg bond order from NBO analysis. ^bCalculated from NBO analysis.

Chapter 2.5 References

- 1 M. Baudler, A. Moog, K. Glinka and U. Kelsch, *Z. Naturforsch. B*, 1973, **28**, 363–369.
- 2 D. M. C. Ould, T. T. P. Tran, J. M. Rawson and R. L. Melen, *Dalton Trans.*, 2019, **48**, 16922–16935.
- 3 O. Kuhl, *Phosphorus-31 NMR spectroscopy: A concise introduction for the synthetic organic and organometallic chemistry*, Springer, Berlin, 2008.
- 4 L. Nyulaszi, G. Keglevich and L. D. Quin, *J. Org. Chem.*, 1996, **61**, 7808–7812.
- 5 F. H. Allen, D. G. Watson, L. Brammer, A. G. Orpen and R. Taylor, *Typical interatomic distances: organic compounds*, International Tables for Crystallography, 2006, ch. 9.5, vol.C, pp. 790–811.
- 6 Y. Zhao and D. G. Truhlar, *Theor. Chem. Account*, 2008, **120**, 215–241.
- 7 R. Ditchfield, W. J. Hehre and J. A. Pople, *J. Chem. Phys.*, 1971, **54**, 724–728.
- 8 F. Weigend and R. Ahlrichs, *Phys. Chem. Chem. Phys.* 2005, **7**, 3297–3305.
- 9 NBO Version 3.1, E. D. Glendening, A. E. Reed, J. E. Carpenter and F. Weinhold.
- 10 T. T. P. Tran, D. M. C. Ould, L. C. Wilkins, D. S. Wright, R. L. Melen and J. M. Rawson, *CrystEngComm*, 2017, **19**, 4696–4699.
- 11 G. Balimann and P. S. Pregosin, *J. Magn. Reson.*, 1977, **26**, 283–289.
- 12 M. J. Collins, U. R. K. Rao and G. J. Schrobilgen, *J. Magn. Reson.*, 1985, **61**, 137–140.
- 13 The Cambridge Structural Database. C. R. Groom, I. J. Bruno, M. P. Lightfoot and S. C. Ward, *Acta Cryst.*, **B72**, 2016, 171-179.
- 14 P. J. Hay and W. R. Wadt, *J. Chem. Phys.*, 1985, **82**, 270–283.
- 15 W. R. Wadt, and P. J. Hay, *J. Chem. Phys.*, 1985, **82**, 284–298.
- 16 P. J. Hay and W. R. Wadt, *J. Chem. Phys.*, 1985, **82**, 299–310.
- 17 L. Weber, J. Kahlert, L. Böhling, A. Brockhinke, H.-G. Stammler, B. Neumann, R. A. Harder, P. J. Low and M. A. Fox, *Dalton Trans.*, 2013, **42**, 2266–2281.
- 18 D. M. C. Ould, A. C. Rigby, L. C. Wilkins, S. J. Adams, J. A. Platts, S. J. A. Pope, E. Richards and R. L. Melen, *Organometallics*, 2018, **37**, 712–719.
- 19 X.-Z. Liu, Y.-H. Wang, F.-Z. Kong, Z.-L. Jin, *Chin. J. Chem.*, 2003, **21**, 494–499.
- 20 J. Gloede and H. Gross, *Journal f. prakt. Chemie.*, 1979, **6**, 1029–1033.
- 21 A. Alparone, H. Reis and M. G. Papadopoulous, *J. Phys. Chem. A*, 2006, **110**, 5909–5918.

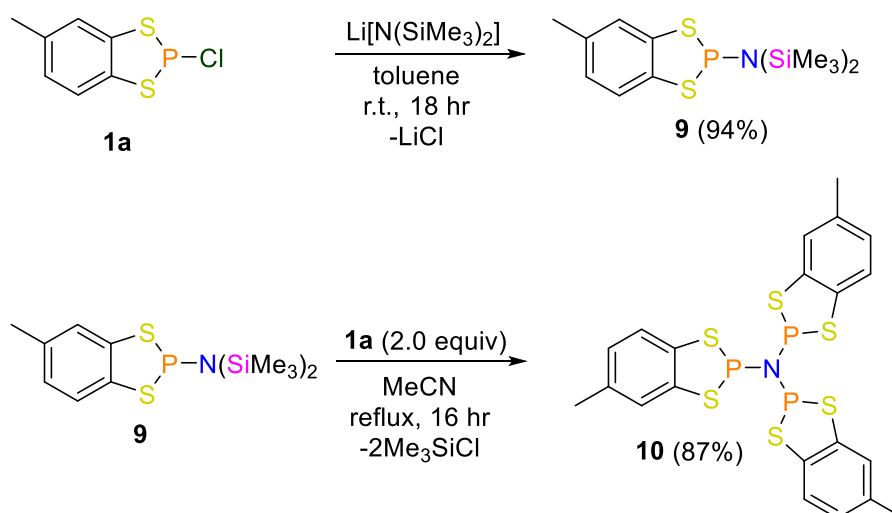
Chapter 3: Reactivity of Dithiaphospholes, Dithiarsoles, Diazaphospholes and Diazarsoles

Chapter 3.1 Paddlewheel Synthesis from Dithiaphosphole and Dithiarsole

With a series of phosphorus and arsenic compounds in hand (Chapter 2), these were then used as precursors for a range of reactions to explore further their reactivity and obtain additional fundamental insight. The first of these reactions made use of the dithiaphosphole **1a** and dithiarsole **3**, which underwent substitution reactions to generate a nitrogen centred paddlewheel, in which a central N atom was flanked by three dithiaphosphole or dithiarsole moieties.¹

3.1.1 Synthesis of tris(5-methylbenzo-1,3,2-dithiaphosphol-2-yl)amine: $(\text{MeC}_6\text{H}_3\text{S}_2\text{P})_3\text{N}$

To begin with, using 2-chloro-5-methylbenzo-1,3,2-dithiaphosphole (**1a**), substitution of the chloride co-ligand was achieved by reacting **1a** with stoichiometric lithium bis(trimethylsilyl)amide (LiHMDS, $\text{Li}[\text{N}(\text{SiMe}_3)_2]$) in toluene. After removal of volatiles and subsequent pentane washings this gave the intermediate 5-methyl-*N,N*-bis(trimethylsilyl)benzo-1,3,2-dithiaphosphol-2-amine (**9**). The solvent was exchanged for acetonitrile and **9** was reacted with two further equivalents of **1a**. The reaction was heated to reflux for 16 hours and then cooled in an ice bath. After filtration *via* a filter cannula, a white solid was removed, which was washed with pentane. Drying *in vacuo* gave the desired paddlewheel product tris(5-methylbenzo-1,3,2-dithiaphosphol-2-yl)amine, $(\text{MeC}_6\text{H}_3\text{S}_2\text{P})_3\text{N}$ (**10**), as a white solid (Scheme 3.1).



Scheme 3.1: Synthesis of *N*-based paddlewheel structure **10** from **1a**.

$^{31}\text{P}\{^1\text{H}\}$ NMR spectroscopy was initially used for characterising the intermediate **9**, which showed a significant upfield shift of the P environment compared to the starting dithiaphosphole **1a**, with a singlet resonance detected at $\delta = 93.9$ ppm. Further to this, ^1H NMR spectroscopy revealed the trimethylsilyl (TMS) groups as a doublet centred at $\delta = 0.27$ ppm, with a $^4J_{\text{PH}}$ coupling constant of 1.9 Hz. The expected three aromatic signals and methyl group from the toluene backbone were also present (Figure 3.1).

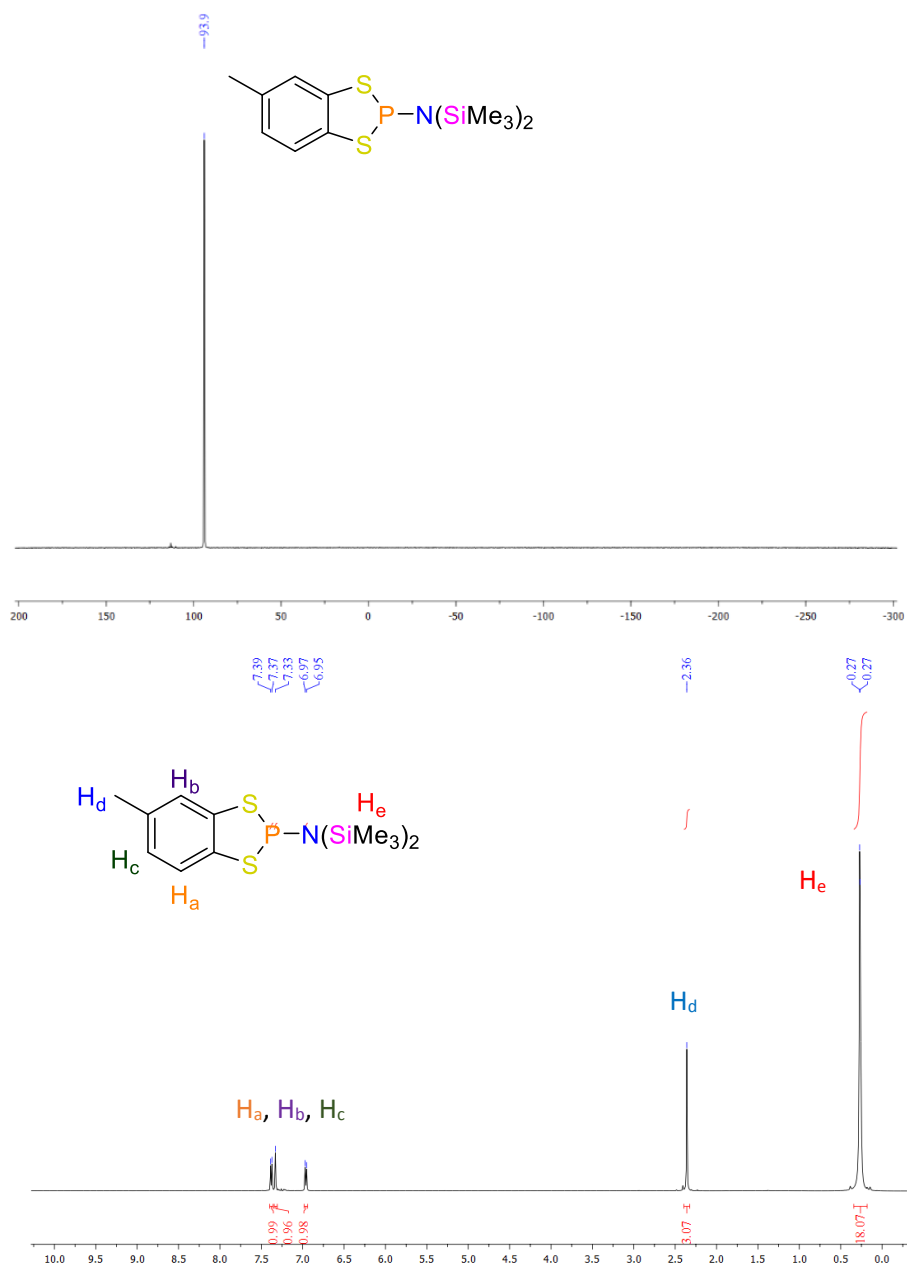


Figure 3.1: $^{31}\text{P}\{^1\text{H}\}$ NMR (202 MHz, CDCl_3 , 295 K) spectrum (top) and ^1H NMR (500 MHz, CDCl_3 , 295 K) spectrum (bottom) of intermediate **9**.

Similar to **9**, $^{31}\text{P}\{^1\text{H}\}$ NMR spectroscopy was first used to characterise the paddlewheel structure **10**. In this case the $^{31}\text{P}\{^1\text{H}\}$ NMR spectrum showed a slight upfield shift from **9** with a resonance at $\delta = 86.6$ ppm. This is significantly upfield from the precursor **1a**; $\delta = 160.4$ ppm. The ^1H NMR spectrum again showed the expected three aromatic and one methyl signals.

3.1.2 Solid-state structure of $(\text{MeC}_6\text{H}_3\text{S}_2\text{P})_3\text{N}$

The solid-state structure of the paddlewheel $(\text{MeC}_6\text{H}_3\text{S}_2\text{P})_3\text{N}$ was obtained by crystals grown by Dr Thao Tran (University of Windsor) from a saturated CH_2Cl_2 solution cooled to -20 °C. Upon structure solution and refinement by Professor Jeremy Rawson (University of Windsor) **10** (Figure 3.2) was found to crystallise in the rhombohedral space group $P\bar{3}$, with $1/3$ molecule in the asymmetric unit (the N atom sits on the three-fold axis) and eight in the unit cell. The solid-state structure of **10** revealed the expected three-coordinate N centre, with a $\text{P}(1)\text{--N}(1)\text{--P}(1')$ bond angle of $119.19(8)^\circ$. The approximate 120° bond angle reveals an sp^2 centred N, meaning that the lone pair present on the N atom is of p -orbital character. A fold angle about the $\text{S}\cdots\text{S}$ vector is still present in the dithiaphosphole ring, but is significantly lower than what is observed in the precursor **1a**, with the fold angle in **10** measuring $20.7(2)^\circ$ compared to $26.07(6)^\circ$ in **1a**. Furthermore, the $\text{P}(1)\text{--N}(1)$ bond distance is found to be $1.7314(18)$ Å (Table 3.1), which lies within the expected bond distance ($1.70\text{--}1.77$ Å).² Lastly, when looking at the packing arrangement in the unit cell of **10**, the eight paddlewheel structures form four supramolecular dimers *via* six $\text{S}\cdots\text{S}$ contacts. Interestingly, these $\text{S}\cdots\text{S}$ contacts generate an S_6 chair-type geometry and measure 3.511 Å, which is less than the sum of the van der Waals radii (3.60 Å) (Figure 3.3).

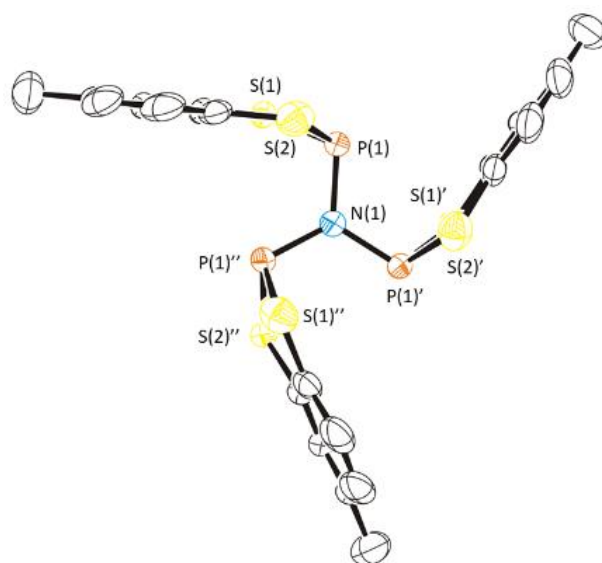


Figure 3.2: Solid-state structure of **10**. Thermal ellipsoids drawn at 50% probability and H-atoms removed for clarity.

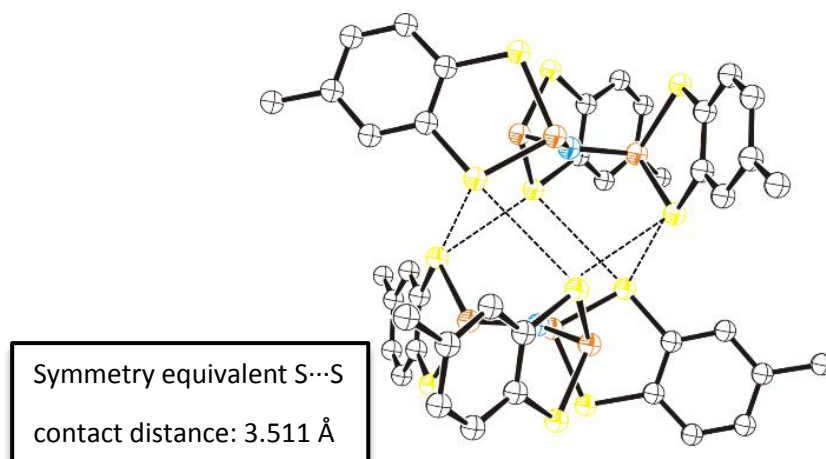


Figure 3.3: Packing of **10** showing the supramolecular dimer formed through S...S contacts. Dashed lines show the close contacts between sulfur atoms. Orange: phosphorus, yellow: sulfur, blue: nitrogen. Thermal ellipsoids drawn at 50% probability and H-atoms removed for clarity.

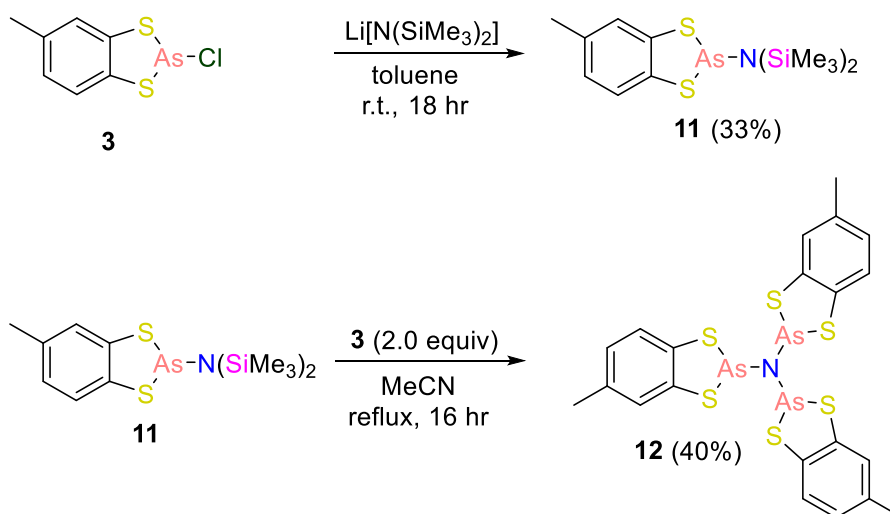
Table 3.1: Selected bond lengths and interior bond angles for paddlewheel **10**.

Selected bond	10 / Å
N(1)–P(1)	1.7314(18)
P(1)–S(1)	2.125(2)
P(1)–S(2)	2.105(2)
S(1)–C(1)	1.748(7)
S(2)–C(2)	1.782(5)
Selected angle	10 / °
S(1)–P(1)–N(1)	94.41(9)
S(1)–P(1)–S(1)	104.6(2)

3.1.3 Synthesis of tris(5-methylbenzo-1,3,2-dithiarsole-2-yl)amine: (MeC₆H₃S₂As)₃N

In an analogous fashion to the procedure used for the synthesis of **10**, synthesis of a dithiarsole derived paddlewheel tris(5-methylbenzo-1,3,2-dithiarsole-2-yl)amine firstly involved reacting **3** with stoichiometric LiHMDS in toluene. This was left to stir at ambient temperature overnight and formed the intermediate 5-methyl-*N,N*-bis(trimethylsilyl)benzo-

1,3,2-dithiarsole-2-amine (**11**). Reacting **11** with two further equivalents of **3** in acetonitrile and again heating to reflux for 16 hours gave the product tris(5-methylbenzo-1,3,2-dithiarsole-2-yl)amine ($(\text{MeC}_6\text{H}_3\text{S}_2\text{As})_3\text{N}$ (**12**) as a white solid (Scheme 3.2).



Scheme 3.2: Synthesis of *N*-based paddlewheel structure **12** from **3**.

Unlike in the synthesis of the dithiaphosphole-derived paddlewheel, multinuclear NMR spectroscopy was less useful in characterising the dithiarsole-derived paddlewheel structure. This again was due to the practical difficulty in performing ^{75}As NMR spectroscopy, as discussed in the previous chapter. For the intermediate 5-methyl-*N,N*-bis(trimethylsilyl)benzo-1,3,2-dithiarsole-2-amine **11**, ^1H NMR spectroscopy did again show the TMS groups as a singlet centred at $\delta = 0.16$ ppm. The three aromatic and methyl signals from the toluene group were additionally seen. For **12**, the ^1H NMR spectrum showed the expected three aromatic and one methyl signal, but furthermore revealed the loss of the TMS groups. Mass spectrometry was more useful in confirming the formation of both **11** and **12**. The electron ionisation (EI) method was used for intermediate **11** and gave a $[\text{M}]^+$ $[\text{C}_{13}\text{H}_{24}\text{NAsS}_2\text{Si}_2]^+$ of 389.0101 (theoretical mass = 389.00992), whereas electrospray ionisation (ES) was used for **12** and detected $[\text{M}+\text{H}]^+$ $[\text{C}_{21}\text{H}_{19}\text{S}_6\text{As}_3\text{N}]^+$ at 701.7516 (theoretical mass = 701.7490).

3.1.4 Solid-state structure of $(\text{MeC}_6\text{H}_3\text{S}_2\text{As})_3\text{N}$

Crystals suitable for single crystal X-ray diffraction were grown by Dr Thao Tran from a saturated CH_2Cl_2 solution cooled to -20 °C. Upon structure solution and refinement by Professor Jeremy Rawson, **12** was found to crystallise in the triclinic space group *P*-1, with one molecule in the asymmetric unit and two in the unit cell (Figure 3.4). The geometry of the dithiarsole derived paddlewheel is similar to that of **10**, in that **12** has a three-coordinate central N atom with As–N–As bond angles ranging from $115.8(4)^\circ$ to $117.9(4)^\circ$. This again

means that the N atom is approximately sp^2 hybridised, with the lone pair being of p -orbital character. The characteristic fold angle is still observed in the dithiarsole ring, measuring $13.8(13)^\circ$ – $17.0(2)^\circ$, which is a reduction when compared to the fold angle present in **3 α** and **3 β** . The As–N bond distance is measured to be $1.843(7)$ – $1.862(7)$ Å, which are within typical values. The As(1)–S(1) and As(1)–S(2) bond distances were found to be $2.215(3)$ Å and $2.252(3)$ Å, respectively (Table 3.2), which are comparable to that found in precursor **3**. When looking at the packing of **12** in the unit cell, the two molecules present form a dimer similar to that seen in **10** *via* short S··S contacts. These contacts form a chair type configuration with the S··S intermolecular interactions measuring $3.428(4)$ – $3.568(4)$ Å, which are well within the sum of the van der Waals radii of 3.60 Å.

Table 3.2: Selected bond lengths and interior bond angles for paddlewheel **12**.

Selected bond	12 / Å
N(1)–As(1)	1.843(7)
N(1)–As(2)	1.862(7)
N(1)–As(3)	1.843(9)
As(1)–S(1)	2.215(3)
As(1)–S(2)	2.252(3)
S(1)–C(1)	1.741(10)
S(2)–C(2)	1.747(12)
Selected angle	12 / °
As(1)–N(1)–As(2)	117.9(4)
S(1)–As(1)–N(1)	101.2(3)
S(1)–As(1)–S(1)	91.14(11)

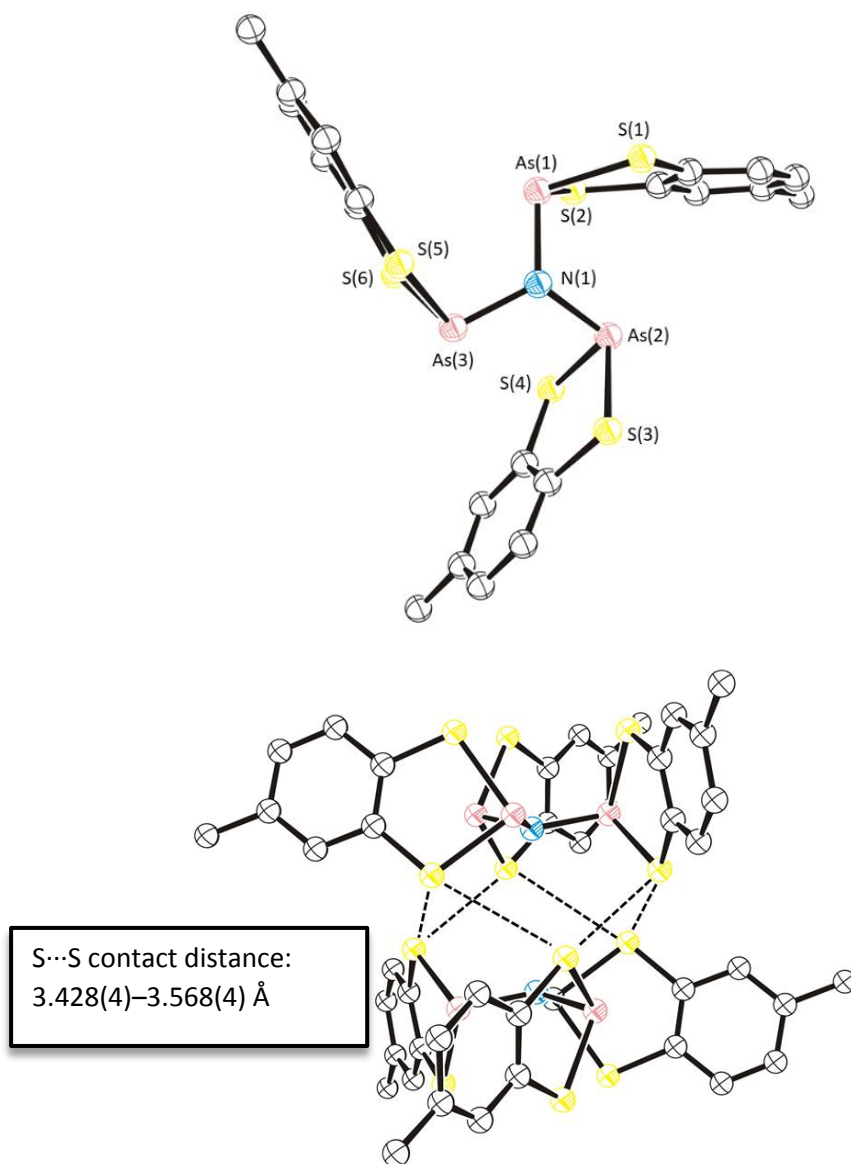


Figure 3.4: Top: Solid-state structure of **12**. Bottom: Packing of **12** showing the supramolecular dimer formed through S...S contacts. Dashed lines show the close contacts between sulfur atoms. Pink: arsenic, yellow: sulfur, blue: nitrogen. Thermal ellipsoids drawn at 50% probability and H-atoms removed for clarity.

Chapter 3.2 Cation Formation

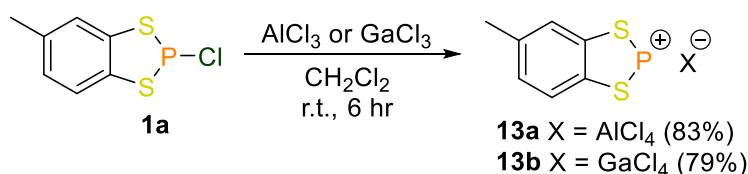
Proceeding from the substitution of the chloride co-ligand reaction to generate paddlewheel type structures, focus then turned to the formation of cationic phosphonium and arsenium complexes.^{1,3,4} These cations were made from the abstraction of the chloride co-ligand using a range of simple Lewis acids. As described in the introduction, the phosphonium cation is a two-coordinate phosphorus species with a formal positive charge on the phosphorus heteroatom, which is isovalent to Arduengo's well-known N-heterocyclic carbenes, but with inverse electronic properties. That is, they are weaker σ -donors, but better π -acceptors.⁵ Likewise, the analogous arsenium cation is a divalent arsenic species with a formal positive charge,⁶ however due to the reduced σ -donation ability compared to phosphonium cations, a Lewis acid description of bonding is more appropriate when describing their coordination to transition metals.^{7,8}

3.2.1 Synthesis of dithiaphospheniums and dithiarseniums

3.2.1.1 Synthesis and NMR analysis of dithiaphosphenium cations from dithiaphosphole

Using the dithiaphosphole **1a**, the corresponding cationic phosphonium species were generated by employing stoichiometric aluminium trichloride or gallium trichloride in CH_2Cl_2 and leaving them to stir at ambient temperature; the solutions immediately turned orange. These orange solutions were left to stir at ambient temperature for six hours, after which the solvent was removed *in vacuo* and the orange solids washed with pentane. After further drying *in vacuo* the dithiaphosphenium products 5-methylbenzo-1,3,2-dithiaphosphenium tetrachloroaluminate (**13a**) and 5-methylbenzo-1,3,2-dithiaphosphenium tetrachlorogallate (**13b**) were obtained as orange solids in excellent yields of 83% and 79%, respectively (Scheme 3.3). These compounds are called dithiaphospheniums from herein.

Notably, the use of trimethylsilyl trifluoromethanesulfonate (TMS triflate) failed to give the cationic dithiaphosphenium complex with a triflate counterion using the same conditions described above. Exchanging the solvent for toluene and heating, as well as increasing the reaction time, still failed to give the dithiaphosphenium complex. Throughout these reactions ^{31}P NMR spectroscopy only showed the starting precursor **1a**. Moreover, when using silver triflate as the triflate source, which would generate silver chloride as the by-product, the reaction still failed to give the desired dithiaphosphenium compound. The intolerance of the triflate counterion is in direct contrast to the diazaphosphole and TMS triflate reaction (*vide infra*).



Scheme 3.3: Synthesis of dithiophosphenium compounds from dithiophosphole **1a**.

Initial characterisation of the dithiophosphenium compounds was attempted by ^{31}P NMR spectroscopy. The dithiophosphenium compounds proved to be partially soluble in CDCl_3 but more soluble in CD_2Cl_2 and bromobenzene- d_5 ($\text{C}_6\text{D}_5\text{Br}$). When looking at the ^{31}P NMR spectrum of the dithiophosphenium compounds they were initially puzzling, as it was expected that the NMR signal should be shifted significantly downfield from the precursor **1a** due to the build-up of positive charge on the phosphorus heteroatom. Contrary to this the ^{31}P NMR spectrum of both **13a** and **13b** showed a signal significantly upfield of **1a**, with a resonance detected at $\delta = 57.4$ ppm for **13a** and $\delta = 58.0$ ppm for **13b**. Additionally, these signals were a well-defined doublet with a coupling constant of 700 Hz and 690 Hz respectively as opposed to being the predicted singlet (or very weak $^3J_{\text{PH}}/^4J_{\text{PH}}$ present).

Some clarity on this confusing result was achieved by recording the $^{31}\text{P}\{^1\text{H}\}$ NMR spectrum, which showed that the doublet collapses into a singlet resonance (Figure 3.5). Given the magnitude of the coupling constant and the fact that J_{PH} coupling was present, it was clear that **13a** and **13b** had oxidised to a +5 phosphorus species. This is because of the large coupling constant which is very typical of a P(V) $^1J_{\text{PH}}$.⁹ The results of the ^{31}P and $^{31}\text{P}\{^1\text{H}\}$ NMR spectra strongly indicated that hydrolysis of the dithiophosphenium cations had taken place, despite the use of dried solvent. This illustrated just how air/moisture sensitive the dithiophosphenium compounds are. In addition, the ^1H NMR spectrum showed the $^1J_{\text{PH}}$ coupling, as a doublet resonance centred at $\delta = 9.37$ ppm was seen with the same magnitude $^1J_{\text{PH}}$ coupling constant. As the dithiophosphenium cations clearly proved too sensitive to attain multinuclear NMR characterisation, solid-state characterisation was heavily relied upon. Mass spectrometry, using EI method, confirmed the presence of the cation, with the mass for $[\text{M}]^+$ $[\text{C}_7\text{H}_6\text{PS}_2]^+$ found at 184.9650 (theoretical = 184.9649). In addition, single crystal X-ray diffraction confirmed the structure of **13b**.

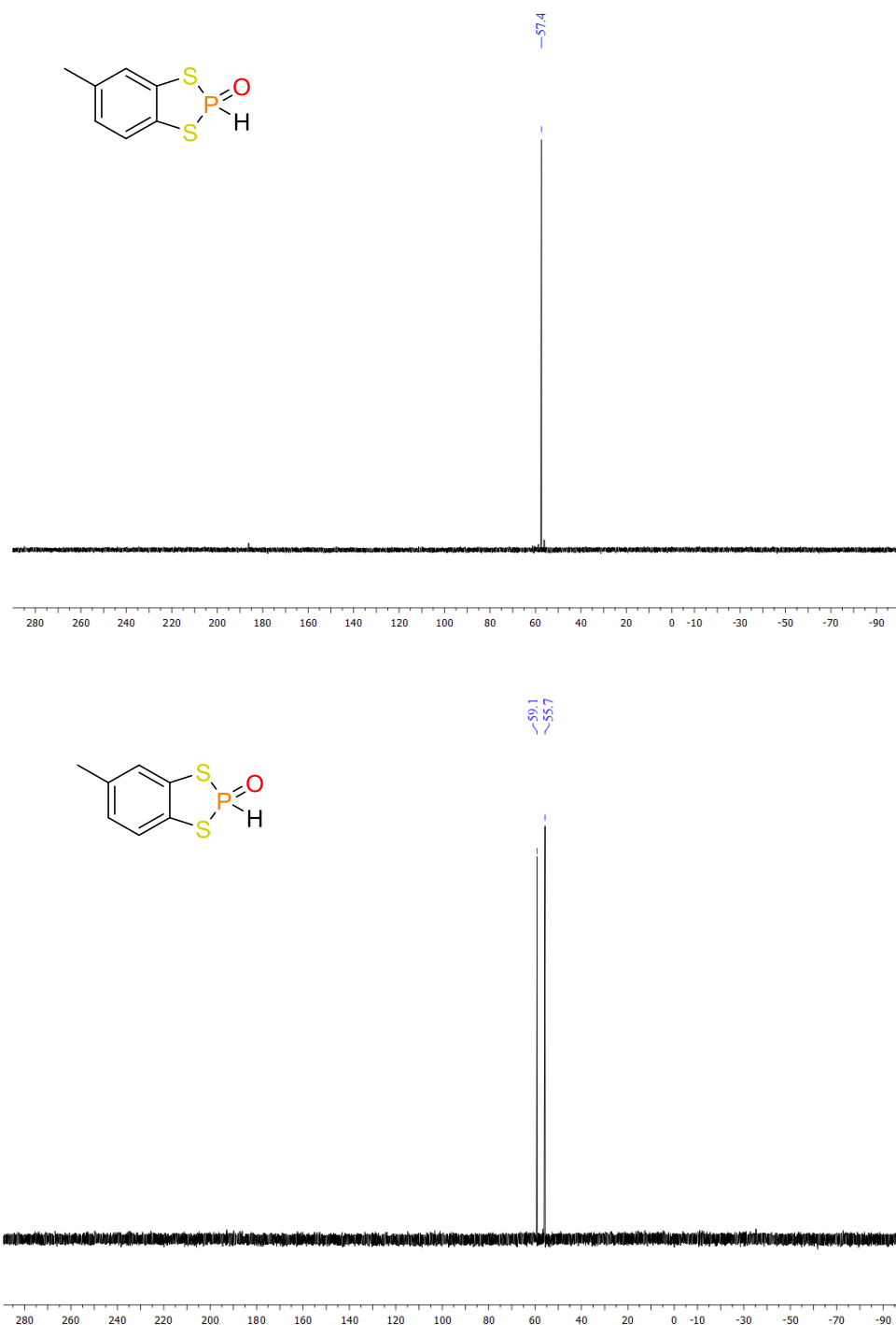


Figure 3.5: ^{31}P NMR (top) and $^{31}\text{P}\{^1\text{H}\}$ NMR (bottom) (162 MHz, CD_2Cl_2 , 295 K) spectra of dithiaphosphenium **13a**.

3.2.1.2 Solid-state structures of dithiaphospheniums

The dithiaphosphenium cations proved difficult to characterise by multinuclear NMR characterisation on due to insolubility and instability issues, so with only mass spectrometry results to go by, X-ray crystallography was employed. The solid-state structure of **13a** has previously been reported by Cameron and Linden.¹⁰ On the other hand, the solid-state structure of **13b** has not previously been described. Therefore, single crystals of **13b** suitable

for X-ray diffraction were grown from a saturated solution of CH_2Cl_2 with a few drops of pentane added and cooled to $-40\text{ }^\circ\text{C}$. Despite multiple recrystallisation attempts and use of different crystallisation methods, crystals of **13b** were consistently plagued with twinning. In this context twinning is where two (or more) crystals of the same material are intergrown, meaning the unit cell of the first crystal is related to the second by a symmetry element. To combat this twinning problem during the refinement process, the twin law $-1\ 0\ 0\ 0\ -1\ 0\ 0\ 0\ 1$ as given in TwinRotMat (within Platon¹¹) was used in the refinement of **13b** alongside the BASF command, which helped remedy the twinning and in turn bring the R_1 and wR_2 values to satisfactory levels ($R_1 = 7\%$ and $wR_2 = 21\%$).

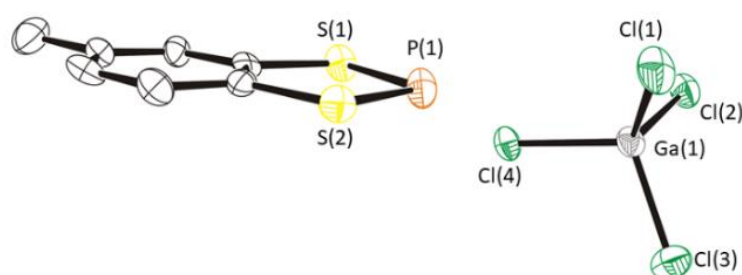


Figure 3.6: Solid-state structure of the dithiaphosphenium **13b**. Thermal ellipsoids drawn at 50% probability and H-atoms removed for clarity.

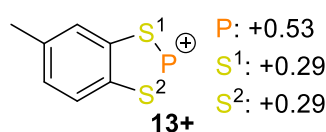
With the refinement completed to an adequate level, **13b** was found to crystallise in the monoclinic space group $P2_1/c$, with one molecule in the asymmetric unit and four in the unit cell (Figure 3.6). Closer inspection of the solid-state structure of **13b** reveals that there are a number of key differences to the geometry when compared to the precursor **1a**. Notably, although there is still the five membered PS_2C_2 dithiaphosphole ring, the distinctive fold angle about the $\text{S}\cdots\text{S}$ vector that is seen in **1a** is effectively no longer present, with a fold angle of just $1.3(3)^\circ$ measured for **13b**. This in turn means that the dithiaphospheniums tend to being molecularly planar, which along with their $10\text{-}\pi$ electrons fulfils the requirements for Hückel aromaticity. The delocalisation of electrons within the $10\text{-}\pi$ aromatic system along with $3p\text{-}3p$ π -conjugation explains the shorter P–S bond metrics, with P–S bond lengths now measuring $2.004(3)\text{--}2.022(4)$ Å. That compares to P–S bond lengths of $2.0936(7)$ Å and $2.0954(7)$ Å in the precursor **1a**. The $\text{S}(1)\text{--P}(1)\text{--S}(2)$ bond angle also expands in relation to **1a**, increasing from $95.43(3)^\circ$ to $98.37(15)^\circ$ (Table 3.3). When looking at the packing structure of the unit cell of **13b**, the closest cation \cdots anion association is a $\text{P}\cdots\text{Cl}$ contact at $3.3175(5)$ Å, which is well within the combined van der Waals radii of 3.55 Å.

Table 3.3: Selected bond lengths and interior bond angles for dithiaphosphenium **13b**.

Selected bond	13b / Å (X = GaCl ₄)
P(1)–S(1)	2.022(4)
P(1)–S(2)	2.004(3)
S(1)–C(1)	1.760(9)
S(2)–C(2)	1.717(8)
Selected angle	13b / °
S(1)–P(1)–S(2)	98.37(15)

3.2.1.3 Computational analysis of dithiaphosphenium cation

To obtain a deeper understanding on the structure and bonding present in the dithiaphosphenium cation, DFT studies were employed. Geometry optimisation and vibrational frequency calculations were performed on the cationic part of the dithiaphosphenium cation (**13+**); the counterion was neglected in the calculations as focus was on the changes that occur to the C₂S₂P five membered ring. As was the case with the dithiaphospholes, the functional M06-2X and basis set 6-311+G(2d,p) were employed, which would allow for a direct comparison to **1a**. NBO calculations performed on **13+** showed the expected large build-up of positive charge on the phosphorus heteroatom, with a natural charge of +0.53. Interestingly, this positive charge is the same as was seen in **1a**, which again highlights how polarised the P–Cl bond in **1a** is.



P–S bond order^a: 1.36

C–S bond order^a: 1.14

Figure 3.7: NBO analysis of dithiaphosphenium cation **13+**. All atoms treated with M06-2X functional and 6-311G+(2d,p) basis set. ^aAverage values taken.

On the other hand, the sulfur heteroatoms show an increase in positive charge with respect to that seen in **1a**, with natural charges of +0.06 in **1a** and +0.29 in **13+** (Figure 3.7). As was seen in the solid-state structure of **13b**, the P–S bonds were shorter than those measured in **1a**, which was rationalised by the 10- π aromatic nature and 3*p*-3*p* π -conjugation present.

This observation is supported by NBO analysis when looking at the Wiberg bond order of the P–S bonds, which increases from an average of 1.04 in **1a** to 1.36 in **13+**.

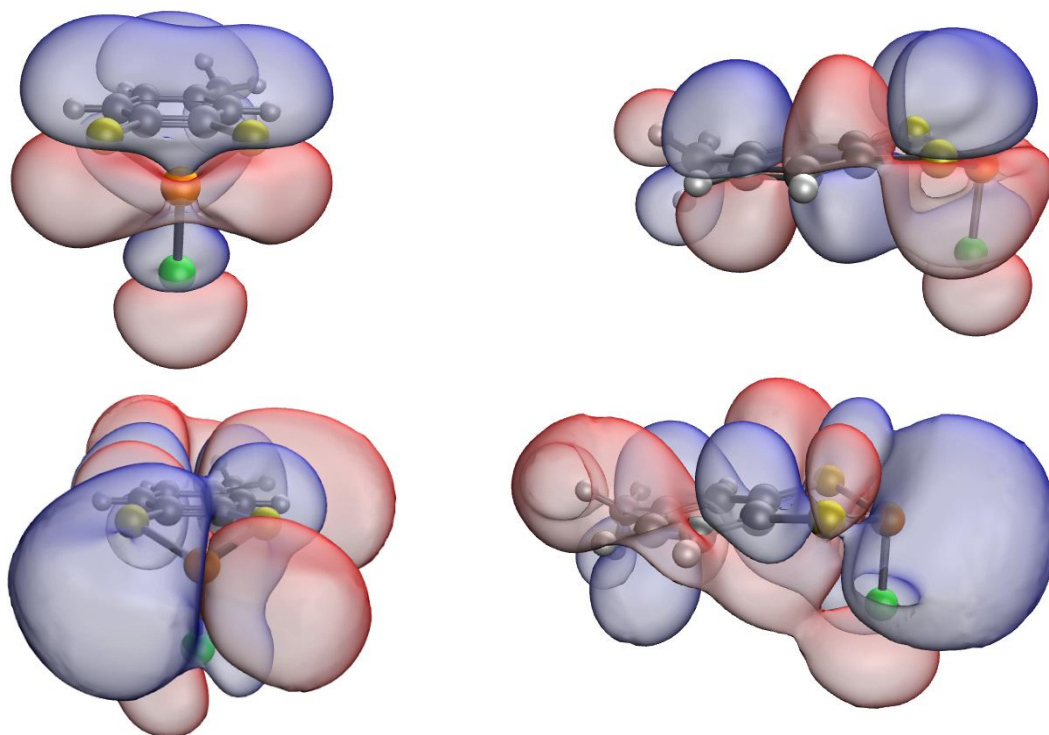


Figure 3.8: Images of the HOMO (top) and LUMO (bottom) of 2-chloro-5-methylbenzo-1,3,2-dithiaphosphole (**1a**). Blue = positive area of electron density, red = negative area of electron density. Calculated at M06-2X and 6-311+G(2d,p) level.

Molecular orbitals are an important concept in chemistry as they help describe not only the nature of the bonding in a given complex but can also help explain the reactivity it possesses. This is because traditionally structures with a large energy gap between the highest molecular orbital (HOMO) and lowest molecular orbital (LUMO) are more stable and unreactive, whereas structures with a low HOMO–LUMO energy gap are more reactive.¹² Given the cationic nature of **13+** and the delocalisation of electron density, the HOMO–LUMO was visualised to see exactly how this electron density was distributed. For comparison, molecular orbital calculations were also performed on the precursor **1a**. The HOMO in **1a** is delocalised over the entire structure, including the P–Cl bond, and is of π -symmetry. The LUMO is also delocalised over the entire complex, *vide supra* (Figure 3.8). Turning attention to the dithiaphosphenium **13+**, the HOMO looks similar to **1a**, in that it is delocalised over the entire structure and is of π -symmetry, but has the obvious exception of the exclusion of the P–Cl bond. The LUMO on the other hand shows some localisation in the *p*-orbitals of phosphorus and sulfur in the PS₂C₂ ring with some delocalisation over the

fused toluene ring (Figure 3.9). Although DFT methodology when using common functionals is known to have difficulty in accurately calculating orbital energies,^{12,13} it can nevertheless be useful for comparing the relative HOMO–LUMO energy differences between different molecules. On that theme, the HOMO–LUMO energy barrier decreases by 1.8 eV (band gap is 7.1 eV in **1a** and 5.3 eV in **13+**) upon abstraction of the chloride and formation of the dithiaphosphenium **13+**, with both the HOMO and LUMO lower in energy for the latter.

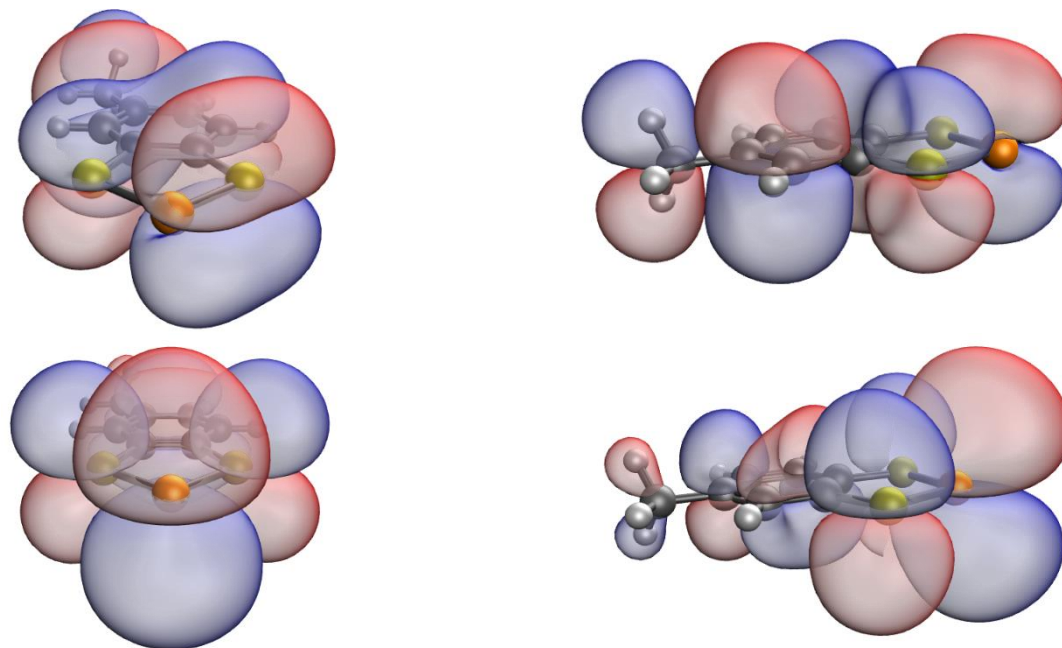
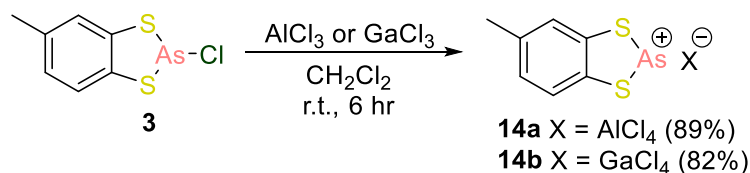


Figure 3.9: Images of the HOMO (top) and LUMO (bottom) of 5-methylbenzo-1,3,2-dithiaphosphenium (**13+**). Blue = positive area of electron density, red = negative area of electron density. Calculated at M06-2X and 6-311+G(2d,p) level.

3.2.1.4 Synthesis and NMR analysis of dithiarsenium cations from dithiarsole

Formation of the dithiarsenium cations have previously been reported by Burford and Royan.¹⁴ The synthesis of these cations proceeded in an analogous way to the dithiaphosphenium cations. Starting from the dithiarsole precursor, **3**, stoichiometric aluminium trichloride or gallium trichloride was added in CH_2Cl_2 solvent. A dark red solution immediately formed and was left to stir at room temperature for six hours. After this period the solvent was removed *in vacuo* and the resulting solid was washed with pentane. Upon drying the products 5-methylbenzo-1,3,2-dithiarsenium tetrachloroaluminate (**14a**) and 5-methylbenzo-1,3,2-dithiarsenium tetrachlorogallate (**14b**) were isolated as red solids in excellent yields of 89% and 82% accordingly (Scheme 3.4). Once more the triflate counterion was attempted through the reaction of **3** with TMSOTf and AgOTf, but again no reaction was found to occur.



Scheme 3.4: Synthesis of dithiarsenium compounds from dithiarsole **3**.

Interestingly, unlike in the dithiaphosphenium case, the solubility of the dithiarseniums was higher, as C_6D_6 proved to be a good NMR solvent. In the case of **14a** the presence of AlCl_4^- as the counterion meant that ^{27}Al NMR spectroscopy could be performed, which showed a sharp singlet resonance at $\delta = 104.6$ ppm, which is known to correspond to AlCl_4^- .¹⁵ Analysis of the ^1H NMR spectrum of both **14a** and **14b** did not show $^1J_{\text{AsH}}$ coupling, which strongly suggests hydrolysis of the dithiarseniums does not occur in solution, as was seen with the dithiaphospheniums. Indeed the ^1H NMR spectra of **14a** and **14b** show the expected three aromatic signals along with the one methyl resonance. To further support the formation of the arsenium cations, mass spectrometry using EI method found $[\text{M}]^+ [\text{C}_7\text{H}_6\text{S}_2\text{As}]^+$ of 228.9131 for **14a** and 228.9132 for **14b** (calculated = 228.9121).

3.2.1.5 Solid-state structures of dithiarseniums

As mentioned above, the dithiarsenium cations have previously been reported, but notably analysis of the structural properties is absent. The closely related $[(\text{CH}_2)_2\text{S}_2\text{As}]^+$ cation has been reported with both AlCl_4^- and GaCl_4^- counterions; here the salts form centrosymmetric dimers of the type $[(\text{CH}_2)_2\text{S}_2\text{As}]_2[\text{MCl}_4]_2$ ($\text{M} = \text{Al}$ or Ga).¹⁶ As the solid-state structures of **14a** and **14b** had not been reported, single crystals suitable for X-ray diffraction of both **14a** and **14b** were grown by Dr Rebecca Melen from slow evaporation of CH_2Cl_2 (Figures 3.10 and 3.11). Structure refinement by Dr John Davies showed that both **14a** and **14b** crystallise in the monoclinic space group $P2_1/m$, with two molecules in the asymmetric unit; increasing to four molecules in the unit cell. **14a** and **14b** do not form dimers as seen in $[(\text{CH}_2)_2\text{S}_2\text{As}]^+$ but instead remain as two crystallographically independent structures. The characteristic fold angle seen in the dithiarsole **3** is no longer present, and in fact both **14a** and **14b** are rigorously planar with no fold angle about the $\text{S}\cdots\text{S}$ vector. This is in contrast to the dithiaphospheniums where a very small fold angle was measured (*vide supra*).

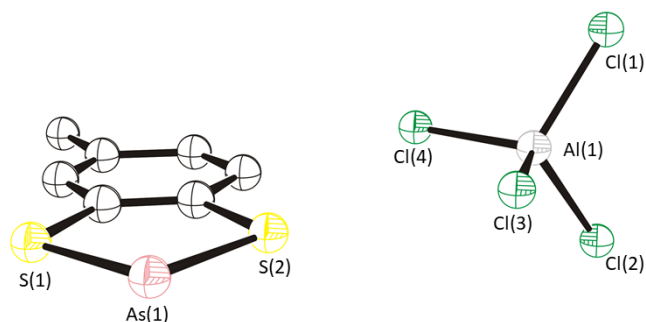


Figure 3.10: Solid-state structure of the dithiarsenium **14a**. Thermal ellipsoids drawn at 50% probability and H-atoms removed for clarity.

When measuring the As–S bond lengths in **14a**, they are found to have metrics 2.148(5)–2.161(6) Å, whereas in **14b** they measure 2.1417(9)–2.1514(11) Å. In both cases the As–S bond lengths are shorter than in the dithiarsole precursor, which like the dithiaphospheniums is attributed to the π -bonding in the formally 10- π aromatic system. The S(1)–As(1)–S(2) bond angle in **14a** shows expansion compared to **3 β** and **4**, measuring 94.8(2)° and 94.5(2)° for the two crystallographically independent molecules. In **14b** the S(1)–As(1)–S(2) internal bond angle is 94.38(3)° and 94.81(4)° (Table 3.4). When looking at the close packing structures of **14a** and **14b** As \cdots Cl cation \cdots anion contacts were found, measuring 3.2946(10)–3.5376(10) Å, which are well within the combined sum of the van der Waals radii of 3.60 Å.

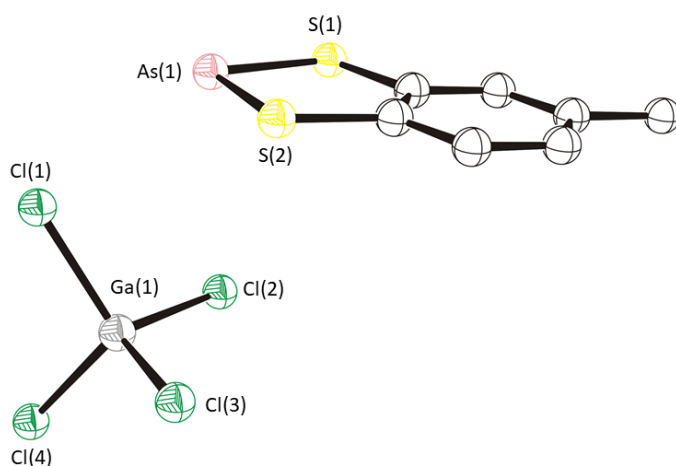


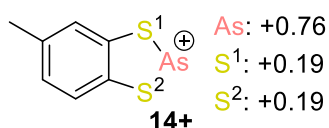
Figure 3.11: Solid-state structure of the dithiarsenium **14b**. Only one molecule shown. Thermal ellipsoids drawn at 50% probability and H-atoms removed for clarity.

Table 3.4: Selected bond lengths and interior bond angles for diazarseniums **14a** and **14b**.

Selected bond	14a / Å (X = AlCl ₄)	14b / Å (X = GaCl ₄)
As(1)–S(1)	2.148(5)–2.161(6)	2.1417(9)–2.1461(10)
As(1)–S(2)	2.155(6)–2.160(7)	2.1459(11)–2.1514(11)
S(1)–C(1)	1.72(2)–1.75(2)	1.729(3)–1.734(3)
S(2)–C(2)	1.76(2)–1.786(19)	1.730(2)–1.734(3)
Selected angle	14a / °	14b / °
S(1)–As(1)–S(2)	94.5(2)–94.8(2)	94.38(3)–94.81(4)

3.2.1.6 Computational analysis of dithiarsenium cation

As with the dithiaphospheniums, NBO analysis on the dithiarsenium cation part (**14+**) was undertaken. Geometry optimisation and vibrational frequency calculations were performed on the cationic part of the dithiarsenium using the functional M06-2X and basis set 6-311+G(2d,p) on all atoms, with the exception of the arsenic heteroatom. Again for arsenic heteroatom the ECP LANL2DZ basis set was used. As expected, a large build-up of positive charge was seen on the arsenic heteroatom, with a natural charge of +0.76. The two sulfur atoms have an average natural charge of +0.19, which like the dithiaphosphenium case is a small increase compared to the dithiarsole precursor, which had an average natural charge of –0.03. The As–S bond shows a deviation from single bond character and has an average Wiberg bond order of 1.27 (Figure 3.12), which is in line with the shortened As–S bond lengths when compared to **3**. The As–S Wiberg bond order in **3** was 0.98.



As–S bond order^a: 1.27

C–S bond order^a: 1.15

Figure 3.12: NBO analysis of dithiarsenium cation **14+**. All atoms treated with M06-2X functional and 6-311G+(2d,p) basis set, with the exception of As, which used LANL2DZ.

^aAverage values taken.

Molecular orbitals of the dithiarsenium cation **14+** as well as the dithiarsole **3** were then visualised (Figure 3.13). Dealing with the former first, the HOMO and LUMO in **14+** have the same visual appearance to the dithiaphosphenium **13+** where the HOMO shows delocalisation over the entire structure. The LUMO is of *p*-orbital character in the C₂S₂As ring and shows some delocalisation in the attached toluene ring; the HOMO–LUMO energy gap is 4.9 eV. Comparing this to the precursor **3**, the visual appearance of the HOMO and LUMO is as described for the dithiaphosphole **1a**, with a greater HOMO–LUMO energy gap of 6.6 eV. In addition, the HOMO and LUMO in the dithiarsenium are both lower in energy than the dithiarsole (**3**: HOMO –7.6 eV, LUMO –1.0 eV; **14+**: HOMO –12.3 eV, LUMO –7.4 eV). This decrease in frontier orbital energy upon cation formation was seen in the dithiaphosphole/phosphenium case above. Figure 3.14 below shows the frontier orbital energy levels for the dithia pnictole compounds **1a**, **13+**, **3** and **14+**.

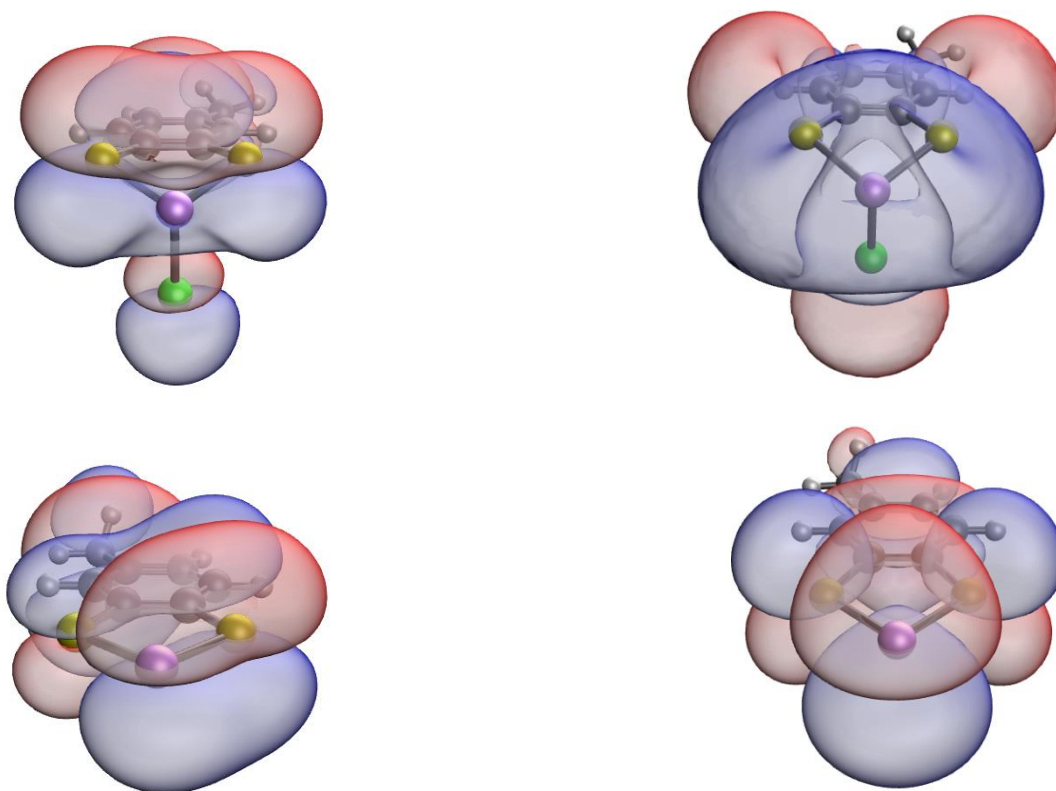


Figure 3.13: Top: HOMO (left) and LUMO (right) of 2-chloro-5-methylbenzo-1,3,2-dithiarsole (**3**). Bottom: HOMO (left) and LUMO (right) of 5-methylbenzo-1,3,2-dithiarsenium (**14+**). Blue = positive area of electron density, red = negative area of electron density. Calculated at M06-2X and 6-311+G(2d,p) level with the exception of As, which used LANL2DZ.

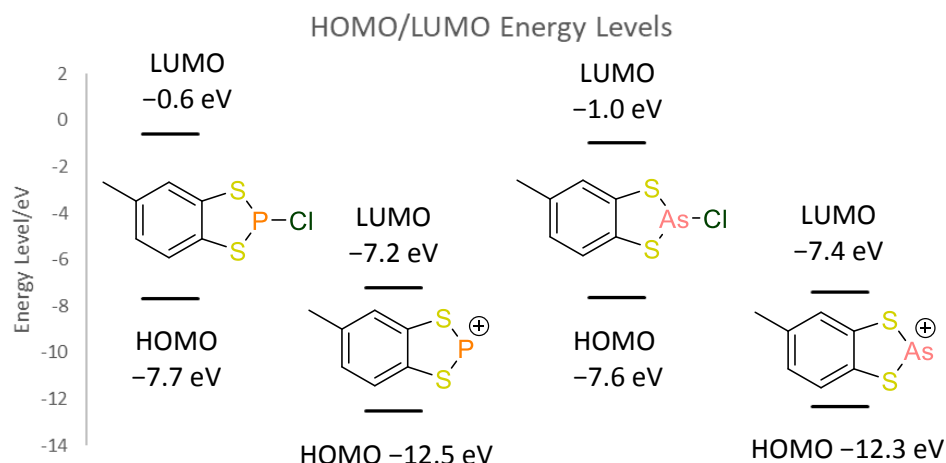
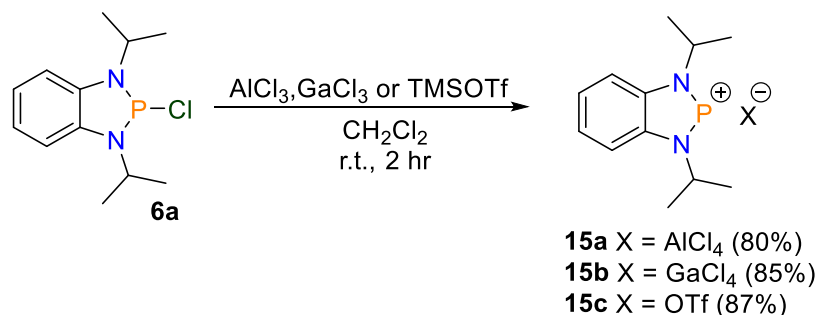


Figure 3.14: Frontier orbital energy levels of the dithiaphosphole **1a**, dithiaphosphenium cation **13+**, dithiarsole **3** and dithiarsenium cation **14+**. Values in eV. Calculated at M06-2X and 6-311+G(2d,p) level with the exception of As, which used LANL2DZ.

3.2.2 Synthesis of diazaphosphenium cations

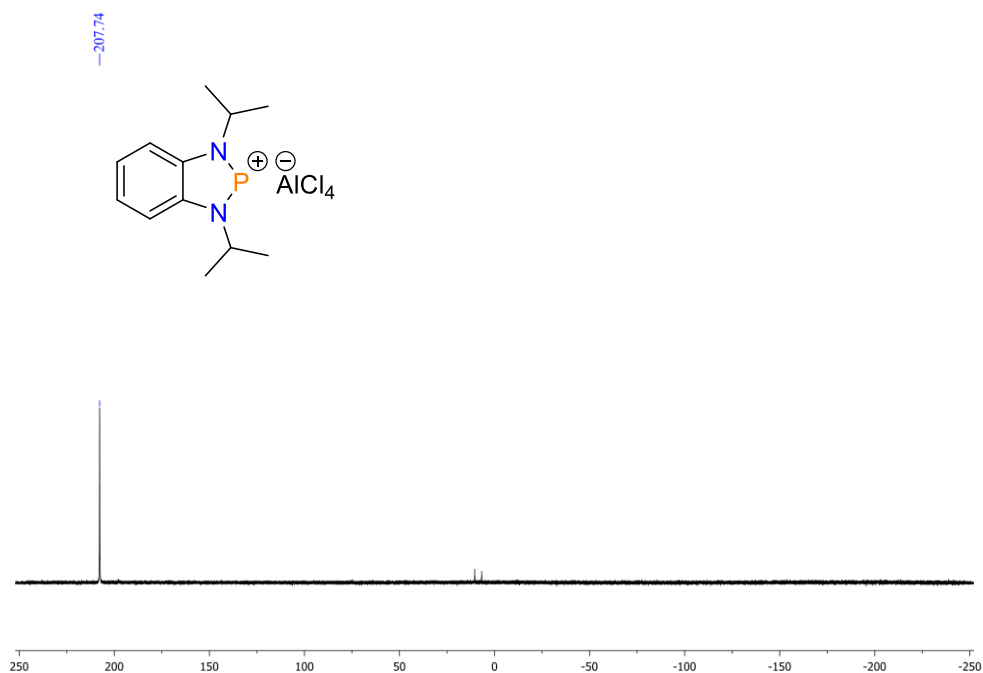
3.2.2.1 Synthesis and NMR analysis of diazaphosphenium cations from diazaphosphole

In an analogous fashion to the dithiaphosphole case, cation formation proceeded by reacting the diazaphosphole **6a** with halide abstracting reagents. **6a** was added to stoichiometric amounts of either aluminium trichloride or gallium trichloride in CH_2Cl_2 solvent and left to stir at ambient temperature for two hours. During this time the solution had turned red/yellow. The solvent was removed *in vacuo* and the solids were washed with pentane. After drying the products 1,3-diisopropyl-benzodiphosphenium tetrachloroaluminate (**15a**) and 1,3-diisopropyl-benzodiphosphenium tetrachlorogallate (**15b**) were obtained as red-yellow solids. In the case of using TMS triflate 1.2 equivalents were used, otherwise the reaction proceeded as just described to give the product 1,3-diisopropyl-benzodiphosphenium triflate (**15c**). Note that unlike for the dithiaphosphenium case where the triflate counterion was not tolerated, the synthesis here proceeded smoothly (Scheme 3.5).



Scheme 3.5: Synthesis of dithiaphosphenium compounds from dithiaphosphole **1a**.

Unlike in the dithiaphosphenium case where hydrolysis readily occurred in solution, $^{31}\text{P}\{^1\text{H}\}$ NMR spectroscopy of the diazaphosphenium cations showed the expected downfield shift compared to the starting precursor **6a**. The $^{31}\text{P}\{^1\text{H}\}$ NMR chemical shifts for **15a–c** were $\delta = 207.7$ ppm ($X = \text{AlCl}_4$), $\delta = 212.9$ ppm ($X = \text{GaCl}_4$) and $\delta = 216.0$ ppm ($X = \text{OTf}$) respectively, which is typical for compounds of this type. For reference, the $^{31}\text{P}\{^1\text{H}\}$ NMR chemical shift is at $\delta = 147.2$ ppm for **6a**. In the case of **15a**, ^{27}Al NMR spectroscopy showed a singlet signal at $\delta = 103.8$ ppm, confirming the presence of AlCl_4^- . For **15c**, ^{19}F NMR spectroscopy could be used due to the CF_3 group present in the triflate counterion. The ^{19}F NMR spectrum showed a singlet centred at $\delta = -78.4$ ppm, which corresponds to the triflate counterion. Unfortunately, although gallium has two NMR active nuclei, ^{69}Ga and ^{71}Ga , both are quadrupolar and yield very broad signals.^{17,18} Thus, gallium NMR spectroscopy is not routinely performed. Using **15a** as an example, the ^1H NMR spectrum showed four signals; the aromatic signals do not coalesce into one like in **6a** (Chapter Two). The aromatic signals appear as broad multiplets at $\delta = 7.30$ and 7.22 ppm and both integrate to two. The septet and doublet corresponding to the isopropyl group have approximately the same chemical shift as in **6a**; their chemical shifts are at $\delta = 4.45$ and 1.50 ppm respectively (Figure 3.15).



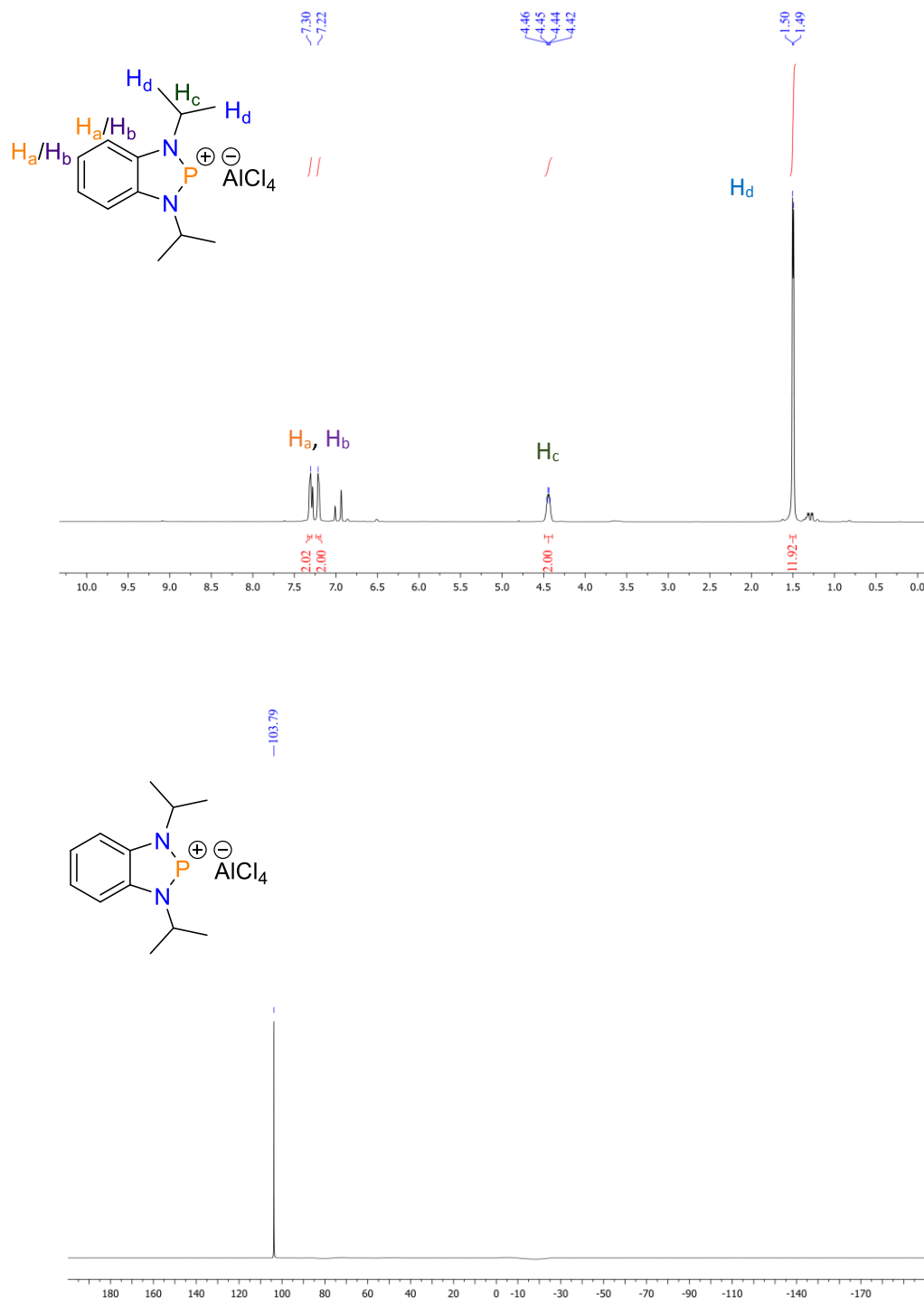


Figure 3.15: Top: $^{31}\text{P}\{^1\text{H}\}$ NMR (162 MHz, $\text{C}_6\text{D}_5\text{Br}$, 295 K), middle: ^1H NMR spectrum (500 MHz, $\text{C}_6\text{D}_5\text{Br}$, 295 K), bottom: ^{27}Al NMR spectrum (130 MHz, $\text{C}_6\text{D}_5\text{Br}$, 295 K) of diazaphosphenium **15a**.

3.2.2.2 Solid-state structures of diazaphospheniums

With the diazaphosphenium well characterised by multinuclear NMR spectroscopy, single crystals of **15a–c** suitable for X-ray diffraction were then grown in collaboration with Alex Rigby from a saturated solution of CH_2Cl_2 with a few drops of pentane added and cooled to $-40\text{ }^\circ\text{C}$ (Figures 3.16, 3.17 and 3.18). Upon data collection, solution and refinement by Dr Lewis Wilkins, **15a** and **15b** were found to crystallise in the orthorhombic space group $Pbca$ with one molecule in the asymmetric unit, increasing to eight in the unit cell. On the other hand, **15c** crystallised in the monoclinic space group $P2_1/n$ with one molecule in the asymmetric unit and four in the unit cell. The diazaphospheniums show a tendency towards molecular planarity, a feature that was seen in the dithiaphospheniums. The fold angle across the $\text{N}\cdots\text{N}$ vector slightly increases upon moving from **15a** to **15c**; for **15a** it is calculated at $0.66(13)^\circ$, $0.76(14)^\circ$ for **15b** and $1.01(11)^\circ$ for **15c**. The molecular planarity is again attributed to the $3p\text{-}3p$ π -conjugation and delocalisation of electrons within the $10\text{-}\pi$ aromatic system.

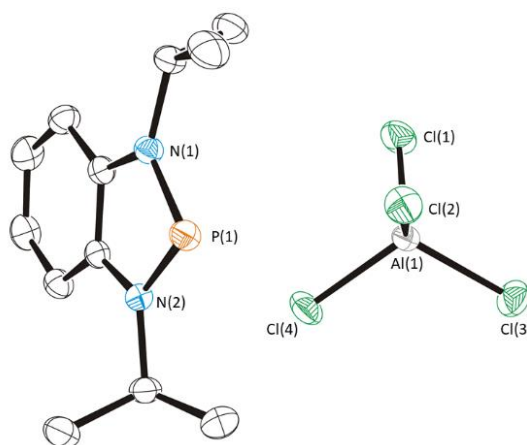


Figure 3.16: Solid-state structure of 1,3-diisopropyl-benzodiphosphenium tetrachloroaluminate **15a**. Thermal ellipsoids drawn at 50% probability and H-atoms removed for clarity.

In **15a**, the P–N bond lengths are 1.6543(17) Å and 1.6550(17) Å, which are shorter than that seen in the precursor **6a** (*cf.* 1.6713(16)–1.6740(15) Å). Moreover, this decrease is larger than that seen in the dithiaphosphole to dithiaphosphenium case and is rationalised by the aromatic nature of **15a**. Like **13b**, **15a** shows an expansion in the N(1)–P(1)–N(2) bond angle, increasing from 90.95(8)°–91.04(8)° in **6a** to 92.00(9)° (Table 3.5). Inspection of the close packing in the unit cell of **15a** shows the closest cation⋯anion association is a P⋯Cl contact at 3.4967(7) Å. This is inside the combined van der Waals radii of 3.55 Å. Additionally, P⋯ π interactions between the phosphorus heteroatom and the fused benzene ring of a neighbouring dithiaphosphenium was seen, similar to that in the solid-state packing arrangement in **3a**.

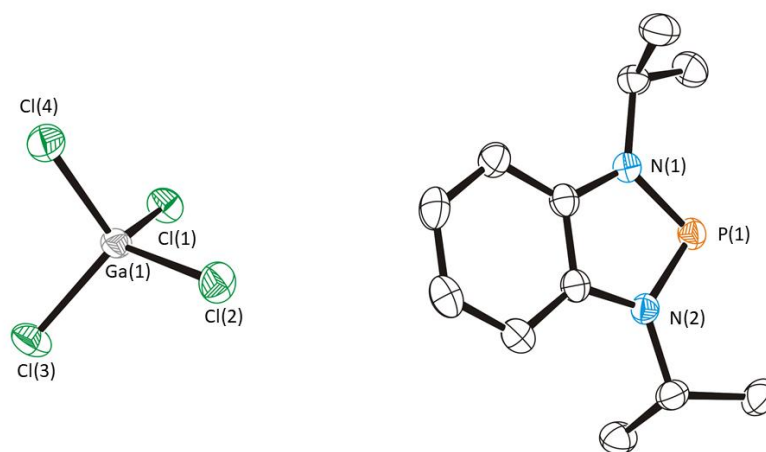


Figure 3.17: Solid-state structure of 1,3-diisopropyl-benzodiphosphenium tetrachlorogallate **15b**. Thermal ellipsoids drawn at 50% probability and H-atoms removed for clarity.

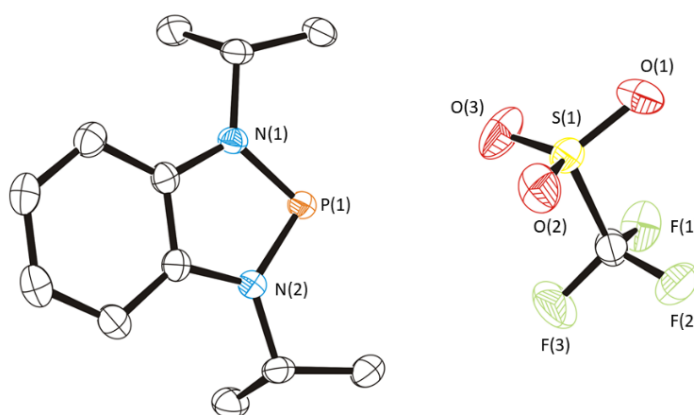


Figure 3.18: Solid-state structure of 1,3-diisopropyl-benzodiphosphenium triflate (**15c**). Thermal ellipsoids drawn at 50% probability and H-atoms removed for clarity.

15b and **15c** show similar features to that just detailed for **15a**, with P–N bond lengths that are contracted and an increase in the N(1)–P(1)–N(2) bond angle compared to the precursor **6a**. The closest cation⋯anion contact in **15b** is again between the phosphorus and chloride, which measures 3.4963(9) Å, and also shows the P⋯π interactions detailed in **15a**. For **15c** the closest cation⋯anion association is a P⋯O contact at 3.5455(18) Å, which is just within the sum of the combined van der Waals radii.

Table 3.5: Selected bond lengths and interior bond angles for diazaphospheniums **15a–c**.

Selected bond	15a / Å (X = AlCl ₄)	15b / Å (X = GaCl ₄)	15c / Å (X = OTf)
P(1)–N(1)	1.6543(17)	1.6549(19)	1.6526(16)
P(1)–N(2)	1.6550(17)	1.6553(19)	1.6470(17)
N(1)–C(1)	1.395(3)	1.390(3)	1.393(3)
N(2)–C(2)	1.389(3)	1.384(3)	1.396(2)
Selected angle	15a / °	15b / °	15c / °
N(1)–P(1)–N(2)	92.00(9)	91.82(10)	91.92(8)

3.2.2.3 Computational analysis of diazaphosphenium cation

Geometry optimisation and vibrational frequency calculations were then performed on the cation of the diazaphosphenium (**15+**), with the counterion ignored. Again the functional M06-2X and basis set 6-311+G(2d,p) were utilised. NBO calculations performed on **15+** showed a large build-up of positive charge on the phosphorus heteroatom, with a natural charge of +1.24. This is much greater than what is seen for the dithiaphosphenium **13+** (*cf.* +0.53) but again comparable to the precursor **6a**; highlighting the high polarisation present in the P–Cl bond. The N heteroatoms have a natural charge of –0.70, which is a small decrease compared to **6a**. Like **13+**, which showed an increase in P–S bond order upon cation formation, **15+** has an increase in the P–N bond order. In **6a** the Wiberg P–N bond order was found to be low, at just 0.84, which was explained by donation of electron density into the antibonding P–N orbital. In **15+** this bond order increases to 1.04 (Figure 3.19). Although donation into the P–N antibonding orbital is still observed, the stabilisation energy gain from this is much lower, at 6.4 KJ mol^{–1} (*cf.* 46.3 KJ mol^{–1} in **6a**).

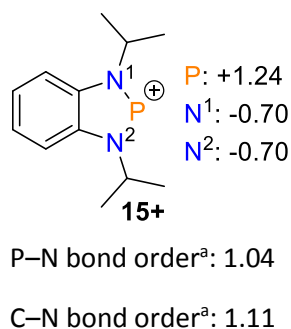


Figure 3.19: NBO analysis of diazaphosphenium cation **15+**. All atoms treated with M06-2X functional and 6-311G+(2d,p) basis set. ^aAverage values taken.

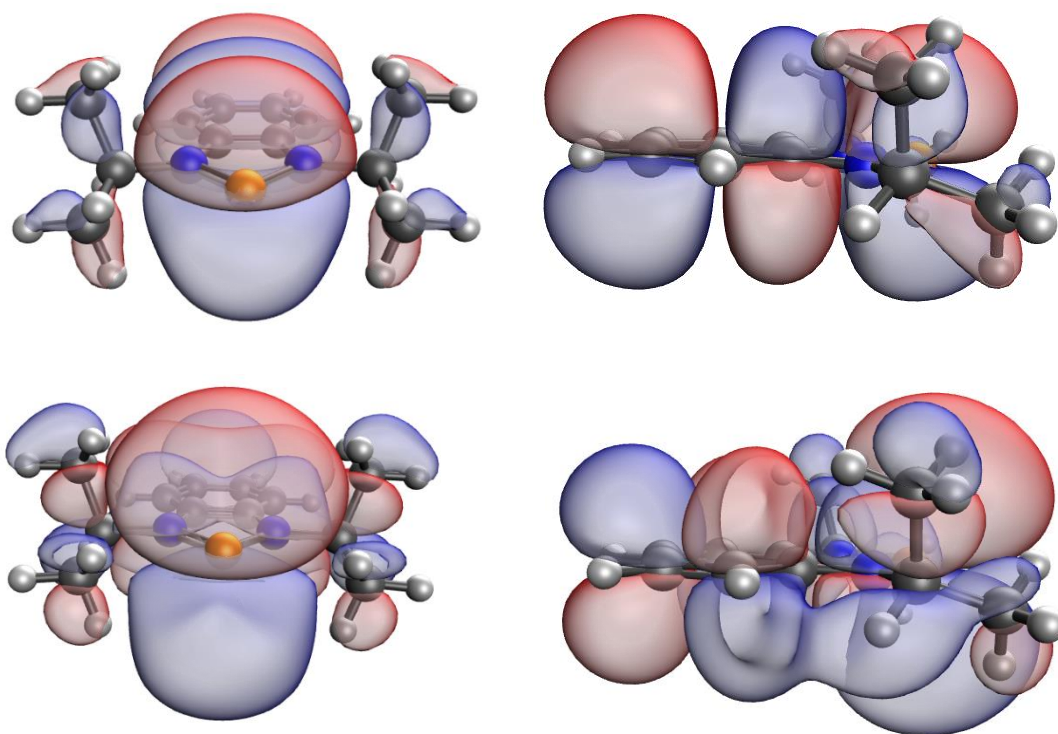


Figure 3.20: Images of the HOMO (top) and LUMO (bottom) of 1,3-diisopropylbenzodiphosphenium (**15+**). Blue = positive area of electron density, red = negative area of electron density. Calculated at M06-2X and 6-311+G(2d,p) level.

The frontier orbitals of **15+** were visualised, which showed that the HOMO was delocalised over the entire species and of π -symmetry, similar to that seen in **13+**. The LUMO is also fully delocalised and includes the p -orbital on the phosphorus heteroatom (Figure 3.20). The energy difference between the HOMO and LUMO is 6.3 eV (HOMO -11.8 eV, LUMO -5.5 eV), which is 1.0 eV higher than **13+** but is lower, albeit just, than in the precursor **6a**. In **6a** the HOMO–LUMO energy difference is 6.8 eV, with both the HOMO and LUMO lying higher in energy (HOMO -6.9 eV, LUMO -0.1 eV). Visual representations of the frontier orbitals of **6a** are shown below (Figure 3.21).

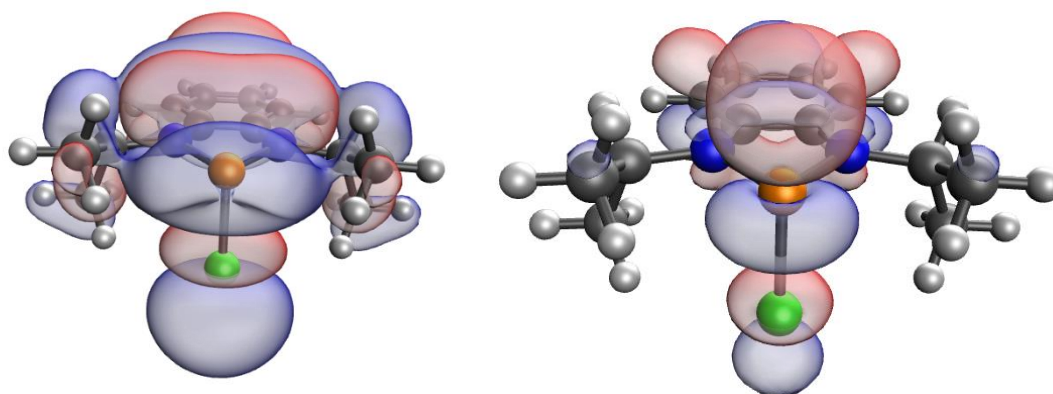
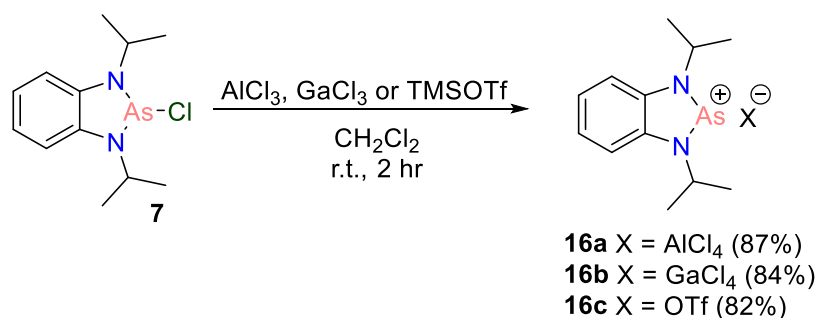


Figure 3.21: Images of the HOMO (left) and LUMO (right) of 2-chloro-1,3-diisopropylbenzodiazaphosphole (**6a**). Blue = positive area of electron density, red = negative area of electron density. Calculated at M06-2X and 6-311+G(2d,p) level.

3.2.2.4 Synthesis and NMR analysis of diazarsenium cations from diazarsole



Scheme 3.6: Synthesis of diazarsenium compounds from diazarsole **7**.

Similarly to the diazaphosphenium case, the diazarsole precursor **7** was added to stoichiometric quantities of the halide abstraction reagents aluminium trichloride or gallium trichloride in CH₂Cl₂ solvent. The reaction was left to stir at ambient temperature for two hours, and after solvent removal, pentane washings and further drying, the products 1,3-diisopropylbenzodiazarsenium tetrachloroaluminate (**16a**) and 1,3-diisopropylbenzodiazarsenium tetrachlorogallate (**16b**) were obtained as red-orange solids in excellent yields of 87% and 84% respectively. In the case of using TMS triflate 1.2 equivalents were again used, giving the product 1,3-diisopropylbenzodiazarsenium triflate (**16c**) in 82% yield (Scheme 3.6). ²⁷Al NMR spectroscopy and ¹⁹F NMR spectroscopy showed a signal at $\delta = 104.5$ ppm for the former and at $\delta = -78.1$ ppm for the latter, confirming formation of the respective counterions. ¹H NMR spectroscopy showed the expected two aromatic signals as well as the two signals for the isopropyl groups. In addition to multinuclear NMR spectroscopy, high resolution mass spectrometry (ES⁺ method) confirmed the cation

formation, which using **16a** as an example gave a mass of $[M]^+ [C_{12}H_{18}AsN_2]^+ 265.0692$ (theoretical 265.0686). The use of single-crystal X-ray diffraction gave further evidence of product formation.

3.2.2.5 Solid-state structures of diazarseniums

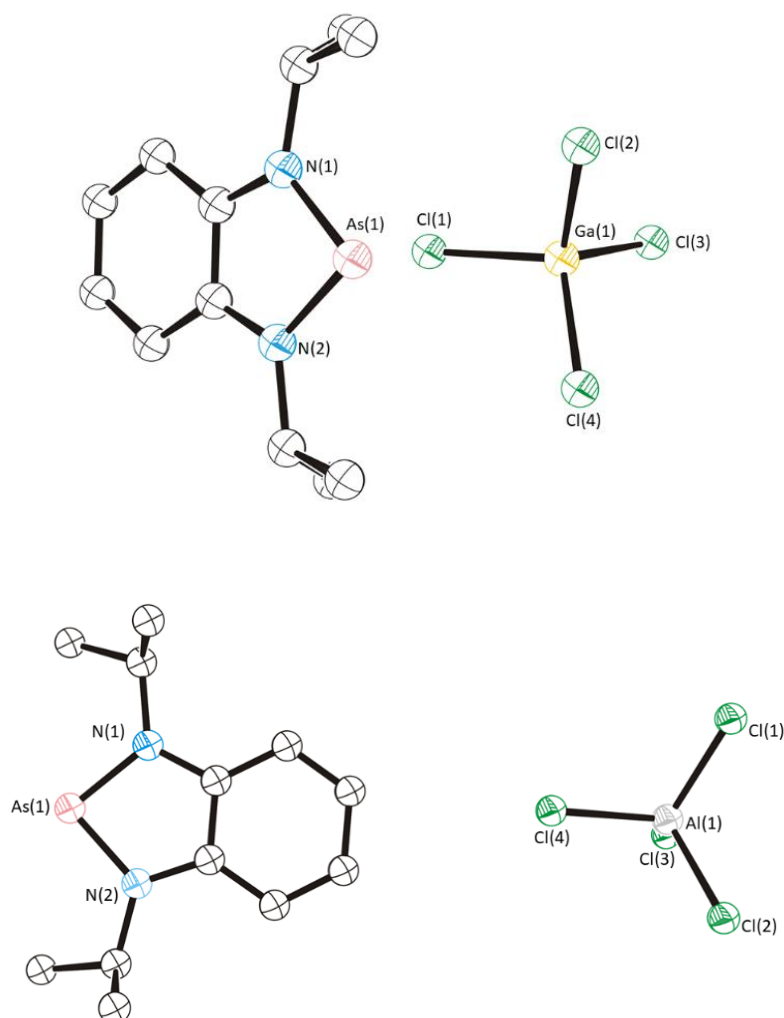


Figure 3.22: Solid-state structures of 1,3-diisopropyl-benzodiazarsenium tetrachloroaluminate (**16a**) and 1,3-diisopropyl-benzodiazarsenium tetrachlorogallate (**16b**). Thermal ellipsoids drawn at 50% probability and H-atoms removed for clarity.

Single crystals of **16a–c** suitable for X-ray diffraction were grown in collaboration with Alex Rigby from a saturated solution of CH_2Cl_2 with a few drops of pentane added and cooled to $-40\text{ }^\circ\text{C}$ (Figures 3.22 and 3.23). Upon data collection, solution and refinement by Dr Lewis Wilkins, the diazarsoles were found to crystallise in the monoclinic space group $P2_1/n$ with one molecule in the asymmetric unit, increasing to four in the unit cell. The distinctive fold angles about the $N\cdots N$ vector are lower than in **7**, but are greater than that seen in the dithiarseniums where no fold was observed and are rigorously planar. For **16a** and **16b** the

fold angles were measured at $0.82(13)^\circ$ and $0.93(16)^\circ$ accordingly, whereas for **16c** the fold angle is noticeably lower at just $0.03(16)^\circ$. The diazarseniums show contraction in the As–N bond lengths, a feature that has been seen in the cationic complexes already discussed. For example, in **16a** the two As–N bond lengths measure $1.7987(19)$ Å and $1.8053(19)$ Å, compared to $1.809(3)$ Å and $1.812(3)$ Å for **7**. The N(1)–As(1)–N(2) bond angle is expanded, but not by as much as was witnessed in the diazaphospheniums, with the N(1)–As(1)–N(2) bond angle in **16a** measuring $86.85(8)^\circ$ (*cf.* $86.45(14)^\circ$ in **7**) (Table 3.6). The close-packing structure of **16a** and **16b** are analogous and show As⋯Cl cation⋯anion contacts that are well within the combined sum of the van der Waals radii ($3.5677(8)$ – $3.5754(6)$ Å, combined van der Waals radii = 3.80 Å). Similarly, in the case of **16c** As⋯O cation⋯anion contacts are observed, which also fall within the range of the van der Waals radii.

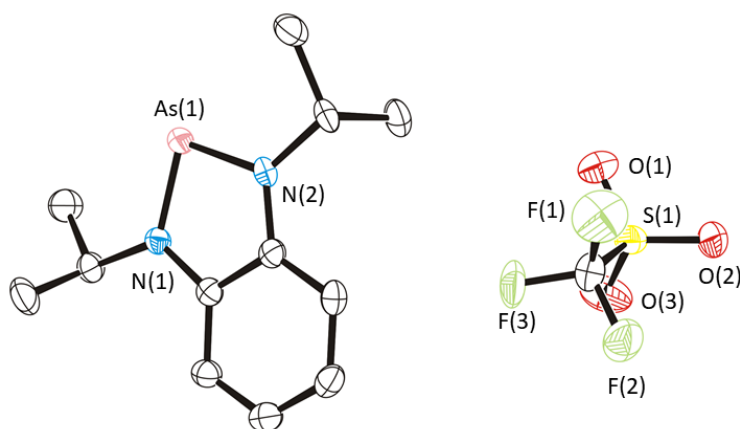


Figure 3.23: Solid-state structures of 1,3-diisopropyl-benzodiazarsenium triflate **16c**. Thermal ellipsoids drawn at 50% probability and H-atoms removed for clarity.

Table 3.6: Selected bond lengths and interior bond angles for diazaphospheniums **16a–c**.

Selected bond	16a / Å (X = AlCl ₄)	16b / Å (X = GaCl ₄)	16c / Å (X = OTf)
As(1)–N(1)	1.8053(19)	1.797(2)	1.796(2)
As(1)–N(2)	1.7987(19)	1.801(2)	1.797(3)
N(1)–C(1)	1.375(3)	1.371(4)	1.377(4)
N(2)–C(2)	1.380(3)	1.375(4)	1.377(3)
Selected angle	16a / °	16b / °	16c / °
N(1)–As(1)–N(2)	86.85(8)	86.794(2)	86.61(2)

3.2.2.6 Computational analysis of diazarsenium cation

Geometry optimisation and vibrational frequency calculations were performed on the cation, **16+**, using the functional M06-2X and basis set 6-311+G(2d,p) on all atoms, with the exception of the arsenic heteroatom. Again, for the arsenic heteroatom the ECP LANL2DZ basis set was used. NBO calculations on **16+** showed the expected build-up of positive charge on the arsenic heteroatom, with a natural charge of +1.35, which is significantly greater than that seen in the dithiarsenium **14+** (*cf.* natural charge = 0.76). Nevertheless, this does fit the theme seen in the dithiaphosphenium vs. diazaphosphenium where the phosphorus heteroatom is much more positively charged in the latter. The natural charge of the nitrogen heteroatom was averaged at –0.74, which is comparable to the diazaphosphole (–0.70) (Figure 3.24).

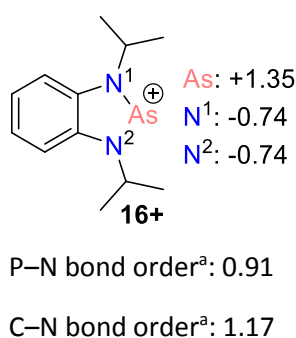


Figure 3.24: NBO analysis of diazarsenium cation **16+**. All atoms treated with M06-2X functional and 6-311G+(2d,p) basis set, with the exception of As, which used LANL2DZ.

^aAverage values taken.

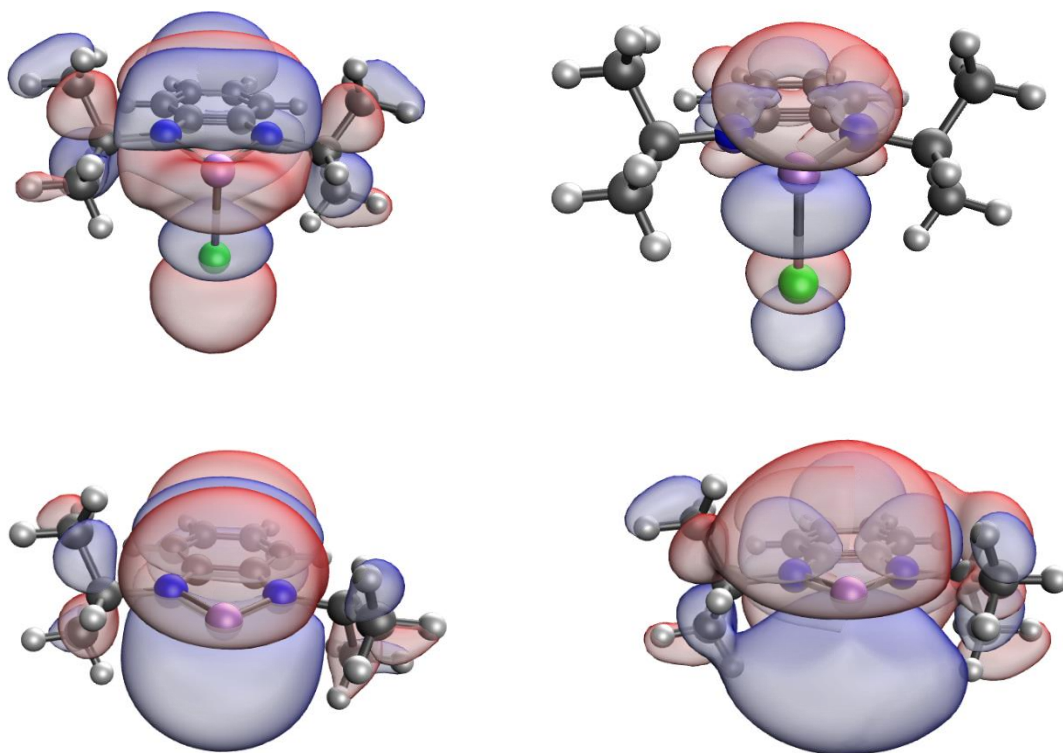


Figure 3.25: Top: HOMO (left) and LUMO (right) of 2-chloro-1,3-diisopropyl-benzodiazarsole (**7**). Bottom: HOMO (left) and LUMO (right) of 1,3-diisopropyl-benzodiarsenium (**16+**). Blue = positive of electron density, red = negative area of electron density. Calculated at M06-2X and 6-311+G(2d,p) level with the exception of As, which used LANL2DZ.

After NBO calculations were performed, molecular orbitals of the diazarsenium cation **16+** and the diazarsole precursor **7** were undertaken (Figure 3.25). As was seen in the dithiaphosphole vs. diazaphosphole case, the HOMO and LUMO of **16+** look the same as was seen in the diazaphosphenium **15+**; *vide supra*. Both the HOMO and LUMO of **16+** are delocalised over the full structure and are of π -symmetry. The HOMO–LUMO energy barrier is 5.7 eV, which is 0.8 eV higher in energy than the dithiarsenium cation **14+**, with both frontier orbitals at lower energy in **16+** (HOMO –12.3 eV, LUMO –7.4 eV in **14+** and HOMO –11.5 eV, LUMO –5.8 eV in **16+**). For the diazarsole precursor **7**, again the HOMO and LUMO orbitals visually look the same as the diazaphosphole **6a**, with an increased HOMO–LUMO energy barrier compared to **16+** also observed. In **7** this energy barrier is 6.4 eV, with the HOMO at –6.8 eV and LUMO –0.4 eV. These are both significantly at higher energy than the diazarsenium. These orbital energies are visualised below in Figure 3.26.

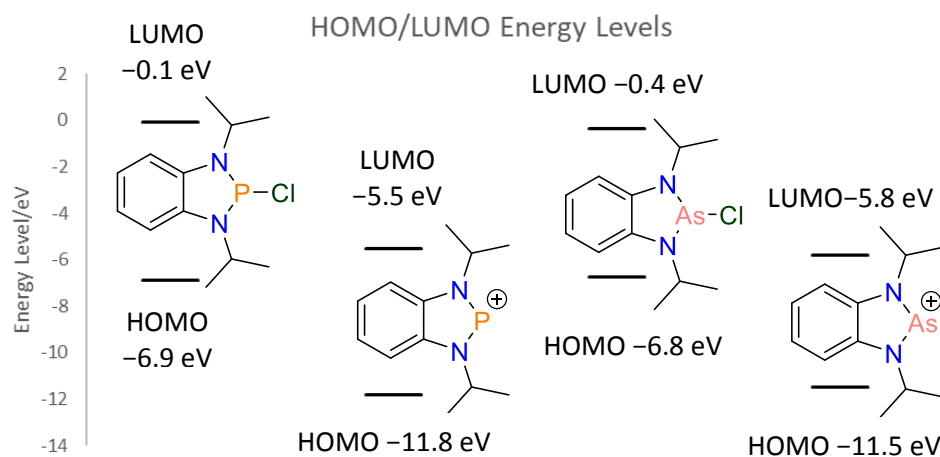
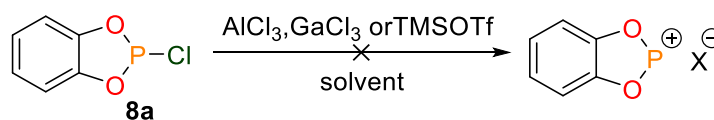


Figure 3.26: Frontier orbital energy levels of the diazaphosphole **6a**, diazaphosphenium cation **15+**, diazarsole **7** and diazarsenium cation **16+**. Values in eV. Calculated at M06-2X and 6-311+G(2d,p) level with the exception of As, which used LANL2DZ.

3.2.3 Attempted Synthesis of dioxaphosphenium cations from dioxaphosphole



Scheme 3.7: Attempted synthesis of dioxaphosphenium compounds.

In analogous fashion to the synthesis of the cationic complexes described so far, the formation of the dioxaphosphenium cation was attempted using simple Lewis acids (Scheme 3.7). Here though using CH_2Cl_2 solvent and addition of the halide abstraction reagent (aluminium trichloride, gallium trichloride and TMS triflate), tracking the reaction *via in situ* ^{31}P NMR spectroscopy showed no formation of the desired phosphonium cation, with only the starting dioxaphosphole observed. Indeed, using toluene as a solvent and increasing the reaction temperature to $90\text{ }^\circ\text{C}$ still resulted in no product formation. It is possible that given the calculated large Lewis acidity of the dioxaphosphenium, *vide infra*, the “free” cation is too unstable to exist in solution and the cation would need to be stabilised. The addition of 1,4-diazabicyclo[2.2.2]octane (DABCO) would potentially achieve this, but as the free cation was desired this reaction was not attempted.

3.2.4 Lewis acidity and aromaticity of phospheniums and arseniums

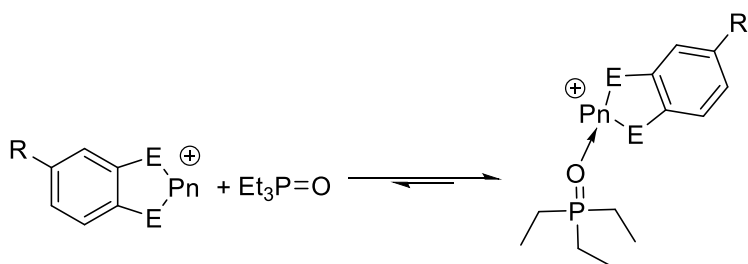
Given the cationic nature and presence of a vacant *p*-orbital of the phosphonium and arsenium cations, an interesting question to ask was how Lewis acidic these compounds are. One popular method that is widely used for experimentally determining this is the Gutmann-Beckett method,^{19,20} which has been extensively used for triarylboranes.²¹ In this test, a given Lewis acidic species is added to triethylphosphine oxide and the ^{31}P NMR spectrum is

recorded. The adduct formation between the molecular species and triethylphosphine oxide gives a chemical shift in the ^{31}P NMR spectrum, and by using Equation 3.1 an acceptor number is generated. An acceptor number (AN) of zero corresponds to the weak Lewis acidity of hexane solvent to triethylphosphine oxide, whereas an acceptor number of 100 is the value of the strongly Lewis acidic SbCl_5 . Acceptor numbers greater than 100 usually correspond to super Lewis acids. As the dithiaphospheniums underwent complete hydrolysis it was decided that they should not be used for this experiment, but as there was no issue with the dithiarsenium, diazaphosphenium and diazarsenium, these would be used. As the Gutmann-Beckett experiment is sensitive to solvent choice, reactions were used in CDCl_3 solvent. For the dithiarsenium **14b**, with GaCl_4^- counterion, the ^{31}P NMR spectrum gave a chemical shift of $\delta = 80.8$ ppm, which gave a corresponding acceptor number of 88.2, thus showing how highly Lewis acidic the dithiarseniums are (Figure 3.27). In contrast to this, the diazaphosphenium triflate, **15c**, and diazarsenium triflate, **16c**, were significantly less Lewis acidic. The former had a ^{31}P NMR chemical shift of $\delta = 56.9$ ppm and acceptor number of just 35.1, whereas the latter showed a ^{31}P NMR chemical shift of $\delta = 54.3$ ppm, which gave an even lower acceptor number of 29.4. For reference the well-known strong Lewis acid tris(pentafluorophenyl)borane, BCF, in CDCl_3 has an acceptor number of 77.5 (Table 3.7). The difference in Lewis acidity between the dithiarsenium and diazaphosphenium/diazarsenium is significant, but may be explained due to the greater π -donation from the N atoms in the diaza pnictole ring.²²

$$AN = (\delta - 41.0) \frac{100}{86.14 - 41.0}$$

Equation 3.1: Gutmann-Beckett equation. Where δ is the chemical shift of the adduct in the ^{31}P NMR spectrum.

Table 3.7: Gutmann-Beckett method Lewis acidity values. Pn = P or As, E = S or N and R = Me or H.



Compound	³¹ P NMR chemical shift/ ppm	Acceptor number	Relative Lewis acidity/ %
14b	80.8	88.2	100
15c	56.9	35.1	40
16c	54.3	29.4	33
B(C ₆ F ₅) ₃	76.0	77.5	88

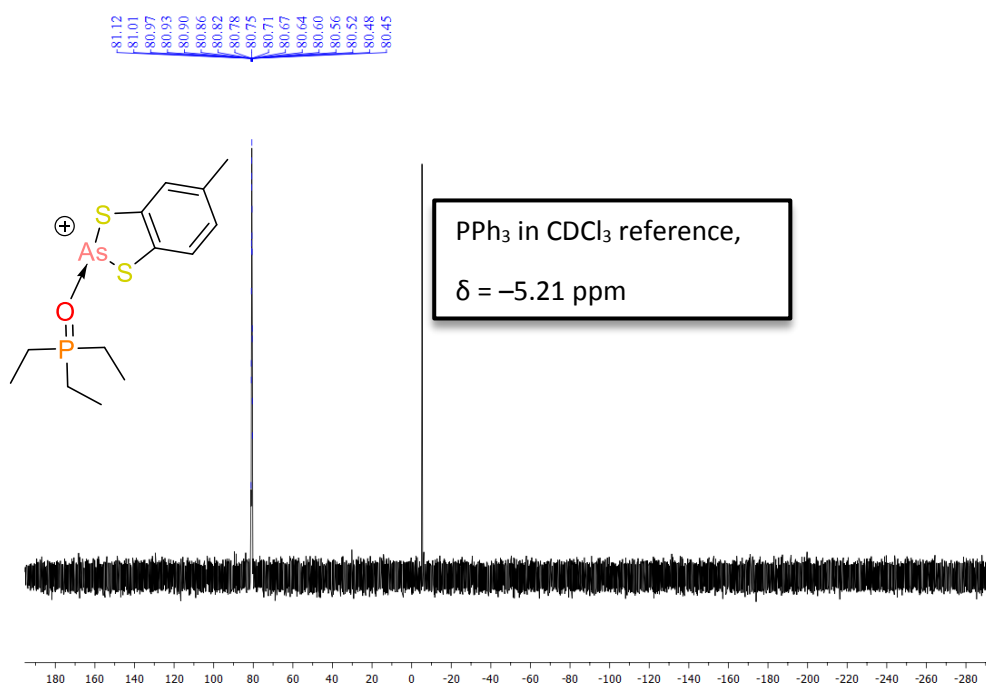
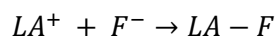


Figure 3.27: ³¹P NMR (162 MHz, CDCl₃, 295 K) spectrum of Gutmann-Beckett method for 5-methylbenzo-1,3,2-dithiarsenium tetrachlorogallate (**14b**). Spectrum referenced to PPh₃ in CDCl₃ at δ = -5.21 ppm.

The Lewis acidity of these cations was then further investigated computationally by determining their Fluoride Ion Affinity (FIA). As the fluoride ion is relatively small and highly basic, it will interact with most Lewis acids.²³ Calculating the reaction enthalpy of this interaction can therefore give a good indication to the Lewis acidity and this is what is known as the FIA. Previous work by Slattery, at MP2 (RI-)BP86/SV(P) level of theory, has looked at

the FIA of a wide range of phosphonium cations and included a dithiaphosphonium, diazaphosphonium and dioxaphosphonium.²⁴ Here the trend was that the dioxaphosphonium was by far the most Lewis acidic, with an FIA of 874 KJ mol⁻¹, after which the dithiaphosphonium has an FIA of 771 KJ mol⁻¹ and diazaphosphonium 683 KJ mol⁻¹. As the work of Slattery did not include arsenium cations, the FIA for **14+** and **16+** was calculated, using M06-2X/6-311G+(2d,p) (LANL2DZ for As heteroatom) theory level, which gave an FIA for **14+** of 758 KJ mol⁻¹ and 667 KJ mol⁻¹ for **16+** (Figure 28). Thus, the FIA calculations support the Gutmann-Beckett findings that the dithiarsenium cation is much more Lewis acidic than the diazaphosphonium/diazarsenium. Note that when calculating the FIA of **14+** and **16+**, a counterpoise correction was performed at the end; this is because of the effect known as basis set superposition effect (BSSE), which gives rise to error when studying an intermolecular reaction using an incomplete basis set.²⁵ In short, the coordinated complex (for example **14-F**) has a larger number of basis sets available to it than the two monomers, in this case the cation and F⁻, which gives a more flexible description of the wavefunction and in turn lower energy for the coordinated complex. To remedy this, it is possible to use a very large basis set, but as this is computationally very expensive a counterpoise correction is generally used instead. This keeps the description of the coordinated complex the same and provides the two monomers with a basis set of identical size to the product.



Equation 3.2: General definition of a Fluoride Ion Affinity, where LA = Lewis acid, F⁻ = fluoride ion and LA-F = coordinated complex.

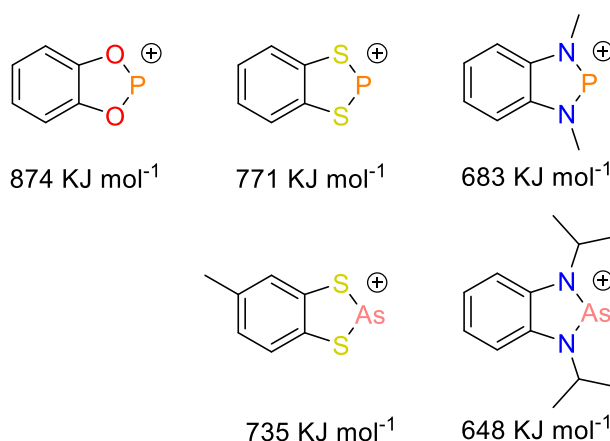


Figure 28: Top: FIA of phosphonium cations calculated by Slattery (MP2 (RI-)BP86/SV(P)). Bottom: FIA of arsenium cations (M06-2X/6-311G+(2d,p) (LANL2DZ for As heteroatom)).

In addition to Lewis acidity, the aromaticity of these compounds is an interesting area to explore, especially as it has been mentioned throughout this chapter but not yet been quantified. In the introduction an experimental method for quantifying the aromaticity of heterocycles was presented; harmonic oscillator model of heterocyclic electron delocalisation, or HOMHED for short. This was first used by Matins and colleagues but recently adopted by the group of Heeney to discuss the aromaticity of phospholes and arsoles.²⁶ HOMHED, which is given by Equation 3.3, works by comparing bond lengths determined from X-ray diffraction (R_i) with “optimal” bond lengths (R_{opt}), which are calculated by inputting reference single (R_s) and double (R_d) bond lengths into Equation 3, where ω is given the value 2. α is a normalisation constant and takes into account the difference between the bond types and n is the total number of bonds measured. The end result is a value between 0 and 1 (aromaticity of benzene), where HOMHED >0.5 shows aromatic character, between 0 and 0.5 no aromatic character and negative values indicate anti-aromatic behaviour.

$$\text{HOMHED} = 1 - \frac{1}{n} \sum_{i=1}^n \alpha (R_{opt} - R_i)^2$$

$$R_{opt} = \frac{R_s + \omega R_d}{1 + \omega}$$

$$\alpha = 2 \left[(R_{opt} - R_s)^2 + (R_{opt} - R_d)^2 \right]^{-1}$$

Equations 3.3, 3.4 and 3.5: Equations used in determining the aromaticity of the phosphonium and arsenium complexes by the HOMHED methodology.

Using this HOMHED methodology, it was applied to determine how aromatic the dithiaphosphonium (**13+**), dithiarsenium (**14+**), diazaphosphonium (**15+**) and diazarsenium cations (**16+**) are. Tables 3.8 and 3.9 show the values used to determine HOMHED for the phosphoniums and arseniums respectively, while Table 3.10 gives the HOMHED value. Looking at the results from Table 3.10 it is clear to see that firstly the cations are all aromatic, with HOMHED values all > 0.5. Secondly, the dithiaphosphonium and dithiarsenium are approximately as aromatic as each other (HOMHED \cong 0.86), as are the diazaphosphonium and diazarsenium (HOMHED = 0.9295 for **15+** and 0.9504 for **16+**). This is particularly surprising given that phospholes have been shown to be more aromatic than arsoles.²⁶ Lastly it can also be seen from Table 3.10 that the diazaphosphonium and diazarsenium complexes are more aromatic than the dithiaphosphonium and dithiarsenium compounds.

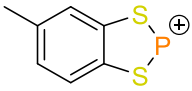
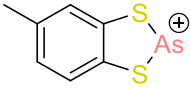
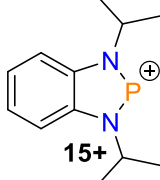
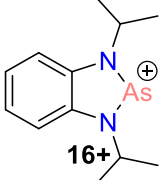
Table 3.8: Values used for calculating HOMHED of phosphenium cations.

	C-C	C-S	C-N	S-As	N-As
R_s (Å)	1.530	1.819	1.474	2.275	1.858
R_d (Å)	1.316	1.599	1.271	2.083	1.762
R_{opt} (Å)	1.387	1.672	1.339	2.147	1.794
α	78.6	74.4	87.4	97.7	391

Table 3.9: Values used for calculating HOMHED of arsenium cations.

	C-C	C-S	C-N	S-P	N-P
R_s (Å)	1.530	1.819	1.474	2.132	1.718
R_d (Å)	1.316	1.599	1.271	1.954	1.599
R_{opt} (Å)	1.387	1.672	1.339	2.013	1.639
α	78.6	74.4	87.4	114	254

Table 3.10: HOMHED values for phosphenium and arsenium cations.

				
	13+	14+	15+	16+
HOMHED	0.8632	0.8553	0.9295	0.9504

Chapter 3.3 Photophysical Properties of Diazaphosphenium and Diazarsenium Cations

Following structural analyses of the diazaphosphenium and diazarsenium complexes which showed close-contact interactions in the solid-state, the photophysical properties were probed on account of the 10- π Hückel aromaticity.³ To date, there are few examples in the literature where the optical properties of phosphole derived compounds have been investigated,²⁷⁻³⁰ and much fewer cases where these properties have been looked at in arsoles.^{31,32} Furthermore, when looking for examples of the absorption and/or emission of phosphonium and arsenium complexes, no relevant literature could be sourced.

On that note, for these photophysical studies, the diazaphosphole 2-chloro-1,3-diisopropyl-benzodiazaphosphole (**6a**) and diazaphosphenium complexes 1,3-diisopropyl-benzodiphosphenium tetrachloroaluminate (**15a**), 1,3 diisopropyl-benzodiphosphenium tetrachlorogallate (**15b**) and 1,3-diisopropyl-benzodiphosphenium triflate (**15c**) were chosen. The arsenic analogues 2-chloro-1,3-diisopropyl-benzodiazarsole (**7**), 1,3-diisopropyl-benzodiarsenium tetrachloroaluminate (**16a**), 1,3-diisopropyl-benzodiarsenium tetrachlorogallate (**16b**) and 1,3-diisopropyl-benzodiarsenium triflate (**16c**) were additionally utilised. This would allow for a thorough comparison between not only the effect of using different counterions but the effect of changing the heteroatom.

3.3.1 Absorption Properties

The UV-visible (UV-vis) absorption spectra of diaza pnictole species **6a**, **15a-c**, **7** and **16a-c** were performed in collaboration with Dr Samuel Adams and Professor Simon Pope from degassed solutions of acetonitrile and chloroform (Table 3.11). These spectra are complex but revealed changes on varying the cationic heteroatom, counterion and the solvent. With regards to the former, the diazaphosphole **6a** shows two absorption shoulders at $\lambda_{\text{abs}} = 269$ and 280 nm in CHCl_3 , whereas changing the heteroatom from phosphorus to arsenic, **7**, showed an absorption band at $\lambda_{\text{abs}} = 332$ nm, as well as two shoulder peaks at 282 and 269 nm. Comparing **6a** and **15a-c**, the absorption band positions are identical with the exception of **15a**, which was the only species to exhibit a discrete peak between 300 and 400 nm. More differences were observed in the appearance of the spectra when comparing the arsenic complexes **7** and **16a-c**, suggesting a greater degree of cation-anion aggregation in solution for these compounds. For example, the acetonitrile solution of **16a** showed a band at $\lambda_{\text{abs}} = 284$ nm and a shoulder at 247 nm, whereas for **16b** bands appear at $\lambda_{\text{abs}} = 310$ nm and 254 nm.

Interestingly, while performing the UV-vis measurements it was noted that the spectra in the more polar acetonitrile solution were blue shifted (decrease in wavelength; hypsochromic shift) with respect to the chloroform solutions (dielectric constant $\epsilon = 37.5$ and 4.81 accordingly), which may be ascribed to the inherent (ground state) dipole moment caused by the P^+/As^+ centre (Figure 3.29). In all cases these bands are ascribed to $^1\pi \rightarrow \pi^*$ transitions, which is supported by time-dependent DFT (TD-DFT) calculations.

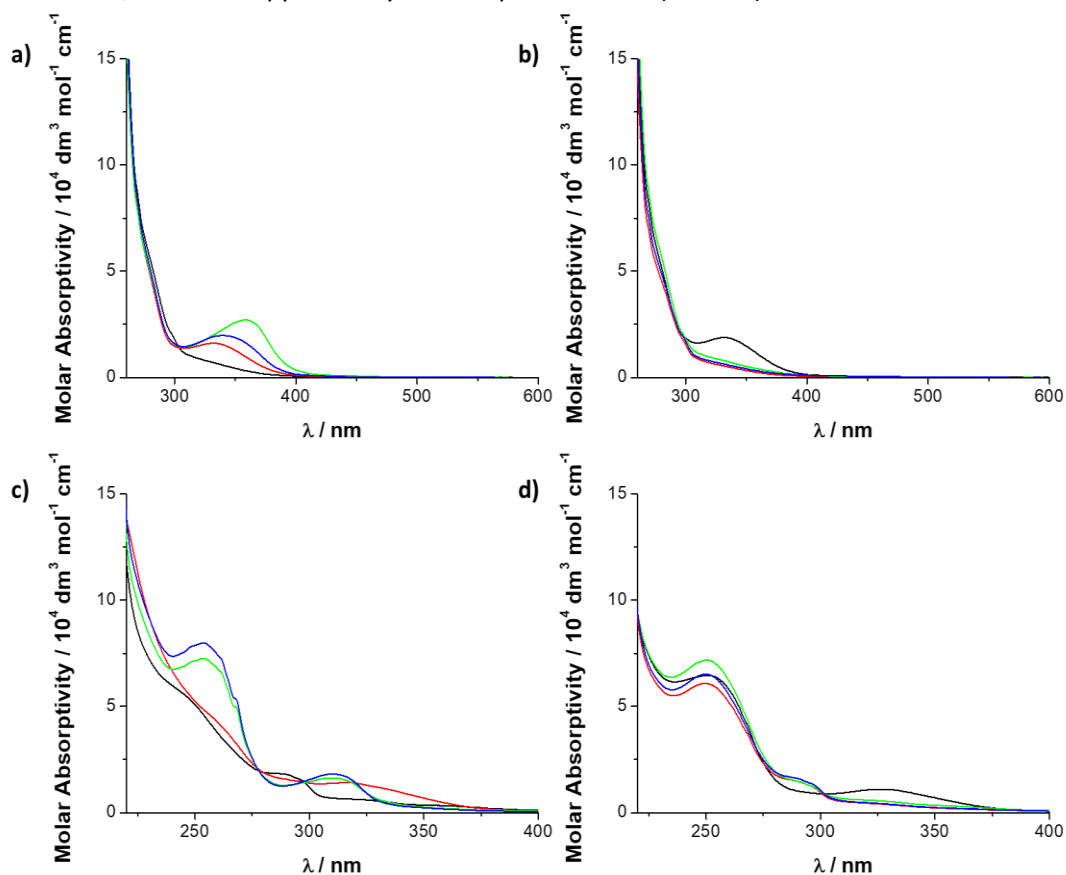


Figure 3.29: UV-Visible absorption spectra of diazarsole and diazaphosphole derivatives in chloroform (a and b respectively) and acetonitrile (c and d respectively). Counterions are Cl⁻ (red), AlCl₄⁻ (black), GaCl₄⁻ (green) and OTf⁻ (blue). $C = 1.0 \times 10^{-5} \text{ M}$.

For the TD-DFT, the diazaphosphenium cation **15+** was used; geometry optimised and vibrational frequency calculations proceeded as before but made use of a polarisable continuum solvation model (PCM) of acetonitrile. Use of PCM is common in computational chemistry when the inclusion of solvation is important and it works by modelling the solvent as a polarisable continuum as opposed to looking at every single solvent molecule, which would be computationally prohibitively expensive.³³ After this, excited states and UV-vis calculations were performed on the free cation **15+**, again using the PCM acetonitrile model, which showed that the lowest energy transition corresponds from the HOMO to LUMO.

Table 3.11: Absorption spectroscopy data for compounds **6a**, **15a–c**, **7** and **16a–c**.

Compound	Solvent	$\lambda_{\text{abs}}/ \text{nm}$ ($\epsilon/ 10^4 \text{ M}^{-1} \text{ cm}^{-1}$)
6a	CHCl ₃	269 (8.3) sh, 280 (4.5) sh
	MeCN	250 (6.1), 287 (1.6) sh
15a	CHCl ₃	269 (7.0) sh, 280 (5.2) sh, 333 (1.6)
	MeCN	251 (6.5), 325 (1.1)
15b	CHCl ₃	269 (8.9) sh, 280 (5.7) sh
	MeCN	250 (7.2), 287 (1.6) sh
15c	CHCl ₃	269 (7.6) sh, 280 (4.9) sh
	MeCN	250 (6.5), 287 (2.7) sh
7	CHCl ₃	269 (8.0) sh, 282 (4.3) sh, 332 (1.6)
	MeCN	265 (3.7) sh, 315 (1.4)
16a	CHCl ₃	269 (8.8) sh, 282 (5.1) sh
	MeCN	247 (5.4) sh, 284 (1.9)
16b	CHCl ₃	269 (7.9) sh, 282 (4.4) sh, 355 (2.7)
	MeCN	254 (7.3), 310 (1.6)
16c	CHCl ₃	269 (8.4) sh, 282 (4.5) sh, 341 (2.0)
	MeCN	254 (8.0), 310 (1.8)

3.3.2 Emissive Properties

The diazaphosphole and diazarsole derivatives were found to be emissive following irradiation of the lowest energy absorption bands ($\lambda_{\text{exc}} = 310 \text{ nm}$) (Table 3.12). Like the absorption measurements, emission spectra were recorded by Dr Samuel Adams and Professor Simon Pope in degassed solutions of chloroform and acetonitrile. The appearance of the emission spectra is generally similar and shows broad bands with some vibrational features centred at 393 and 384 nm respectively. Quantum yields for the excitation were calculated and are within the range of 0.1–2%, thus the emission is poorly efficient. Intriguingly, the quantum yield increased when using acetonitrile as a solvent as opposed to chloroform. Time-resolved emission measurements at $\lambda_{\text{exc}} = 295 \text{ nm}$ produced profiles that fit best to a biexponential decay, giving a short lifetime component of approximately 1 ns and a second longer component ranging from 2.8 ns for **15c** in chloroform to 9.9 ns for **7** in chloroform. The biexponential decay suggests two species are present in the decay process and potentially may be explained by the hemi-lability of the counterion.

Analysis of the lifetime of emissions showed that in the case of the diazaphosphole/diazaphospheniums a variation of lifetime was observed as a function of counterion choice, although in general it was found that the decays were shorter than the arsenic counterparts. Nevertheless, the lifetimes in both cases suggested a fluorescence process. The fluorescent lifetimes of the diazarsole/diazarsenium complexes also show a trend in solvent choice, as the longer lifetime component decreases when moving from chloroform to acetonitrile. For example, in **7** the longer lifetime component decreased from 9.0 ns in chloroform to 5.0 ns in acetonitrile. Note that this trend is not seen in the diazaphosphole/diazaphosphenium case. Due to the relatively small Stokes shifts of the emission, short lifetimes (nanosecond timescale) and small shifts (9 nm) in emission maxima between using chloroform or acetonitrile, the emissive state of these spectra is ascribed to ${}^1\pi \rightarrow \pi^*$ character (Figure 3.30).

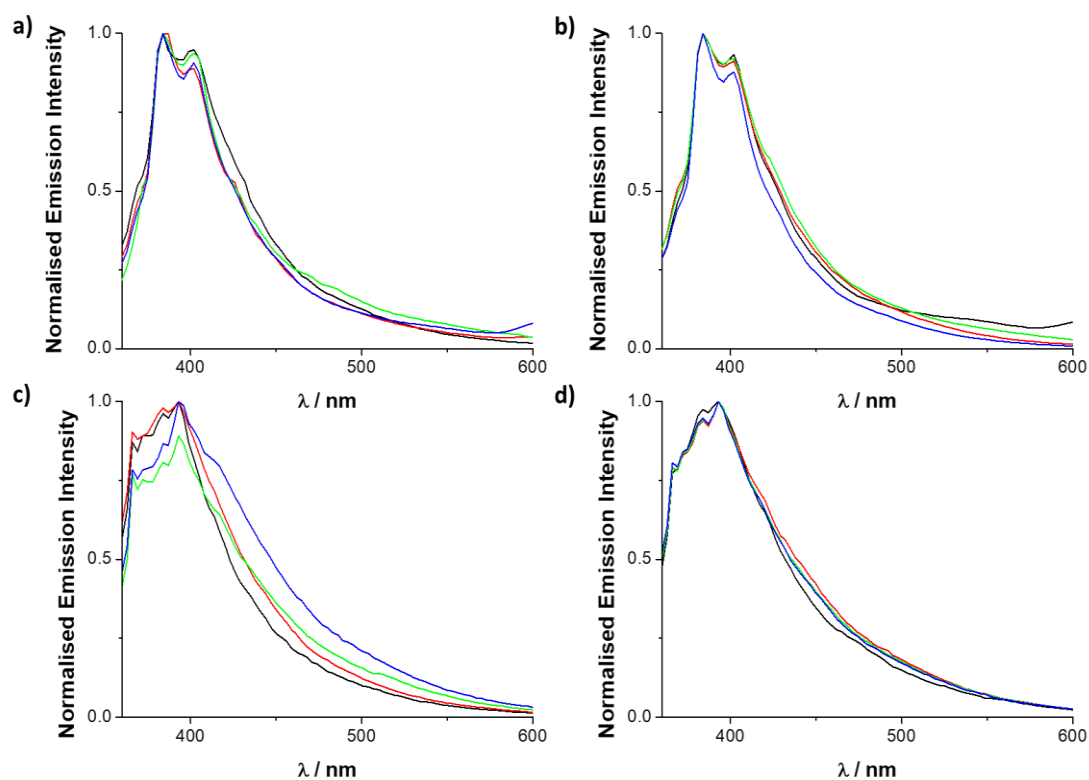


Figure 3.30: Steady-state emission spectra of diazarsole and diazaphosphole derivatives in chloroform (a and b respectively) and acetonitrile (c and d respectively). Counterions are Cl⁻ (red), AlCl₄⁻ (black), GaCl₄⁻ (green) and OTf⁻ (blue). $\lambda_{\text{exc}} = 330 \text{ nm}$, $C = 1.0 \times 10^{-5} \text{ M}$.

Table 3.12: Emission spectroscopy data for compounds **6a**, **15a–c**, **7** and **16a–c**. ^aValues in parentheses are the percentage the lifetime contributes to the overall decay.

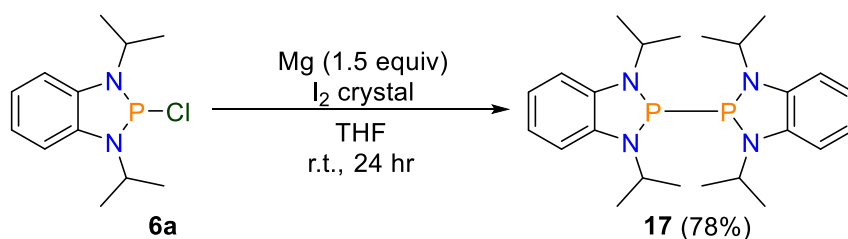
Compound	Solvent	λ_{\max}/nm	τ/ns^a	$\phi/\%$
6a	CHCl ₃	384	1.4 (32%) 8.3 (68%)	0.5
	MeCN	393	1.3 (51%) 5.9 (49%)	0.7
15a	CHCl ₃	384	1.3 (57%) 5.1 (43%)	0.1
	MeCN	393	1.5 (50%) 5.7 (50%)	1.7
15b	CHCl ₃	384	0.9 (45%) 3.7 (55%)	0.3
	MeCN	393	1.4 (51%) 5.9 (49%)	1.4
15c	CHCl ₃	384	0.8 (33%) 2.8 (67%)	0.2
	MeCN	393	1.3 (49%) 5.0 (51%)	1.7
7	CHCl ₃	387	1.6 (39%) 9.9 (61%)	0.09
	MeCN	393	1.6 (54%) 5.0 (46%)	1.1
16a	CHCl ₃	384	1.2 (45%) 8.6 (55%)	0.3
	MeCN	393	1.3 (52%) 5.0 (48%)	0.5
16b	CHCl ₃	384	1.3 (54%) 8.9 (46%)	0.08
	MeCN	393	1.6 (49%) 6.1 (51%)	0.7
16c	CHCl ₃	384	1.1 (34%) 9.5 (66%)	0.1
	MeCN	393	1.6 (46%) 5.4 (54%)	1.2

Chapter 3.4 Reduction of Diazaphosphole and Diazarsole

Further to substitution and cation formation, reduction of the starting diazaphosphole was undertaken to form a dimeric species using magnesium turnings.³ This reduction has previously been performed on the related diazaphospholene compounds, with the groups of Gudat,^{34–36} Masuda³⁷ and Wright³⁸ all having examples of these dimers.

3.4.1 Synthesis and multinuclear NMR analysis of benzodiazaphosphoryl dimer

To synthesise the desired dimer, the diazaphosphonium **6a** was dissolved in THF solvent and a small excess of magnesium turnings were added. A crystal of iodine was added to initiate the reaction and left to stir at ambient temperature for 24 hours. After this time the solvent was removed *in vacuo* and CHCl₂ was added. This was to reduce the solubility of the magnesium chloride by-product. The resulting orange solution was filtered through Celite twice and the solvent was removed *in vacuo* to afford the pure product 1,3-diisopropyl-benzodiazaphosphoryl dimer (**17**) in good yield (78%) (Scheme 3.8).



Scheme 3.8: Synthesis of 1,3-diisopropyl-benzodiazaphosphoryl dimer (**17**).

Initial characterisation of dimer **17** came from ³¹P{¹H} NMR spectroscopy, which gave a significantly upfield chemical shift of $\delta = 87.2$ ppm compared to the starting diazaphosphole (*cf.* $\delta = 147.2$ ppm). The ¹H NMR spectrum of **17** is different to **6a**; there are two aromatic resonances for **17** as opposed to the one for **6a**, but more interestingly the isopropyl groups are no longer equivalent and two signals are now observed for the CH₃ groups, with chemical shifts of $\delta = 1.44$ and 1.05 ppm. However, there still remains one CH signal from the isopropyl group at $\delta = 3.63$ ppm.

3.4.2 Solid-state structures of benzodiazaphosphoryl dimer

Single crystals of **17** suitable for X-ray diffraction were grown in collaboration with Alex Rigby from a concentrated solution of CH₂Cl₂ with a few drops of pentane added and cooled to -40 °C (Figure 3.31). Structure solution and refinement performed by Dr Lewis Wilkins showed that **17** crystallises in the monoclinic space group *P2*₁/*c* with half a molecule present in the asymmetric unit; increasing to four in the unit cell. The solid-state structure of the dimer showed an *anti*-configuration, where the two diazaphosphole units are on opposite sides of the central P-P bond and form a Z-like structure. Presumably this *anti*-configuration

is favoured over the *syn*-configuration due to the minimisation of steric repulsion between the isopropyl groups on the two diazaphosphole units. This is further evidenced by the inequivalence of the isopropyl groups in the ^1H NMR spectrum; *vide supra*. The central P–P bond length is 2.2379(8) Å, which is comparable to other dimers of this type.³⁸ The diazaphosphole ring has metrics that are different to the starting diazaphosphole **6a**. The P–N bond length is appreciably elongated in **17**, measuring 1.7275(16) Å and 1.7264(15) Å respectively. This compares to P–N bond lengths of 1.6713(16)–1.6740(15) Å in **6a**. The N–C bond lengths in the PN_2C_2 unit also show a small increase compared to **6a**. This bond elongation is accompanied by an expansion in the N(1)–P(1)–N(2) bond angle, which increases from 90.95(8)°–91.04(8)° in **6a** to 93.88(7)° in **17** (Table 3.13).

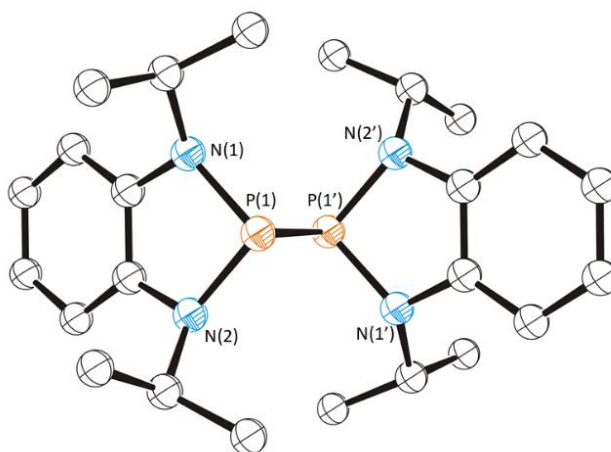


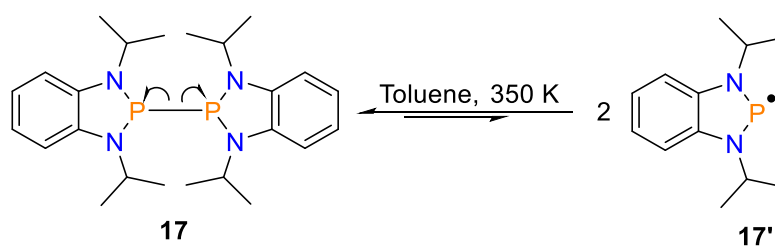
Figure 3.31: Solid-state structures of 1,3-diisopropyl-benzodiazaphosphoryl dimer **17**. Thermal ellipsoids drawn at 50% probability and H-atoms removed for clarity.

Table 3.13: Selected bond lengths and interior bond angles for 1,3-diisopropyl-benzodiazaphosphoryl dimer **17**.

Selected bond	17 / Å
P(1)–N(1)	1.7275(16)
P(1)–N(2)	1.7264(15)
N(1)–C(1)	1.417(3)
N(2)–C(2)	1.408(2)
P(1)–P(1')	2.2379(8)
<hr/>	
Selected angle	17 / °
N(1)–P(1)–N(1)	93.88(7)

3.4.3 EPR measurements on benzodiazaphosphoryl dimer

Given the possibility for the benzodiazaphosphoryl dimer to homolytically break and form a radical species, electron paramagnetic resonance (EPR) studies were performed by Dr Emma Richards (Scheme 3.9). In the solid-state **17** was found to be EPR silent, even when heated to 350 K (76.9 °C). When dissolved in toluene the isotropic solution-state EPR spectrum did not show a resonance, but when heated to 350 K a well-defined doublet signal, centred at $g_{\text{iso}} = 2.0025$, was observed (Figure 3.32). The hyperfine coupling had a value of $a_{\text{iso}} = 130$ MHz, which arises from the unpaired electron to one ^{31}P nucleus. This is comparable with previous reports of similar radical species formed upon P–P bond cleavage of $[(\text{CH})_2(\text{NR})_2\text{P}]_2$ dimers. Although no further hyperfine coupling could be resolved, despite using an experimental modulation amplitude of 0.5 G, inclusion of two equivalent ^{14}N nuclei with $a_{\text{iso}} = 10$ MHz resulted in an improved fit to the experimental line shape.



Scheme 3.9: Formation of radical species **17'** from 1,3-diisopropyl-benzodiazaphosphoryl dimer (**17**).

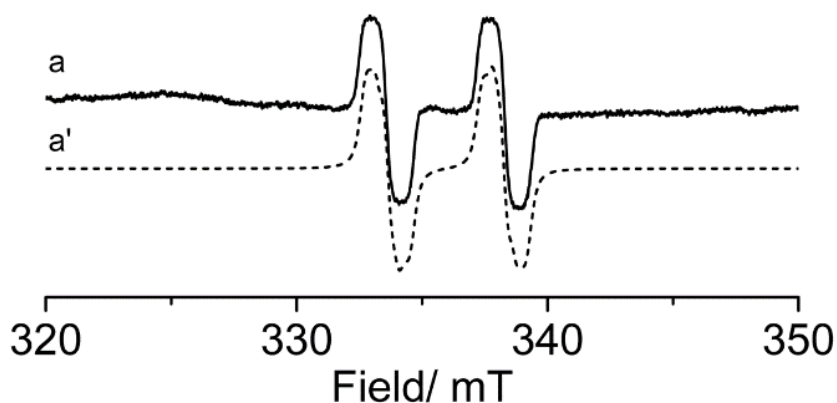


Figure 3.32: (a) Continuous-wave EPR spectrum recorded at 350 K of a toluene solution of **17**. (a') The corresponding EPR simulation.

2.4.4 Computational Analysis of Benzodiazaphosphoryl Dimer

DFT calculations were performed on the radical species by Dr James Platts using the ORCA package,³⁹ which predicted an a_{iso} value of 113.7 MHz from P and 8.6 MHz from N, which are both in good agreement with the experimental data. Informatively the DFT results supported the localisation of the radical on the phosphorus heteroatom, with spin charges of 0.67 e on P and 0.11 e on each N lying in p -orbitals perpendicular to the N–P–N plane (Figures 3.33, 3.34 and 3.35).

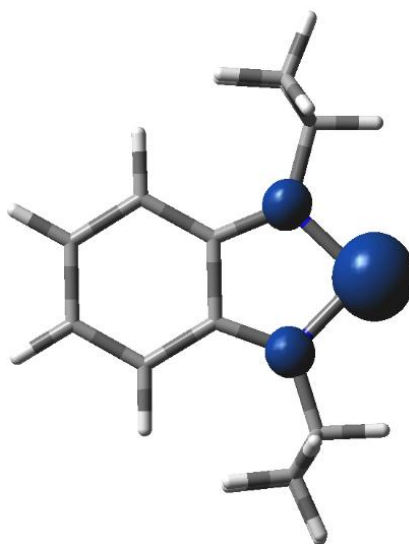


Figure 3.33: Theoretical spin density top/down view plot of the radical **17'** formed from **17**.

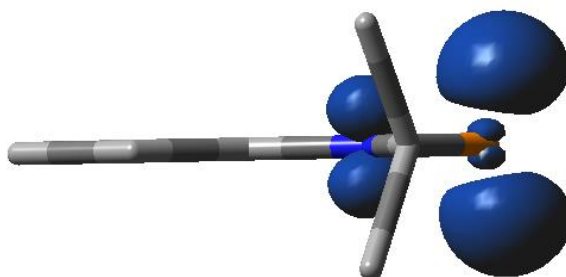


Figure 34: Theoretical spin density side view plot of the radical **17'** formed from **17**.

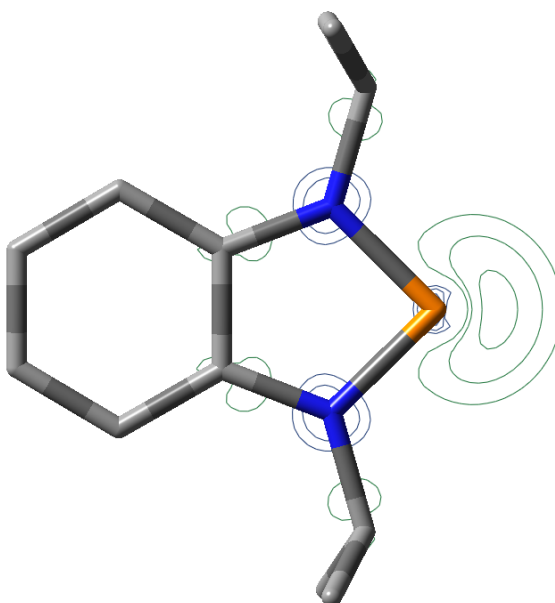
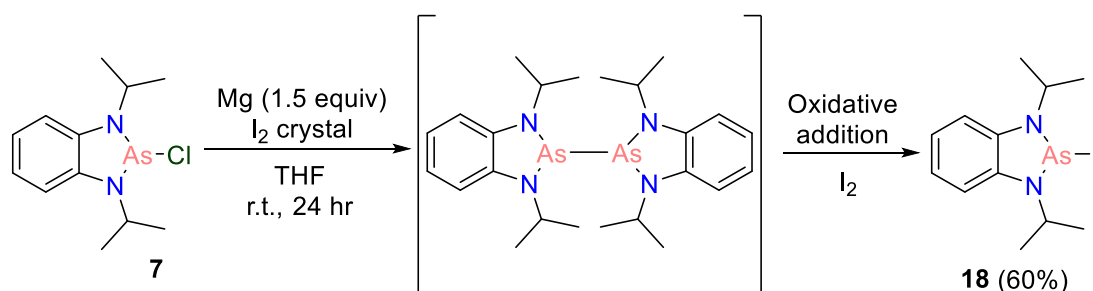


Figure 35: $C_6H_4N_2(iPr)_2P\cdot$ radical spin density contour plot of **17'**.

3.4.5 Attempted synthesis and characterisation of benzodiazarsole dimer

In an equivalent fashion to the formation of the benzodiazaphosphoryl dimer, the arsenic analogous reaction was attempted (Scheme 3.10). This followed the same procedure as described above. Analysis of the 1H NMR spectrum of the product revealed differences compared to **17**; principally the aromatic protons appeared as one singlet as opposed to two signals and the methyl groups of the isopropyl groups were magnetically equivalent. This is in contrast to the two isopropyl signals witnessed in **17**. The observations from the 1H NMR spectrum therefore casted doubt about the formation of the diazarsole derived dimer. Needing further information to determine the nature of the formed product, attention turned to single crystal X-ray diffraction. Crystals were grown from a concentrated solution of CH_2Cl_2 with a few drops of pentane added and cooled to $-40\text{ }^\circ C$ (Figure 3.36). Structure solution and refinement performed by Dr Lewis Wilkins showed that the desired As–As dimer had not formed, but instead the product was 2-iodo-1,3-diisopropyl-benzodiazarsole

(**18**). The formation of **18** initially proved puzzling, but it is hypothesised that the desired As–As dimer had formed *in situ*, but then undergoes oxidative addition with the iodine present in the reaction to form **18**.



Scheme 3.10: Attempted synthesis of diazarsole derived dimer; actually formed product **18**.

The fact that under the same conditions **18** formed from the synthesis described above whereas the benzodiazaphosphoryl dimer **17** was successfully produced shows that the As–As bond is much weaker and in turn more reactive than the P–P bond. Further attempts were undertaken to synthesise the diazarsole derived dimer, including using 1,2 dibromoethane as the initiator and grinding magnesium turnings to remove the oxide surface. In these cases the ^1H NMR spectra proved to be complicated with multiple signals present and as a result attempts to synthesise the dimer had terminated. It is believed that the As–As dimer is too unstable and reactive to be isolated.

3.4.6 Solid-state structure of 2-chloro-1,3-diisopropyl-benzodiazarsole

The solid-state structure of **18** crystallises in the monoclinic space group *Cc* and revealed a similar geometry and metrics to that already discussed for 2-chloro-1,3-diisopropyl-benzodiazarsole (**7**). The arsenic heteroatom is three-coordinate with an exocyclic iodide co ligand. The As–I bond length is 2.9442(10) Å, which although typical As–I bond metrics are not readily available, it is significantly longer than the 2.579 Å and 2.590 Å seen in the CSD database⁴⁰ for an arsenic(III) complex with two As–I bonds (CSD search code OPIMAS). The characteristic fold angle about the N···N vector is still observed, measuring 2.2(5)°, which is substantially less than in **7** (*cf.* 6.4(2)°) (Table 3.14). Inspection of the unit cell of **18** showed four molecules in the unit cell, contrasted to the one in the asymmetric unit, with close contacts between the iodide co-ligand on one diazarsole and the arsenic heteroatom on another that are well within the sum of the combined van der Waals radii (van der Waals radii = 3.83 Å, contact distance = 3.449 Å).

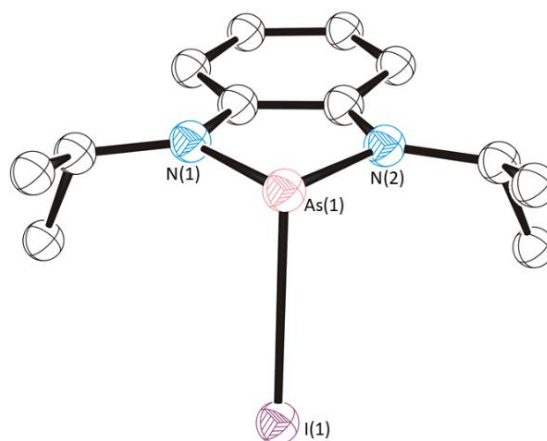


Figure 3.36: Solid-state structure of **18**. Thermal ellipsoids drawn at 50% probability and H-atoms removed for clarity.

Table 3.14: Selected bond lengths and interior bond angles for **18**.

Selected bond	18 / Å
As(1)–N(1)	1.820(8)
As(1)–N(2)	1.808(10)
N(1)–C(1)	1.377(15)
N(2)–C(2)	1.400(11)
As(1)–I(1)	2.9442(10)
Selected angle	18 / °
N(1)–As(1)–N(2)	86.8(4)

Chapter 3.5 Conclusion

In this chapter the dithiaphospholes, diazaphospholes, dithiarsoles and diazarsoles synthesised in Chapter 2 were used as precursors for additional reactions in which a range of new products were formed. To begin with, the dithiaphosphole **1a** and dithiarsole **3** were used to make novel paddlewheel structures, where a central *N* atom is flanked by three dithiaphosphole or dithiarsole moieties. From paddlewheel construction attention moved to phosphonium and arsenium cationic generation. In the case of the dithia pnictoles **1a** and **3**, the halide abstraction reagents aluminium trichloride and gallium trichloride were used, which generated the corresponding cations with AlCl_4^- and GaCl_4^- counterions. Attempts were made to give the triflate counterion but no reactivity was found to occur. Furthermore, the dithiaphospheniums proved to be highly air and moisture sensitive, with complete hydrolysis observed in the ^{31}P NMR spectra. Contrary to this, the diazaphospheniums and diazarseniums proved much more stable and were synthesised with AlCl_4^- , GaCl_4^- and OTf^- counterions. The Lewis acidity of the cations were evaluated using the Gutmann-Beckett method, which found that the dithiarseniums are much more Lewis acidic than either the diazaphospheniums and diazarseniums, which was further supported by Fluoride Ion Affinity computational calculations. After this the aromaticity was probed, which revealed that the cations are all aromatic, but the diazaphosphenium and diazarsenium complexes are more aromatic than the dithiaphosphenium and dithiarsenium compounds.

With the diazaphosphole (**6a**), diazaphospheniums (**15a–c**), diazarsole (**7**) and diazarseniums (**16a–c**), their photophysical properties were investigated. The absorption spectra showed that the band positions depended on both the cationic heteroatom (i.e. phosphorus or arsenic) and the counterion; the variance in wavelength with the counterion choice suggested a degree of cation-anion aggregation in solution. These complexes were also found to be emissive when irradiating at $\lambda_{\text{exc}} = 330$ nm, with broad bands which exhibited some vibrational features centred at 393 and 384 nm. Quantum yields were low, at 0.1% to 2%.

Lastly, having achieved substitution and cationic generation from the starting phosphole and arsole compounds, reduction of the diazaphosphole and diazarsole was attempted. This was achieved by reacting the diazaphosphole **6a** with magnesium turnings and leaving to stir for 24 hours. The product of this reaction is a benzodiazaphosphoryl dimer, which possesses a central P–P bond and has an *anti*-configuration, as found by single crystal X-ray diffraction. EPR measurements were recorded on this dimer, which showed that at 350 K homolytic cleavage takes places, as was seen by the well-defined doublet in the EPR spectrum.

Chapter 3.6 References

- 1 T. T. P. Tran, D. M. C. Ould, L. C. Wilkins, D. S. Wright, R. L. Melen and J. M. Rawson, *CrystEngComm*, 2017, **19**, 4696–4699.
- 2 F. H. Allen, D. G. Watson, L. Brammer, A. G. Orpen and R. Taylor, *Typical interatomic distances: organic compounds*, International Tables for Crystallography, 2006, ch. 9.5, vol.C, pp. 790–811.
- 3 D. M. C. Ould, A. C. Rigby, L. C. Wilkins, S. J. Adams, J. A. Platts, S. J. A. Pope, E. Richards and R. L. Melen, *Organometallics*, 2018, **37**, 712–719.
- 4 D. M. C. Ould, T. T. P. Tran, J. M. Rawson and R. L. Melen, *Dalton Trans.*, 2019, **48**, 16922–16935.
- 5 A. H. Cowley and R. A. Kemp, *Chem. Rev.*, 1985, **85**, 367–382.
- 6 S. Burck, J. Daniels, T. Gans-eichler, D. Gudat, K. Nättinen and M. Nieger, *Z. Anorg. Allg. Chem.*, 2005, **631**, 1403–1412.
- 7 N. Burford, J. A. C. Clyburne, P. Losier, T. M. Parks and T. S. Cameron, *Phosphorus, Sulfur and Silicon*, 1994, **93–94**, 301–304.
- 8 K. A. Porter, A. C. Willis, J. Zank and S. B. Wild, *Inorg. Chem.*, 2002, **41**, 6380–6386.
- 9 O. Kuhl, *Phosphorus-31 NMR spectroscopy: A concise introduction for the synthetic organic and organometallic chemistry*, Springer, Berlin, 2008.
- 10 T. S. Cameron and A. Linden, *Phosphorus, Sulfur and Silicon*, 1989, **41**, 75–81.
- 11 A. L. Spek, *Acta Cryst. D*, 2009, **D65**, 148–155.
- 12 G. Zhang and C. B. Musgrave, *J. Phys. Chem. A.*, 2007, **111**, 1554–1561.
- 13 M. D. Wodrich, P. R. Schreiner, A. A. Fokin and P. Von Rague, *Org. Lett.*, 2007, **9**, 1851–1854.
- 14 N. Burford and B. W. Royan, *J. Chem. Soc., Chem. Commun.*, 1989, 19–21.
- 15 H. Nöth, R. Rurländer and P. Wolfgardt, *Z. Naturforsch.*, 1981, **37b**, 29–37.
- 16 N. Burford, T. M. Parks, B. W. Royan, B. Borecka, T. S. Cameron, J. F. Richardson, E. J. Gabe and R. Hynes, *J. Am. Chem. Soc.*, 1992, **114**, 8147–8153.
- 17 Z. Černý, J. Macháček, J. Fusek, O. Kříž, B. Čásenský and D. G. Tuck, *J. Organomet. Chem.*, 1993, **456**, 25–30.
- 18 B. R. McGarvey, M. J. Taylor and D. G. Tuck, *Inorg. Chem.* 1981, **20**, 2010–2013.
- 19 M. A. Beckett, G. C. Strickland, J. R. Holland and K. S. Varma, *Polym. Commun.* 1996, **37**, 4629–4631.
- 20 U. Mayer, V. Gutmann and W. Gerger, *Monatshefte für Chemie*, 1978, **106**, 1235–1257.
- 21 M. Santi, D. M. C. Ould, J. Wenz, Y. Soltani, R. L. Melen and T. Wirth, *Angew. Chem. Int. Ed.*, 2019, **58**, 7861–7865.

- 22 C. Payraastre, Y. Madaule, J. G. Wolf, T. C. Kim, M. R. Mazieres, R. Wolf and M. Sanchez, *Heteroat. Chem.*, 1992, **3**, 157–162.
- 23 K. O. Christe, D. A. Dixon, D. Mclemore, W. W. Wilson, J. A. Sheehy and J. A. Boatz, *J. Fluor. Chem.*, 2000, **101**, 151–153.
- 24 J. M. Slattery and S. Hussein, *Dalton Trans.*, 2012, **41**, 1808–1815.
- 25 Ł. M. Mentel and E. J. Baerends, *J. Chem. Theory Comput.*, 2014, **10**, 252–267.
- 26 J. P. Green, S. J. Cryer, J. Marafie, A. J. P. White and M. Heeney, *Organometallics*, 2017, **36**, 2632–2636.
- 27 Y. Matano, Y. Motegi, S. Kawatsu and Y. Kimura, *J. Org. Chem.* 2015, **80**, 5944–5950.
- 28 M. Matsumura, M. Yamada, A. Muranaka, M. Kanai, N. Kakusawa, D. Hashizume, M. Uchiyama and S. Yasuike, *Beilstein J. Org. Chem.* 2017, **13**, 2304–2309.
- 29 Y. Koyanagi, Y. Kimura and Y. Matano, *Dalton Trans.*, 2016, **45**, 2190–2200.
- 30 T. Sanji, K. Shiraishi and M. Tanaka, *Org. Lett.*, 2007, **9**, 3611–3614.
- 31 M. Ishidoshiro, H. Imoto, S. Tanaka and K. Naka, *Dalton Trans.*, 2016, **45**, 8717–8723.
- 32 M. Ishidoshiro Y. Matsumura, H. Imoto, Y. Irie, T. Kato, S. Watase, K. Matsukawa, S. Inagi, I. Tomita and K. Naka, *Org. Lett.*, 2015, **17**, 4854–4857.
- 33 B. Mennucci, *WIREs Computational Molecular Science*, 2012, **2**, 386–404.
- 34 O. Puntigam, I. Hajdók, M. Nieger, M. Niemeyer, S. Strobel and D. Gudat, *Z. Anorg. Allg. Chem.*, 2011, **637**, 988–994.
- 35 D. Förster, H. Dilger, F. Ehret, M. Nieger and D. Gudat, *Eur. J. Inorg. Chem.*, 2012, 3989–3994.
- 36 O. Puntigam, D. Förster, N. A. Giffin, S. Burck, J. Bender, F. Ehret, A. D. Hendsbee, M. Nieger, J. D. Masuda and D. Gudat, *Eur. J. Inorg. Chem.*, 2013, 2041–2050.
- 37 N. A. Gi, A. D. Hendsbee, T. L. Roemmele, M. D. Lumsden, C. C. Pye and J. D. Masuda, *Inorg. Chem.*, 2012, **51**, 11837–11850.
- 38 V. Naseri, R. Edge, R. J. Less, E. J. L. Mcinnes, K. Mu, J. M. Rawson and D. S. Wright, *Chem. Commun.*, 2009, 1691–1693.
- 39 F. Neese, Wiley Interdisciplinary Reviews. *Computational Molecular Science*, 2012, **2**, 73–78.
- 40 The Cambridge Structural Database. C. R. Groom, I. J. Bruno, M. P. Lightfoot and S. C. Ward, *Acta Cryst.*, **B72**, 2016, 171–179

Chapter 4: Aldehyde Reduction Catalysis Using Dithia- and Diaza-Derived Phosphole and Arsole Complexes

Chapter 4.1 Hydroboration of Aldehydes Using Benzo-Fused Dithiarsoles and Diazarsoles

4.1.1 Pre-catalyst synthesis and NMR spectroscopy characterisation

To probe the reactivity of the arsenic complexes described in this thesis, the dithiarsole and dithiarsenium compounds **3** and **14a** as well as the diazarsole and diazarsenium complexes **7**, **16a** and **16c** were used as pre-catalysts for the hydroboration reduction of aldehydes (Figure 4.1).^{1,2} These compounds were all prepared as previously discussed, *vide supra*. The use of the diazarsenium triflate (**16c**) would be particularly interesting to use as the phosphorus analogue, diazaphosphenium **15c** which we first reported, was used previously by the group of Kinjo to hydroborate pyridines with pinacolborane (HBpin). Thus, one of the objectives with this catalytic study was to compare how the diazarsenium triflate would fare against the diazaphosphenium triflate.

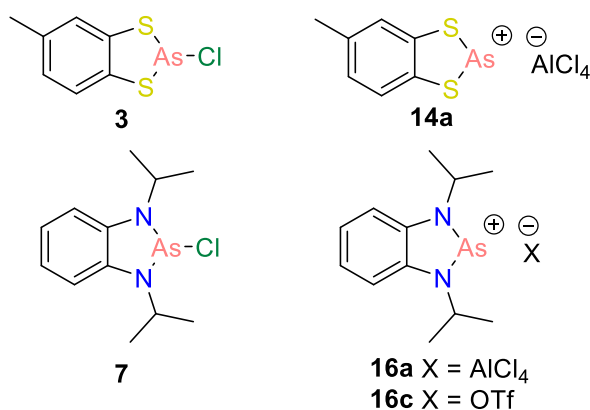
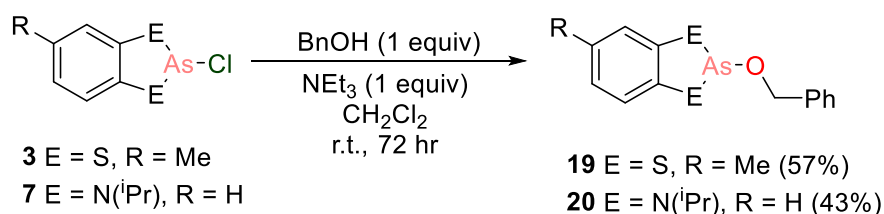


Figure 4.1: Range of arsenic compounds from Chapters 2 and 3 used as pre-catalysts.

A literature search into related reduction catalysis showed that the use of an alkoxy-derived co-ligand was advantageous. This is highlighted by the groups of Kinjo, Speed and Cramer who have used the very closely related diazaphospholene species with a benzyloxy (Bn), neopentyloxy (Np) or methoxy co-ligand for hydroboration chemistry with the reductant HBpin.³⁻⁷ It should be noted that much of this catalysis is recent and was undertaken during the time of this thesis. Given this it was decided to synthesise both dithiarsole and diazarsole complexes that had an alkoxy-derived co-ligand that could also be used as a pre-catalyst for reduction. The dithiarsole **3** and diazarsole **7** were both added to one equivalent of benzyl alcohol (BnOH) and triethylamine in CH_2Cl_2 and left to stir at ambient temperature for 72 hours. After this the solvent was removed *in vacuo* and toluene was added, which reduced the solubility of the ammonium salt by-product. Filtering the mixture *via* a Celite plug and

further solvent removal and drying produced the products 2-(benzyloxy)-5-methylbenzo-1,3,2-dithiarsole (**19**) and 2-(benzyloxy)-1,3-diisopropyl-1,3,2-diazarsole (**20**) as oils in moderate yields of 57% and 43% respectively (Scheme 4.1).⁸ **19** and **20** are herein referred to as benzyloxy-dithiarsole and benzyloxy-diazarsole accordingly. The yields of both **19** and **20** are appreciably lower than their precursor dithiarsole and diazarsole complexes and the majority of the compounds so far discussed in this thesis. Predominantly this is due to the quantity of ammonium salt produced, which requires a large volume of toluene to recover the desired product from the crude mixture during the filtering process. A greater volume of toluene solvent results in a higher yield, as more product is recovered from the crude mixture. On the other hand, this increased usage of toluene means much more time is required to remove the solvent, which due to its relatively high boiling point can be expensive with respect to time.



Scheme 4.1: Synthesis of arsenic pre-catalysts containing a benzyloxy group.

¹H NMR spectroscopy proved useful for **19** and **20**. For **19** the ¹H NMR spectrum showed the expected aromatic signals, which integrated collectively to eight, but more informatively a singlet centred at $\delta = 4.34$ ppm was observed. This singlet, which integrated to two, corresponds to the $-\text{CH}_2$ group of the benzyloxy co-ligand and gave strong evidence for the formation of **19**. The methyl group from the toluene backbone has a chemical shift of $\delta = 2.36$ ppm. For **20** similar observations were seen with the aromatic signals, but more interestingly the isopropyl groups that were chemically equivalent in **7** are no longer in **20**, with chemical shifts of $\delta = 1.54$ and 1.52 ppm respectively (Figure 4.2). Problematically the $-\text{CH}_2$ group of the benzyloxy moiety has a chemical shift of $\delta = 4.15$ ppm, which overlaps with the septet corresponding to the $-\text{CH}$ group of the isopropyl group. Nevertheless, both the $-\text{CH}_2$ and $-\text{CH}$ groups could be identified and again the presence of the former from the benzyloxy moiety helped confirm the identity of **20**.

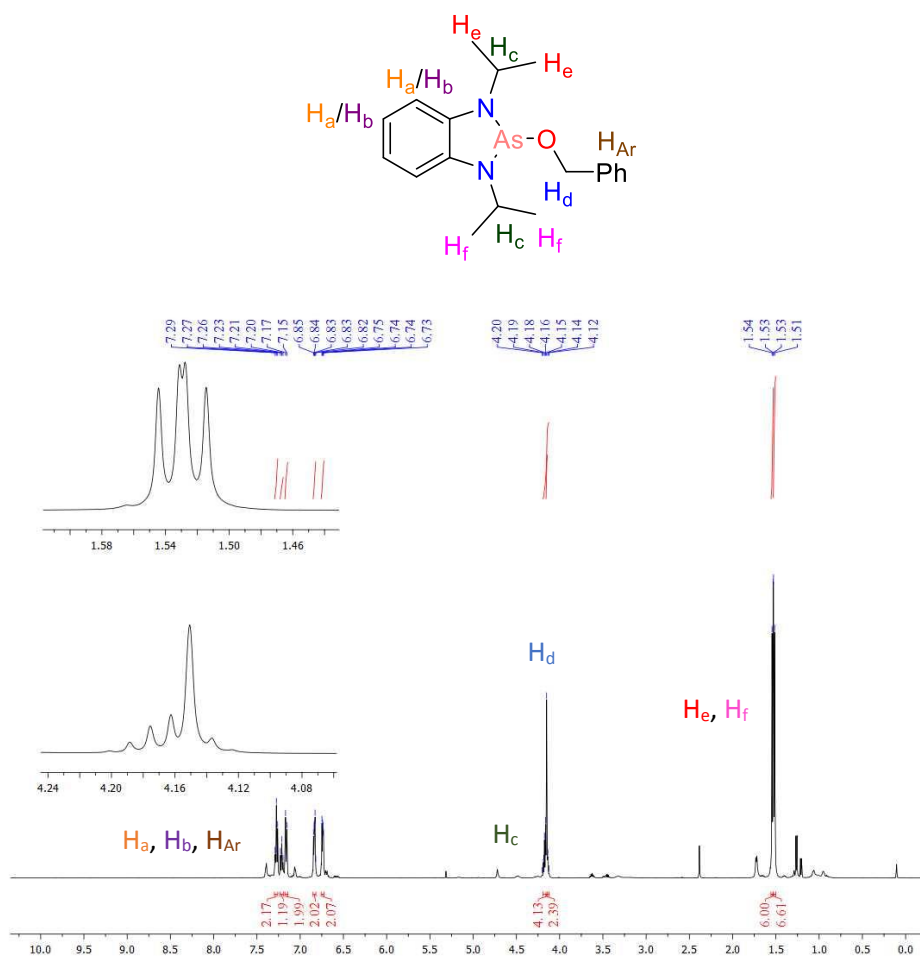


Figure 4.2: ¹H NMR spectrum (500 MHz, CDCl₃, 295 K) of the diazarsole pre-catalyst **20**.

4.1.2 Solid-state structural analysis of 2-(benzyloxy)-5-methylbenzo-1,3,2-dithiarsole and 2-(benzyloxy)-1,3-diisopropyl-1,3,2-diazarsole

¹H NMR spectroscopy proved useful in characterising the benzyloxy-dithiarsole and benzyloxy-diazarsole, but NMR spectroscopy alone was not conclusive. Although high resolution mass spectrometry gave molecular ion peaks fitting those of the expected products, to get further evidence of the formation of **19** and **20**, single crystals suitable for X-ray diffraction were grown. Again, these were grown from a saturated solution of CH₂Cl₂ with a few drops of pentane added and cooled to -40 °C. The resulting structure solution and refinement revealed both **19** and **20** crystallise in the monoclinic space group *P2₁/c*, with one molecule in the asymmetric unit for **19** and two for **20** (Figure 4.3). This increases to four and eight molecules in the unit cell for the former and latter. The solid-state structures both showed the expected connectivity of the pre-catalysts benzyloxy-dithiarsole and benzyloxy-diazarsole, with the exocyclic chloride in **3** and **7** substituted for the benzyloxy group. In **3** the S(1)–As(1)–Cl(1) and S(2)–As(1)–Cl(1) bond angles for the exocyclic chloride co-ligand measure 99.619(18)° and 99.863(18)° respectively. The corresponding

S(1)–As(1)–O(1) and S(2)–As(1)–O(1) bond angles are marginally expanded in **19**, measuring 102.31(8)° and 102.74(7)° respectively. On the other hand, for **20** no expansion in this bond angle is seen, with the N–As–Cl and N–As–O bond angles roughly comparable. In **7** the N(1)–As(1)–Cl(1) bond angle is 102.53(12)° and the N(2)–As(1)–Cl(1) bond angle 101.45(11)°, whereas the N–As–O bond angle ranges from 100.89(7)° to 102.68(7)°.

The characteristic fold angle about the S⋯S vector resulting from the envelope-type geometry in the dithiarsole ring is preserved in **19**, albeit it is significantly reduced when compared to precursor **3** (19.44(8)–21.51(8) in **3β** and 9.66(9)° in **19**). For the two benzyloxy-diazarsole molecules in the asymmetric unit of **20** the fold angles about the N⋯N vector are 4.95(11)° and 4.94(11)°, which is a small but not significant decrease when compared to the fold angle in precursor **7** (6.4(2)°). The As(1)–O(1) bond length in **19** were found to be 1.789(2) Å, whereas in **20** they are 1.8196(16) Å and 1.8241(15) Å for the two molecules in the asymmetric unit (Table 4.1). The As(1)–O(1)–C(7) interior bond angle measures 123.1(2) in **19**, which is comparable to the As(1)–O(1)–C(13) interior bond angle present in **20**, which is 119.06(12)° and 120.79(12)° for the two crystallographically independent molecules. When looking at the metrics of the dithia pnictole ring, the As–S bond lengths in **19** are 2.2285(8) Å and 2.2325(9) Å, which shows slight lengthening when contrasted to **3β**. For the diaza pnictole ring in **20**, the As–S bond lengths range from 1.8355(17) to 1.8389(17), which again shows elongation in comparison to **7**.

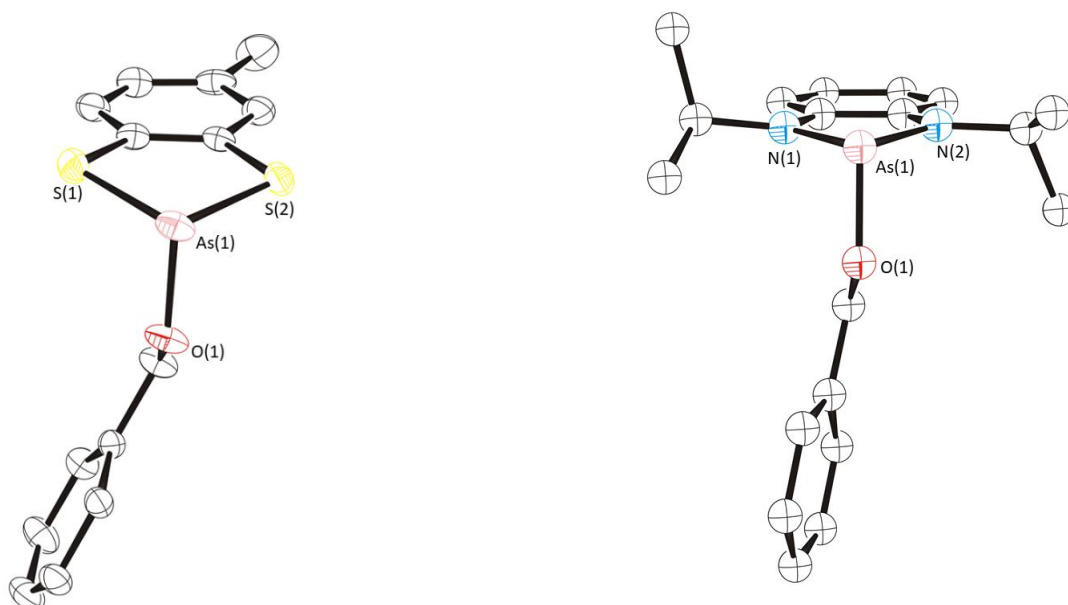


Figure 4.3: Solid-state structure of benzyloxy-dithiarsole **19** (left) and benzyloxy-diazarsole (right). Thermal ellipsoids drawn at 50% probability and H-atoms removed for clarity.

Inspection of the unit cell of the four benzyloxy-dithiarsole species shows a packing arrangement where the benzyloxy co-ligand alternates between pointing up and down along the crystallographic a axis (Figure 4.4). This positioning of the benzyloxy group allows for short contacts to exist between pairs of benzyloxy-dithiarsole complexes, with the sulfur atom from the dithia ring of one species having a close contact to the oxygen atom of another. This contact measures 3.186 Å, which is well within the combined sum of the van der Waals radii (3.32 Å). A similar packing arrangement exists for **20**, except the benzyloxy groups alternate between pointing up and down along the c axis of the unit cell. Unlike **19** analogous short contacts between the nitrogen and oxygen atoms do not exist.

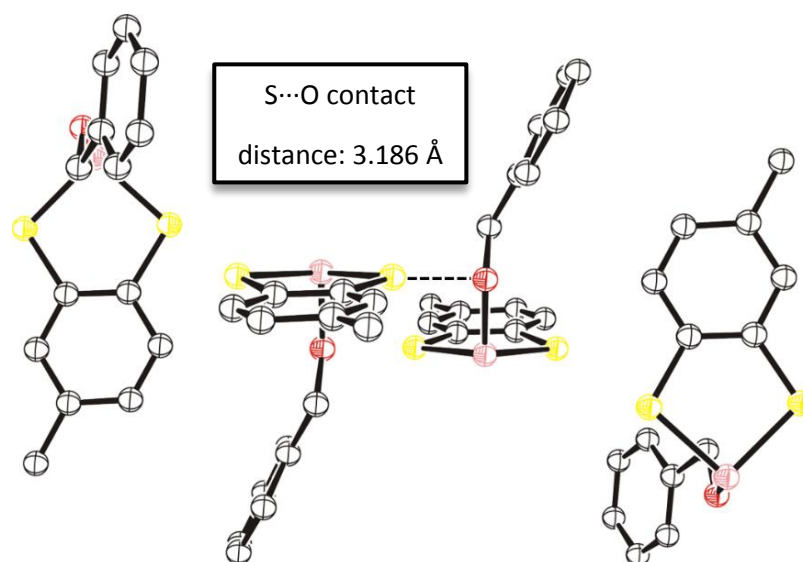
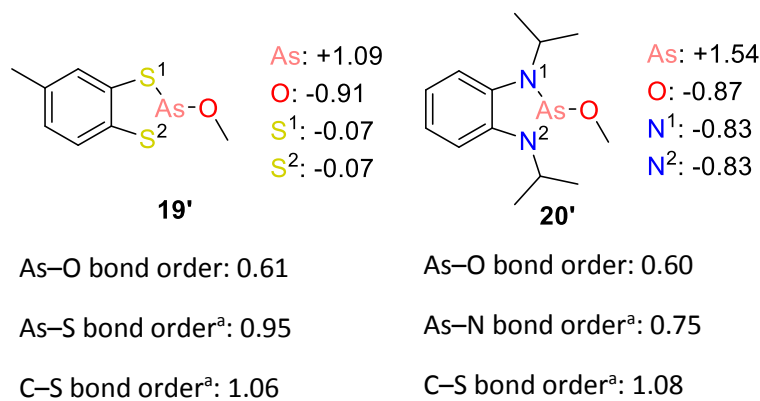


Figure 4.4: Packing arrangement in the unit cell of **19**. Pink: arsenic, yellow: sulfur, red: oxygen. Dashed lines show the close contact between the sulfur and oxygen atom. Thermal ellipsoids drawn at 50% probability and H-atoms removed for clarity.

Table 4.1: Selected bond lengths and interior bond angles for pre-catalysts **19** and **20**.

Selected bond	19 / Å (E = S)	20 / Å (E = N)
As(1)–E(1)	2.2325(9)	1.8375(18)–1.8376(17)
As(1)–E(2)	2.2285(8)	1.8355(17)–1.8389(17)
E(1)–C(1)	1.762(3)	1.394(3)–1.398(3)
E(2)–C(2)	1.762(3)	1.393(2)–1.394(2)
As(1)–O(1)	1.789(2)	1.8196(16)–1.8241(15)
Selected angle	19 / °	20 / °
E(1)–As(1)–E(1)	92.65(3)	85.73(8)–85.79(7)
As(1)–O(1)–C(7/13)	123.1(2)	119.06(12)–120.79(12)

4.1.3 Computational analysis of alkoxy derived dithiarsole and diazarsole

**Figure 4.5:** NBO analysis of analogous compounds **19'** and **20'**. All atoms treated M06-2X functional and 6-311G+(2d,p) basis set, with the exception of As, which used LANL2DZ.

^aAverage values taken.

To understand better the fundamental bonding in the benzyloxy-dithiarsole and benzyloxy-diazarsole pre-catalysts, NBO calculations were performed. This again made use of the M06-2X functional and 6-311+G(2d,p) basis set on all atoms except for the arsenic heteroatom, which again used the ECP LANL2DZ functional. Given the relatively large size of the pre-catalysts, geometry optimisation and vibrational frequency calculations made use

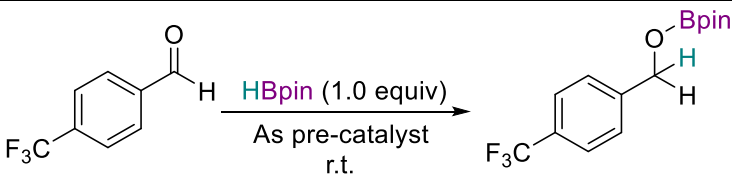
of a methoxy co-ligand as opposed to the benzyloxy group, which significantly reduced computational time. Comparisons where applicable between the solid-state structure obtained from single crystal X-ray diffraction and the computational model gave good agreement. Analysing the results from the NBO calculations showed polarisation in the As–O bond, akin to that seen in the precursors **3** and **7** with the As–Cl bond. The natural charge on the arsenic heteroatom was found to be +1.09 in **19'** and +1.54 in **20'**, whereas the natural charge on the oxygen atom is –0.91 and –0.87 for **19'** and **20'** respectively. Like the precursor compounds **3** and **7** the Wiberg As–O bond orders are low, and were found to be 0.61 and 0.60 for the former and latter accordingly. The sulfur heteroatom in **19** has an average natural charge of –0.07 and the nitrogen heteroatom in **20** has an average natural charge of –0.83. The results are summarised in Figure 4.5.

4.1.4 Homogeneous hydroboration reduction using arsenic pre-catalysts

With a wide range of arsenic containing species that could potentially act as pre-catalysts in hand, these compounds were tested in the hydroboration of aldehydes with pinacolborane (HBpin). To begin with, 4-(trifluoromethyl)-benzaldehyde was used as a test substrate as this allowed for the reaction conversion to be easily monitored *via in situ* ^{19}F NMR spectroscopy. Using 10 mol% pre-catalyst loading, one equivalent of aldehyde, one equivalent of HBpin and toluene as the solvent, the suitability and activity of the arsenic complexes was first screened (Table 4.2).

Use of the chloride precursors **3** and **7** showed poor activity for the reduction catalysis, giving just 38% and 49% conversion, respectively, after 24 hours. The benzyloxy derived pre-catalysts **19** and **20** showed an improvement on this, producing 64% product conversion after 12 hours for the former and impressively quantitative conversion after 30 minutes for the latter benzyloxy-diazarsole. Differing to this, use of the dithiarsenium and diazarsenium compounds proved less effective, despite using an array of solvents. In the case of the diazarsenium compounds **16a** and **16c**, the highest product conversion was 50% when using **16c** in CH_2Cl_2 after 24 hours. For **16a** just 28% product conversion could be achieved when using bromobenzene- d^5 ($\text{C}_6\text{D}_5\text{Br}$). Comparing this to the dithiarsenium **14a**, which proved to be highly insoluble in most solvents except $\text{C}_6\text{D}_5\text{Br}$, quantitative conversion was achieved after 12 hours. This result showed a marked difference in activity between the dithiarsenium and diazarsenium cations. Although there were a number of positive results, clearly the results just discussed revealed that the benzyloxy-diazarsole **20** was the best pre-catalyst to proceed with.

Table 4.2: Screening of arsenic pre-catalysts.



Entry	Pre-catalyst	Loading/ mol%	Solvent	Time/ hr	Conversion/ % ^a
1	None	N/A	toluene	24	<10
2	3	10	toluene	24	38
3	7	10	toluene	24	49
4	19	10	toluene	12	64
5	20	10	toluene	0.5	>95
6	14a	10	C ₆ D ₅ Br	12	>95
7	16a	10	CH ₂ Cl ₂	24	27
8	16a	10	MeCN	24	19
9	16a	10	C ₆ D ₅ Br	24	28
10	16c	10	toluene	24	48
11	16c	10	CH ₂ Cl ₂	24	50
12	16c	10	MeCN	24	10
13	16c	10	C ₆ D ₅ Br	24	15

^aConversion measured using *in situ* ¹⁹F NMR spectroscopy.

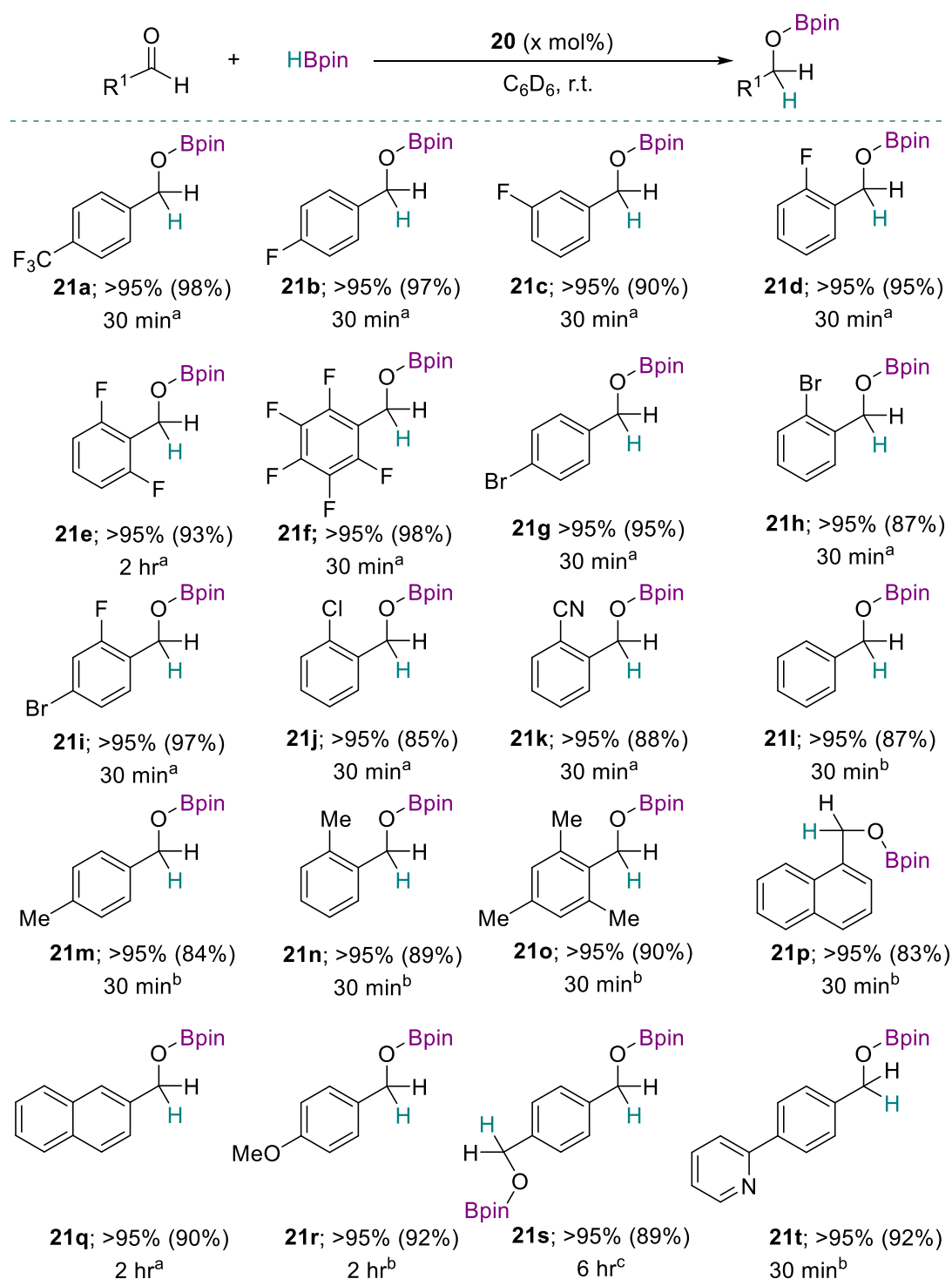
Knowing pre-catalyst **20** was the most active pre-catalyst, the reaction conditions were optimised (Table 4.3). Reducing the catalytic loading from 10 mol% to 5 mol% gave no deleterious effects, however further decreases to 2 mol% and 1 mol% gave poorer conversion, with 78% and 51% of the reduced product **21a** detected respectively by *in situ* ¹⁹F NMR spectroscopy. Proceeding with 5 mol% pre-catalyst loading, the reaction conditions were further optimised. Solvent effects were examined, using a range of coordinating, non-coordinating, polar and non-polar solvents. The catalysis using 5 mol% **20** proved effective with most solvents used, with toluene, CH₂Cl₂, CHCl₃, Et₂O, CD₃CN and C₆D₆ all affording quantitative conversion within 30 minutes. Note that the use of deuterated chloroform (CDCl₃) proved problematic for the catalysis and gave much lower conversion than CHCl₃. On the other hand, use of THF and C₆D₅Br were detrimental to the catalysis, with 41% and 58% conversion to **21a** detected after six hours. Although a number of solvents were found to be effective, for the purpose of evaluating the substrate scope C₆D₆ was

chosen as the solvent of choice. Primarily this was to allow easy *in situ* monitoring of the catalysis. This would be in combination with 5 mol% **20** pre-catalyst loading and one equivalent of both aldehyde and HBpin.

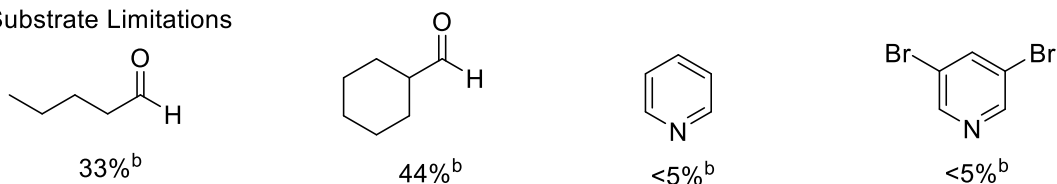
Table 4.3: Optimisation reaction conditions.

Entry	Loading/ mol%	Solvent	Time/ hr	Conversion/ % ^a
1	10	toluene	0.5	>95
2	5	toluene	0.5	>95
3	2	toluene	12	78
4	1	toluene	12	51
5	5	CH ₂ Cl ₂	0.5	>95
6	5	CHCl ₃	0.5	>95
7	5	Et ₂ O	0.5	>95
8	5	CD ₃ CN	0.5	>95
9	5	C ₆ D ₆	0.5	>95
10	5	THF	6	41
11	5	C ₆ D ₅ Br	6	58

^aConversion measured using *in situ* ¹⁹F NMR spectroscopy.



Substrate Limitations



Scheme 4.2: Hydroboration of aldehydes using pre-catalyst **20**. 0.6 ml C₆D₆ solvent, NMR yield calculated from *in situ* ¹H NMR spectrum, value in parentheses isolated yield. ^a5 mol% **20**. ^b10 mol% **20**. ^c20 mol% **20**; 2 equiv HBpin.

Using the optimised conditions, the substrate scope was expanded to evaluate the effectiveness of pre-catalyst **20** for hydroboration reduction catalysis (Scheme 4.2). Electron withdrawing aldehydes proved very effective for the catalysis, with most substrates undergoing full conversion within 30 minutes as detected by *in situ* ^1H NMR spectroscopy. 4-(trifluoromethyl)-benzaldehyde has already been demonstrated to undergo conversion to the hydroborated product **21a** within 30 minutes. On that theme the fluorinated aldehydes 4-fluorobenzaldehyde, 3-fluorobenzaldehyde, 2-fluorobenzaldehyde and 2,3,4,5,6-pentafluorobenzaldehyde were all readily converted to the products **21b–d** and **21f** respectively within 30 minutes, as shown by both ^1H and ^{19}F NMR spectroscopy. These results showed that pre-catalyst **20** is not sensitive to the substitution pattern of the substituent around the benzaldehyde moiety. The di-fluoro substituted 2,6-difluorobenzaldehyde was reduced to **21e** within two hours.

In a similar vein, other electron withdrawing substituents worked well, with the bromo-, chloro- and cyano-substituted benzaldehydes giving quantitative conversion within 30 minutes. Again, the use of 4-bromobenzaldehyde and 2-bromobenzaldehyde which smoothly produced **21g** and **21h** accordingly highlights the substitution pattern versatility of **20** as a pre-catalyst. The mixed poly-halo 4-bromo-2-fluorobenzaldehyde was an interesting substrate, but nevertheless proceeded to give full product conversion to **21i** within 30 minutes. In all cases described so far isolated yields were excellent, and generally >90%.

Having showed that electron withdrawing substituents worked well, attention turned to more electron neutral and electron donating substituents. Under the initial optimised conditions this proved problematic, with a number of substrates failing to go to quantitative conversion within 24 hours. To remedy this the temperature was increased to 70 °C, but it was soon noticed that precipitate was forming in the NMR tube, which was assumed to be pre-catalyst degradation. It was at that point decided to instead increase the pre-catalyst loading from 5 mol% to 10 mol% and re-run the electron neutral/donating substrates at ambient temperature. Benzaldehyde worked well under these conditions, giving full conversion within 30 minutes. The series of methyl substituted benzaldehydes also worked well and were all successfully converted to products **21m–o** after 30 minutes. For the conjugated aromatic naphthaldehydes, initial use of 5 mol% pre-catalyst loading led to 59% conversion of 1-naphthaldehyde after 24 hours. However, after using 10 mol% pre-catalyst loading gave quantitative conversion after just 30 minutes. Contrary to this, 2-naphthaldehyde was fully hydroborated using 5 mol% pre-catalyst after 2 hours. The

difference in performance between 1-naphthaldehyde and 2-naphthaldehyde can be explained by steric arguments.

More electron-rich aldehydes were also successfully reduced, with 4-methoxybenzaldehyde giving the hydroborated product **21r** in a 92% isolated yield after two hours using 10 mol% pre-catalyst. In the case of the bis aldehyde terephthaldehyde, where the aldehyde group is present in the 1- and 4-positions of the benzene moiety, hydroboration of both aldehyde groups was observed when using two equivalents of HBpin. 20 mol% pre-catalyst loading was used in this case (10 mol% for each aldehyde group) and a longer reaction time of six hours was required to give full conversion to **21s**, with 89% isolated yield. In addition to aromatic aldehydes, aliphatic aldehydes were probed with pre-catalyst **20**. Use of both 5 mol% and 10 mol% pre-catalyst loading was trialled, however only 33% and 44% conversion of pentanal and cyclohexanecarbaldehyde was detected after 24 hours using 10 mol% pre-catalyst loading.

Recent work by the groups of Speed and Kinjo has shown that pyridines can be reduced with HBpin using diazaphospholene⁶ and diazaphosphenium⁹ based pre-catalysts. With that pre-catalyst **20** was used in the attempted reduction of pyridine as well as the more reactive 2-chloropyridine and 3,5-dibromopyridine with HBpin. All these substrates showed little consumption after 24 hours using 10 mol% pre-catalyst loading at ambient temperature. In fact 10 mol% of the diazarsenium triflate **16c** was used as a pre-catalyst at room temperature to attempt the hydroboration of pyridine, analogous to the work of Kinjo using a diazaphosphenium.⁹ In this case again no conversion to the hydroborated product was observed. The lack of reactivity to pyridines was further exemplified when using the substrate 4-(2-pyridyl)benzaldehyde, which has a pyridine group in the 4-position of the benzaldehyde. In this case exclusive reduction of the aldehyde was observed, with the pyridine group remaining untouched and the product **21t** detected after 30 minutes using 10 mol% pre-catalyst. This result clearly demonstrates differences in the reactivity and selectivity between the use of phosphorus and arsenic based catalysts. This idea is explored further in this chapter; *vide infra*.

During the course of the substrate scope, additional functional groups were also trialled. The ketones acetophenone, 4'-fluoroacetophenone, 4'-methoxyacetophenone, 4'-nitroacetophenone and benzophenone were used, but using the optimised conditions used for the aldehydes minimal conversion was largely observed by both ^1H NMR and ^{11}B NMR spectroscopy. The exception was the case of 4'-nitroacetophenone, where full consumption of HBpin occurred, however the ^1H NMR spectrum did not show the characteristic signal expected at approximately 5.0 ppm, corresponding to the proton delivered from HBpin to give the tertiary carbon centre. It is unknown what the product from this reaction was. In addition to ketones, imines were also attempted. The substrate scope made use of (*E*)-*N*,1-diphenylethan-1-imine, (*E*)-1-(4-fluorophenyl)-*N*-phenylethan-1-imine, (*E*)-1-(4-nitrophenyl)-*N*-phenylethan-1-imine, (*E*)-1-(4-methoxyphenyl)-*N*-phenylethan-1-imine and (*E*)-*N*-(perfluorophenyl)-1-phenylethan-1-imine, but in all cases although some consumption of HBpin was detected by ^{11}B NMR spectroscopy, additional resonances that did not match up to the expected reduced products were seen in the ^1H NMR spectrum. As a result, it was decided not to pursue with the hydroboration of imines with HBpin. These attempted substrates are shown below in Figure 4.6.

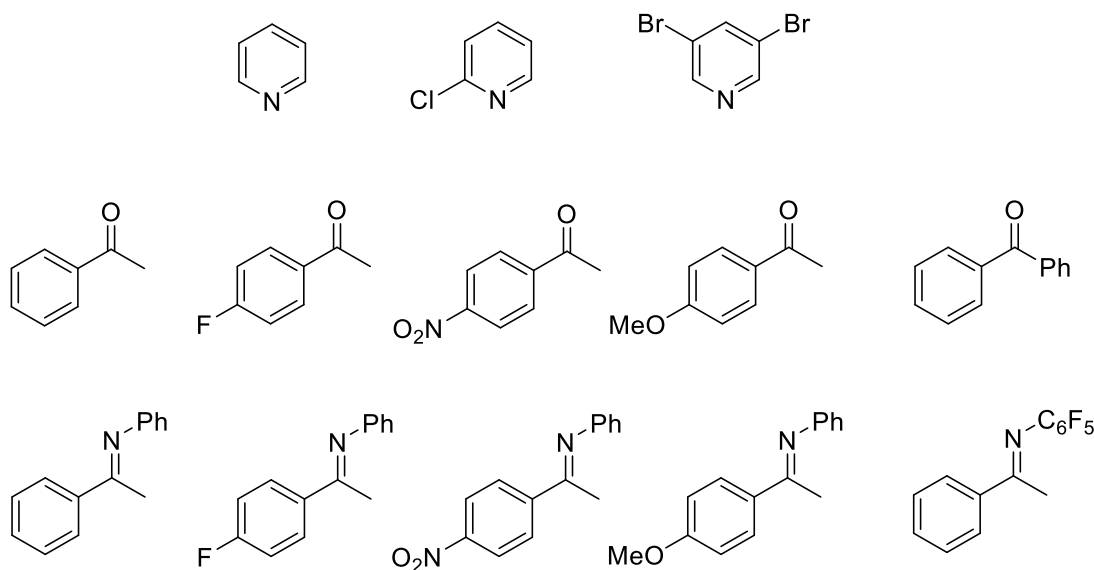
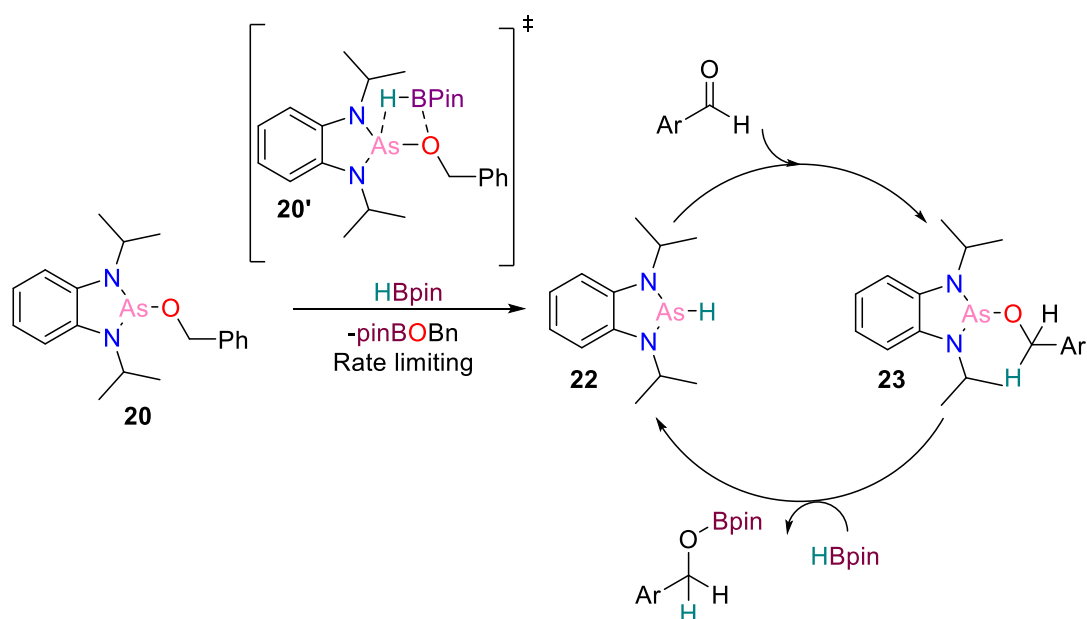


Figure 4.6: Pyridine, ketone and imine substrate limitations in the hydroboration catalysis with pre-catalyst **20**.

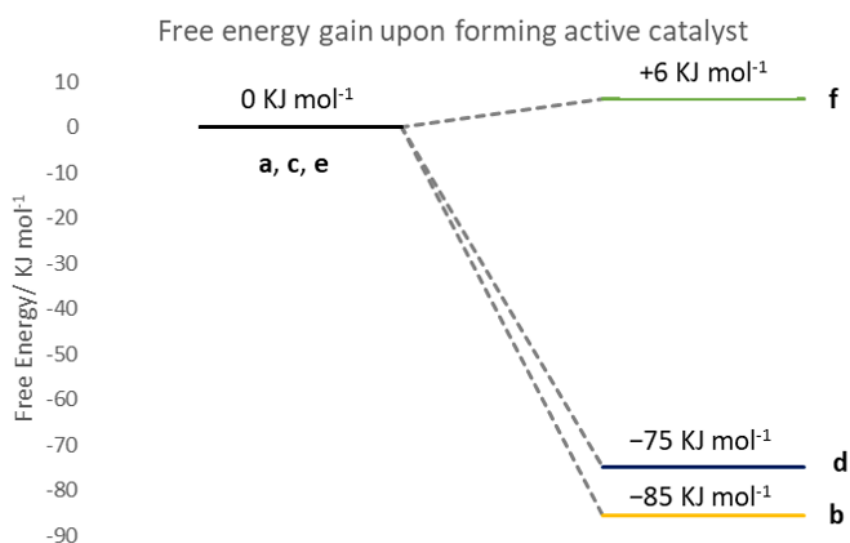
Having evaluated the effectiveness of **20** as a pre-catalyst, mechanistic insight was investigated. This was first done by reacting **20** with stoichiometric HBpin, which gave a clear colour change from orange to deep red within five minutes. Analysis of the ^1H NMR spectrum taken after 15 minutes in C_6D_6 solvent showed a clear downfield shift in the CH_2 protons of the benzyl group, from $\delta = 4.03$ to 4.77 ppm. Meanwhile the ^{11}B NMR spectrum displayed loss of the doublet resonance at $\delta = 28.4$ ppm and formation of a new singlet signal at $\delta = 22.8$ ppm. These two spectroscopic observations are consistent with the loss of HBpin and the formation of 2-(benzyloxy)-4,4,5,5-tetramethyl-1,3,2-dioxaborolane (BnO–Bpin). In addition to the formation of BnO–Bpin, the arsenic hydride species 1,3-diisopropyl-2,3-dihydro-1H-benzo-1,3,2-diazarsole (**22**) is synthesised by the addition of HBpin to **20**. Although the hydridic proton in **22** was not seen in the ^1H NMR spectrum, the formation of **22** was detected HRMS. The arsenic hydride complex **22** is believed to be the active catalyst and the synthesis proceeds *via* a σ -bond metathesis step from pre-catalyst **20** and HBpin; this step is known from the work of Kinjo to be rate limiting.³ From here the active catalyst **22** is postulated to react with the aldehyde substrate to give the second catalytic intermediate **23**. This was confirmed by the stoichiometric 1:1:1 addition of pre-catalyst **20** to HBpin and the aldehyde 4-(trifluoromethyl)benzaldehyde, where intermediate **23** was detected again by HRMS and BnO–Bpin was seen by both ^1H and ^{19}F NMR spectroscopy. At this point HBpin reacts with the second intermediate **23** to give the desired hydroborated aldehyde and reform the first catalytic intermediate **22**, and catalytic turnover occurs (Scheme 4.3).



Scheme 4.3: Proposed catalytic cycle for the hydroboration of aldehydes using benzyloxy-diazarsole (**20**) as a pre-catalyst.

With the catalytic cycle established, the reactivity difference between pre-catalysts **19** and **20** were investigated, as from the optimisation studies use of **19** as the pre-catalyst only gave 64% after 12 hours when using toluene solvent, whereas pre-catalyst **20** gave quantitative conversion after just 30 minutes. Knowing that the σ -bond metathesis step was rate limiting,³ **19** was added to stoichiometric HBpin and the reaction was monitored by *in situ* ^1H and ^{11}B NMR spectroscopy. This spectroscopic analysis revealed a much slower reaction compared to using **20**, where ^{11}B NMR spectroscopy showed it took six hours for loss of the doublet signal corresponding to HBpin and formation of BnO–Bpin. Therefore, it can be concluded that formation of the active catalyst is at least partly responsible for the difference in catalytic performance of **19** and **20**.

Interestingly, when looking at the formation of the active catalyst from the pre-catalyst by computational methods, a large thermodynamic free energy gain is seen. This free energy gain for the diazarsole active catalyst **22** along with BnO–Bpin was found to be 75 kJ mol^{-1} lower in energy than the pre-catalyst **20** and HBpin, whereas for the analogous dithiarsole case an 85 kJ mol^{-1} decrease occurs. This therefore suggests that for the benzyloxy-dithiarsole it is the slow kinetic rate in forming the active catalyst, as demonstrated above, and not thermodynamics that results in its poor ability to act as a pre-catalyst. Further to this, the diazarsole **7** was also investigated given it was also a very poor pre-catalyst. In this case going from **7** to the active catalyst **22** gave a small free energy increase of 6 kJ mol^{-1} , suggesting that this reaction is not particularly favourable. The results of this are summarised in Figure 4.7.



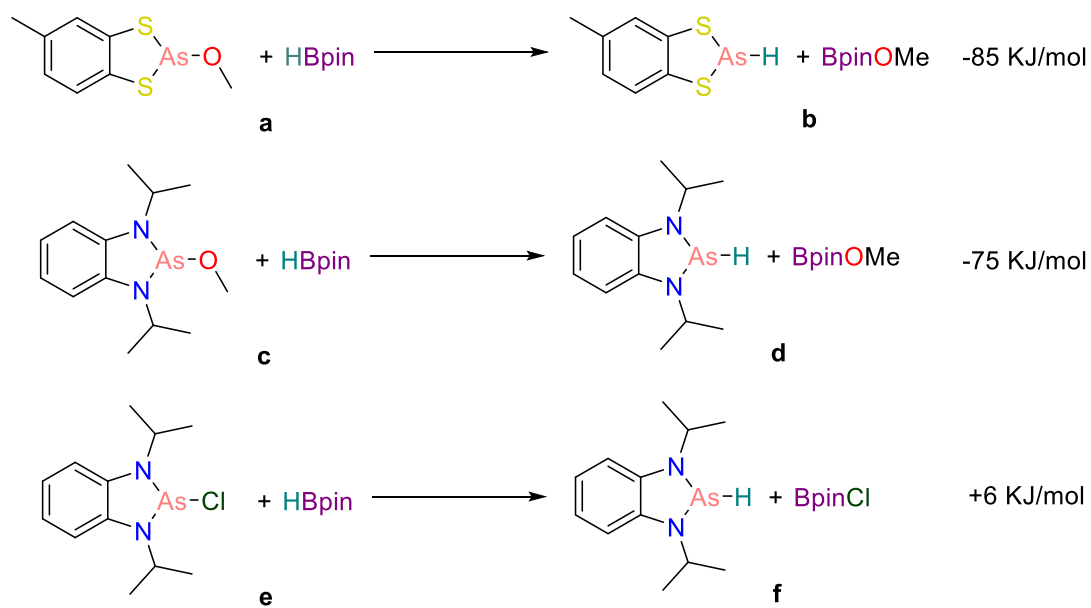


Figure 4.7: Free energy graph going from pre-catalyst and HBpin to active catalyst and BpinOMe or BpinCl. All atoms treated with M06-2X functional and 6-311G+(2d,p) basis set, with the exception of As, which used LANL2DZ. ^aAverage values taken.

Chapter 4.2 Hydroboration of Aldehydes Using Benzo-Fused Dithiaphospholes and Diazaphospholes

4.2.1 Pre-catalyst synthesis and NMR spectroscopy characterisation

Knowing that the diazarsole **20** was an effective pre-catalyst for hydroboration reduction catalysis, the question of how these arsenic derived pre-catalysts compare with their less toxic phosphorus counterparts arose. Some insight could immediately be given to this from the studies reported by Kinjo, Speed and Cramer when using the closely related diazaphospholene complexes as pre-catalysts,³⁻⁷ which show that they are highly active for this catalysis, but nevertheless these are not true comparisons to the arsenic complexes used above. With that, a series of dithiaphosphole and dithiaphosphenium complexes were used in the hydroboration reduction of aldehydes with HBpin, with emphasis focussed on how they compared to their arsenic analogues.¹⁰

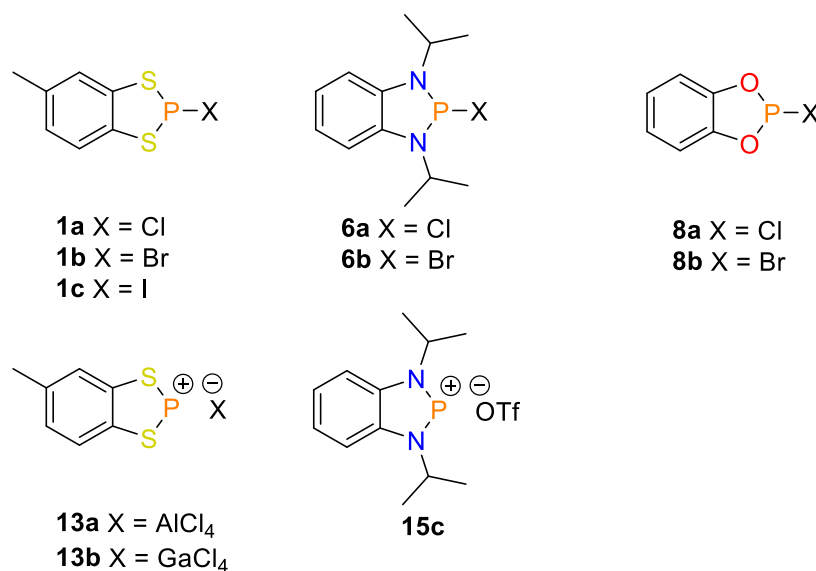
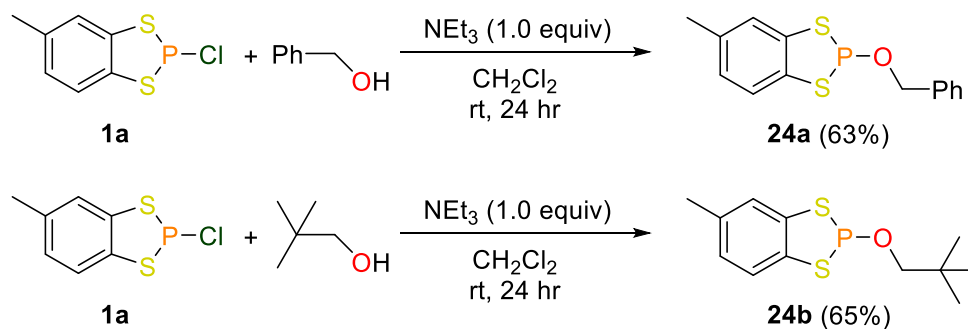


Figure 4.8: Range of phosphorus compounds from Chapters 2 and 3 used as pre-catalysts.

For this catalysis, compounds **1a–1c**, **6a**, **6b**, **8a**, **8b**, **13a**, **13b** and **15c** were used as pre-catalysts (Figure 4.8).^{1,2,10} As was seen in the diazarsole case, the use of a benzyloxy co-ligand was very effective for the catalysis, so this was emulated for the phosphole catalysis. To that end, benzyl alcohol or neopentyl alcohol was added to dithiaphosphole **1a**, which was dissolved in CH₂Cl₂ solvent, and stoichiometric triethylamine was added. This solution was left to stir at ambient temperature for 24 hours, after which the solvent was removed *in vacuo* and toluene was added. This solution was filtered to remove the ammonium salt by-product and the resulting solvent was removed *in vacuo*. Washes with pentane and further drying gave the products 2-(benzyloxy)-5-methylbenzo-1,3,2-dithiaphosphole (**24a**)

and 5-methyl-2-(neopentyloxy)benzo-1,3,2-dithiaphosphole (**24b**) as yellow oils in moderate yields of 63% and 65% respectively (Scheme 4.4). This is shortened to benzyloxy-dithiaphosphole and neopentyloxy-dithiaphosphole respectively. As was discussed with the synthesis of the benzyloxy-dithiarsole and benzyloxy-diazarsole, the moderate yields are attributed to the filtering of the ammonium salt by-product.



Scheme 4.4: Synthesis of benzyloxy-dithiaphosphole and neopentyloxy-dithiaphosphole pre-catalysts.

Confirmation of the synthesis of both **24a** and **24b** was first determined by ³¹P NMR spectroscopy, which revealed upfield shifts compared to **1a** of $\delta = 124.5$ and 123.6 ppm for **24a** and **24b** respectively (*cf.* **1a** $\delta = 160.4$ ppm). These signals were triplets, with ³J_{PH} coupling constant values of 6.6 Hz and 6.1 Hz for **24a** and **24b** respectively. The coupling is due to the presence of the adjoining benzyloxy/neopentyloxy group; *vide infra*. For **24a** the ¹H NMR spectrum showed the expected signals already discussed for the toluene backbone, but in addition a doublet resonance with a ³J_{PH} = 6.5 Hz coupling constant centred at $\delta = 4.22$ ppm was observed for the -CH₂ group of the benzyloxy co-ligand. The aromatic signals from the phenyl group were also seen but overlapped with the signals from the toluene backbone. In the case of compound **24b**, the ¹H NMR spectrum again showed a doublet resonance at $\delta = 2.85$ ppm with a coupling constant of ³J_{PH} = 6.1 Hz. Note the more upfield position of the -CH₂ moiety in **24a** than **24b**. Furthermore, the tert-butyl group on the neopentyloxy co-ligand has a distinctive singlet resonance centred at $\delta = 0.77$ ppm. The ³¹P NMR and ¹H NMR spectrum of **24a** are shown below in Figures 4.9 and 4.10.

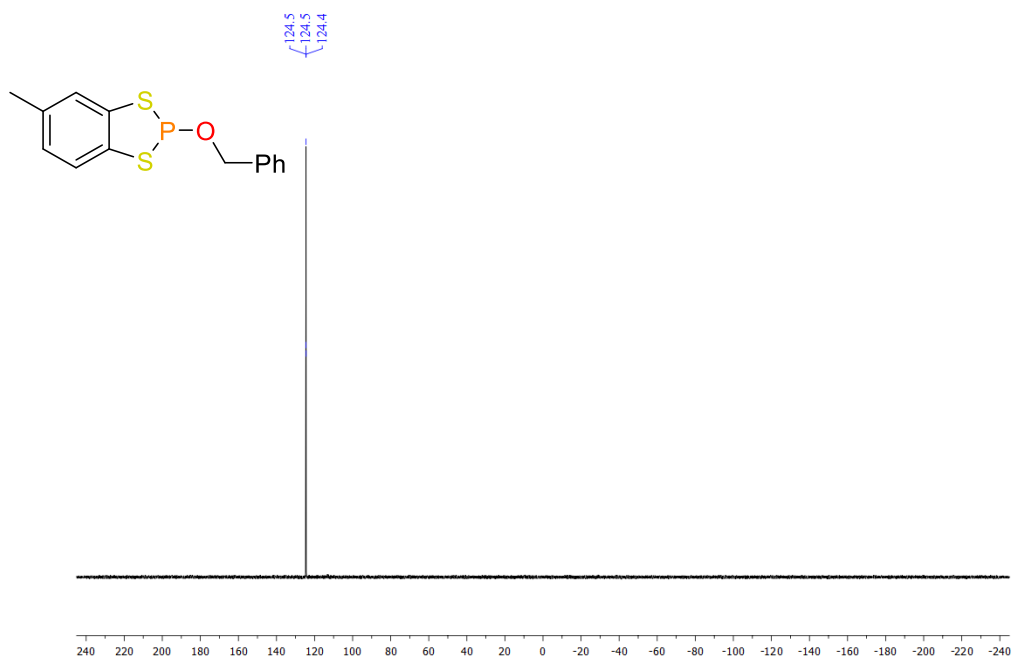


Figure 4.9: ^{31}P NMR spectrum (162 MHz, CDCl_3 , 295 K) of the benzyloxy-dithiaphosphole pre-catalyst **24a**.

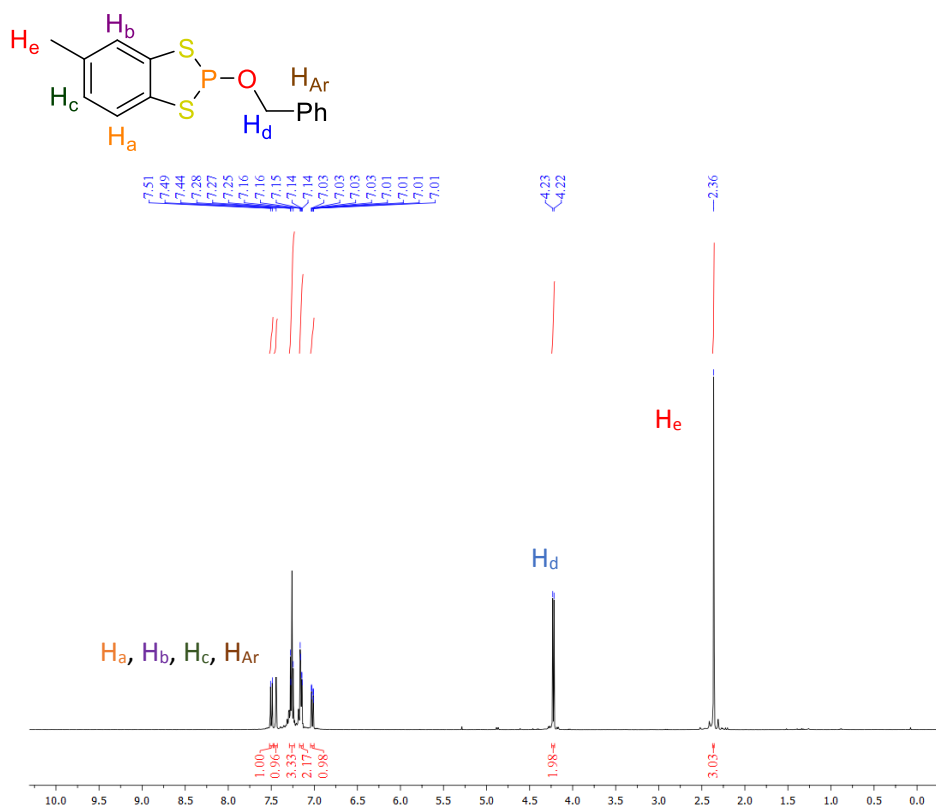
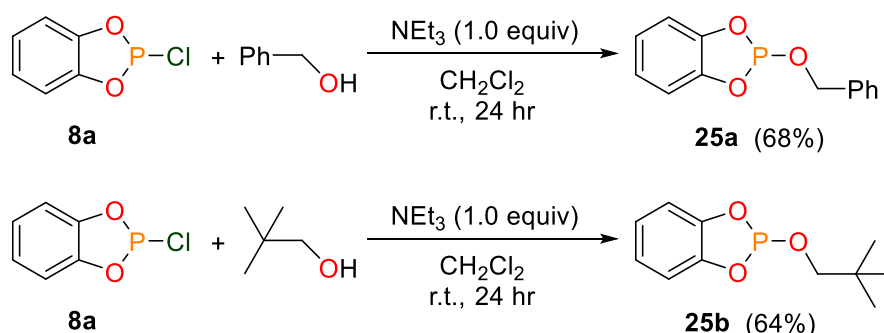


Figure 4.10: ^1H NMR spectrum (400 MHz, CDCl_3 , 295 K) of the benzyloxy-dithiaphosphole pre-catalyst **24a**.

This synthetic procedure was extended to synthesise the alkoxy-derived diazaphosphole and dioxaphosphole species. In the case of the former, addition of the starting precursor **6a** with benzyl alcohol and triethylamine gave the desired product, with the ^{31}P NMR spectrum showing a singlet at $\delta = 95.3$ ppm. However, a much smaller intensity doublet signal was also observed centred at $\delta = 6.0$ ppm ($^1J_{\text{PH}} = 643$ Hz), which is believed to arise due to partial hydrolysis of the product. This is despite multiple attempts with the use of dried solvents and starting material. The reaction of **6a** with neopentyl alcohol and triethylamine had a similar fate and the *in situ* $^{31}\text{P}\{^1\text{H}\}$ NMR spectrum showed four species were present, with signals at $\delta = 147.0, 138.3, 95.3$ and 6.0 ppm (Figure 4.11). The signal at $\delta = 147.0$ ppm could be assigned to the starting product **6a**, $\delta = 95.3$ ppm the desired product and $\delta = 6.0$ ppm partial hydrolysis. The identity of the product with a moderately intense signal at $\delta = 138.3$ ppm remains unknown. Given the inability to produce pure complexes of the diazaphosphole with an alkoxy derived co-ligand it was decided not to pursue these further.

On the other hand, for the dioxaphosphole the synthesis proceeded smoothly as described above and the products 2-(benzyloxy)benzo-1,3,2-dioxaphosphole (**25a**) and 2-(neopentyloxy)benzo-1,3,2-dioxaphosphole (**25b**) were obtained as dark yellow/orange coloured oils in moderate yields of 68% and 64% respectively (Scheme 4.5). These are abbreviated to benzyloxy-dioxaphosphole and neopentyloxy-dioxaphosphole for compounds **25a** and **25b**. Analysis of the multinuclear NMR spectra for **25a** and **25b** revealed similar observations to the benzyloxy-dithiaphosphole and neopentyloxy-dithiaphosphole complexes, with the $^{31}\text{P}\{^1\text{H}\}$ NMR spectra again showing upfield signals at $\delta = 126.9$ and 127.4 ppm accordingly. The ^1H NMR spectra of **25a** and **25b** showed the coordination of the alkoxy-derived co-ligand and is similar to **24a** and **24b** already discussed.



Scheme 4.5: Synthesis of benzyloxy-dioxaphosphole and neopentyloxy-dioxaphosphole pre-catalysts.

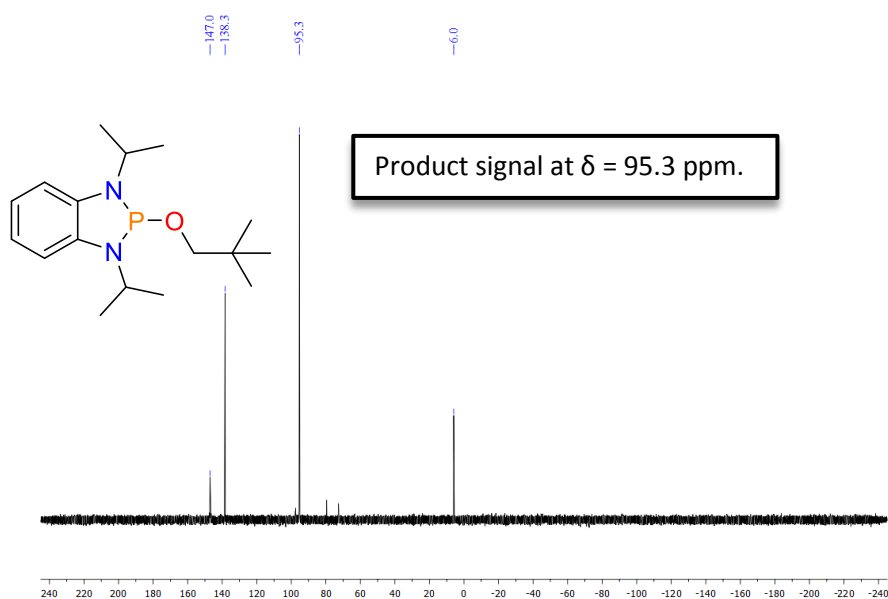


Figure 4.11: *In situ* $^{31}\text{P}\{^1\text{H}\}$ NMR spectrum (162 MHz, CDCl_3 , 295 K) of the neopentyloxy-diazaphosphole pre-catalyst reaction.

4.2.2 Solid-state structural analysis of 2-(benzyloxy)-5-methylbenzo-1,3,2-dithiaphosphole
 In addition to multinuclear NMR characterisation, for the benzyloxy-dithiaphosphole **24a** the solid-state structure was determined (Figure 4.12). Crystals suitable for single-crystal X-ray diffraction were grown by slow vapour diffusion from a CH_2Cl_2 solution. It should be noted that multiple attempts were undertaken to crystallise **24a** and this proved the most effective way. Problems soon arose with the quality of the single crystals as the diffraction pattern on the diffractometer proved weak (given the relative molecular weight of the phosphorus atom present) and potentially twinned. Nevertheless, a data set was collected which allowed for structure solution and refinement.

During the structure solution and refinement process the toluene ring backbone showed significant disorder (arisen due to the relatively poor data set due to problematic crystal growth), with bond lengths and angles that meant that the ring was non-planar and non-hexagonal. To remedy this, the geometrical constraint AFIX 66 was used, which forces the six carbon atoms to form a planar regular hexagon. The thermal ellipsoids showed slight elongation on the toluene ring but not so severe that modelling by-parts was required, with the exception of the methyl group. In this case no suggestion of a second site appeared in the .lst file and no obvious Q peak was present in the difference Fourier map that would be suitable, thus it was again decided not to model this disordered thermal ellipsoid. The end

result of the structure refinement gave a relatively high $R_1 = 11\%$ and $wR_2 = 26\%$, but nevertheless showed the connectivity of the benzyloxy-dithiaphosphole.

24a crystallises in the monoclinic space group $P2_1/c$ with one molecule in the asymmetric unit; increasing to four molecules in the unit cell. Although the structure shows significant disorder, metrics can still be measured from the dithia pnictole ring as the disorder is localised on the toluene backbone. The characteristic envelope geometry is still preserved in **24a**, with a fold angle about the $S\cdots S$ vector of $21.16(15)^\circ$, which is appreciably lower than seen in the precursor **1a** ($26.07(6)^\circ$). The P–S bond lengths are marginally longer than in **1a**, with metrics of $2.117(3)$ Å for P(1)–S(1) and $2.110(3)$ Å for P(1)–S(2). A decrease in the S–P–S interior bond angle compared to **1a** accompanies the slight elongation in the P–S bond length, with the S(1)–P(1)–S(2) interior bond angle measuring 94.18° in **24a**, whereas in **1a** this bond angle is $95.43(3)^\circ$ (Table 4.4). Given the disorder on the toluene backbone no further parameters were measured. When looking at the unit cell, no significant close contacts were found to exist in the packing structure of **24a**.

Table 4.4: Selected bond lengths and interior bond angles for pre-catalyst **24a**.

Selected bond	24a / Å
P(1)–S(1)	2.117(3)
P(1)–S(2)	2.110(3)
S(1)–C(1)	1.744(5)
S(2)–C(2)	1.781(5)
P(1)–O(1)	1.618(4)
Selected angle	24a / °
S(1)–P(1)–S(2)	94.18(10)
P(1)–O(1)–C(8)	123.0(4)

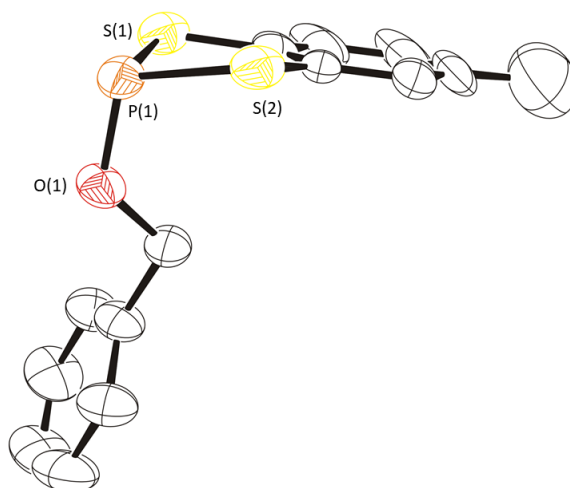


Figure 4.12: Solid-state structure of benzyloxy-dithiaphosphole **24a**. Thermal ellipsoids drawn at 50% probability and H-atoms removed for clarity.

4.2.3 Computational analysis of alkoxy derived dithiaphosphole and dioxaphosphole

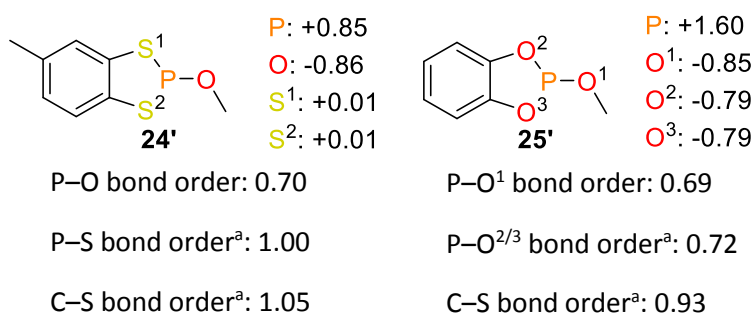


Figure 4.13: NBO analysis of analogous compounds **24'** and **25'**. All atoms treated with M06-2X functional and 6-311G+(2d,p) basis set. ^aAverage values taken.

As was performed for the arsenic analogues, NBO calculations were undertaken for the alkoxy-derived dithiaphosphole and dioxaphosphole pre-catalysts, using the functional M06-2X and 6-311+G(2d,p) basis set. Again, due to the relatively large size of these compounds geometry optimisation and vibrational frequency calculations made use of a methoxy co-ligand as opposed to the benzyloxy and neopentyloxy groups (Figure 4.13). Like the arsenic complexes **19'** and **20'**, the P–O bond of the alkoxy co-ligand in **24'** and **25'** was found to be highly polarised, with a Wiberg bond order in both cases of approximately 0.70. This translates to natural charges of +0.85 and +1.60 for the phosphorus heteroatom and –0.86 and –0.85 for the oxygen atom in **24'** and **25'** respectively. Indeed, the electronics in these two alkoxy-derived phospholes are very different, as the averaged natural charge on the sulfur heteroatoms in **24'** is almost neutral, whereas for the oxygen heteroatoms in the

dioxaphosphole ring in **25'** is -0.79 . This difference is further exemplified when looking at the Wiberg bond order of the P–S bond vs. the P–O bond in the respective dithiaphosphole and dioxaphosphole ring. As is seen in Figure 4.13 these values are 1.00 and 0.72 for the former and latter accordingly.

4.2.4 Homogeneous hydroboration reduction using phosphorus pre-catalysts

To attempt to answer the question of how these heterocyclic phosphorus compounds compare in catalytic performance to their arsenic counterparts, the hydroboration of aldehydes was repeated. Procedurally this was the same as the arsenic catalysis and made use of compounds **1a–1c**, **6a**, **6b**, **8a**, **8b**, **13a**, **13b**, **15c**, **24a**, **24b**, **25a** and **25b**. To begin with the phosphorus complexes were screened to determine which was the most active and therefore best to proceed with (Table 4.5). With that, 4-(trifluoromethyl)-benzaldehyde was again used as a test substrate and added to stoichiometric HBpin and 10 mol% pre-catalyst. CDCl_3 was used as the solvent for the initial optimisation and the conversion was detected by multinuclear NMR spectroscopy.

The dithiaphosphole **1a** proved to be catalytically inactive under these conditions, with $<5\%$ conversion seen in the ^1H NMR spectrum after 24 hours. A small improvement occurred when using **1b**, with 14% conversion found in the ^1H NMR spectrum after 24 hours. More interestingly though was the use of **1c**, which gave a considerable improvement of 60% product conversion after 24 hours. These differences between compounds **1a** to **1c** can be rationalised by their structural electronic properties, which was discussed in Chapter 2. In short, the P–X bond undergoes significant change with respect to partial charges upon changing X from Cl, Br and I.

The diazaphosphole and dioxaphosphole pre-catalysts **6a**, **6b**, **8a** and **8b** all failed to give product conversion, with $<5\%$ conversion detected. On the other hand, moving to the cationic complexes **13a**, **13b** and **15c** saw considerable improvement and all gave quantitative conversion to the hydroborated product **21a**. In the case of the dithiaphosphenium cations **13a** and **13b** this took 12 hours, whereas for the diazaphosphenium **15c** this was reduced to six hours. Knowing that it was possible for dynamic exchange to occur in solution between one of the chlorides on AlCl_4^- and the phosphorus centre to reform **1a** and give free AlCl_3 (Chapter 3), a control reaction was undertaken in which 10 mol% AlCl_3 was used as the pre-catalyst for the hydroboration catalysis. Using AlCl_3 , ^1H NMR spectroscopy showed that after 24 hours a reduced conversion of 68% to the reduced hydroborated product **21a** had occurred. Likewise, a

control reaction was performed using TMS triflate as the catalyst to ensure SiMe₃ was not responsible for the catalysis. Using TMS triflate, ¹H NMR spectroscopy revealed that after 24 hours only 56% conversion to the reduced hydroborated product had occurred. It should be noted that from Chapter 3 the dithiaphospheniums **13a** and **13b** in solution are likely to be hydrolysed.

Table 4.5: Optimisation of pre-catalysts.

Entry	Pre-catalyst	Loading/ mol%	Solvent	Time/ hr	Conversion/ % ^a
1	None	N/A	CDCl ₃	24	<5
2	1a	10	CDCl ₃	24	<5
3	1b	10	CDCl ₃	24	14
4	1c	10	CDCl ₃	24	61
5	6a	10	CDCl ₃	24	<5
6	6b	10	CDCl ₃	24	<5
7	8a	10	CDCl ₃	24	<5
8	8b	10	CDCl ₃	24	<5
9	13a	10	CDCl ₃	12	>95
10	13b	10	CDCl ₃	12	>95
11	15c	10	CDCl ₃	6	>95
12	24a	10	CDCl ₃	24	9
13	24b	10	CDCl ₃	24	8
14	25a	10	CDCl ₃	24	30
15	25b	10	CDCl ₃	24	35
16	AlCl ₃	10	CDCl ₃	24	68
17	TMSOTf	10	CDCl ₃	24	56

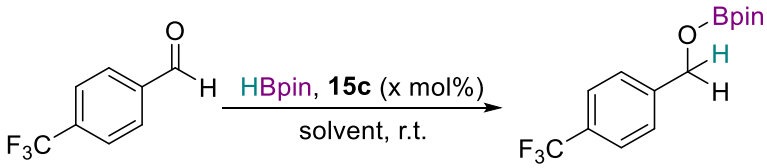
^aConversion measured using *in situ* ¹H NMR spectroscopy.

Of interest was the use of the benzyloxy and neopentyloxy derived pre-catalysts **24a–25b**, which all failed to give quantitative conversion after 24 hours. **24a** and **24b** gave 9% and 8% product conversion respectively, whereas **25a** and **25b** gave a moderate increase of 30% and 35% conversion accordingly. From these results it was therefore clear that the

phosphenium species were the most active pre-catalysts and given the faster rate that **15c** provided, the diazaphosphenium **15c** was used for future study (Table 4.5).

As **15c** was the most suitable pre-catalyst, the reaction conditions were optimised (Table 4.6). Again using 4-(trifluoromethyl)-benzaldehyde, stoichiometric HBpin and now 10 mol% **15c**, a variety of solvents were utilised to examine their effects on the catalytic performance. The use of CDCl₃ has been discussed but switching to CH₂Cl₂ still gave quantitative conversion, albeit it took 12 hours to complete. The difference may be explained by the almost double dielectric constant value CH₂Cl₂ has compared to CDCl₃ ($\epsilon = 8.93$ and 4.81 respectively). Moving away from halogenated solvents, MeCN and THF gave deleterious effects to the catalysis, with 39% and 76% product conversion detected respectively by ¹H NMR spectroscopy after 24 hours. In addition, toluene was attempted as a solvent but the pre-catalyst proved to be partially insoluble and thus the catalysis was not attempted.

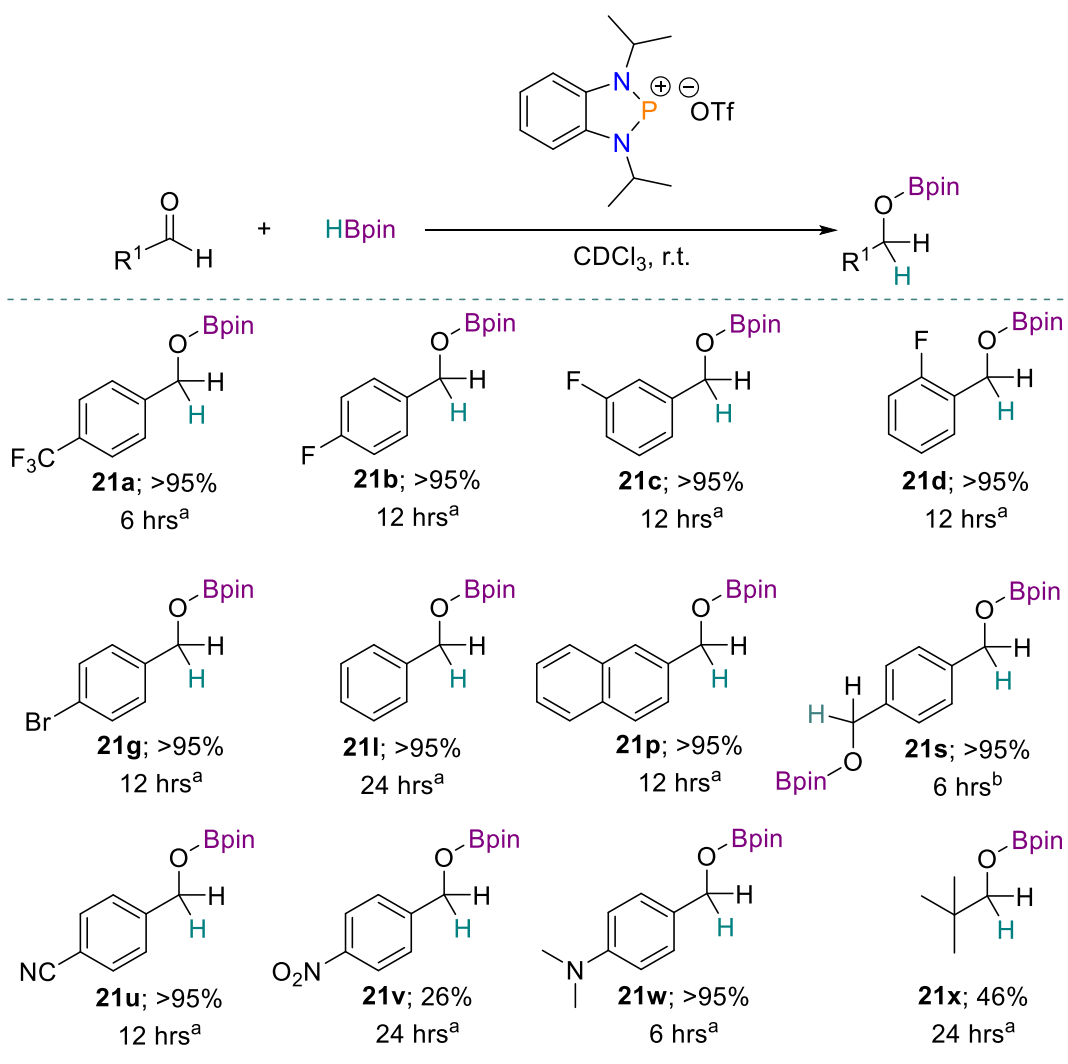
Knowing that CDCl₃ was the best solvent, the conditions were further optimised. Reducing the catalytic loading from 10 mol% to 5 mol% still gave full product conversion, but 12 hours were needed compared to six hours for 10 mol%. When reducing the catalytic loading lower to 2 mol% and 1 mol% the product conversions were reduced to 48% and 27% respectively. Although the catalysis still worked well using 5 mol% pre-catalyst loading, it was decided to use 10 mol% when investigating the substrate scope. Lastly, two equivalents of HBpin was trialled as well as using 10 mol% pre-catalyst and CDCl₃ solvent, but as before quantitative conversion proceeded after six hours and so no benefit was found from the increased HBpin.

Table 4.6: Optimisation of solvent and pre-catalyst loading.

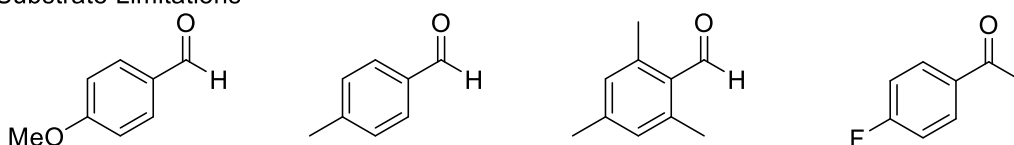
Entry	Loading/ mol%	Solvent	HBpin/ equiv	Time/ hr	Conversion/ %
1	10	CDCl ₃	1.0	6	>95 ^a
2	10	CH ₂ Cl ₂	1.0	12	>95 ^b
3	10	MeCN	1.0	24	39 ^b
4	10	THF	1.0	24	76 ^b
5	10	CDCl ₃	2.0	6	>95 ^a
6	5	CDCl ₃	1.0	12	>95 ^a
7	2	CDCl ₃	1.0	24	48 ^a
8	1	CDCl ₃	1.0	24	27 ^a

^aConversion measured using *in situ* ¹H NMR spectroscopy. ^bConversion measured using *in situ* ¹⁹F NMR spectroscopy.

With the optimised conditions of 10 mol% of the diazaphosphenium triflate **15c**, one equivalent of HBpin and CDCl₃ solvent, a substrate scope was performed to evaluate how effective **15c** was for this reduction catalysis (Scheme 4.6). As already discovered from the optimisation reactions 4-(trifluoromethyl)-benzaldehyde was hydroborated to **21a** in six hours. On that theme, the fluorinated aldehydes 4-fluorobenzaldehyde, 3-fluorobenzaldehyde, 2-fluorobenzaldehyde were readily converted to **21b**, **21c** and **21d** accordingly within 12 hours. Furthermore, other electron withdrawing aldehydes were investigated. The aldehydes 4-bromobenzaldehyde and 4-formylbenzotrile gave >95% conversion to the respected reduced products **21e** and **21u** within 12 hours. Contrary to this, when using 4-nitrobenzaldehyde only 67% conversion to **21v** was detected by ¹H NMR spectroscopy.



Substrate Limitations



Scheme 4.6: Hydroboration of aldehydes using 1,3-diisopropyl-benzodiphosphenium triflate (**15c**). 0.6 ml CDCl₃ solvent, NMR yield calculated from *in situ* ¹H NMR spectrum. ^a10 mol% **15c**. ^b20 mol% **15c**; 2.0 equiv HBpin.

Moving away from electron withdrawing aldehydes, benzaldehyde was much slower to undergo hydroboration, but nevertheless went to full completion to product **21i** within 24 hours. The related terephthalaldehyde, which has an aldehyde moiety in the 1- and 4-position, was reduced to **21s** in six hours, albeit 20 mol% catalytic loading was used due to the double aldehyde group presence. The electron donating dimethylamino functional group was also tolerated, with the starting aldehyde 4-(dimethylamino)benzaldehyde

reduced to **21w** in six hours. The more sterically hindered 2-naphthaldehyde was readily reduced to **21p** in 12 hours. Lastly, hydroboration on the aliphatic pivalaldehyde was attempted, which gave 46% conversion to **21x** after 24 hours. The approximate half conversion can in part be explained by the high steric demand.

While performing the substrate scope, 4-methoxybenzaldehyde, 4-methylbenzaldehyde and 2,4,6-trimethylbenzaldehyde substrates were also examined. In these cases the ^1H NMR spectra gave additional unidentified signals that did not correspond to the reactant or product formation and consequently although consumption of the starting aldehyde was observed, their results are not included in Scheme 4.6. As well as aldehydes, the ketone 4'-fluoroacetophenone was also trialed in the substrate scope, giving 57% consumption as detected by ^{19}F NMR spectroscopy. However, additional signals to the reactant or product formation were identified.

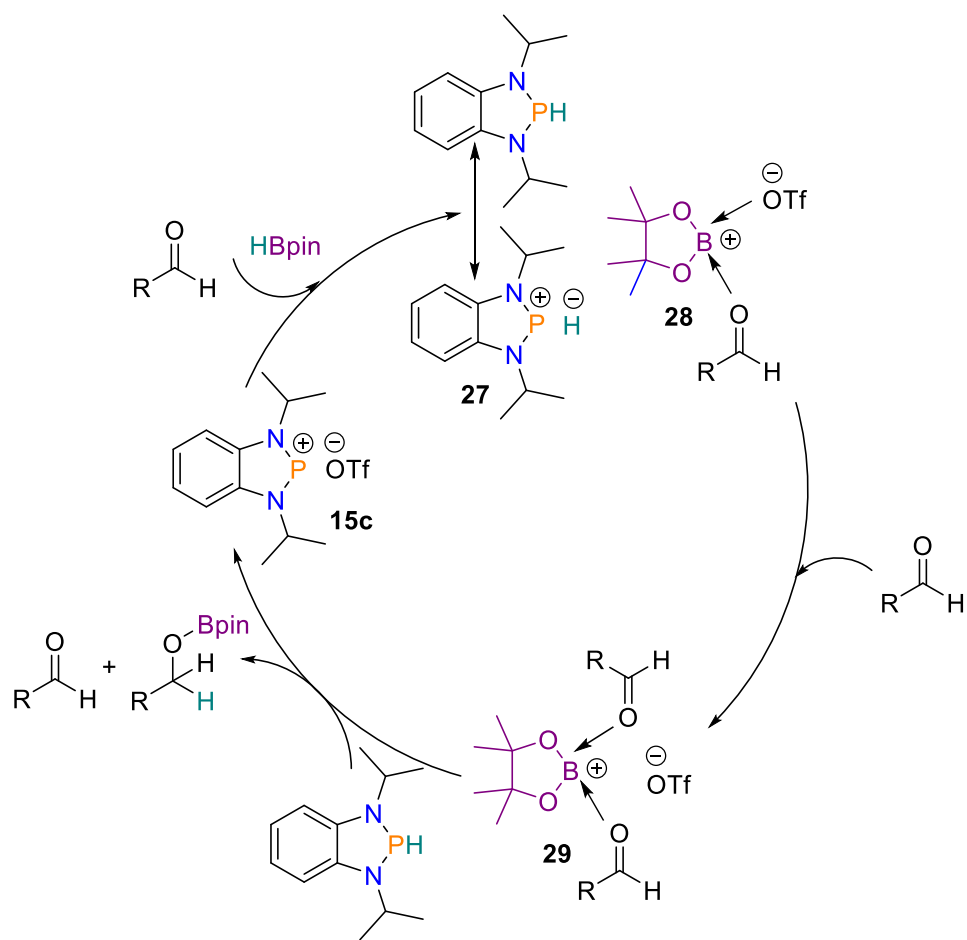
As was the case for the diazarsole catalysis, once the substrate scope was completed attention turned to investigating the catalytic cycle to explain how the catalysis proceeds (Scheme 4.7). The cationic nature of diazaphosphenium **15c** means that the catalytic cycle is different to the neutral benzyloxy-diazarsole **20**. To rule out that the diazaphosphenium cation simply acts as a Lewis acid, **15c** was added to a stoichiometric amount of 4-(trifluoromethyl)benzaldehyde, where no appreciable change in the ^{31}P NMR spectrum occurred. The lack of a strong interaction and any adduct formation between the pre-catalyst and aldehyde substrate eliminated the possibility of Lewis acid catalysis, and instead the catalysis was presumed to follow a similar route to the hydroboration of pyridines with HBpin using a diazaphosphenium pre-catalyst, which was recently reported by the Kinjo group.⁹

Initially a B–H bond activation takes place to generate the diazaphosphenium hydride **27** and aldehyde·Bpin·OTf (**28**) complex. From the ground breaking work of Gudat, which showed the hydridic nature of the P–H bond in the closely related diazaphospholene species,¹¹ it is believed that **27** also exhibits this feature. This nucleophilicity of the P–H bond in **27** is supported by the recent work by Cheng *et al.* who developed a method to determine the hydridic nature of the P–H bond in these heterocyclic phosphorus compounds. Cheng and colleagues found that the diazaphosphole 2-chloro-1,3-di-tert-butyl-benzodiazaphosphole (**27** but with isopropyl groups) was significantly nucleophilic and comparable to the diazaphospholenes.¹² From here a second aldehyde substrate is introduced and forms the boronium complex **29**, which gives rise to the activated aldehyde

intermediate. One of the aldehyde substrates is then reduced *via* hydride transfer from **27** to give the hydroborated product, releasing the aldehyde and regenerating the pre-catalyst.

Upon trying to observe these catalytic cycle intermediates, stoichiometric amounts of **15c** were added to HBpin to form the active catalyst **27**. However, ^{31}P NMR spectroscopy instead revealed significant product decomposition and the formation of phosphine, PH_3 , as identified by a quartet signal centred at $\delta = -238.5$ ppm, with a $^1J_{\text{PH}} = 189$ Hz. Furthermore, the intermediate en route to PH_3 was also observed in the ^{31}P NMR spectrum, with a low intensity triplet centred at $\delta = -79.5$ ppm and $^1J_{\text{PH}} = 199$ Hz. This suggested the formation of a primary phosphine with two P–H bonds formed *via* endocyclic cleavage. Similar observations have previously been reported by the Speed group for the catalytic reduction of imines using a diazaphospholene pre-catalyst.⁵

Lastly, given the poor performance of the alkoxy-derived dithiaphosphole and dioxaphosphole pre-catalysts, their activity was investigated by reacting **24a** and **25a** with stoichiometric amount of HBpin in CDCl_3 to monitor how quickly the respective active hydride species formed. In the case of the former, after 24 hours both the ^{31}P and ^{11}B NMR spectra of **24a** showed little appreciable change, with no indication of the desired active hydride catalyst being formed. For the latter, multinuclear NMR spectroscopy again showed no formation of the active catalyst being formed after 24 hours, with only a small quantity of hydrolysis product detected, as identified by a doublet resonance centred at $\delta = -7.7$ ppm ($^1J_{\text{PH}} = 706$ Hz) in the ^{31}P NMR spectrum. It should be noted that neither case showed the formation of the by-product BnO–Bpin which would also be expected. Therefore, it can be concluded from these studies that the slow formation of the active hydride catalyst is the cause of the poor activity in complexes **24a**, **24b**, **25a** and **25b**, as was seen in the case for the benzyloxy-dithiarsole.



Scheme 4.7: Proposed catalytic cycle for the hydroboration of aldehydes using 1,3-diisopropyl-benzodiphosphonium triflate (**15c**) as a pre-catalyst.

Chapter 4.3 Comparing the Phosphorus and Arsenic Pre-Catalysts

Given the large number of phosphorus and arsenic compounds used in this chapter, it is interesting to compare their ability to act as pre-catalysts for hydroboration reduction of aldehydes with HBpin (Figure 4.14). Firstly, when comparing the precursor dithiaphosphole and diazaphosphole species **1a** and **6a** against their arsenic analogues **3** and **7**, the results taken from the optimisation Tables 3 and 7 showed less than 5% conversion of the hydroborated product of 4-(trifluoromethyl)-benzaldehyde when using 10 mol% of **1a** and **6a** respectively in CDCl₃ solvent. Contrary to this, using 10 mol% of **3** and **7** gave 38% and 49% product conversion to the reduced aldehyde when using toluene as the solvent. Although none of these four complexes proved good pre-catalysts, these results nevertheless clearly show the dithiarsole and diazarsole as the more active species. Although the solvent choices were different, repeating the optimisation reactions with toluene as the solvent for **1a** and **6a** gave <5% and 8% conversion after 24 hours respectively.

As the benzyloxy-diazaphosphole was not possible to synthesise purely, a direct comparison cannot be made between this and the arsenic analogue **20**, however a comparison can be made between the benzyloxy-dithiaphosphole **24a** and the benzyloxy-dithiarsole **19**. The optimisation Tables 3 and 7 show that for **24a** 9% conversion to the hydroborated product was achieved after 24 hours, meanwhile the same reaction for **19** achieved a much more impressive 64% product conversion after 12 hours. Again, the former was performed in CDCl₃ whereas the latter in toluene, but when **19** was repeated in toluene only 6% conversion was detected. From the results so far, it can be concluded that for the neutral species the arsenic complexes (despite their high toxicity) perform much better as pre-catalysts for hydroboration reduction than the phosphorus species.

A less clear picture emerges though when comparing the cationic phosphorus and arsenic complexes. For 10 mol% of the dithiaphosphenium **13a** and dithiarsenium **14a**, both with the tetrachloroaluminate (AlCl₄⁻) counterion, **13a** and **14a** gave quantitative conversion in 12 hours to the hydroborated product. On the other hand, when looking at the diazaphosphenium **15c** and diazarsenium **16c**, with the triflate (OTf⁻) counterion, the diazaphosphenium proved significantly better. Full product conversion was seen for **15c** in six hours with CDCl₃ solvent, whereas the diazarsenium only gave 50% conversion with CH₂Cl₂ as the solvent. A less clear conclusion can be drawn from the cationic phosphorus vs. arsenic results with regards to which is the superior pre-catalyst choice, however on balance the fact that the diazaphosphenium **15c** performed so well indicates this is the best cationic complex.

Lastly, to evaluate which phosphorus and arsenic compound is the superior pre-catalyst, the performance of the diazaphosphenium **15c** can be compared to the benzyloxy-diazarsole **20**. In this case the benzyloxy-diazarsole was the clear victor as when operating at 10 mol% the rate of hydroboration was much greater than for **15c**; 30 minutes vs. six hours for full conversion. Furthermore, **20** could be optimised to work with no deleterious effects at 5 mol% pre-catalyst loading, whereas when using **15c** at 5 mol% for the substrate scope a number of problems were found, with most substrates trialled failing to go to complete conversion.

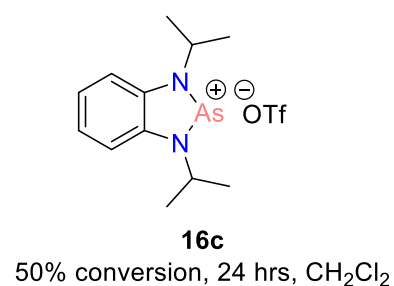
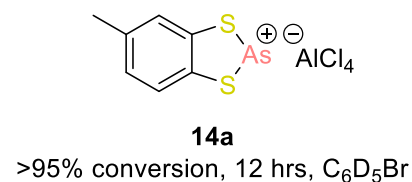
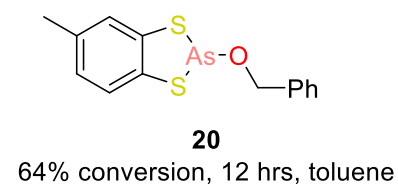
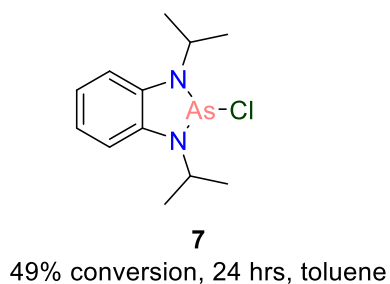
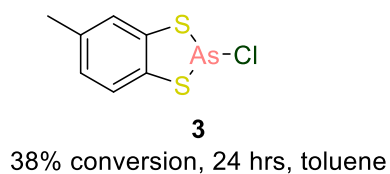
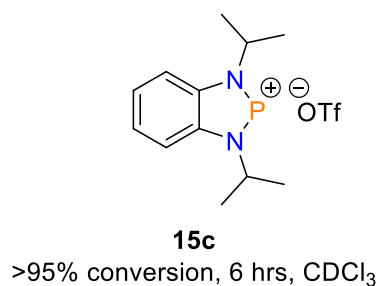
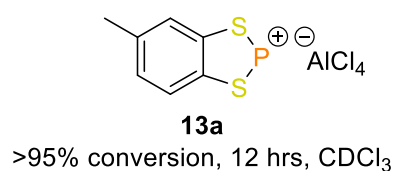
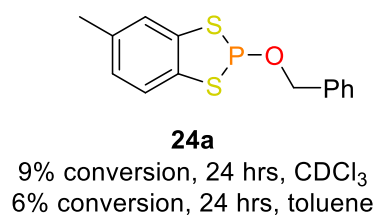
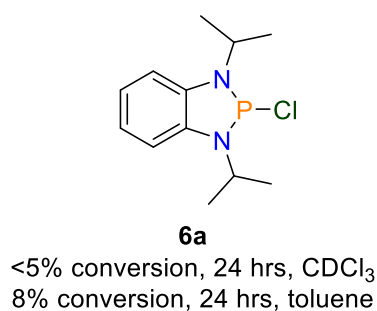
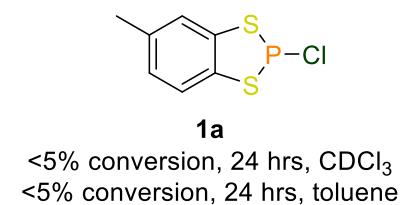
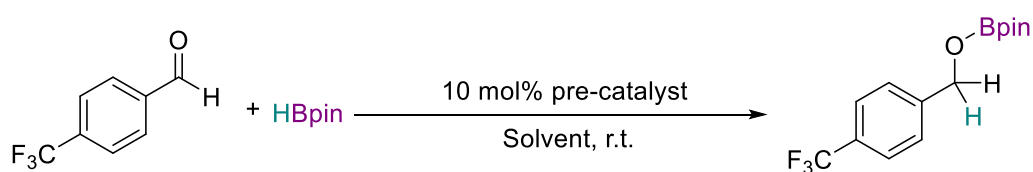


Figure 4.14: Comparison of phosphorus and arsenic complexes used as pre-catalysts for the hydroboration of 4-(trifluoromethyl)-benzaldehyde with HBpin.

Chapter 4.4 Conclusion

In this chapter the metal-free hydroboration of aldehydes with pinacolborane (HBpin) has been demonstrated, making use of the first reported example of arsenic homogenous catalysis. Optimisation studies found that the benzyloxy-diazarsole, **20**, was the most effective pre-catalyst to use, with conditions of 5 mol% catalytic loading, room temperature, one equivalence of HBpin and C₆D₆ solvent. The substrate scope showed that electron withdrawing aldehydes worked very well, but electron neutral and donating substituents proved more difficult. The catalytic cycle was investigated, which found that an arsenic hydride species was the active catalyst and its formation proved rate limiting.

After this the catalysis was performed with the phosphorus analogues so a number of comparisons could be made between arsenic and phosphorus catalytic ability. This was to see if any underlying trends could be established. This analysis found that the neutral dithiarsoles and diazarsoles were better pre-catalysts than the phosphorus versions, whether that be with the chloride co-ligand or benzyloxy co-ligand. The diazarsoles were also found to be better than the dithiarsoles. Contrary to this, the cationic phosphoniums proved more active than the arsenium species, with a noticeable discrepancy between the diazaphosphonium **15c** and the diazarsenium **16c**. For the arseniums the diazarsenium was more active than the dithiarsenium, but the reverse trend was true for the diazaphosphonium vs. dithiaphosphonium. Note though that the dithiaphosphonium is likely to be hydrolysed in solution (Chapter 3). The ultimate pre-catalyst though proved to be the benzyloxy diazarsole **20**, which operated at lower catalytic loadings than the best phosphorus pre-catalyst **15c** and gave much more rapid conversion times. Thus, it can be concluded that despite the increased toxicity surrounding arsenic catalysis, the benzyloxy-diazarsole **20** proved to be a very effective pre-catalyst for this hydroboration reduction.

Chapter 4.5 References

- 1 T. T. P. Tran, D. M. C. Ould, L. C. Wilkins, D. S. Wright, R. L. Melen and J. M. Rawson, *CrystEngComm*, 2017, **19**, 4696–4699.
- 2 D. M. C. Ould, A. C. Rigby, L. C. Wilkins, S. J. Adams, J. A. Platts, S. J. A. Pope, E. Richards and R. L. Melen, *Organometallics*, 2018, **37**, 712–719.
- 3 C. C. Chong, H. Hirao and R. Kinjo, *Angew. Chem. Int. Ed.*, 2015, **54**, 190–194.
- 4 M. R. Adams, C. Tien, R. McDonald and A. W. H. Speed, *Angew. Chem. Int. Ed.*, 2017, **56**, 16660–16663.
- 5 M. R. Adams, C. H. Tien, B. S. N. Huchenski, M. J. Ferguson and A. W. H. Speed, *Angew. Chem. Int. Ed.*, 2017, **56**, 6268–6271.
- 6 T. Hynes, E. N. Welsh, R. McDonald, M. J. Ferguson and A. W. H. Speed, *Organometallics*, 2018, **37**, 841–844.
- 7 S. Miaskiewicz, J. H. Reed, P. A. Donets, C. C. Oliveira and N. Cramer, *Angew. Chem. Int. Ed.*, 2018, **57**, 4039–4042.
- 8 D. M. C. Ould and R. L. Melen, *Chem. Eur. J.*, 2018, **24**, 15201–15204.
- 9 B. Rao, C. C. Chong and R. Kinjo, *J. Am. Chem. Soc.*, 2018, **140**, 652–656.
- 10 D. M. C. Ould, T. T. P. Tran, J. M. Rawson and R. L. Melen, *Dalton Trans.*, 2019, **48**, 16922–16935.
- 11 D. Gudat, A. Haghverdi and M. Nieger, *Angew. Chem. Int. Ed.*, 2000, **39**, 3084–3086.
- 12 J. Zhang, J. Yang and J. Cheng, *Angew. Chem. Int. Ed.*, 2019, **58**, 5983–5987.

Chapter 5: Conclusions and Future Work

The prominent aim of this thesis was to synthesise a range of novel heterocyclic benzo-fused-phosphole and benzo-fused-arsole derived compounds in order to attain a better fundamental insight into this class of underexplored heterocycle. This thesis has succeeded in this by producing a range of dithiaphospholes, dithiarsoles, diazaphospholes, diazarsoles and dioxaphospholes in Chapter 2, which were characterised by multinuclear NMR spectroscopy and X-ray crystallography. The solid-state structures interestingly revealed an envelope geometry and an elongated P/As–X (X = Cl, Br or I) bond length.

Chapter 3 built on this by using these phosphole and arsole compounds as pre-cursors to explore their reactivity, something which has notably been missing in the literature as most early reports of these compounds have focussed purely on structural analyses. A *N*-centred paddlewheel which is flanked by three dithiaphosphole or dithiarsole species was first synthesised, after which attention turned to the production of phosphonium and arsenium cations. As there has previously been no attempts to understand the optical properties of these cations, their photophysical properties were probed, which showed complex absorption spectra but nevertheless a dependence on both the heteroatom (P or As) and the choice of counterion. Lastly, Chapter 3 looked at reduction of the diazaphosphole and diazarsole. For the former the expected P–P dimer was synthesised, which using EPR spectroscopy showed homolytic cleavage at 350 K in solution. Meanwhile, for the latter the analogous As–As dimer was not produced and instead single crystal X-ray diffraction revealed the diazarsole 2-iodo-1,3-diisopropyl-benzodiazarsole formed from oxidative addition.

Proceeding this, Chapter 4 looked at using these compounds as pre-catalysts for the hydroboration of aldehydes with HBpin. Initially the first reported use of arsenic homogenous catalysis was explored, which along with using the compounds already described also used a benzyloxy-dithiarsole and diazarsole. Optimisation studies revealed the benzyloxy-diazarsole was the most active pre-catalyst and proceeding at 5 mol% a wide substrate scope was performed, which showed the catalyst was tolerant to a variety of steric and electronic effects. For a comparison, the phosphorus complexes were then used as pre-catalysts, with the diazaphosphonium triflate this time proving to be the most suitable pre-catalyst. However, compared to the benzyloxy-diazarsole it proved a much poorer with respect to catalytic loading and conversion time. The neutral arsenic compounds proved better pre-catalysts, but a less clear picture was observed for the cationic complexes.

This thesis has described an in-depth study into advancing the knowledge of benzo-fused-phosphole and benzo-fused-arsole derived compounds. To further advance our understanding into this underexplored area, a number of interesting avenues should be explored.

Chapter 2. The benzo-fused dioxarsole should be synthesised and a comparison between this and the benzo-fused dioxaphospholes could be performed.

Chapter 3. It would be interesting to perform photophysical studies of the dithia and dioxa derived pnictoles and compare them to their diaza pnictole counterparts. The optical results through the introduction of a non-coordinating anion (such as $\text{BAr}^{\text{F}_4^-}$) to the cations would also be important and attempts could be undertaken to increase the quantum yield. With regards to the formation of the As–As dimer, further work could be undertaken to synthesise this. The use of sodium metal as the reductant could be attempted for this.

Chapter 4. The main interest in development here would be to increase catalytic performance of the arsenic pre-catalysts. From the introduction section the use of tert-butyl groups on the nitrogen atoms were used by the groups of Kinjo, Speed and Cramer on related systems, so this is the first thing to try. Secondly, formation of the hydride species should be performed, as although this will reduce its air/moisture stability, it would prevent a rate limiting step. From here a number of different compounds to be reduced could be explored, such as imines, and the first example of chiral reduction using arsenic homogeneous catalysis performed.

Chapter 6: Experimental

Chapter 6.1 General Experimental

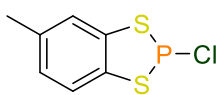
Unless stated otherwise, all reactions were carried out under an atmosphere of dinitrogen using standard Schlenk and glove box techniques. With the exception of THF, Et₂O and deuterated solvents, all solvents used were dried by passing through an alumina column incorporated into an MB SPS-800 solvent purification system, degassed and finally stored in an ampoule fitted with a Teflon valve under a dinitrogen atmosphere. THF was dried over molten potassium for three days and distilled over argon, whereas Et₂O was dried over sodium wire and benzophenone before being distilled over argon. Deuterated solvents were dried over calcium hydride, distilled, freeze-pump-thawed degassed and stored over 3 Å molecular sieves in a glove box. Starting materials were purchased from commercial suppliers and used as received. ¹H, ¹³C{¹H}, ¹⁹F, ¹¹B, ³¹P, and ²⁷Al NMR spectra were recorded on a Bruker Avance 300, 400, or 500 MHz spectrometer. Chemical shifts are expressed as parts per million (ppm, δ) and are referenced to CDCl₃ (7.26/77.16 ppm), C₆D₆ (7.16/128.06 ppm), or C₆D₅Br (7.28/122.4 ppm for the most downfield resonance) as internal standards. Multinuclear NMR spectra were referenced to BF₃·Et₂O/CDCl₃ (¹¹B), CFCl₃ (¹⁹F), H₃PO₄ (³¹P), and Al(NO₂)₃ (²⁷Al). The description of signals includes s = singlet, d = doublet, t = triplet, q = quartet, sept = septet and m = multiplet. All coupling constants are absolute values and are expressed in Hertz (Hz). IR-Spectra were measured on a Shimadzu IR Affinity-1 photospectrometer. The description of signals includes s = strong, m = medium, w = weak, sh = shoulder, and br = broad. Mass spectra were measured by the School of Chemistry in Cardiff University on a Waters LCT Premier/XE or a Waters GCT Premier spectrometer.

Chapter 6.2 Experimental for Synthesis of Dithia-, Diaza-, and Dioxo-based Benzphospholes and Benzarsoles

6.2.1 Synthesis of benzo-fused dithiaphospholes and dithiarsoles

General Procedure 1. Phosphorus(III) chloride (1.2 equiv) or phosphorus(III) bromide (1.0 equiv) was added dropwise to a solution of toluene-3,4-dithiol (1.0 equiv) or benzene dithiol (1.0 equiv) in CH_2Cl_2 (3 mL), with the evolution of gas observed. The reaction was allowed to stir at ambient temperature for 24 hours, after which the solvent was removed *in vacuo*. To the resulting oil, pentane (2 mL) was added and cooled to $-40\text{ }^\circ\text{C}$ for 4 hours to give the product 2-chloro-5-methylbenzo-1,3,2-dithiaphosphole (**1a**), 2-bromo-5-methylbenzo-1,3,2-dithiaphosphole (**1b**), 2-chlorobenzo-1,3,2-dithiaphosphole (**2a**) or 2-bromobenzo-1,3,2-dithiaphosphole (**2b**) as a white powder.

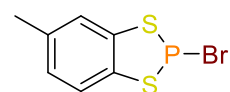
2-chloro-5-methylbenzo-1,3,2-dithiaphosphole (**1a**)



Compound **1a** was synthesised according to *general procedure 1* using phosphorus(III) chloride (880 mg, 6.40 mmol, 1.2 equiv) and toluene-3,4-dithiol (1.00 g, 4.74 mmol, 1.0 equiv). **Yield:** 1.363 g, 6.18 mmol, 96%. Crystals suitable for single crystal X-ray diffraction were grown from a saturated solution of CH_2Cl_2 with a few drops of pentane added.

^1H NMR (500 MHz, CDCl_3 , 295 K) δ /ppm: 7.55 (dd, $^3J_{\text{HH}} = 8.1\text{ Hz}$, $^4J_{\text{PH}} = 1.2\text{ Hz}$, 1H, Ar-H), 7.50 (s, 1H, Ar-H), 7.12 (ddd, $^3J_{\text{HH}} = 8.1\text{ Hz}$, $^4J_{\text{HH}} = 1.2\text{ Hz}$, $^5J_{\text{PH}} = 0.6\text{ Hz}$, 1H, Ar-H), 2.39 (s, 3H, CH_3). **$^{13}\text{C}\{^1\text{H}\}$ NMR** (126 MHz, CDCl_3 , 295 K) δ /ppm: 137.9 (d, $^3J_{\text{PC}} = 3.3\text{ Hz}$, 1C, Ar), 137.3 (1C, Ar), 134.4 ($^3J_{\text{PC}} = 3.6\text{ Hz}$, 1C, Ar), 128.1 (1C, Ar), 126.6 (d, $^2J_{\text{PC}} = 5.5\text{ Hz}$, 1C, Ar), 125.8 (d, $^2J_{\text{PC}} = 5.5\text{ Hz}$, 1C, Ar), 21.1 (1C, Ar- CH_3). **$^{31}\text{P}\{^1\text{H}\}$ NMR** (202 MHz, CDCl_3 , 295 K) δ /ppm: 160.4 (s, 1P). **IR** ν_{max} (cm^{-1}): 1458 (m), 1375 (sh), 1258 (w), 1146 (w), 1036 (w), 874 (w), 804 (s), 685 (w) and 635 (w). **HRMS** (EI^+) m/z calculated for $[\text{M}]^+$ $[\text{C}_7\text{H}_6\text{ClPS}_2]^+$: 219.9337, found: 219.9341. **Melting point** 38–41 $^\circ\text{C}$.

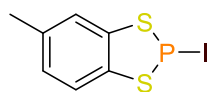
2-bromo-5-methylbenzo-1,3,2-dithiaphosphole (**1b**)



Compound **1b** was synthesised according to *general procedure 1* using phosphorus(III) bromide (346 mg, 1.28 mmol, 1.0 equiv) and toluene dithiol (200 mg, 1.28 mmol, 1.0 equiv). **Yield:** 288 mg, 1.09 mmol, 85%. Crystals suitable for single crystal X-ray diffraction were grown from a saturated solution of CH_2Cl_2 with a few drops of pentane added.

¹H NMR (400 MHz, CDCl₃, 295 K) δ/ppm: 7.57 (dd, ³J_{HH} = 8.1 Hz, ⁴J_{PH} = 1.1 Hz, 1H, Ar–H), 7.51 (s, 1H, Ar–H), 7.14 (dd, ³J_{HH} = 8.1 Hz, ⁴J_{HH} = 1.1 Hz, 1H, Ar–H), 2.40 (s, 3H, CH₃). **¹³C{¹H} NMR** (101 MHz, CDCl₃, 295 K) δ/ppm: 138.8 (d, ³J_{PC} = 3.2 Hz, 1C, Ar), 137.4 (1C, Ar), 135.3 (d, ³J_{PC} = 3.4 Hz, 1C, Ar), 128.2 (1C, Ar), 126.7 (d, ²J_{PC} = 5.6 Hz, 1C, Ar), 125.9 (d, ²J_{PC} = 5.5 Hz, 1C, Ar), 21.1 (1C, Ar–CH₃). **³¹P{¹H} NMR** (162 MHz, CDCl₃, 295 K) δ/ppm: 163.3 (s, 1P). **IR** ν_{max} (cm⁻¹): 1456 (m), 1440 (sh), 1375 (w), 1258 (w), 1142 (w), 1115 (w), 1036 (w), 999 (w), 947 (w), 876 (w), 817 (s), 687 (w), 635 (w) and 541 (w). **HRMS** (EI⁺) *m/z* calculated for [M]⁺ [C₇H₆BrPS₂]⁺: 263.8832, found: 263.8838. **Melting point** 60–64 °C.

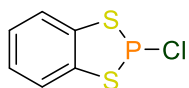
2-iodo-5-methylbenzo-1,3,2-dithiaphosphole (**1c**)



Phosphorus(III) iodide (334 mg, 0.08 mmol, 1.0 equiv) in CH₂Cl₂ (2 mL) was added dropwise to a solution of toluene-3,4-dithiol (127 mg, 0.08 mmol, 1.0 equiv) in CH₂Cl₂ (3 mL). The reaction was allowed to stir at ambient temperature for 24 hours, after which time the solvent was removed *in vacuo*. The resulting orange solid was washed with pentane (3 × 2 mL) and again dried *in vacuo*, to give the product 2-iodo-5-methylbenzo-1,3,2-dithiaphosphole as an orange solid. **Yield:** 185 mg, 0.59 mmol, 73%. Crystals suitable for single crystal X-ray diffraction were grown from a saturated solution of CH₂Cl₂ with a few drops of pentane added.

¹H NMR (500 MHz, CDCl₃, 295 K) δ/ppm: 7.55 (dd, ³J_{HH} = 8.1 Hz, ⁴J_{PH} = 1.3 Hz, 1H, Ar–H), 7.50 (s, 1H, Ar–H), 7.15 (ddd, ³J_{HH} = 8.1 Hz, ⁴J_{HH} = 1.6 Hz, ⁵J_{PH} = 0.7 Hz, 1H, Ar–H), 2.41 (s, 3H, CH₃). **¹³C{¹H} NMR** (126 MHz, CDCl₃, 295 K) δ/ppm: 140.2 (d, ³J_{PC} = 3.1 Hz, 1C, Ar), 137.5 (1C, Ar), 136.7 (³J_{PC} = 3.1 Hz, 1C, Ar), 128.2 (1C, Ar), 127.0 (d, ²J_{PC} = 5.6 Hz, 1C, Ar), 126.2 (d, ²J_{PC} = 5.6 Hz, 1C, Ar), 21.1 (1C, Ar–CH₃). **³¹P{¹H} NMR** (202 MHz, CDCl₃, 295 K) δ/ppm: 155.0 (s, 1P). **IR** ν_{max} (cm⁻¹): 1458 (w), 1379 (w), 1254 (w), 854 (w), 804 (s), 692 (w), 637 (w) and 538 (w). **HRMS** (EI⁺) *m/z* calculated for [M]⁺ [C₇H₆IPS₂]⁺: 311.8693, found: 311.8687. **Melting point** 86–90 °C.

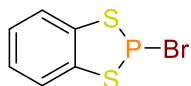
2-chlorobenzo-1,3,2-dithiaphosphole (**2a**)



Compound **2a** was synthesised according to *general procedure 1* using phosphorus(III) chloride (89 mg, 0.65 mmol, 1.2 equiv) and benzene dithiol (77 mg, 0.54 mmol, 1.0 equiv). **Yield:** 104 mg, 0.50 mmol, 93%. Crystals suitable for single crystal X-ray diffraction were grown from a saturated solution of CH₂Cl₂ with a few drops of pentane added.

¹H NMR (400 MHz, CDCl₃, 295 K) δ/ppm: 7.69 (ddd, ³J_{HH} = 5.9 Hz, ⁴J_{HH} = 3.3 Hz, ⁴J_{PH} = 1.3 Hz, 2H, Ar–H), 7.32 (dd, ³J_{HH} = 5.9 Hz, ⁴J_{HH} = 3.3 Hz, 2H, Ar–H). **¹³C{¹H} NMR** (101 MHz, CDCl₃, 295 K) δ/ppm: 137.8 (d, ³J_{PC} = 3.3 Hz, 2C, Ar), 126.9 (2C, Ar), 126.1 (d, ²J_{PC} = 5.6 Hz, 2C, Ar). **³¹P{¹H} NMR** (162 MHz, CDCl₃, 295 K) δ/ppm: 158.3 (s, 1P). **IR** ν_{max} (cm⁻¹): 1441 (m), 1429 (sh), 1252 (w), 1103 (w), 937 (w), 743 (s) and 662 (w). **HRMS** (EI⁺) *m/z* calculated for [M]⁺ [C₆H₄ClPS₂]⁺: 205.9181, found: 205.9176. **Melting point** 40–42 °C.

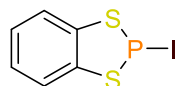
2-bromobenzo-1,3,2-dithiaphosphole (2b)



Compound **2b** was synthesised according to *general procedure 1* using phosphorus(III) bromide (186 mg, 0.69 mmol, 1.0 equiv) and benzene dithiol (98 mg, 0.69 mmol, 1.0 equiv). **Yield:** 157 mg, 0.62 mmol, 91%. Crystals suitable for single crystal X-ray diffraction were grown from a saturated solution of CH₂Cl₂ with a few drops of pentane added.

¹H NMR (400 MHz, CDCl₃, 295 K) δ/ppm: 7.70 (ddd, ³J_{HH} = 5.9 Hz, ⁴J_{HH} = 3.3 Hz, ⁴J_{PH} = 1.3 Hz, 2H, Ar–H), 7.33 (dd, ³J_{HH} = 5.9 Hz, ⁴J_{HH} = 3.3 Hz, 2H, Ar–H). **¹³C{¹H} NMR** (101 MHz, CDCl₃, 295 K) δ/ppm: 138.6 (d, ³J_{PC} = 3.3 Hz, 2C, Ar), 127.0 (2C, Ar), 126.3 (d, ²J_{PC} = 5.7 Hz, 2C, Ar). **³¹P{¹H} NMR** (162 MHz, CDCl₃, 295 K) δ/ppm: 160.9 (s, 1P). **IR** ν_{max} (cm⁻¹): 1441 (m), 1425 (sh), 1252 (w), 936 (w), 741 (s) and 662 (w). **HRMS** (EI⁺) *m/z* calculated for [M]⁺ [C₆H₄BrPS₂]⁺: 249.8675, found: 249.8682. **Melting point** 62–64 °C.

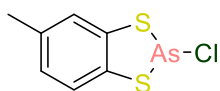
2-iodobenzo-1,3,2-dithiaphosphole (2c)



Phosphorus(III) iodide (517 mg, 1.26 mmol, 1.0 equiv) in CH₂Cl₂ (2 mL) was added dropwise to a solution of benzene dithiol (179 mg, 1.26 mmol, 1.0 equiv) in CH₂Cl₂ (3 mL). The reaction was allowed to stir at ambient temperature for 24 hours, after which time the solvent was removed *in vacuo*. The resulting red solid was washed with pentane (3 × 2 mL) and again dried *in vacuo*, to give the product 2-iodobenzo-1,3,2-dithiaphosphole as a red solid. **Yield:** 312 mg, 1.0 mmol, 83%. Crystals suitable for single crystal X-ray diffraction were grown from a saturated solution of CH₂Cl₂ with a few drops of pentane added.

¹H NMR (500 MHz, CDCl₃, 295 K) δ/ppm: 7.68 (ddd, ³J_{HH} = 5.9 Hz, ⁴J_{HH} = 3.3 Hz, ⁴J_{PH} = 1.3 Hz, 2H, Ar–H), 7.34 (dd, ³J_{HH} = 5.9 Hz, ⁴J_{HH} = 3.3 Hz, 2H, Ar–H). **¹³C{¹H} NMR** (126 MHz, CDCl₃, 295 K) δ/ppm: 140.0 (d, ³J_{PC} = 3.3 Hz, 2C, Ar), 127.0 (2C, Ar), 126.5 (d, ²J_{PC} = 5.7 Hz, 2C, Ar). **³¹P{¹H} NMR** (202 MHz, CDCl₃, 295 K) δ/ppm: 152.4 (s, 1P). **IR** ν_{max} (cm⁻¹): 1439 (m), 1420 (sh), 784 (s) and 662 (w). **HRMS** (EI⁺) *m/z* calculated for [M]⁺ [C₆H₄IP₂S₂]⁺: 297.8537, found: 297.8537. **Melting point** 76–78 °C.

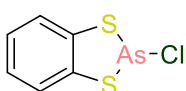
2-chloro-5-methylbenzo-1,3,2-dithiarsole (**3**)



Arsenic(III) chloride (0.68 g, 3.84 mmol, 1.2 equiv) in CH_2Cl_2 (2 mL) was added dropwise to a solution of toluene-3,4-dithiol (0.50 g, 3.20 mmol, 1 equiv) in CH_2Cl_2 (2 mL) and immediate effervescence occurred. The resulting solution was stirred at ambient temperature for 24 hours, after which the solvent was removed *in vacuo* to give a pale yellow solid. The resulting yellow solid was washed with pentane (3×2 mL) and again dried *in vacuo*, to give the product 2-chloro-5-methylbenzo-1,3,2-dithiarsole as a yellow solid. **Yield:** 0.73 g, 2.75 mmol, 86%. Crystals suitable for single crystal X-ray diffraction were grown from either a saturated solution of MeOH (**3 α**) or MeCN (**3 β**).

^1H NMR (500 MHz, CDCl_3 , 295 K) δ /ppm: 7.48 (d, $^3J_{\text{HH}} = 8.1$ Hz, 1H, Ar-H), 7.43 (s, 2H, Ar-H), 7.05 (s, $^3J_{\text{HH}} = 8.1$ Hz, 2H, Ar-H), 2.37 (s, 3H, Ar- CH_3). **$^{13}\text{C}\{^1\text{H}\}$ NMR** (126 MHz, CDCl_3 , 295 K) δ /ppm: 139.6 (1C, Ar), 136.7 (1C, Ar), 136.1 (1C, Ar), 127.5 (1C, Ar), 127.4 (1C, Ar), 126.7 (1C, Ar), 20.9 (1C, Ar). **IR** ν_{max} (cm^{-1}): 1740 (s), 1458 (w), 1437 (w), 1366 (m), 1229 (m), 1217 (m), 802 (m) and 536 (w). **HRMS** (EI^+) m/z calculated for $[\text{M}]^+$ [$\text{C}_7\text{H}_6\text{AsClS}_2$] $^+$: 263.88099, found: 263.8810. **Melting point** 67–70 °C.

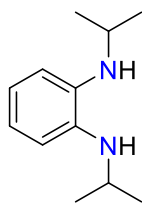
2-chlorobenzo-1,3,2-dithiarsole (**4**)



Arsenic(III) chloride (0.31 g, 1.73 mmol, 1.2 equiv) in CH_2Cl_2 (2 mL) was added dropwise to a solution of benzene dithiol (0.21 g, 1.44 mmol, 1.0 equiv) in CH_2Cl_2 (2 mL) and immediate effervescence occurred. The resulting solution was stirred at ambient temperature for 24 hours, after which the solvent was removed *in vacuo* to give a pale-yellow solid. The resulting yellow solid was washed with pentane (3×2 mL) and again dried *in vacuo*, to give the product 2-chlorobenzo-1,3,2-dithiarsole as a yellow solid. **Yield:** 0.31 g, 1.22 mmol, 85%. Crystals suitable for single crystal X-ray diffraction were grown from a saturated solution of THF.

^1H NMR (500 MHz, CDCl_3 , 295 K) δ /ppm: 7.62 (dd, $^3J_{\text{HH}} = 6.0$ Hz, $^4J_{\text{HH}} = 3.3$ Hz, 2H, Ar-H), 7.24 (dd, $^3J_{\text{HH}} = 6.0$ Hz, $^4J_{\text{HH}} = 3.3$ Hz, 2H, Ar-H). **$^{13}\text{C}\{^1\text{H}\}$ NMR** (126 MHz, CDCl_3 , 295 K) δ /ppm: 139.4 (2C, Ar), 127.0 (2C, Ar), 126.3 (2C, Ar). **IR** ν_{max} (cm^{-1}): 1680 (w), 1481 (w), 1447 (m), 1422 (m), 739 (s), 660 (m) and 339 (m). **HRMS** (EI^+) m/z calculated for $[\text{M}]^+$ [$\text{C}_6\text{H}_4\text{AsClS}_2$] $^+$: 249.86534, found: 249.8655. **Melting point** 62–64 °C.

6.2.2 Synthesis of benzo-fused diazaphopholes and diazarsoles
N,N'-diisopropylbenzene-1,2-diamine (5)

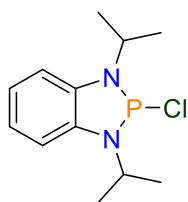


A round-bottomed flask equipped with a magnetic stirrer bar was charged with *o*-phenylenediamine (2.00 g, 18.49 mmol, 1.0 equiv), potassium carbonate (5.10 g, 36.90 mmol, 2.0 equiv) and excess 2-iodopropane (20.40 g, 120.0 mmol, 6.5 equiv). The solution was heated to reflux for 2 hours, after which time the solution was cooled to ambient temperature. Hexane (30 mL) was subsequently added and the mixture was washed with water (50 mL). The product was extracted from the aqueous phase using hexane (3 × 20 mL), the organic phases being combined after each extraction. The solution was dried using anhydrous magnesium sulfate, and the solvent was removed under reduced pressure to afford a viscous dark brown oil. Subsequently, the oil was passed through a silica plug (0.2 cm, toluene) and the solvent was again removed under reduced pressure to give a red-brown oil. The resulting oil was purified further using a Kugelrohr short-path distillation (180 °C, 5 mbar) to yield a colourless oil. **Yield:** 2.9 g, 15.1 mmol, 80%.

¹H NMR (500 MHz, δ /ppm: 6.87–6.85 (m, 2H, Ar-H), 6.80–6.76 (m, 2H, Ar-H), 3.65 (sept, $^3J_{\text{HH}} = 6.3$ Hz, 2H, $\text{CH}(\text{CH}_3)_2$), 3.23 (br s, 2H, NH), 1.32 (d, $^3J_{\text{HH}} = 6.3$ Hz, 12H, $\text{CH}(\text{CH}_3)_2$). **¹³C{¹H} NMR** (126 MHz, CDCl_3 , 295 K) δ /ppm: 136.8 (2C, Ar), 118.9 (2C, Ar), 113.2 (2C, Ar), 44.4 (2C, $\text{CH}(\text{CH}_3)_2$), 23.3 (4C, $\text{CH}(\text{CH}_3)_2$). **IR** ν_{max} (cm^{-1}): 2962 (m), 1599 (m), 1506 (m), 1253 (m), 1177 (m), 741 (m) and 399 (s, sh). **HRMS** (EI⁺) m/z calculated for $[\text{M}]^+$ [$\text{C}_{12}\text{H}_{20}\text{N}_2$]⁺: 192.1626, found: 192.1624.

General Procedure 2. To a solution of *N,N'*-diisopropylbenzene-1,2-diamine (1.0 equiv) dissolved in toluene (40 mL) and cooled to 0 °C, phosphorus(III) chloride (1.2 equiv) or phosphorus(III) bromide (1.2 equiv) and triethylamine (2.4 equiv) were added dropwise. The reaction turned yellow and was allowed to stir at ambient temperature for 24 hours. The solution was filtered *via* filter canula to a new Schlenk tube to remove the ammonium salt generated, after which the solvent was removed *in vacuo* to give a powder. The powder was washed with pentane (3 × 2 mL) and again dried *in vacuo* to give the pure product as a solid powder.

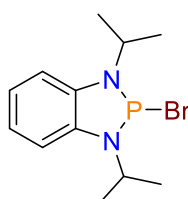
2-chloro-1,3-diisopropyl-benzodiazaphosphole (6a)



Compound **6a** was synthesised according to *general procedure 2* using phosphorus(III) chloride (0.35 mL, 4.00 mmol, 1.2 equiv), *N,N'*-diisopropylbenzene-1,2-diamine (640 mg, 3.33 mmol, 1.0 equiv), and triethylamine (1.11 mL, 8.0 mmol, 2.4 equiv). The product is a yellow powder. **Yield:** 692 mg, 2.70 mmol, 81%. Crystals suitable for single crystal X-ray diffraction were grown from a saturated solution of CH_2Cl_2 with a few drops of pentane added.

$^1\text{H NMR}$ (400 MHz, CDCl_3 , 295 K) δ /ppm: 7.08 (s, 4H, Ar-H), 4.32 (sept, $^3J_{\text{HH}} = 6.6$ Hz, 2H, $\text{CH}(\text{CH}_3)_2$), 1.69 (dd, $^3J_{\text{HH}} = 6.6$ Hz, $^4J_{\text{PH}} = 1.0$ Hz, 12H, $\text{CH}(\text{CH}_3)_2$). $^{13}\text{C}\{^1\text{H}\}$ NMR (101 MHz, CDCl_3 , 295 K) δ /ppm: 136.9 (d, $^2J_{\text{PC}} = 10.5$ Hz, 2C, Ar), 121.3 (2C, Ar), 111.6 (d, $^3J_{\text{PC}} = 1.6$ Hz, 2C, Ar), 48.1 (d, $^2J_{\text{PC}} = 12.7$ Hz, 2C, $\text{CH}(\text{CH}_3)_2$), 22.3 (4C, $\text{CH}(\text{CH}_3)_2$). $^{31}\text{P}\{^1\text{H}\}$ NMR (162 MHz, CDCl_3 , 295 K) δ /ppm: 147.1 (s, 1P). IR ν_{max} (cm^{-1}): 2978 (w), 1487 (m), 1371 (w), 1260 (m), 1159 (m), 930 (m), 741 (s), 492 (m). HRMS (EI^+) m/z calculated for $[\text{M}]^+$ $[\text{C}_{12}\text{H}_{18}\text{PN}_2\text{Cl}]^+$: 256.0896, found 256.0901. **Melting point** 95–98 °C.

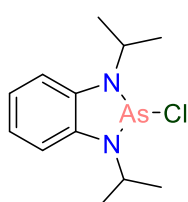
2-bromo-1,3-diisopropyl-benzodiazaphosphole (6b)



Compound **6b** was synthesised according to *general procedure 2* using phosphorus(III) bromide (0.11 mL, 1.19 mmol, 1.2 equiv), *N,N'*-diisopropylbenzene-1,2-diamine (191 mg, 0.99 mmol, 1.0 equiv), and triethylamine (0.3 mL, 2.38 mmol, 2.4 equiv). The product was an orange powder. **Yield:** 227 mg, 0.75 mmol, 76%.

$^1\text{H NMR}$ (400 MHz, CDCl_3 , 295 K) δ /ppm: 7.18–7.17 (m, 4H, Ar-H), 4.44 (sept, $^3J_{\text{HH}} = 6.6$ Hz, 2H, $\text{CH}(\text{CH}_3)_2$), 1.76 (dd, $^3J_{\text{HH}} = 6.6$ Hz, $^4J_{\text{PH}} = 1.0$ Hz, 12H, $\text{CH}(\text{CH}_3)_2$). $^{13}\text{C}\{^1\text{H}\}$ NMR (101 MHz, CDCl_3 , 295 K) δ /ppm: 137.2 (d, $^2J_{\text{PC}} = 10.2$ Hz, 2C, Ar), 122.3 (2C, Ar), 112.4 (d, $^3J_{\text{PC}} = 1.6$ Hz, 2C, Ar), 49.0 (d, $^2J_{\text{PC}} = 11.8$ Hz, 2C, $\text{CH}(\text{CH}_3)_2$), 21.8 (d, $^3J_{\text{PC}} = 1.6$ Hz, 4C, $\text{CH}(\text{CH}_3)_2$). $^{31}\text{P}\{^1\text{H}\}$ NMR (162 MHz, CDCl_3 , 295 K) δ /ppm: 169.2 (s, 1P). IR ν_{max} (cm^{-1}): 1477 (m), 1369 (m), 1288 (w), 1159 (m), 1007 (m), 932 (m) and 752 (m). HRMS (EI^+) m/z calculated for $[\text{M}]^+$ $[\text{C}_{12}\text{H}_{18}\text{BrN}_2\text{P}]^+$: 300.0391, found: 300.0384. **Melting point** 100–106 °C.

2-chloro-1,3-diisopropyl-benzodiazarsole (7)



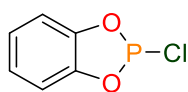
N,N'-diisopropylbenzene-1,2-diamine (**5**) (450 mg, 2.33 mmol, 1.0 equiv) was added to toluene (10 mL). Arsenic(III) chloride (510 mg, 2.80 mmol, 1.2 equiv) was then added dropwise and the resulting solution was cooled to 0 °C using an ice bath. To this triethylamine (0.78 mL, 5.59 mmol,

2.4 equiv) was added dropwise; the reaction was slowly warmed to ambient temperature and left to stir overnight. With the use of a filter cannula, the solution was transferred to a new Schlenk tube and the solvent was removed *in vacuo* to give the product as a yellow solid. **Yield:** 0.55 g, 1.82 mmol, 78%. Crystals suitable for single crystal X-ray diffraction were grown from a saturated solution of CH₂Cl₂ with a few drops of pentane added.

¹H NMR (500 MHz, CDCl₃, 295 K) δ/ppm: 7.04 (s, 4H, Ar-H), 4.46 (sept, ³J_{HH} = 6.5 Hz, 2H, CH(CH₃)₂), 1.70 (d, ³J_{HH} = 6.5 Hz, 12H, CH(CH₃)₂). **¹³C{¹H} NMR** (126 MHz, CDCl₃, 295 K) δ/ppm: 139.1 (2C, Ar), 120.7 (2C, Ar), 111.8 (2C, Ar), 49.1 (2C, CH(CH₃)₂), 23.5 (4C, CH(CH₃)₂). **IR** ν_{max} (cm⁻¹): 2974 (w), 1477 (m), 1388 (m), 1292 (s, sh), 1153 (m), 998 (m), 891 (m), 745 (m), 550 (m) and 473 (m). **HRMS** (ES⁺) *m/z* calculated for [M]⁺ [C₁₂H₁₈AsN₂Cl]⁺: 300.0374, found: 300.0376. **Melting point** 96–99 °C.

General Procedure 3. A solution of catechol (1.0 equiv) in toluene (40 mL) was cooled to 0 °C, phosphorus(III) chloride (1.2 equiv) or phosphorus(III) bromide (1.2 equiv) and triethylamine (2.4 equiv) were added dropwise. The reaction immediately turned yellow and was left to stir at ambient temperature for 24 hours. The solution was filtered *via* filter cannula to a new Schlenk tube to remove the ammonium salt generated, after which the solvent was removed *in vacuo* to give a yellow oil. ³¹P NMR spectroscopy revealed that this oil contained a mixture of both product and an unidentified side product. Therefore, the oil was subjected to an air sensitive distillation, in which the pure product distils with heating and under vacuum (5 mbar) to give the product as a colourless oil.

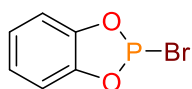
6.2.3 Synthesis of benzo-fused dioxaphospholes 2-chlorobenzo-1,3,2-dioxaphosphole (**8a**)



Compound **8a** was synthesised according to *general procedure 3* using phosphorus(III) chloride (3.0 mL, 34.90 mmol, 1.2 equiv), catechol (3.20 g, 29.06 mmol, 1.0 equiv) and triethylamine (9.7 mL, 69.80 mmol, 2.4 equiv). Distils at 44–52 °C under vacuum (5 mbar). **Yield:** 1.84 g, 10.5 mmol, 36%.

¹H NMR (500 MHz, CDCl₃, 295 K) δ/ppm: 7.19–7.17 (m, 2H, Ar-H), 7.07–7.05 (m, 2H, Ar-H). **¹³C{¹H} NMR** (126 MHz, CDCl₃, 295 K) δ/ppm: 144.4 (d, ²J_{PC} = 7.5 Hz, 2C, Ar), 124.5 (2C, Ar), 114.2 (d, ³J_{PC} = 0.9 Hz, 2C, Ar). **³¹P{¹H} NMR** (202 MHz, CDCl₃, 295 K) δ/ppm: 173.6 (s, 1P). **IR** ν_{max} (cm⁻¹): 1470 (s), 1327 (w), 1217 (s), 1092 (w), 1009 (w), 893 (s), 739 (s), 716 (sh) and 617 (m). **HRMS** (EI⁺) *m/z* calculated for [M]⁺ [C₆H₄ClO₂P]⁺: 173.9637, found: 173.9640.

2-bromobenzo-1,3,2-dioxaphosphole (8b)



Compound **8b** was synthesised according to *general procedure 3* using phosphorus(III) bromide (1.30 mL, 13.90 mmol, 1.2 equiv), catechol (1.27 g, 11.53 mmol, 1.0 equiv) and triethylamine (3.9 mL, 27.80 mmol, 2.4 equiv). Distills at 60–62 °C under vacuum (5 mbar). **Yield:** 1.04 g, 4.76 mmol, 41%.

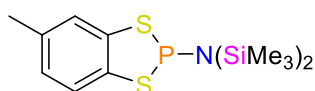
¹H NMR (500 MHz, CDCl₃, 295 K) δ/ppm: 7.31 (ddd, ³J_{HH} = 5.9 Hz, ⁴J_{HH} = 3.4 Hz, ⁴J_{PH} = 0.8 Hz, 2H, Ar–H), 7.19 (dd, ³J_{HH} = 5.9 Hz, ⁴J_{HH} = 3.4 Hz, 2H, Ar–H). **¹³C{¹H} NMR** (126 MHz, CDCl₃, 295 K) δ/ppm: 144.8 (d, ²J_{PC} = 7.5 Hz, 2C, Ar), 124.7 (2C, Ar), 114.4 (d, ³J_{PC} = 1.0 Hz, 2C, Ar). **³¹P{¹H} NMR** (202 MHz, CDCl₃, 295 K) δ/ppm: 195.3 (s, 1P). **IR** ν_{max} (cm⁻¹): 1497 (s), 1422 (sh), 1169 (m, br), 1098 (m), 984 (m), 937 (m), 826 (m) and 748 (m). **HRMS** (EI⁺) *m/z* calculated for [M]⁺ [C₆H₄BrO₂P]⁺: 217.9132, found: 217.9135.

Chapter 6.3 Experimental for Reactivity of Dithiaphospholes, Dithiarsoles, Diazaphospholes and Diazarsoles

6.3.1 Synthesis of paddlewheel complexes

General Procedure 4. The starting dithiaphosphole or dithiarsole **1a** or **3** (1.0 equiv) dissolved in toluene (5 mL) was added dropwise to lithium bis(trimethylsilyl)amide (1.0 equiv) dissolved in toluene (5 mL) at 0 °C, using an ice bath. The reaction was allowed to slowly warm to ambient temperature and left to stir for 18 hours. LiCl salt was removed *via* filter cannula of the yellow solution, and the solvent was removed *in vacuo* to give the product as a yellow oil.

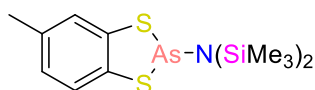
5-methyl-N,N-bis(trimethylsilyl)benzo-1,3,2-dithiaphosphol-2-amine (**9**)



Compound **9** was synthesised according to *general procedure 4* using dithiaphosphole **1a** (241 mg, 1.09 mmol, 1.0 equiv) and lithium bis(trimethylsilyl)amide (183 mg, 1.09 mmol, 1.0 equiv). **Yield:** 354 mg, 1.02 mmol, 94%.

¹H NMR (500 MHz, CDCl₃, 295 K) δ/ppm: 7.38 (d, ³J_{HH} = 8.0 Hz, 1H, Ar-H), 7.33 (s, 1H, Ar-H), 6.96 (d, ³J_{HH} = 8.0 Hz, 1H, Ar-H), 2.36 (s, 3H, CH₃), 0.27 (d, ⁴J_{PH} = 1.9 Hz, 18H, SiMe₃). **¹³C{¹H} NMR** (126 MHz, CDCl₃, 295 K) δ/ppm: 141.1 (1C, Ar), 137.7 (1C, Ar), 134.9 (1C, Ar), 126.2 (1C, Ar), 124.7 (d, ²J_{PC} = 8.3 Hz, 1C, Ar), 123.9 (d, ²J_{PC} = 8.3 Hz, 1C, Ar), 20.9 (1C, Ar-CH₃), 4.26 (d, ¹J_{SiC} = 9.7 Hz, 6C, SiMe₃). **³¹P{¹H} NMR** (202 MHz, CDCl₃, 295 K) δ/ppm: 93.9 (s, 1P). **IR** ν_{max} (cm⁻¹): 1740 (s), 1458 (w), 1437 (w), 1366 (m), 1254 (w), 1229 (m), 1217 (m), 802 (m), 685 (w) and 536 (m). **HRMS** (ES⁺) *m/z* calculated for [M+H]⁺ [C₁₃H₂₅NSi₂PS₂]⁺: 346.0705, found: 346.0714.

5-methyl-N,N-bis(trimethylsilyl)benzo-1,3,2-dithiarsole-2-amine (**11**)



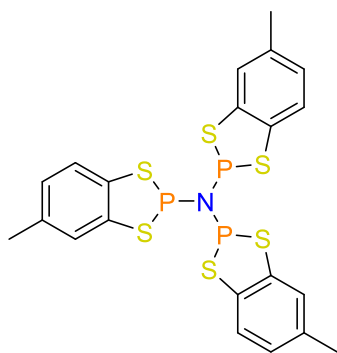
Compound **11** was synthesised according to *general procedure 4* using dithiarsole **3** (0.519g, 1.96 mmol, 1.0 equiv) and lithium bis(trimethylsilyl)amide (0.328 g, 1.96 mmol, 1.0 equiv). **Yield:** 0.252 g, 0.65 mmol, 33%.

¹H NMR (500 MHz, CDCl₃, 295 K) δ/ppm: 7.25 (s, 1H, Ar-H), 7.20 (s, 1H, Ar-H), 6.84 (d, ³J_{HH} = 7.4 Hz, 1H, Ar-H), 2.28 (s, 3H, CH₃), 0.16 (s, 18H, SiMe₃). **¹³C{¹H} NMR** (126 MHz, CDCl₃, 295 K) δ/ppm: 141.6(1C, Ar), 138.1 (1C, Ar), 134.8 (1C, Ar), 126.4 (1C, Ar), 126.0 (1C, Ar), 125.7 (1C, Ar), 20.8 (1C, Ar-CH₃), 4.7(6C, SiMe₃). **IR** ν_{max} (cm⁻¹): 1458 (s), 1252 (w), 907 (s),

827 (w), 681 (w) and 496 (s). **HRMS** (EI⁺) *m/z* calculated for [M]⁺ [C₁₃H₂₄NAsS₂Si₂]⁺: 389.00992, found: 389.0101.

General Procedure 5. The intermediates **9** or **11** (1.0 equiv) in MeCN (10 mL) was added dropwise to a solution of dithiaphosphole **1a** or dithiarsole **3** (2.0 equiv) in MeCN (10 mL) at 0 °C. The mixture was allowed to slowly warm to ambient temperature before being heated to reflux for 16 hours. The resulting solution was cooled in an ice bath at 0 °C for three hours to give a white precipitate. The MeCN was removed *via* filter cannula and the white solid was washed with pentane (3 × 10 mL). After which the solid was dried *in vacuo* to give the product as a white solid.

tris(5-methylbenzo-1,3,2-dithiaphosphol-2-yl)amine (10)

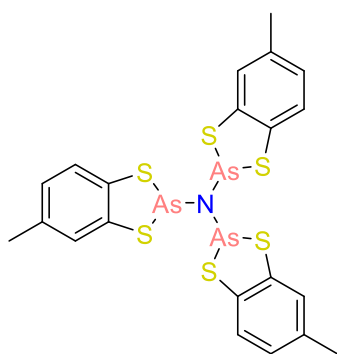


Compound **10** was synthesised according to *general procedure 5* using intermediate **9** (300 mg, 0.91 mmol, 1.0 equiv) and dithiaphosphole **1a** (401 mg, 1.82 mmol, 2.0 equiv). **Yield:** 451 mg, 0.79 mmol, 87%.

¹H NMR (500 MHz, CDCl₃, 295 K) δ/ppm: 7.42 (d, ³J_{HH} = 8.1 Hz, 1H, Ar-H), 7.36 (s, 1H, Ar-H), 6.99 (d, ³J_{HH} = 8.1 Hz, 1H, Ar-H), 2.34 (s, 3H, CH₃). **¹³C{¹H} NMR** (126 MHz, CDCl₃, 295 K)

δ/ppm: 139.7 (1C, Ar), 136.3 (1C, Ar), 136.1 (1C, Ar), 127.3 (1C, Ar), 125.1 (1C, Ar), 124.3 (1C, Ar), 21.1 (1C, Ar-CH₃). **³¹P{¹H} NMR** (202 MHz, CDCl₃, 295 K) δ/ppm: 86.6 (s, 1P). **IR** ν_{max} (cm⁻¹): 1456 (m), 1375 (w), 1258 (w), 1115 (w), 775 (br, s) and 685 (w). **HRMS** (AP⁺) *m/z* calculated for [M+H]⁺ [C₂₁H₁₉NP₃S₆]⁺: 569.9055, found: 569.9059. **Melting point** 150-152 °C.

5-methyl-N,N-bis(trimethylsilyl)benzo-1,3,2-dithiarsole-2-amine (11)



Compound **12** was synthesised according to *general procedure 5* using intermediate **11** (287 mg, 0.737 mmol, 1.0 equiv) and dithiaphosphole **1a** (389 mg, 1.47 mmol, 2.0 equiv). **Yield:** 0.208 g, 0.30 mmol, 40%.

¹H NMR (500 MHz, CDCl₃, 295 K) δ/ppm: 7.35(d, ³J_{HH} = 8.1 Hz, 3H, Ar-H), 7.28 (s, 3H, Ar-H), 6.92 (d, ³J_{HH} = 8.1 Hz, 3H, Ar-H), 2.32 (s, 9H, CH₃). **¹³C{¹H} NMR** (126 MHz, CDCl₃, 295 K)

δ/ppm: 140.6 (3C, Ar), 137.1 (3C, Ar), 135.9 (3C, Ar), 126.9 (3C, Ar), 126.7 (3C, Ar), 126.0 (3C, Ar), 20.9 (3C, CH₃). **IR** ν_{max} (cm⁻¹): 1456 (w), 1256 (w), 1032 (w), 860 (w), 796 (s), 692 (s) and

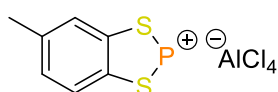
442 (s). **HRMS** (ES⁺) *m/z* calculated for [M+H]⁺ [C₂₁H₁₉S₆As₃N]⁺: 701.7490, found 701.7516.

Melting point 78–82 °C.

6.3.2 Synthesis of cationic complexes

General procedure 6. Dithiaphosphole **1a** or dithiarsole **3** (1.0 equiv) in CH₂Cl₂ (3 mL) was added to the halide abstracting reagent (1.0 equiv) in CH₂Cl₂ (2 mL) and left to stir at ambient temperature for six hours. After this the solvent was removed *in vacuo* and washed with pentane (3 × 2 mL) and dried again *in vacuo*, giving the products **13a**, **13b**, **14a** or **14b** as red/ orange solids. Single crystals suitable for X-ray diffraction were grown from a concentrated solution of CH₂Cl₂ with a few drops of pentane and cooled to –40 °C or from slow evaporation of CH₂Cl₂.

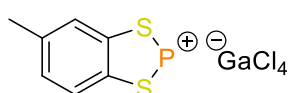
5-methylbenzo-1,3,2-dithiaphosphenium tetrachloroaluminate (**13a**)



Compound **13a** was synthesised according to *general procedure 6* as a highly air sensitive orange powder using dithiaphosphole **1a** (103 mg, 0.47 mmol, 1.0 equiv) and aluminium trichloride (62 mg, 0.47 mmol, 1.0 equiv). Multinuclear NMR spectroscopy showed hydrolysis product and thus not included. **Yield:** 139 mg, 0.39 mmol, 83%.

HRMS (EI⁺) *m/z* calculated for [M]⁺ [C₇H₆PS₂]⁺: 184.9649, found: 184.9649. **IR** ν_{\max} (cm⁻¹): 1582 (w), 1458 (m), 1381 (w), 1261 (w), 1168 (br, m), 964 (br, m), and 802 (w). **Melting point** 126–130 °C.

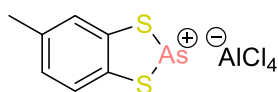
5-methylbenzo-1,3,2-dithiaphosphenium tetrachlorogalate (**13b**)



Compound **13b** was synthesised according to *general procedure 6* as a highly air sensitive orange powder using dithiaphosphole **1a** (347 mg, 1.57 mmol, 1.0 equiv) and gallium trichloride (277 mg, 1.57 mmol, 1.0 equiv). Multinuclear NMR spectroscopy showed hydrolysis product and thus not included. **Yield:** 492 mg, 1.24 mmol, 79%.

HRMS (EI⁺) *m/z* calculated for [M]⁺ [C₇H₆PS₂]⁺: 184.9649, found: 184.9650. **IR** ν_{\max} (cm⁻¹): 1582 (w), 1462 (m), 1383 (w), 1312 (w), 1099 (br, s), 966 (br, m), 872 (w) and 810 (s). **Melting point** 104–106 °C.

5-methylbenzo-1,3,2-dithiarsenium tetrachloroaluminate (**14a**)

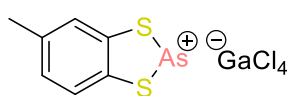


Compound **14a** was synthesised according to *general procedure 6* as a red-yellow solid using dithiarsole **3** (66 mg, 0.25 mmol,

1.0 equiv) and aluminium trichloride (33 mg, 0.25 mmol, 1.0 equiv). **Yield:** 89 mg, 0.22 mmol, 89%.

¹H NMR (500 MHz, C₆D₆, 295 K) δ/ppm: 7.03 (d, ³J_{HH} = 8.1 Hz, 1H, Ar–H), 6.88 (s, 1H, Ar–H), 6.47 (d, ³J_{HH} = 8.1 Hz, 1H, Ar–H), 1.82 (s, 3H, CH₃). **¹³C{¹H} NMR** (126 MHz, C₆D₆, 295 K) δ/ppm: 141.1 (1C, Ar), 137.6 (1C, Ar), 136.5 (1C, Ar), 127.5 (1C, Ar), 127.4 (1C, Ar), 126.6 (1C, Ar), 20.4 (1C, CH₃). **²⁷Al NMR** (130 MHz, C₆D₆, 295 K) δ/ppm: 104.6 (s, AlCl₄[−]). **IR** ν_{max} (cm^{−1}): 1638 (w), 1456 (w), 1115 (w), 808 (s) and 484 (s). **HRMS** (EI⁺) *m/z* calculated for [M]⁺ [C₇H₆S₂As]⁺: 228.9121, found: 228.9131. **Melting point** 108–110 °C.

5-methylbenzo-1,3,2-dithiarsenium tetrachlorogalate (**14b**)

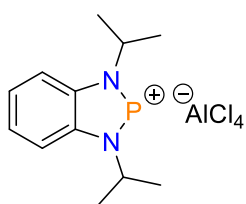


Compound **14b** was synthesised according to *general procedure 6* as a red-yellow solid using dithiarsole **3** (61 mg, 0.23 mmol, 1.0 equiv) and aluminium trichloride (40 mg, 0.23 mmol, 1.0 equiv). **Yield:** 83 mg, 0.19 mmol, 82%.

¹H NMR (500 MHz, C₆D₅Br, 295 K) δ/ppm: 7.03 (d, ³J_{HH} = 8.5 Hz, 1H, Ar–H), 6.81 (s, 1H, Ar–H), 6.52 (dd, ³J_{HH} = 8.5 Hz, ⁴J_{HH} = 1.0 Hz, 1H, Ar–H), 1.61 (s, 1H, Ar–H). **¹³C{¹H} NMR** (126 MHz, C₆D₅Br, 295 K) δ/ppm: 151.8 (1C, Ar), 148.7 (1C, Ar), 140.3 (1C, Ar), 130.3 (1C, Ar), 127.6 (1C, Ar), 127.3 (1C, Ar), 20.7 (1C, CH₃). **IR** ν_{max} (cm^{−1}): 1585 (s), 1528 (s), 1444 (s), 1371 (s), 1256 (s), 1101 (s), 808 (s), 750 (s), 689 (s), 538 (w) and 432 (s). **HRMS** (EI⁺) *m/z* calculated for [M]⁺ [C₇H₆S₂As]⁺: 228.9121, found 228.9132. **Melting point** 116–120 °C.

General Procedure 7. Compound **6a** (1.0 equiv) or **7** (1.0 equiv) was dissolved in CH₂Cl₂ (2 mL) and added to a stirred solution of the halide abstracting reagent (1.0 equiv) in CH₂Cl₂ (2 mL). The red/ orange solution was stirred for 2 hours at ambient temperature, after which the solvent was removed *in vacuo* to afford a red-yellow solid. The solid was washed with pentane (3 × 2 mL) and further dried *in vacuo* to afford the products **15a–c** and **16a–c**. Single crystals suitable for X-ray diffraction were grown from a concentrated solution of CH₂Cl₂ with a few drops of pentane and cooled to −40 °C.

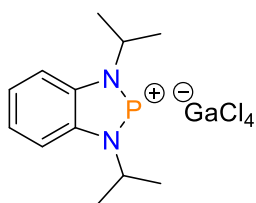
1,3-diisopropyl-benzodiphosphenium tetrachloroaluminate (**15a**)



Compound **15a** was synthesised according to *general procedure 7* using diazaphosphole **6a** (100 mg, 0.39 mmol, 1.0 equiv) and aluminium trichloride (52 mg, 0.39 mmol, 1.0 equiv). **Yield:** 121 mg, 0.31 mmol, 80%.

¹H NMR (500 MHz, C₆D₅Br, 295 K) δ/ppm: 7.30 (br m, 2H, Ar–H), 7.22 (br m, 2H, Ar–H), 4.45 (sept, ³J_{HH} = 6.2 Hz, 2H, CH(CH₃)₂), 1.50 (d, ³J_{HH} = 6.2 Hz, 12H, CH(CH₃)₂). **¹³C{¹H} NMR** (126 MHz, C₆D₅Br, 295 K) δ/ppm: 129.8 (2C, Ar), 118.8 (2C, Ar), 105.4 (2C, Ar), 43.7 (2C, CH(CH₃)₂), 15.0 (4C, CH(CH₃)₂). **³¹P{¹H} NMR** (202 MHz, C₆D₅Br, 295 K) δ/ppm: 207.7 (s, 1P). **²⁷Al NMR** (130 MHz, C₆D₅Br, 295 K) δ/ppm: 103.8 (s, 1 Al, AlCl₄⁻). **IR** ν_{max} (cm⁻¹): 2982 (m), 1585 (w), 1466 (m), 1393 (m), 1153 (m), 1008 (w), 930 (w), 748 (s, sh) and 496 (m). **HRMS** (EI⁺) *m/z* calculated for [M]⁺ [C₁₂H₁₈N₂P]⁺: 221.1208, found: 221.1209. **Melting point** 101–104 °C.

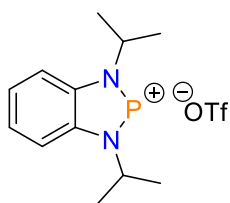
1,3-diisopropyl-benzodiphosphenium tetrachlorogallate (15b)



Compound **15b** was synthesised according to *general procedure 7* using diazaphosphole **6a** (100 mg, 0.39 mmol, 1.0 equiv) and gallium trichloride (69 mg, 0.39 mmol, 1.0 equiv). **Yield:** 143 mg, 0.33 mmol, 85%.

¹H NMR (500 MHz, C₆D₅Br, 295 K) δ/ppm: 7.34 (br m, 2H, Ar–H), 7.24 (br m, 2H, Ar–H), 4.49 (sept, ³J_{HH} = 6.3 Hz, 2H, CH(CH₃)₂), 1.51 (d, ³J_{HH} = 6.3 Hz, 12H, CH(CH₃)₂). **¹³C{¹H} NMR** (126 MHz, C₆D₅Br, 295 K) δ/ppm: 129.9 (2C, Ar), 119.3 (2C, Ar), 105.6 (2C, Ar), 44.0 (2C, CH(CH₃)₂), 15.2 (4C, CH(CH₃)₂). **³¹P{¹H} NMR** (202 MHz, C₆D₅Br, 295 K) δ/ppm: 212.9 (s, 1P). **IR** ν_{max} (cm⁻¹): 2985 (w), 1566 (w), 1472(w), 1395 (w), 1346 (w), 1153 (m), 1115 (m), 989 (m) and 746 (s, sh). **HRMS** (EI⁺) *m/z* calculated for [M]⁺ [C₁₂H₁₈N₂P]⁺: 221.1208, found: 221.1205. **Melting point** 96–99 °C.

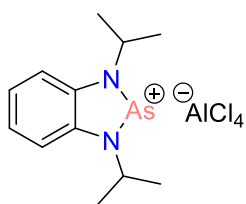
1,3-diisopropyl-benzodiphosphenium triflate (15c)



Compound **15c** was synthesised according to *general procedure 7* using diazaphosphole **6a** (70 mg, 0.27 mmol, 1.0 equiv) and trimethylsilyl trifluoromethanesulfonate (73 mg, 0.33 mmol, 1.2 equiv). **Yield:** 88 mg, 0.24 mmol, 87%.

¹H NMR (400 MHz, CDCl₃, 295 K) δ/ppm: 7.71–7.69 (m, 2H, Ar–H), 7.63–7.60 (m, 2H, Ar–H), 4.98 (sept, ³J_{HH} = 6.6 Hz, 2H, CH(CH₃)₂), 1.87 (dd, ³J_{HH} = 6.6 Hz, ⁴J_{PH} = 1.3 Hz, 12H, CH(CH₃)₂). **¹³C{¹H} NMR** (101 MHz, CDCl₃, 295 K) δ/ppm: 138.6 (d, ²J_{PC} = 6.0 Hz, 2C, Ar), 127.2 (2C, Ar), 114.3 (2C, Ar), 52.6 (d, ²J_{PC} = 10.8 Hz, 2C, CH(CH₃)₂), 23.9 (4C, CH(CH₃)₂). **³¹P{¹H} NMR** (162 MHz, CDCl₃, 295 K) δ/ppm: 216.0 (s, 1P). **¹⁹F{¹H} NMR** (376 MHz, CDCl₃, 295 K) δ/ppm: -78.4 (s, 3F, O₃SCF₃⁻). **IR** ν_{max} (cm⁻¹): 2992 (w), 1474 (w), 1395 (w), 1377 (w), 1246 (s), 1151 (s), 1022 (s), 754 (s), 627 (s), 571 (s), 513 (s), 496 (s) and 417 (m). **HRMS** (EI⁺) *m/z* calculated for [M]⁺ [C₁₂H₁₈N₂P]⁺: 221.1208, found: 221.1207. **Melting point** 108–112 °C.

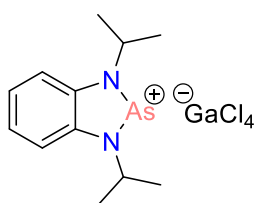
1,3-diisopropyl-benzodiarsenium tetrachloroaluminate (**16a**)



Compound **16a** was synthesised according to *general procedure 7* using diazarsole **7** (100 mg, 0.33 mmol, 1.0 equiv) and aluminium trichloride (44 mg, 0.33 mmol, 1.0 equiv). **Yield:** 124 mg, 0.29 mmol, 87%.

¹H NMR (500 MHz, C₆D₅Br, 295 K) δ /ppm: 7.19 (br m, 2H, Ar-H), 7.04 (br m, 2H, Ar-H), 4.43 (br m, 2H, CH(CH₃)₂), 1.49 (d, ³J_{HH} = 6.2 Hz, 12H, CH(CH₃)₂). **¹³C{¹H} NMR** (126 MHz, C₆D₅Br, 295 K) δ /ppm: 132.4 (2C, Ar), 117.1 (2C, Ar), 105.0 (2C, Ar), 43.8 (2C, CH(CH₃)₂), 15.9 (4C, CH(CH₃)₂). **²⁷Al NMR** (130 MHz, C₆D₅Br, 295 K) δ /ppm: 104.5 (s, 1 Al, AlCl₄⁻). **IR** ν_{\max} (cm⁻¹): 2992 (w), 1568 (w), 1393 (w), 1172 (w), 1153 (w), 989 (w), 746 (m) and 467 (s, br). **HRMS** (ES⁺) m/z calculated for [M]⁺ [C₁₂H₁₈AsN₂]⁺: 265.0686, found: 265.0692. **Melting point** 105–109 °C.

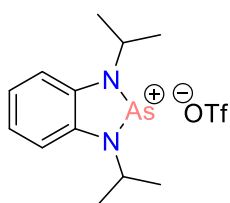
1,3-diisopropyl-benzodiarsenium tetrachlorogallate (**16b**)



Compound **16b** was synthesised according to *general procedure 7* using diazarsole **7** (100 mg, 0.33 mmol, 1.0 equiv) and gallium trichloride (8 mg, 0.33 mmol, 1.0 equiv). **Yield:** 132 mg, 0.28 mmol, 84%.

¹H NMR (500 MHz, C₆D₅Br, 295 K) δ /ppm: 7.26 (m, 2H, Ar-H), 7.11 (m, 2H, Ar-H), 4.54 (sept, ³J_{HH} = 6.3 Hz, 2H, CH(CH₃)₂), 1.51 (d, ³J_{HH} = 6.3 Hz, 12H, CH(CH₃)₂). **¹³C{¹H} NMR** (126 MHz, C₆D₅Br, 295 K) δ /ppm: 133.1 (2C, Ar), 118.7 (2C, Ar), 105.7 (2C, Ar), 45.0 (2C, CH(CH₃)₂), 16.4 (4C, CH(CH₃)₂). **IR** ν_{\max} (cm⁻¹): 2980 (m), 1566 (w), 1462 (w), 1393 (w), 1375 (w), 1269 (w), 1153 (m), 949 (w, br) and 746 (m). **HRMS** (ES⁺) m/z calculated for [M]⁺ [C₁₂H₁₈AsN₂]⁺: 265.0686, found: 265.0692; m/z calculated for [M]⁻ [GaCl₄]⁻: 208.8010, found: 208.8014. **Melting point** 80–82 °C.

1,3-diisopropyl-benzodiphosphenium triflate (**16c**)



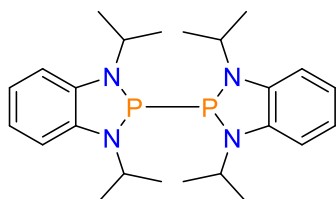
Compound **16c** was synthesised according to *general procedure 7* using diazarsole **7** (100 mg, 0.33 mmol, 1.0 equiv) and trimethylsilyl trifluoromethanesulfonate (88 mg, 0.40 mmol, 1.2 equiv). **Yield:** 112 mg, 0.27 mmol, 82%.

¹H NMR (500 MHz, CDCl₃, 295 K) δ /ppm: 7.59 (br m, 2H, Ar-H), 7.53 (br m, 2H, Ar-H), 5.06 (sept, ³J_{HH} = 6.2 Hz, 2H, CH(CH₃)₂), 1.90 (d, ³J_{HH} = 6.2 Hz, 12 H, CH(CH₃)₂). **¹³C{¹H} NMR** (126 MHz, CDCl₃, 295 K) δ /ppm: 141.4 (2C, Ar), 126.4 (2C, Ar), 114.3 (2C, Ar), 53.4 (2C,

$\underline{\text{C}}\text{H}(\underline{\text{C}}\text{H}_3)_2$, 24.8 (4C, $\underline{\text{C}}\text{H}(\underline{\text{C}}\text{H}_3)_2$). ^{19}F NMR (471 MHz, CDCl_3 , 295 K) δ/ppm : -78.1 (s, 3F, O_3SCF_3^-). IR ν_{max} (cm^{-1}): 2988 (w), 1466 (w), 1393 (w), 1248 (s), 1144 (s), 1024 (s), 766 (m), 633 (s), 571 (m) and 515 (m). HRMS (ES^+) m/z calculated for $[\text{M}]^+$ [$\text{C}_{12}\text{H}_{18}\text{AsN}_2$] $^+$: 265.0686, found: 265.0689; m/z calculated for $[\text{M}]^-$ [$\text{CF}_3\text{O}_3\text{S}$] $^-$: 148.9520, found: 148.9524. **Melting point** 108–112 °C.

6.3.3 Synthesis of dimeric species

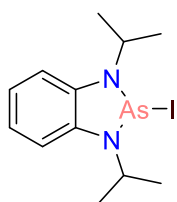
1,3-diisopropyl-benzodiazaphosphoryl dimer (**17**)



The diazaphosphole **6a** (300 mg, 1.17 mmol, 1.0 equiv) was dissolved in THF (5 mL) and magnesium turnings (43 mg, 1.76 mmol, 1.5 equiv) were added. A crystal of iodine was added to initiate the reaction, which was then vigorously stirred for 24 hours. The resulting orange solution was removed *in vacuo* and CH_2Cl_2 (5 mL) was added, after which the solution was filtered twice through Celite to remove any traces of magnesium chloride. The solvent was again removed *in vacuo* and the resulting powder was washed with pentane (3×2 mL) and dried *in vacuo* to give the pure product as a solid yellow/orange powder. **Yield**: 404 mg, 0.91 mmol, 78%. Single crystals suitable for X-ray diffraction were grown from a saturated solution of CH_2Cl_2 with a few drops of pentane and cooled to -40 °C.

^1H NMR (400 MHz, C_6D_6 , 295 K) δ/ppm : 6.98–6.96 (m, 4H, Ar-H), 6.74–6.72 (m, 4H, Ar-H), 3.63 (sept, $^3J_{\text{HH}} = 6.5$ Hz, 4H, $\underline{\text{C}}\text{H}(\underline{\text{C}}\text{H}_3)_2$), 1.44 (d, $^3J_{\text{HH}} = 6.5$ Hz, 12H, $\text{CH}(\underline{\text{C}}\text{H}_3)_2$) and 1.05 (d, $^3J_{\text{HH}} = 6.5$ Hz, 12H, $\text{CH}(\underline{\text{C}}\text{H}_3)_2$). $^{13}\text{C}\{^1\text{H}\}$ NMR (101 MHz, C_6D_6 , 295 K) δ/ppm : 144.7 (4C, Ar), 120.3 (4C, Ar), 113.3 (4C, Ar), 50.2 (4C, $\underline{\text{C}}\text{H}(\underline{\text{C}}\text{H}_3)_2$), 23.8 (4C, $\text{CH}(\underline{\text{C}}\text{H}_3)_2$), 21.4 (4C, $\text{CH}(\underline{\text{C}}\text{H}_3)_2$). $^{31}\text{P}\{^1\text{H}\}$ NMR (162 MHz, C_6D_6 , 295 K) δ/ppm : 87.2 (s, 2P). IR ν_{max} (cm^{-1}): 2978 (m), 1471 (m), 1377 (m), 1248 (m), 1157 (m, br), 1028 (w), 878 (m), 731 (m), 634 (m) and 544 (m). HRMS (EI^+) m/z calculated for $[\text{M}]^+$ [$\text{C}_{12}\text{H}_{18}\text{N}_2\text{P}$] $^+$: 221.1208, found: 221.1211. **Melting point** 142–146 °C.

2-chloro-1,3-diisopropyl-benzodiazarsole (**18**)



The diazarsole **7** (41 mg, 0.14 mmol, 1.0 equiv) was dissolved in THF (2 mL) and magnesium turnings (5 mg, 0.21 mmol, 1.5 equiv) were added. A crystal of iodine was added to initiate the reaction, which was then vigorously stirred for 24 hours. The resulting solution was removed *in vacuo* and CH_2Cl_2 (5 mL) was added, after which the solution was filtered twice through Celite to remove any traces of magnesium chloride. The solvent was again removed *in vacuo*

and the resulting powder was washed with pentane (3 × 2 mL) and dried *in vacuo* to give the pure product as a solid dark red/black powder. **Yield:** 33 mg, 0.08 mmol, 60%. Single crystals suitable for X-ray diffraction were grown from a saturated solution of CH₂Cl₂ with a few drops of pentane and cooled to -40 °C.

¹H NMR (500 MHz, CDCl₃, 295 K) δ/ppm: 7.12 (s, 4H, Ar-H), 4.58 (sept, ³J_{HH} = 5.9 Hz, 2H, CH(CH₃)₂), 1.74 (d, ³J_{HH} = 5.9 Hz, 12H, CH(CH₃)₂). **¹³C{¹H} NMR** (126 MHz, CDCl₃, 295 K) δ/ppm: 139.6 (2C, Ar), 121.6 (2C, Ar), 112.5 (2C, Ar), 50.0 (2C, CH(CH₃)₂) and 22.2 (4C, CH(CH₃)₂). **IR** ν_{max} (cm⁻¹): 2970 (w), 1473 (m), 1389 (m), 1294 (m), 1260 (m), 1153 (m), 1018 (w), 995 (w), 889(w), 739 (m) and 552 (w). **HRMS** (ES⁺) m/z calculated for [M]⁺ [C₁₂H₁₈AsN₂]⁺: 265.0686, found: 265.0675. **Melting point** 114–116 °C.

6.3.4 Photophysical studies

UV–vis studies were performed on a Shimadzu UV-1800 spectrophotometer with deaerated chloroform or acetonitrile solutions (1 × 10⁻⁵ M) as stated. Photophysical data were obtained on a JobinYvon-Horiba Fluorolog spectrometer fitted with a JY TBX picosecond photodetection module with chloroform or acetonitrile solutions as stated. Emission spectra were uncorrected, and excitation spectra were instrument corrected. The pulsed source was a Nano-LED configured for 295 nm output operating at 1 MHz. Luminescence lifetime profiles were obtained using the JobinYvon-Horiba FluoroHub single photon counting module, and the data fits yielded the lifetime values using the provided DAS6 deconvolution software. Quantum yield measurements were obtained on aerated solutions of the compounds using anthracene in deaerated ethanol as a standard (Φ = 0.27).¹

6.3.5 Electron paramagnetic resonance (EPR) studies

The continuous wave (CW) X-band EPR measurements were performed on a Bruker EMX spectrometer utilising an ER4119HS resonator, using 100 kHz field modulation, 1.0 mW microwave power, and <1 G modulation amplitude, at 298 K or 350 K. Simulations of the EPR spectra were performed using the Easyspin software package running within the MathWorks MatLab environment.²

6.3.6 Computational studies

For theoretical EPR studies, geometry optimization of the C₆H₄N₂(ⁱPr)₂P• radical was performed using the Perdew–Burke–Ernzerhof UPBE0 hybrid functional^{3,4} and Pople split valence basis set 6-31+G(2d,p)⁵ on the graphical interface WebMO computational platform, which employed the Gaussian 09 package.⁶ EPR simulations and spin charge density DFT calculations were performed in the ORCA package v4.0⁷ and used the PBE0 functional with

def2-TZVP basis set on all atoms.⁸ Spin-orbit coupling effects were accounted for using a mean field (SOMF(1X)) approach.⁹

6.3.7 Gutmann-Beckett Lewis Acidity Measurements

General Procedure 8. The phosphonium/arsenium cation (1.0 equiv) was dissolved in CDCl₃ (0.5 mL) and was added to triethylphosphine oxide (0.6 equiv). A capillary containing PPh₃ in CDCl₃ was added as a standard and the NMR tube was inverted several times. The ³¹P NMR chemical shift of the triphenylphosphine in CDCl₃ was calibrated to $\delta = -5.21$ ppm according to O. M. Demchuk *et al.*¹⁰ and the acceptor number was calculated according to M. A. Beckett *et al.*¹¹

Table 6.1: Gutmann-Beckett method Lewis acidity values.

Compound	³¹ P NMR chemical shift/ ppm	Acceptor number	Relative Lewis acidity/ %
14b	80.8	88.2	100
15c	56.9	35.1	40
16c	54.3	29.4	33
B(C ₆ F ₅) ₃	76.0	78.1	89

5-methylbenzo-1,3,2-dithiarsenium tetrachlorogalate (14b)

According to *general procedure 8*, using 5-methylbenzo-1,3,2-dithiarsenium tetrachlorogalate **14b** (44 mg, 0.1 mmol, 1.0 equiv) and triethylphosphine oxide (8 mg, 0.06 mmol, 1.0 equiv). ³¹P NMR (162 MHz, CDCl₃, 295 K) δ /ppm: 80.8 (m, 1P).

1,3-diisopropyl-benzodiphosphenium triflate (15c)

According to *general procedure 8*, using 1,3-diisopropyl-benzodiphosphenium triflate **15c** (38 mg, 0.1 mmol, 1.0 equiv) and triethylphosphine oxide (8 mg, 0.06 mmol, 1.0 equiv). ³¹P NMR (162 MHz, CDCl₃, 295 K) δ /ppm: 56.9 (m, 1P).

1,3-diisopropyl-benzodiarsenium triflate (16c)

According to *general procedure 8*, using 1,3-diisopropyl-benzodiarsenium triflate **16c** (43 mg, 0.1 mmol, 1.0 equiv) and triethylphosphine oxide (8 mg, 0.06 mmol, 1.0 equiv). ³¹P NMR (162 MHz, CDCl₃, 295 K) δ /ppm: 54.3 (m, 1P).

Tris(pentafluorophenyl)borane

According to *general procedure 8*, using tris(pentafluorophenyl)borane (20 mg, 0.04 mmol, 1.0 equiv) and triethylphosphine oxide (3.1 mg, 0.02 mmol, 1.0 equiv). ³¹P NMR (162 MHz, CDCl₃, 295 K) δ/ppm: 76.0 (s, 1P).

6.3.8 HOHMED aromaticity calculations

For the HOHMED calculations, the bond length values were either taken from the Heeney paper¹² or from the paper 'Typical Interatomic Distances: organic compounds', by F. H. Allen and colleagues.¹³ In the cases of the P–S, P–N and As=N bonds, these values were not available and instead were taken by averaging a range of bond lengths from the Cambridge Structural Database (CSD).¹⁴

Table 6.2: P–S bond lengths from the CSD.

CSD Code	P–S/ Å
DOYVUI	2.136
ECIDOK	2.117
EGEBAT	2.09
JANDEK	2.108
JUFREH	2.123
SUQLEV	2.117
VAFHIV	2.137
QEMQOR	2.156
TEKDUL	2.161
QIHBER	2.179
Average	2.132

Table 6.3: P–N bond lengths from the CSD.

CSD Code	P–N/ Å
HEJFOU	1.736
VAYSAS	1.771
AGIVAO	1.662
AJOMET	1.768
AJUGUI	1.745
ALIFAE	1.744
ALIFEI	1.672
AWEROJ	1.704
AZUMAK	1.71
BIQLIW	1.669
Average	1.718

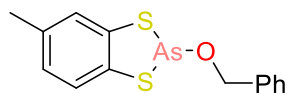
Table 6.4: As=N bond lengths from the CSD.

CSD Code	As=N/ Å
KISXAM	1.785
LASQUR	1.823
TUNYOQ	1.707
FALZAT01	1.733
Average	1.762

Chapter 6.4 Experimental for Aldehyde Reduction Catalysis Using Dithia- and Diaza-Derived Arsole Complexes

6.4.1 Synthesis of arsenic pre-catalyst complexes

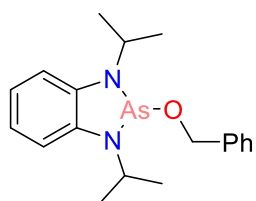
2-(benzyloxy)-5-methylbenzo-1,3,2-dithiarsole (**19**)



Compound **3** (200 mg, 0.76 mmol, 1.0 equiv) was dissolved in CH_2Cl_2 (5 mL) and with stirring, benzyl alcohol (82 mg, 0.76 mmol, 1.0 equiv) followed by triethylamine (76 mg, 0.76 mmol, 1.0 equiv) were added dropwise. The reaction was left to stir at ambient temperature for 3 days. The solvent was then removed *in vacuo* and toluene (5 mL) was added. The solvent was passed through a plug of Celite to remove traces of ammonium salt, after which the solvent was again removed *in vacuo* to give the final product as a white solid. **Yield:** 140 mg, 0.43 mmol, 57%. Single crystals suitable for X-ray diffraction were grown from a saturated solution of CH_2Cl_2 cooled to $-40\text{ }^\circ\text{C}$.

$^1\text{H NMR}$ (500 MHz, CDCl_3 , 295 K) δ /ppm: 7.45 (d, $^3J_{\text{HH}} = 8.1\text{ Hz}$, 1H, Ar-H), 7.39 (s, 1H, Ar-H), 7.32–7.27 (m, 3H, Ar-H), 7.23 (d, $^3J_{\text{HH}} = 8.2\text{ Hz}$, 2H, Ar-H), 6.97 (d, $^3J_{\text{HH}} = 8.2\text{ Hz}$, 1H, Ar-H), 4.34 (s, 2H, O- CH_2), 2.36 (s, 3H, Ar- CH_3). **$^{13}\text{C}\{^1\text{H}\}$ NMR** (126 MHz, CDCl_3 , 295 K) δ /ppm: 140.1 (Ar), 139.1 (Ar), 136.6 (Ar), 135.6 (Ar), 128.5 (Ar), 128.1 (Ar), 127.8 (Ar), 126.7 (Ar), 126.4 (Ar), 125.6 (Ar), 67.7 (1C, Ar- CH_2), 20.8 (1C, Ar- CH_3). **IR** ν_{max} (cm^{-1}): 1456 (w), 1363 (w), 1007 (m), 991 (m), 810 (m) and 731 (m). **HRMS** (EI^+) m/z calculated for $[\text{M}]^+$ [$\text{C}_{14}\text{H}_{13}\text{AsOS}_2$] $^+$: 335.9624, found: 335.9629. **Melting point:** 79–82 $^\circ\text{C}$.

2-(benzyloxy)-1,3-diisopropyl-1,3,2-diazarsole (**20**)



Compound **7** (140 mg, 0.47 mmol, 1.0 equiv) was dissolved in CH_2Cl_2 (5 mL) and with stirring, benzyl alcohol (51 mg, 0.47 mmol, 1.0 equiv) followed by triethylamine (48 mg, 0.47 mmol, 1.0 equiv) were both added dropwise and the reaction was left to stir at ambient temperature for 3 days. The solvent was then removed *in vacuo* and toluene (2 mL) was added. The solvent was passed through a plug of Celite to remove traces of ammonium salt, after which the solvent was again removed *in vacuo* to give the final product as a red/orange viscous oil. **Yield:** 81 mg, 0.22 mmol, 43%. Single crystals suitable for X-ray diffraction were grown from a saturated solution of CH_2Cl_2 cooled to $-40\text{ }^\circ\text{C}$.

$^1\text{H NMR}$ (500 MHz, CDCl_3 , 295 K) δ /ppm: 7.27 (m, 2H, Ar-H), 7.21 (t, $^3J_{\text{HH}} = 7.3\text{ Hz}$, 1H, Ar-H), 7.16 (d, $^3J_{\text{HH}} = 7.2\text{ Hz}$, 2H, Ar-H), 6.85–6.82 (m, 2H, Ar-H), 6.75–6.73 (m, 2H, Ar-H), 4.16 (sept, $^3J_{\text{HH}} = 6.6\text{ Hz}$, 2H, $\text{CH}(\text{CH}_3)_2$), 4.15 (s, 2H, O- CH_2), 1.54 (d, $^3J_{\text{HH}} = 6.6\text{ Hz}$, 6H, $\text{CH}(\text{CH}_3)_2$),

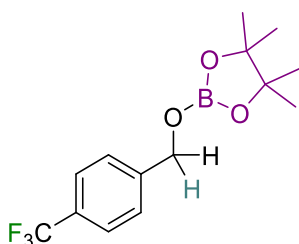
1.52 (d, $^3J_{\text{HH}} = 6.6$ Hz, 6H, $\text{CH}(\underline{\text{C}}\text{H}_3)_2$). $^{13}\text{C}\{^1\text{H}\}$ NMR (126 MHz, CDCl_3 , 295 K) δ /ppm: 141.0 (Ar), 140.4 (Ar), 128.3 (Ar), 127.5 (Ar), 127.1 (Ar), 118.0 (Ar), 108.1 (Ar), 64.7 (1C, $\text{Ar}-\underline{\text{C}}\text{H}_2$), 47.4 (2C, $\underline{\text{C}}\text{H}(\text{CH}_3)_2$), 24.1 (2C, $\text{CH}(\underline{\text{C}}\text{H}_3)_2$), 23.6 (2C, $\text{CH}(\underline{\text{C}}\text{H}_3)_2$). IR ν_{max} (cm^{-1}): 2980 (m), 2884 (w), 1483 (m), 1383 (m), 1277 (m), 1256 (m), 1157 (m), 1153 (m), 995 (m) and 727 (s). HRMS (EI^+) m/z calculated for $[\text{M}]^+$ [$\text{C}_{19}\text{H}_{25}\text{AsN}_2\text{O}$] $^+$: 372.1183, found: 372.1187.

6.4.2 General experimental for hydroboration catalysis

In a glove box under a dinitrogen atmosphere, three separate vials were charged with the arsenic catalyst (10, 5, 2 or 1 mol%), aldehyde (0.1 mmol, 1.0 equiv) and HBpin (12.8 mg, 0.1 mmol, 1.0 equiv). By syringe, solvent (0.6 mL) was added to the vial containing HBpin, and the contents of all three vials were mixed at least twice. The solution was transferred to an NMR tube and multinuclear NMR spectra were acquired at 30 mins, 2 hr, 6 hr, 12 hr and 24 hrs. Product conversion was calculated from the ^1H NMR spectrum by integrating the aldehyde signal and new resonance resulting from the hydride from HBpin.

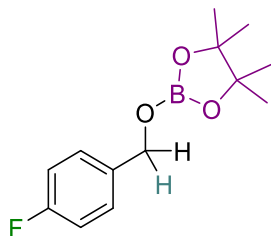
6.4.3 Characterisation of hydroboration products

4,4,5,5-tetramethyl-2-((4-(trifluoromethyl)benzyl)oxy)-1,3,2-dioxaborolane (**21a**)



With pre-catalyst **20**: *in situ* NMR conversion: >95%, **yield**: 29.5 mg, 0.098 mmol, 98%. With pre-catalyst **15c**: *in situ* NMR conversion: >95%. ^1H NMR (500 MHz, CDCl_3 , 295 K) δ /ppm: 7.59 (d, $^3J_{\text{HH}} = 8.1$ Hz, 2H, Ar-H), 7.46 (d, $^3J_{\text{HH}} = 8.1$ Hz, 2H, Ar-H), 4.98 (s, 2H, $\text{Ar}-(\underline{\text{C}}\text{H}_2)\text{OBPin}$), 1.27 (s, 12H, CH_3). $^{13}\text{C}\{^1\text{H}\}$ NMR (126 MHz, CDCl_3 , 295 K) δ /ppm: 143.4 (1C, Ar), 129.7 (q, $^2J_{\text{CF}} = 32.3$ Hz, 1C, Ar), 126.7 (2C, Ar), 125.4 (q, $^3J_{\text{CF}} = 3.8$ Hz, 2C, Ar), 83.4 (2C, $\underline{\text{C}}(\text{CH}_3)_2$), 66.0 (1C, $\text{Ar}-(\underline{\text{C}}\text{H}_2)\text{OBPin}$), 24.7 (4C, CH_3). ^{11}B NMR (160 MHz, CDCl_3 , 295 K) δ /ppm: 22.4 (s, 1B, BPin). ^{19}F NMR (470 MHz, CDCl_3 , 295 K) δ /ppm: -62.5 (s, 1F, $\text{Ar}-\text{CF}_3$). Values in agreement with literature.¹⁵

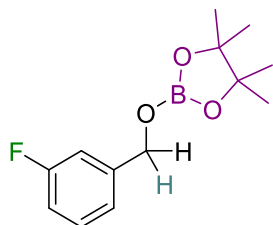
2-((4-fluorobenzyl)oxy)-4,4,5,5-tetramethyl-1,3,2-dioxaborolane (**21b**)



With pre-catalyst **20**: *in situ* NMR conversion: >95%, **yield**: 24.5 mg, 0.097 mmol, 97%. With pre-catalyst **15c**: *in situ* NMR conversion: >95%. ^1H NMR (500 MHz, CDCl_3 , 295 K) δ /ppm: 7.33–7.30 (m, 2H, Ar-H), 7.01 (t, $^3J_{\text{HH}} = 8.8$ Hz, 2H, Ar-H), 4.87 (s, 2H, $\text{Ar}-(\underline{\text{C}}\text{H}_2)\text{OBPin}$), 1.26 (s, 12H, CH_3). $^{13}\text{C}\{^1\text{H}\}$ NMR (126 MHz, CDCl_3 , 295 K) δ /ppm: 162.3 (d, $^1J_{\text{CF}} = 245$ Hz, 1C, Ar-F), 135.1 (d, $^4J_{\text{CF}} = 3.1$ Hz, 1C, Ar), 128.8 (d, $^3J_{\text{CF}} = 8.1$ Hz, 2C, Ar), 115.2 (d, $^2J_{\text{CF}} = 21.4$ Hz, 2C, Ar), 83.2 (1C, $\underline{\text{C}}(\text{CH}_3)_2$), 66.2 (1C, $\text{Ar}-(\underline{\text{C}}\text{H}_2)\text{OBPin}$), 24.7 (4C, CH_3). ^{11}B NMR (160 MHz, CDCl_3 , 295 K) δ /ppm: 22.3 (s, 1B, BPin). ^{19}F NMR (470 MHz, CDCl_3 , 295 K) δ /ppm: ^{19}F NMR

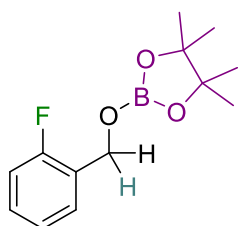
(470 MHz, CDCl₃, 295 K) δ /ppm: -115.3 – -115.4 (m, 1F, Ar-F). Values in agreement with literature.¹⁵

2-((3-fluorobenzyl)oxy)-4,4,5,5-tetramethyl-1,3,2-dioxaborolane (**21c**)



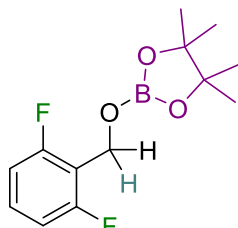
With pre-catalyst **20**: *in situ* NMR conversion: >95%, **yield**: 22.7 mg, 0.090 mmol, 90%. With pre-catalyst **15c**: *in situ* NMR conversion: >95%. **¹H NMR** (500 MHz, CDCl₃, 295 K) δ /ppm: 7.31–7.27 (m, 1H, Ar-H), 7.11–7.06 (m, 2H, Ar-H), 6.97–6.92 (m, 1H, Ar-H), 4.92 (s, 2H, Ar-(C)H₂OBPin), 1.27 (s, 12H, CH₃). **¹³C{¹H} NMR** (126 MHz, CDCl₃, 295 K) δ /ppm: 163.1 (d, ¹J_{CF} = 246 Hz, 1C, Ar-F), 142.0 (d, ³J_{CF} = 7.3 Hz, 1C, Ar), 129.9 (d, ³J_{CF} = 8.2 Hz, 1C, Ar), 122.1 (d, ⁴J_{CF} = 2.9 Hz, 1C, Ar), 114.3 (d, ²J_{CF} = 21.1 Hz, 1C, Ar), 113.7 (d, ²J_{CF} = 22.0 Hz, 1C, Ar), 83.3 (2C, C(CH₃)₂), 66.1 (d, ⁴J_{CF} = 1.9 Hz, 1C, Ar-(C)H₂OBPin), 24.8 (4C, CH₃). **¹¹B NMR** (160 MHz, CDCl₃, 295 K) δ /ppm: 22.4 (s, 1B, BPin). **¹⁹F NMR** (470 MHz, CDCl₃, 295 K) δ /ppm: -113.4 (s, 1F, Ar-F). Values in agreement with literature.¹⁶

2-((2-fluorobenzyl)oxy)-4,4,5,5-tetramethyl-1,3,2-dioxaborolane (**21d**)



With pre-catalyst **20**: *in situ* NMR conversion: >95%, **yield**: 23.9 mg, 0.095 mmol, 95%. With pre-catalyst **15c**: *in situ* NMR conversion: >95%. **¹H NMR** (500 MHz, CDCl₃, 295 K) δ /ppm: 7.38 (t, ³J_{HH} = 7.5 Hz, 1H, Ar-H), 7.20–7.16 (m, 1H, Ar-H), 7.05 (t, ³J_{HH} = 7.5 Hz, 1H, Ar-H), 6.96–6.92 (m, 1H, Ar-H), 4.94 (s, 2H, Ar-(C)H₂OBPin), 1.20 (s, 12H, CH₃). **¹³C{¹H} NMR** (126 MHz, CDCl₃, 295 K) δ /ppm: 160.3 (d, ¹J_{CF} = 247 Hz, 1C, Ar-F), 129.1 (d, ³J_{CF} = 8.0 Hz, 1C, Ar), 128.9 (d, ³J_{CF} = 4.4 Hz, 1C, Ar), 128.4 (1C, Ar), 126.7 (d, ²J_{CF} = 34.9 Hz, 1C, Ar), 115.1 (d, ²J_{CF} = 21.0 Hz, 1C, Ar), 83.2 (2C, C(CH₃)₂), 61.0 (d, ³J_{CF} = 4.9 Hz, 1C, Ar-(C)H₂OBPin), 24.7 (4C, CH₃). **¹¹B NMR** (160 MHz, CDCl₃, 295 K) δ /ppm: 22.4 (s, 1B, BPin). **¹⁹F NMR** (470 MHz, CDCl₃, 295 K) δ /ppm: -119.2 (dt, ³J_{FH} = 10.2 Hz, ⁴J_{FH} = 6.9 Hz, 1F, Ar-F). Values in agreement with literature.¹⁶

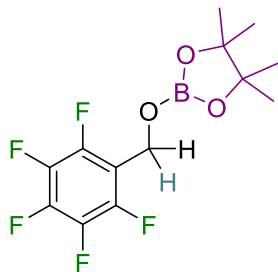
2-((2,6-difluorobenzyl)oxy)-4,4,5,5-tetramethyl-1,3,2-dioxaborolane (**21e**)



With pre-catalyst **20**: *in situ* NMR conversion: >95%, **yield**: 25.0 mg, 0.093 mmol, 93%. **¹H NMR** (500 MHz, CDCl₃, 295 K) δ /ppm: 7.31–7.27 (m, 1H, Ar-H), 6.92–6.89 (m, 2H, Ar-H), 5.05 (s, 2H, Ar-(C)H₂OBPin), 1.31 (s, 12H, CH₃). **¹³C{¹H} NMR** (126 MHz, CDCl₃, 295 K) δ /ppm: 160.3 (dd, ¹J_{CF} = 251 Hz, ³J_{CF} = 8.0 Hz, 2C, Ar-F), 130.2 (t, ³J_{CF} = 10.4 Hz, 1C, Ar), 114.9 (t, ²J_{CF} = 19.1 Hz, 1C, Ar), 111.3 (dd, ²J_{CF} = 20.1 Hz, ⁴J_{CF} = 5.8 Hz, 2C, Ar), 83.2 (2C, C(CH₃)₂), 54.9 (t, ³J_{CF} = 4.3

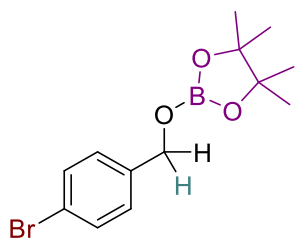
Hz, 1C, Ar-(C)H₂OBPin), 24.7 (4C, CH₃). **¹¹B NMR** (160 MHz, CDCl₃, 295 K) δ/ppm: 22.8 (s, 1B, BPin). **¹⁹F NMR** (470 MHz, CDCl₃, 295 K) δ/ppm: -115.3 (t, ³J_{FH} = 6.7 Hz, 2F, Ar-F). **HRMS** (EI⁺) *m/z* calculated for [M]⁺ [C₁₃H₁₇BF₂O₃]⁺: 270.1239, found: 270.1242.

4,4,5,5-tetramethyl-2-((perfluorophenyl)methoxy)-1,3,2-dioxaborolane (21f)



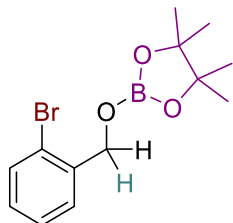
With pre-catalyst **20**: *in situ* NMR conversion: >95%, **yield**: 31.9 mg, 0.098 mmol, 98%. **¹H NMR** (500 MHz, CDCl₃, 295 K) δ/ppm: 5.00 (s, 2H, Ar-(C)H₂OBPin), 1.27 (s, 12H, CH₃). **¹³C{¹H} NMR** (126 MHz, CDCl₃, 295 K) δ/ppm: 146.8–136.7 (m, Ar), 128.5–127.0 (m, Ar), 112.4 (td, ²J_{CF} = 17.8 Hz, ³J_{CF} = 3.9 Hz), 83.7 (2C, C(CH₃)₂), 54.5 (1C, Ar-(C)H₂OBPin), 24.8 (4C, CH₃). **¹¹B NMR** (160 MHz, CDCl₃, 295 K) δ/ppm: 22.4 (s, 1B, BPin). **¹⁹F NMR** (470 MHz, CDCl₃, 295 K) δ/ppm: -143.1 (dd, ³J_{FF} = 22.2 Hz, ⁴J_{FF} = 8.7 Hz, 2F, *o*-F), -154.1 (t, ³J_{FF} = 22.2 Hz, 1F, *p*-F), -162.3 (m, 2F, *m*-F). Values in agreement with literature.¹⁵

2-((4-bromobenzyl)oxy)-4,4,5,5-tetramethyl-1,3,2-dioxaborolane (21g)



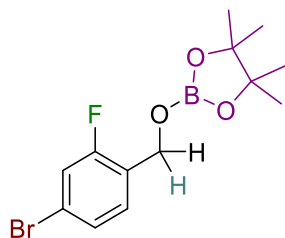
With pre-catalyst **20**: *in situ* NMR conversion: >95%, **yield**: 29.8 mg, 0.095 mmol, 95%. With pre-catalyst **15c**: *in situ* NMR conversion: >95%. **¹H NMR** (500 MHz, CDCl₃, 295 K) δ/ppm: 7.45 (d, ³J_{HH} = 8.6 Hz, 2H, Ar-H), 7.22 (d, ³J_{HH} = 8.6 Hz, 2H, Ar-H), 4.87 (s, 2H, Ar-(C)H₂OBPin), 1.26 (s, 12H, CH₃). **¹³C{¹H} NMR** (126 MHz, CDCl₃, 295 K) δ/ppm: 138.5 (1C, Ar), 131.6 (2C, Ar), 128.6 (2C, Ar), 121.5 (1C, Ar), 83.4 (2C, C(CH₃)₂), 66.2 (1C, Ar-(C)H₂OBPin), 24.9 (4C, CH₃). **¹¹B NMR** (160 MHz, CDCl₃, 295 K) δ/ppm: 22.3 (s, 1B, BPin). Values in agreement with literature.¹⁵

2-((2-bromobenzyl)oxy)-4,4,5,5-tetramethyl-1,3,2-dioxaborolane (21h)



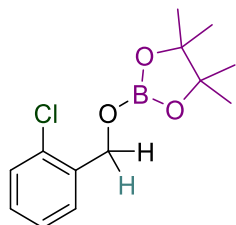
With pre-catalyst **20**: *in situ* NMR conversion: >95%, **yield**: 27.2 mg, 0.087 mmol, 87%. **¹H NMR** (400 MHz, CDCl₃, 295 K) δ/ppm: 7.53–7.50 (m, 2H, Ar-H), 7.32 (td, ³J_{HH} = 7.7 Hz, ⁴J_{HH} = 1.2 Hz, 1H, Ar-H), 7.15–7.11 (m, 2H, Ar-H), 4.98 (s, 2H, Ar-(C)H₂OBPin), 1.28 (s, 12H, CH₃). **¹³C{¹H} NMR** (101 MHz, CDCl₃, 295 K) δ/ppm: 138.5 (1C, Ar), 132.4 (1C, Ar), 128.7 (1C, Ar), 127.9 (1C, Ar), 127.5 (1C, Ar), 121.7 (1C, Ar), 83.3 (2C, C(CH₃)₂), 66.4 (1C, Ar-(C)H₂OBPin), 24.8 (4C, CH₃). **¹¹B NMR** (128 MHz, CDCl₃, 295 K) δ/ppm: 22.4 (s, 1B, BPin). Values in agreement with literature.¹⁵

2-((4-bromo-2-fluorobenzyl)oxy)-4,4,5,5-tetramethyl-1,3,2-dioxaborolane (**21i**)



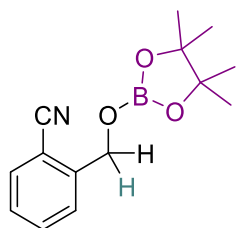
With pre-catalyst **20**: *in situ* NMR conversion: >95%, **yield**: 31.9 mg, 0.097 mmol, 97%. $^1\text{H NMR}$ (400 MHz, CDCl_3 , 295 K) δ /ppm: 7.30–7.27 (m, 1H, Ar–H), 7.23–7.20 (m, 1H, Ar–H), 7.16–7.13 (m, 1H, Ar–H), 4.88 (s, 2H, Ar–(C)H₂OBPin), 1.28 (s, 12H, CH₃). $^{13}\text{C}\{^1\text{H}\}$ NMR (101 MHz, CDCl_3 , 295 K) δ /ppm: 159.8 (d, $^1J_{\text{CF}} = 251$ Hz, 1C, Ar–F), 129.9 (d, $^3J_{\text{CF}} = 5.0$ Hz, 1C, Ar), 127.3 (d, $^4J_{\text{CF}} = 3.7$ Hz, 1C, Ar), 125.7 (d, $^2J_{\text{CF}} = 14.6$ Hz, 1C, Ar), 121.3 (d, $^3J_{\text{CF}} = 9.4$ Hz, 1C, Ar), 118.7 (d, $^2J_{\text{CF}} = 24.3$ Hz, 1C, Ar–F), 83.2 (2C, C(CH₃)₂), 60.4 (d, $^3J_{\text{CF}} = 4.8$ Hz, 1C, Ar–(C)H₂OBPin), 24.6 (4C, CH₃). $^{11}\text{B NMR}$ (128 MHz, CDCl_3 , 295 K) δ /ppm: 22.4 (s, 1B, BPin). $^{19}\text{F}\{^1\text{H}\}$ NMR (376 MHz, CDCl_3 , 295 K) δ /ppm: –116.3 (s, 1F, Ar–F). HRMS (EI⁺) *m/z* calculated for [M]⁺ [C₁₃H₁₇BrFO₃]⁺: 330.0438, found: 330.0446.

2-((2-chlorobenzyl)oxy)-4,4,5,5-tetramethyl-1,3,2-dioxaborolane (**21j**)



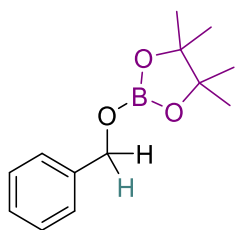
With pre-catalyst **20**: *in situ* NMR conversion: >95%, **yield**: 22.8 mg, 0.085 mmol, 85%. $^1\text{H NMR}$ (400 MHz, CDCl_3 , 295 K) δ /ppm: 7.53–7.51 (m, 1H, Ar–H), 7.35–7.31 (m, 1H, Ar–H), 7.27–7.25 (m, 1H, Ar–H), 7.27–7.25 (m, 1H, Ar–H), 7.23–7.18 (m, 1H, Ar–H), 5.03 (s, 2H, Ar–(C)H₂OBPin), 1.28 (s, 12H, CH₃). $^{13}\text{C}\{^1\text{H}\}$ NMR (101 MHz, CDCl_3 , 295 K) δ /ppm: 136.9 (1C, Ar), 132.0 (1C, Ar), 129.1 (1C, Ar), 128.5 (1C, Ar), 127.8 (1C, Ar), 126.9 (1C, Ar), 83.3 (2C, C(CH₃)₂), 64.2 (1C, Ar–(C)H₂OBPin), 24.7 (4C, CH₃). $^{11}\text{B NMR}$ (128 MHz, CDCl_3 , 295 K) δ /ppm: 22.4 (s, 1B, BPin). Values in agreement with literature.¹⁶

2-(((4,4,5,5-tetramethyl-1,3,2-dioxaborolan-2-yl)oxy)methyl)benzonitrile (**21k**)



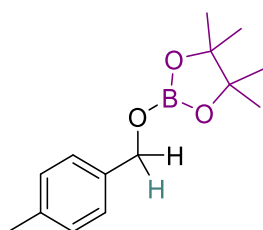
With pre-catalyst **20**: *in situ* NMR conversion: >95%, **yield**: 22.8 mg, 0.088 mmol, 88%. $^1\text{H NMR}$ (400 MHz, CDCl_3 , 295 K) δ /ppm: 7.64–7.58 (m, 3H, Ar–H), 7.38–7.34 (m, 1H, Ar–H), 5.14 (s, 2H, Ar–(C)H₂OBPin), 1.28 (s, 12H, CH₃). $^{13}\text{C}\{^1\text{H}\}$ NMR (101 MHz, CDCl_3 , 295 K) δ /ppm: 142.9 (1C, Ar), 133.1 (1C, Ar), 132.7 (1C, Ar), 127.9 (1C, Ar), 127.5 (1C, Ar), 117.2 (1C, CN), 110.4 (1C, Ar), 83.5 (2C, C(CH₃)₂), 64.6 (1C, Ar–(C)H₂OBPin), 24.8 (4C, CH₃). $^{11}\text{B NMR}$ (128 MHz, CDCl_3 , 295 K) δ /ppm: 22.4 (s, 1B, BPin). Values in agreement with literature.¹⁵

2-(benzyloxy)-4,4,5,5-tetramethyl-1,3,2-dioxaborolane (**21l**)



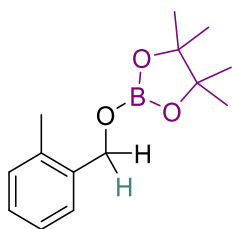
With pre-catalyst **20**: *in situ* NMR conversion: >95%, **yield**: 20.3 mg, 0.087 mmol, 87%. With pre-catalyst **15c**: *in situ* NMR conversion: >95%. **¹H NMR** (500 MHz, CDCl₃, 295 K) δ/ppm: 7.36–7.32 (m, 4H, Ar–H), 7.28–7.25 (m, 1H, Ar–H), 4.93 (s, 2H, Ar–(C)H₂OBPin), 1.27 (s, 12H, CH₃). **¹³C{¹H} NMR** (126 MHz, CDCl₃, 295 K) δ/ppm: 139.4 (1C, Ar), 128.4 (2C, Ar), 127.5 (1C, Ar), 126.9 (2C, Ar), 83.1 (2C, C(CH₃)₂), 66.8 (1C, Ar–(C)H₂OBPin), 24.8 (4C, CH₃). **¹¹B NMR** (160 MHz, CDCl₃, 295 K) δ/ppm: 22.3 (s, 1B, BPin). Values in agreement with literature.¹⁵

4,4,5,5-tetramethyl-2-((4-methylbenzyl)oxy)-1,3,2-dioxaborolane (**21m**)



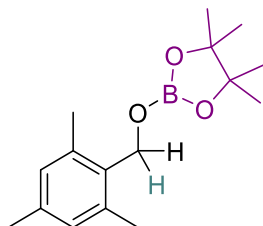
With pre-catalyst **20**: *in situ* NMR conversion: >95%, **yield**: 20.8 mg, 0.084 mmol, 84%. **¹H NMR** (500 MHz, CDCl₃, 295 K) δ/ppm: 7.24 (d, ³J_{HH} = 7.9 Hz, 2H, Ar–H), 7.14 (d, ³J_{HH} = 7.9 Hz, 2H, Ar–H), 4.89 (s, 2H, Ar–(C)H₂OBPin), 2.34 (s, 3H, Ar–CH₃), 1.27 (s, 12H, CH₃). **¹³C{¹H} NMR** (126 MHz, CDCl₃, 295 K) δ/ppm: 137.1 (1C, Ar), 136.4 (1C, Ar), 129.1 (2C, Ar), 127.0 (2C, Ar), 83.0 (2C, C(CH₃)₂), 66.7 (1C, Ar–(C)H₂OBPin), 24.7 (4C, CH₃), 21.3 (1C, Ar–CH₃). **¹¹B NMR** (160 MHz, CDCl₃, 295 K) δ/ppm: 22.3 (s, 1B, BPin). Values in agreement with literature.¹⁵

4,4,5,5-tetramethyl-2-((2-methylbenzyl)oxy)-1,3,2-dioxaborolane (**21n**)



With pre-catalyst **20**: *in situ* NMR conversion: >95%, **yield**: 22.1 mg, 0.089 mmol, 89%. **¹H NMR** (400 MHz, CDCl₃, 295 K) δ/ppm: 7.41–7.39 (m, 1H, Ar–H), 7.20–7.13 (m, 3H, Ar–H), 4.93 (s, 2H, Ar–(C)H₂OBPin), 2.31 (s, 3H, Ar–CH₃), 1.27 (s, 12H, CH₃). **¹³C{¹H} NMR** (101 MHz, CDCl₃, 295 K) δ/ppm: 137.3 (1C, Ar), 135.7 (1C, Ar), 130.1 (1C, Ar), 127.6 (1C, Ar), 127.3 (1C, Ar), 126.0 (1C, Ar), 83.1 (2C, C(CH₃)₂), 65.1 (1C, Ar–(C)H₂OBPin), 24.8 (4C, CH₃), 18.8 (1C, Ar–CH₃). **¹¹B NMR** (128 MHz, CDCl₃, 295 K) δ/ppm: 22.3 (s, 1B, BPin). Values in agreement with literature.¹⁷

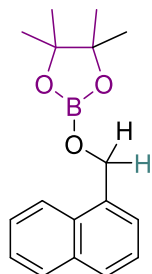
4,4,5,5-tetramethyl-2-((2,4,6-trimethylbenzyl)oxy)-1,3,2-dioxaborolane (**21o**)



With pre-catalyst **20**: *in situ* NMR conversion: >95%, **yield**: 24.9 mg, 0.090 mmol, 90%. **¹H NMR** (500 MHz, CDCl₃, 295 K) δ/ppm: 6.84 (s, 2H, Ar–H), 4.96 (s, 2H, Ar–(C)H₂OBPin), 2.39 (s, 6H, Ar–CH₃), 2.26 (s, 3H, Ar–CH₃), 1.27 (s, 12H, CH₃). **¹³C{¹H} NMR** (126 MHz, CDCl₃,

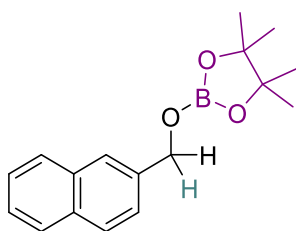
295 K) δ /ppm: 137.9 (2C, Ar), 137.7 (1C, Ar), 132.3 (1C, Ar), 129.0 (2C, Ar), 82.9 (2C, $\underline{C}(\text{CH}_3)_2$), 61.3 (1C, Ar-(\underline{C})H₂OBPin), 24.8 (4C, CH₃), 21.1 (1C, Ar-CH₃), 19.5 (2C, Ar-CH₃). **¹¹B NMR** (160 MHz, CDCl₃, 295 K) δ /ppm: 22.2 (s, 1B, BPin). Values in agreement with literature.¹⁵

4,4,5,5-tetramethyl-2-(naphthalen-1-ylmethoxy)-1,3,2-dioxaborolane (21p)



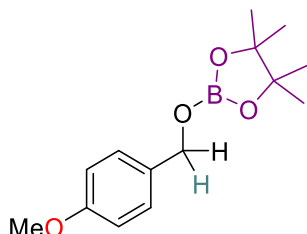
With pre-catalyst **20**: *in situ* NMR conversion: >95%, **yield**: 23.6 mg, 0.083 mmol, 83%. **¹H NMR** (400 MHz, CDCl₃, 295 K) δ /ppm: 8.06–8.04 (m, 1H, Ar-H), 7.88–7.86 (m, 1H, Ar-H), 7.80 (d, ³J_{HH} = 8.2 Hz, 1H, Ar-H), 7.59 (dd, ³J_{HH} = 7.0 Hz, ⁴J_{HH} = 1.0 Hz, 1H, Ar-H), 7.54–7.49 (m, 2H, Ar-H), 7.47–7.43 (m, 1H, Ar-H), 5.42 (s, 2H, Ar-(\underline{C})H₂OBPin), 1.29 (s, 12H, CH₃). **¹³C{¹H} NMR** (101 MHz, CDCl₃, 295 K) δ /ppm: 134.8 (1C, Ar), 133.7 (1C, Ar), 131.1 (1C, Ar), 128.7 (1C, Ar), 128.3 (1C, Ar), 126.2 (1C, Ar), 125.8 (1C, Ar), 125.5 (1C, Ar), 125.0 (1C, Ar), 123.6 (1C, Ar), 83.2 (2C, $\underline{C}(\text{CH}_3)_2$), 65.1 (1C, Ar-(\underline{C})H₂OBPin), 24.8 (4C, CH₃). **¹¹B NMR** (128 MHz, CDCl₃, 295 K) δ /ppm: 22.4 (s, 1B, BPin). Values in agreement with literature.¹⁸

4,4,5,5-tetramethyl-2-(naphthalen-2-ylmethoxy)-1,3,2-dioxaborolane (21q)



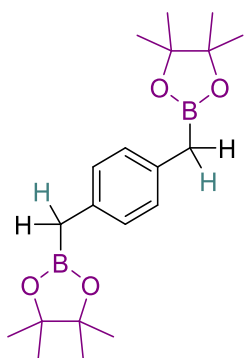
With pre-catalyst **20**: *in situ* NMR conversion: >95%, **yield**: 25.6 mg, 0.090 mmol, 90%. With pre-catalyst **15c**: *in situ* NMR conversion: >95%. **¹H NMR** (400 MHz, CDCl₃, 295 K) δ /ppm: 7.84–7.81 (m, 4H, Ar-H), 7.48–7.44 (m, 3H, Ar-H), 5.10 (s, 2H, Ar-(\underline{C})H₂OBPin), 1.29 (s, 12H, CH₃). **¹³C{¹H} NMR** (101 MHz, CDCl₃, 295 K) δ /ppm: 136.8 (1C, Ar), 133.5 (1C, Ar), 132.9 (1C, Ar), 128.1 (1C, Ar), 128.1 (1C, Ar), 127.8 (1C, Ar), 126.2 (1C, Ar), 125.8 (1C, Ar), 125.3 (1C, Ar), 125.0 (1C, Ar), 83.2 (2C, $\underline{C}(\text{CH}_3)_2$), 66.9 (1C, Ar-(\underline{C})H₂OBPin), 24.8 (4C, CH₃). **¹¹B NMR** (128 MHz, CDCl₃, 295 K) δ /ppm: 22.4 (s, 1B, BPin). Values in agreement with literature.¹⁵

2-((4-methoxybenzyl)oxy)-4,4,5,5-tetramethyl-1,3,2-dioxaborolane (21r)



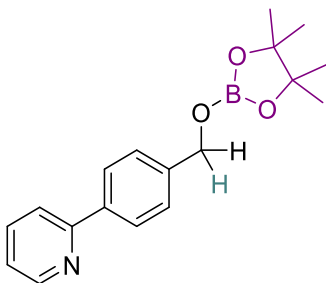
With pre-catalyst **20**: *in situ* NMR conversion: >95%, **yield**: 24.3 mg, 0.092 mmol, 92%. **¹H NMR** (400 MHz, CDCl₃, 295 K) δ /ppm: 7.28 (d, ³J_{HH} = 8.6 Hz, 2H, Ar-H), 6.86 (d, ³J_{HH} = 8.6 Hz, 2H, Ar-H), 4.85 (s, 2H, Ar-(\underline{C})H₂OBPin), 3.80 (s, 3H, O-CH₃), 1.26 (s, 12H, CH₃). **¹³C{¹H} NMR** (101 MHz, CDCl₃, 295 K) δ /ppm: 159.1 (1C, Ar), 131.6 (1C, Ar), 128.6 (2C, Ar), 113.8 (2C, Ar), 83.0 (2C, $\underline{C}(\text{CH}_3)_2$), 66.6 (1C, Ar-(\underline{C})H₂OBPin), 55.4 (3C, O-CH₃), 24.8 (4C, CH₃). **¹¹B NMR** (128 MHz, CDCl₃, 295 K) δ /ppm: 22.3 (s, 1B, BPin). Values in agreement with literature.¹⁵

1,4-bis((4,4,5,5-tetramethyl-1,3,2-dioxaborolan-2-yl)methyl)benzene (21s)



With pre-catalyst **20**: *in situ* NMR conversion: >95%, **yield**: 31.9 mg, 0.089 mmol, 89%. With pre-catalyst **15c**: *in situ* NMR conversion: >95%. **¹H NMR** (400 MHz, CDCl₃, 295 K) δ/ppm: 7.31 (s, 4H, Ar-H), 4.91 (s, 4H, Ar-(C)H₂OBPin), 1.26 (s, 24H, CH₃). **¹³C{¹H} NMR** (101 MHz, CDCl₃, 295 K) δ/ppm: 138.5 (2C, Ar), 126.8 (2C, Ar), 83.1 (4C, C(CH₃)₂), 66.6 (2C, Ar-(C)H₂OBPin), 24.8 (8C, CH₃). **¹¹B NMR** (128 MHz, CDCl₃, 295 K) δ/ppm: 22.4 (s, 1B, BPin). Values in agreement with literature.¹⁹

2-(4-(((4,4,5,5-tetramethyl-1,3,2-dioxaborolan-2-yl)oxy)methyl)phenyl)pyridine (21t)



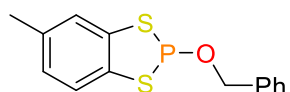
With pre-catalyst **20**: *in situ* NMR conversion: >95%, **yield**: 31.1 mg, 0.092 mmol, 92%. **¹H NMR** (400 MHz, CDCl₃, 295 K) δ/ppm: 8.70–8.68 (m, 1H, Ar-H), 7.97 (d, ³J_{HH} = 8.4 Hz, 2H, Ar-H), 7.74–7.72 (m, 2H, Ar-H), 7.46 (d, ³J_{HH} = 8.6 Hz, 2H, Ar-H), 7.23–7.20 (m, 1H, Ar-H), 4.99 (s, 2H, Ar-(C)H₂OBPin), 1.27 (s, 12H, CH₃). **¹³C{¹H} NMR** (101 MHz, CDCl₃, 295 K) δ/ppm: 157.3 (1C, Ar), 149.8 (1C, Ar), 140.2 (1C, Ar), 138.6 (1C, Ar), 136.9 (1C, Ar), 127.1 (2C, Ar), 127.0 (2C, Ar), 122.2 (1C, Ar), 120.6 (1C, Ar), 83.2 (2C, C(CH₃)₂), 66.5 (1C, Ar-(C)H₂OBPin), 24.8 (4C, CH₃). **¹¹B NMR** (128 MHz, CDCl₃, 295 K) δ/ppm: 22.4 (s, 1B, BPin). **HRMS** (EI⁺) m/z calculated for [M]⁺ [C₁₈H₂₂BNO₃]⁺: 311.1693, found: 311.1699.

Chapter 6.5 Experimental for Aldehyde Reduction Catalysis Using Dithia-, Diaza- and Dioxo-Derived Phosphole Complexes

6.5.1 Synthesis of phosphorus pre-catalyst complexes

General Procedure 9. To a solution of 2-chloro-5-methylbenzo-1,3,2-dithiaphosphole (**1a**) (1.0 equiv) in CH₂Cl₂ (5 mL), benzyl alcohol (1.0 equiv) or neopentyl alcohol (1.0 equiv) and triethylamine (1.0 equiv) were added dropwise. The reaction was allowed to stir at ambient temperature for 24 hours, after which the solvent was removed *in vacuo*. Toluene (2 mL) was subsequently added and the resulting solution was filtered through a plug of Celite to remove traces of ammonium salt, after which the solvent was again removed *in vacuo* to give the final product as a colourless oil.

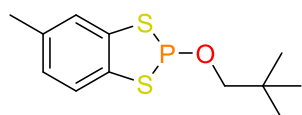
2-(benzyloxy)-5-methylbenzo-1,3,2-dithiaphosphole (**24a**)



Compound **24a** was synthesised to *general procedure 9* using **1a** (199 mg, 0.91 mmol, 1.0 equiv), benzyl alcohol (97 mg, 0.91 mmol, 1.0 equiv) and triethylamine (1.27 mL, 0.91 mmol, 1.0 equiv). **Yield:** 167 mg, 0.57 mmol, 63%.

¹H NMR (400 MHz, CDCl₃, 295 K) δ/ppm: 7.50 (d, ³J_{HH} = 8.1 Hz, 1H, Ar-H), 7.44 (s, 1H, Ar-H), 7.28–7.25 (m, 3H, Ar-H), 7.16–7.14 (m, 2H, Ar-H), 7.02 (ddd, ³J_{HH} = 8.1 Hz, ⁴J_{HH} = 1.7 Hz, ⁵J_{PH} = 0.7 Hz, 1H, Ar-H), 4.22 (d, ³J_{PH} = 6.5 Hz, 2H, OCH₂), 2.36 (s, 3H, Ar-CH₃). **¹³C{¹H} NMR** (101 MHz, CDCl₃, 295 K) δ/ppm: 139.7 (d, ³J_{PC} = 3.0 Hz, 1C, Ar), 136.8 (³J_{PC} = 2.5 Hz, 1C, Ar), 136.2 (³J_{PC} = 3.2 Hz, 1C, Ar), 136.1 (1C, Ar), 129.2 (1C, Ar), 128.5 (1C, Ar), 128.2 (1C, Ar), 128.0 (1C, Ar), 127.1 (1C, Ar), 125.4 (1C, Ar), 124.9 (d, ²J_{PC} = 6.4 Hz, 1C, Ar), 124.1 (d, ²J_{PC} = 6.3 Hz, 1C, Ar), 67.9 (d, ²J_{PC} = 9.1 Hz, 1C, Ar-CH₂) 21.0 (1C, Ar-CH₃). **³¹P NMR** (162 MHz, CDCl₃, 295 K) δ/ppm: 124.5 (t, ³J_{PH} = 6.5 Hz, 1P). **IR** ν_{max} (cm⁻¹): 1456 (m), 1364 (sh), 1217 (w), 1115 (w), 955 (s), 910 (sh), 725 (m), 689 (m) and 586 (w). **HRMS** (EI⁺) *m/z* calculated for [M]⁺ [C₁₅H₁₃OPS₂]⁺: 292.0145, found: 292.0148.

5-methyl-2-(neopentyloxy)benzo-1,3,2-dithiaphosphole (**24b**)



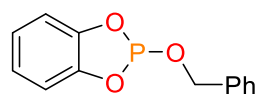
Compound **24b** was synthesised according to *general procedure 9* using **1a** (223 mg, 1.01 mmol, 1.0 equiv), neopentyl alcohol (89 mg, 1.01 mmol, 1.0 equiv) and triethylamine (1.40 mL, 1.01 mmol, 1.0 equiv). **Yield:** 179 mg, 0.66 mmol, 65%.

¹H NMR (400 MHz, CDCl₃, 295 K) δ/ppm: 7.46 (d, ³J_{HH} = 8.1 Hz, 1H, Ar-H), 7.40 (s, 1H, Ar-H), 6.99 (ddd, ³J_{HH} = 8.1 Hz, ⁴J_{HH} = 1.2 Hz, ⁵J_{PH} = 0.5 Hz, 1H, Ar-H), 2.85 (d, ³J_{PH} = 6.1 Hz, 2H, OCH₂),

2.36 (s, 3H, Ar-CH₃), 0.77 (s, 9H, CH₂(CH₃)₃). **¹³C{¹H} NMR** (101 MHz, CDCl₃, 295 K) δ/ppm: 139.9 (d, ³J_{PC} = 2.9 Hz, 1C, Ar), 136.4 (d, ³J_{PC} = 3.2 Hz, 1C, Ar), 135.8 (1C, Ar), 126.9 (1C, Ar), 124.8 (d, ²J_{PC} = 6.5 Hz, 1C, Ar), 123.9 (d, ²J_{PC} = 6.4 Hz, 1C, Ar), 75.4 (d, ²J_{PC} = 9.9 Hz, 1C, C(CH₃)-CH₂), 31.6 (d, ³J_{PC} = 2.3 Hz, 1C, C(CH₃)₃-CH₂), 26.5 (3C, C(CH₃)₃-CH₂), 21.0 (1C, Ar-CH₃). **³¹P NMR** (162 MHz, CDCl₃, 295 K) δ/ppm: 123.6 (t, ³J_{PH} = 6.1 Hz, 1P). **IR** ν_{max} (cm⁻¹): 1456 (m), 1364 (sh), 1258 (w), 1217 (w), 1117 (w), 972 (s), 789 (m), 727 (m) and 687 (sh). **HRMS** (EI⁺) *m/z* calculated for [M]⁺ [C₁₂H₁₇OPS₂]⁺: 272.0458, found: 272.0452.

General Procedure 10. To a solution of 2-chlorobenzo-1,3,2-dioxaphosphole (**8a**) (1.0 equiv) in CH₂Cl₂ (5 mL), benzyl alcohol (1.0 equiv) or neopentyl alcohol (1.0 equiv) and triethylamine (1.0 equiv) were added dropwise. The reaction was allowed to stir at ambient temperature for 24 hours, after which the solvent was removed *in vacuo*. Toluene (2 mL) was subsequently added and the resulting solution was filtered through a plug of Celite to remove traces of ammonium salt, after which the solvent was again removed *in vacuo* to give the product as an oil.

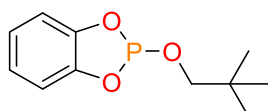
2-(benzyloxy)benzo-1,3,2-dioxaphosphole (**25a**)



Compound **25a** was synthesised according to *general procedure 10* using 2-chlorobenzo-1,3,2-dioxaphosphole (**8a**) (206 mg, 1.18 mmol, 1.0 equiv), benzyl alcohol (128 mg, 1.18 mmol, 1.0 equiv), and triethylamine (119 mg, 1.18 mmol, 1.0 equiv). Product is a dark yellow/orange oil. **Yield:** 198 mg, 0.80 mmol, 68%.

¹H NMR (400 MHz, CDCl₃, 295 K) δ/ppm: 7.32–7.30 (m, 3H, Ar-H), 7.21–7.19 (m, 2H, Ar-H), 7.12–7.10 (m, 2H, Ar-H), 7.02–7.00 (m, 2H, Ar-H), 4.60 (d, ³J_{PH} = 6.9 Hz, 2H, OCH₂). **¹³C{¹H} NMR** (101 MHz, CDCl₃, 295 K) δ/ppm: 146.0 (d, ²J_{PC} = 7.6 Hz, 2C, Ar), 136.7 (d, ³J_{PC} = 2.9 Hz, 2C, Ar), 128.7 (Ar), 128.4 (Ar), 127.7 (Ar), 123.0 (Ar), 112.2 (Ar), 65.9 (d, ²J_{PC} = 2.0 Hz, 1C, C(CH₃)₃-CH₂). **³¹P{¹H} NMR** (162 MHz, CDCl₃, 295 K) δ/ppm: 126.9 (s, 1P). **IR** ν_{max} (cm⁻¹): 1474 (s), 1373 (w), 1229 (s), 980 (m), 916 (w), 824 (s), 729 (s), 692 (s) and 625 (m). **HRMS** (EI⁺) *m/z* calculated for [M]⁺ [C₁₃H₁₁O₃P]⁺: 246.0446, found: 246.0441.

2-(neopentyloxy)benzo-1,3,2-dioxaphosphole (**25b**)



Compound **25b** was synthesised according to *general procedure 10* using 2-chlorobenzo-1,3,2-dioxaphosphole (**8a**) (203 mg, 1.16 mmol, 1.0 equiv), neopentyl alcohol (103 mg, 1.16 mmol,

1.0 equiv) and triethylamine (117 mg, 1.16 mmol, 1.0 equiv). Product is a faint orange/yellow coloured oil. **Yield:** 168 mg, 0.74 mmol, 64%.

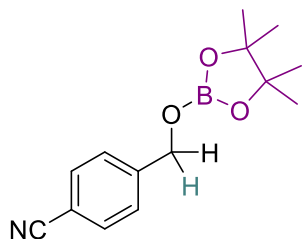
¹H NMR (400 MHz, CDCl₃, 295 K) δ/ppm: 7.08–7.05 (m, 2H, Ar–H), 6.99–6.96 (m, 2H, Ar–H), 3.21 (d, ³J_{PH} = 6.5 Hz, 2H, OCH₂), 0.83 (s, 9H, CH₂CH₃). **¹³C{¹H} NMR** (101 MHz, CDCl₃, 295 K) δ/ppm: 146.0 (d, ²J_{PC} = 7.7 Hz, 2C, Ar), 122.7 (2C, Ar), 111.9 (2C, Ar), 73.6 (d, ²J_{PC} = 2.0 Hz, 1C, C(CH₃)₃–CH₂), 31.9 (d, ³J_{PC} = 2.7 Hz, 1C, C(CH₃)₃–CH₂), 26.2 (3C, C(CH₃)₃–CH₂). **³¹P{¹H} NMR** (162 MHz, CDCl₃, 295 K) δ/ppm: 127.4 (s, 1P). **IR** ν_{max} (cm⁻¹): 1476 (s), 1366 (w), 1333 (w), 1231 (s), 1003 (s), 824 (s), 739 (m), 698 (m), 623 (m) and 536 (w). **HRMS** (EI⁺) *m/z* calculated for [M]⁺ [C₁₁H₁₅O₃P]⁺: 226.0759, found: 226.0756.

6.5.2 General experimental for hydroboration catalysis

In a glovebox under a dinitrogen atmosphere, three separate vials were charged with the phosphorus catalyst (10, 5, 2 or 1 mol%), aldehyde (0.1 mmol, 1 equiv) and HBpin (12.8 mg, 0.1 mmol, 1 equiv). By syringe, solvent (0.6 mL) was added to the vial containing HBpin and then mixed between the three vials at least twice. The solution was transferred to a J. Young NMR tube and multinuclear NMR spectra were acquired at 2 hr, 6 hr, 12 hr and 24 hrs. Product conversion was calculated from the *in-situ* ¹H NMR spectrum by integrating the aldehyde signal and new resonance resulting from the hydride from HBpin.

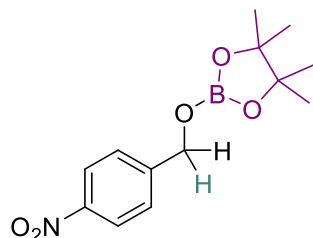
6.5.3 Characterisation of hydroboration products

4-(((4,4,5,5-tetramethyl-1,3,2-dioxaborolan-2-yl)oxy)methyl)benzonitrile (**21u**)



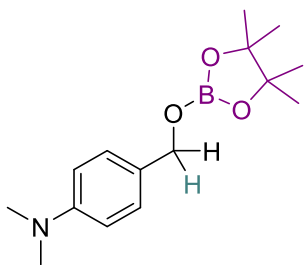
With pre-catalyst **15c**: *in situ* NMR conversion: >95%. **¹H NMR** (400 MHz, CDCl₃, 295 K): δ/ppm 7.64–7.60 (m, 2H, Ar–H), 7.45–7.43 (m, 2H, Ar–H), 4.97 (s, 2H, CH₂), 1.26 (s, 12H, CH₃). **¹¹B NMR** (128 MHz, CDCl₃, 295 K): δ/ppm 22.4 (s, 1B, Bpin). Values in agreement with literature.²⁰

4,4,5,5-tetramethyl-2-((4-nitrobenzyl)oxy)-1,3,2-dioxaborolane (**21v**)



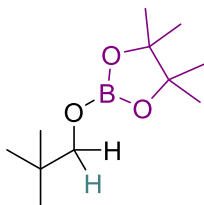
With pre-catalyst **15c**: *in situ* NMR conversion: 26%. **¹H NMR** (500 MHz, CDCl₃, 295 K) δ/ppm: 8.18 (d, ³J_{HH} = 8.9 Hz, 2H, Ar–H), 7.49 (d, ³J_{HH} = 8.9 Hz, 2H, Ar–H), 5.01 (s, 2H, CH₂), 1.26 (s, 12H, CH₃). **¹¹B NMR** (160 MHz, CDCl₃, 295 K) δ/ppm: 21.1 (s, 1B, Bpin). Values in agreement with literature.¹⁶

N,N-dimethyl-4-(((4,4,5,5-tetramethyl-1,3,2-dioxaborolan-2-yl)oxy)methyl)aniline (**21w**)



With pre-catalyst **15c**: *in situ* NMR conversion: >95%. **¹H NMR** (400 MHz, CDCl₃, 295 K) δ/ppm: 7.25 (d, ³J_{HH} = 8.8 Hz, 2H, Ar-H), 6.75 (d, ³J_{HH} = 8.8 Hz, 2H, Ar-H), 4.82 (s, 2H, CH₂), 2.95 (s, 6H, N(CH₃)₂), 1.26 (s, 12H, CH₃). **¹¹B NMR** (128 MHz, CDCl₃, 295 K) δ/ppm: 22.3 (s, 1B, Bpin). Values in agreement with literature.¹⁶

4,4,5,5-tetramethyl-2-(neopentyloxy)-1,3,2-dioxaborolane (**21x**)



With pre-catalyst **15c**: *in situ* NMR conversion: 46%. **¹H NMR** (400 MHz, CDCl₃, 295 K) δ/ppm: 3.50 (s, 2H, CH₂), 1.07 (s, 12H, CH₃), 0.88 (s, 9H, CH₃). **¹¹B NMR** (128 MHz, CDCl₃, 295 K) δ/ppm: 22.1 (s, 1B, BPin). Values in agreement with literature.²¹

Chapter 6.6 X-ray Crystallography

6.6.1 General X-ray experimental

Crystallographic studies on **1a–1c**, **2a–2c**, **6a**, **7**, **13b**, **15a–15c**, **16a–16c**, **19**, **20** and **24a** were undertaken on single crystal mounted in paratone and studied on an Agilent SuperNova Dual Atlas three-circle diffractometer using Mo- or Cu-K α radiation and a CCD detector. Measurements were taken at 150(2) K with temperatures maintained using an Oxford Cryostream. Data were collected and integrated and data corrected for absorption using a numerical absorption correction based on Gaussian integration over a multifaceted crystal model within CrysAlisPro.²² The structures were solved by direct methods and refined against F^2 within SHELXL-2013.²³

Single crystals of **3**, **4**, **12**, **14a** and **14b** were grown under a dinitrogen inert atmosphere. Crystallographic studies were undertaken on single crystal mounted in paratone and studied on a Nonius Kappa CCD (**3b**, **4** and **14a**) or a Bruker APEX diffractometer (**10**, **12** and **14b**) using CCD detectors. Data for **3b**, **4** and **14a** were measured using COLLECT²⁴ and processed using Denzo and Scalepack²⁵ whereas for **10**, **12** and **14b** data were collected and processed with SAINT.²⁶ Absorption corrections for all structures were applied using the multi-scan approach of Blessing²⁷ (**3b**, **4** and **14a**) or through Sadabs.²⁸ All structures were solved by direct methods to reveal all non-H atoms which were refined anisotropically except where stated within SHELXL-2014/7²⁹ (SHELXL 2017/1 for **10**)³⁰. H atoms were added at calculated positions and refined with a riding model.

Crystals of **13b** were plagued with persistent twinning, despite multiple recrystallisation attempts. To remedy this twinning, during the refinement the law $-1\ 0\ 0\ 0\ -1\ 0\ 0\ 0\ 1$ as given in TwinRotMat (within Platon³¹) was used in the refinement of **13b** alongside the BASF command, which helped remedy the twinning and in turn bring the R_1 and wR_2 values to satisfactory levels ($R_1 = 7\%$ and $wR_2 = 21\%$).

For the structure of **10**, the data reported were the best from multiple crystals examined which were persistently twinned. Structure initially solved in $P-1$ with one molecule in the asymmetric unit but large residuals. ADDSYM within Platon³¹ identified the higher symmetry $P-3$ space group and refinement improved but stalled at $R_1 = 13\%$. TWINROTMAT identified an inversion twin and led to a further reduction in R_1 by 4%. Although the residuals are still high the connectivity is clear and the refinement was stable and estimated standard deviations (esds) on geometric parameters were small with molecular connectivity consistent with other analytical data.

In the case of **24a**, crystals suitable for single crystal X-ray diffraction were difficult to grow, with previous attempts showing very weak diffraction patterns. The dataset for **24a** initially showed significant disorder in the toluene backbone, with the ring being non-planar and non-hexagonal. Therefore, the geometrical constraint AFIX 66 was used. The thermal ellipsoids on the methyl group of the toluene ring showed significant elongation, but no second obvious site from either the .lst file or in the difference Fourier map was seen. Consequently, the disorder on this ellipsoid was not modelled. The end result of the structure refinement gave a relatively high $R_1 = 11\%$ and $wR_2 = 26\%$, but nevertheless showed the connectivity of the benzyloxy-dithiaphosphole.

With the exception of **13b** and **24a**, all the structures listed have been deposited with the Cambridge Structural Database (CCDC deposition numbers 1951113-1951115, 1951125-1951127, 1951132, 824860, 1563566-1563575, 1852464-1852465 and 1546788-1546793). These can be obtained free of charge from the Cambridge Crystallographic Data Centre *via* www.ccdc.cam.ac.uk/data_request/cif.

6.6.2 X-ray refinement data

Table 6.5: X-ray refinement data for compounds **1a–1c**.

Compound	1a	1b	1c
Empirical formula	C ₇ H ₆ ClPS ₂	C ₇ H ₆ BrPS ₂	C ₇ H ₆ IPS ₂
Formula Weight	220.66	265.12	312.11
Temperature/ K	150(2)	150(2)	150(2)
Wavelength/ Å	1.54178	0.71073	0.71073
Crystal System	Monoclinic	Monoclinic	Monoclinic
Space Group	<i>P</i> 2 ₁ / <i>c</i>	<i>P</i> 2 ₁ / <i>c</i>	<i>P</i> 2 ₁ / <i>c</i>
<i>a</i> / Å	7.9254(2)	8.1065(5)	9.6874(7)
<i>b</i> / Å	14.9999(5)	8.4575(5)	12.2726(9)
<i>c</i> / Å	7.5269(2)	13.4463(8)	8.3795(7)
α / °	90	90	90
β / °	91.739(3)	93.273(6)	102.702(8)
γ / °	90	90	90
Volume/ Å ³	894.38(4)	920.39(9)	971.85(13)
Z	4	4	4
Density (calc)/ g cm ⁻³	1.639	1.913	2.133
Absorption coefficient/ mm ⁻¹	9.255	5.023	3.823
F(000)	448	520	592
Crystal size/ mm ³	0.260 x 0.150 x 0.133	0.313 x 0.133 x 0.055	0.186 x 0.127 x 0.054
θ range/ °	5.584 to 74.035	3.484 to 29.529	3.320 to 29.684
Index ranges	-9 ≤ <i>h</i> ≤ 9 -18 ≤ <i>k</i> ≤ 17 -9 ≤ <i>l</i> ≤ 9	-11 ≤ <i>h</i> ≤ 7 -8 ≤ <i>k</i> ≤ 11 -18 ≤ <i>l</i> ≤ 16	-13 ≤ <i>h</i> ≤ 12 -16 ≤ <i>k</i> ≤ 11 -11 ≤ <i>l</i> ≤ 8
Reflections collected	8622	4305	5189
Independent reflections	1792	2191	2301
R(int)	0.0342	0.0276	0.0303
Absorption Correction	Gaussian	Gaussian	Gaussian
Data / restraints / parameters	1792/0/101	2191 / 0 / 101	2301 / 0 / 101
Goodness of fit, S	1.027	1.030	1.050
Final R indices [<i>I</i> > 2 σ (<i>I</i>)]	R ₁ = 0.0329 wR ₂ = 0.0856	R ₁ = 0.0360 wR ₂ = 0.0822	R ₁ = 0.0342 wR ₂ = 0.0653
R indices (all data)	R ₁ = 0.0360 wR ₂ = 0.0889	R ₁ = 0.0486 wR ₂ = 0.0899	R ₁ = 0.0446 wR ₂ = 0.0715
Max/min residual electron density/ e ⁻ Å ⁻³	+0.533 -0.337	+0.660 -0.636	+1.536 -1.097

Table 6.6: X-ray refinement data for compounds **2a–2c**.

Compound	2a	2b	2c
Empirical formula	C ₆ H ₄ ClPS ₂	C ₆ H ₄ BrPS ₂	C ₆ H ₄ IPS ₂
Formula Weight	206.63	251.09	298.08
Temperature/ K	150(2)	150(2)	150(2)
Wavelength/ Å	0.71073	0.71073	0.71073
Crystal System	Monoclinic	Triclinic	Triclinic
Space Group	<i>P</i> 2 ₁ / <i>n</i>	<i>P</i> -1	<i>P</i> -1
<i>a</i> / Å	5.9973(4)	8.9636(5)	9.0077(6)
<i>b</i> / Å	17.0236(15)	9.1854(7)	9.3261(7)
<i>c</i> / Å	7.9817(5)	11.3840(10)	11.6087(7)
α / °	90	69.213(7)	69.446(6)
β / °	97.205(7)	73.956(6)	77.324(5)
γ / °	90	78.555(5)	79.406(6)
Volume/ Å ³	808.47(11)	836.88(12)	884.76(11)
Z	4	4	4
Density (calc)/ g cm ⁻³	1.698	1.993	2.238
Absorption coefficient/ mm ⁻¹	1.100	5.518	4.193
F(000)	416	488	560
Crystal size/ mm ³	0.638 x 0.199 x 0.103	0.700 x 0.225 x 0.216	0.341 x 0.207 x 0.194
θ range/ °	3.514 to 29.530	3.409 to 29.722	3.468 to 29.889
Index ranges	-6 ≤ <i>h</i> ≤ 8 -17 ≤ <i>k</i> ≤ 23 -10 ≤ <i>l</i> ≤ 9	-12 ≤ <i>h</i> ≤ 11 -12 ≤ <i>k</i> ≤ 12 -12 ≤ <i>l</i> ≤ 14	-12 ≤ <i>h</i> ≤ 12 -12 ≤ <i>k</i> ≤ 13 -15 ≤ <i>l</i> ≤ 11
Reflections collected	4133	6707	7548
Independent reflections	1952	3932	4222
R(int)	0.0253	0.0262	0.0275
Absorption Correction	Gaussian	Gaussian	Gaussian
Data / restraints / parameters	1952 / 0 / 91	3932 / 0 / 181	4222 / 0 / 181
Goodness of fit, S	1.017	0.973	1.013
Final R indices [<i>I</i> > 2 σ (<i>I</i>)]	R ₁ = 0.0342 wR ₂ = 0.0653	R ₁ = 0.0324 wR ₂ = 0.0527	R ₁ = 0.0340 wR ₂ = 0.0652
R indices (all data)	R ₁ = 0.0517 wR ₂ = 0.0701	R ₁ = 0.0468 wR ₂ = 0.0595	R ₁ = 0.0499 wR ₂ = 0.0742
Max/min residual electron density/ e ⁻ Å ⁻³	+0.385 -0.304	+0.461 -0.479	+0.660 -1.199

Table 6.7: X-ray refinement data for compounds **3 β** and **4**.

Compound	3β	4
Empirical formula	C ₇ H ₆ AsClS ₂	C ₆ H ₄ AsClS ₂
Formula Weight	264.61	250.58
Temperature/ K	150(2)	180(2)
Wavelength/ Å	0.71073	0.7107
Crystal System	Triclinic	Triclinic
Space Group	<i>P</i> -1	<i>P</i> -1
<i>a</i> / Å	9.2240(2)	12.4186(2)
<i>b</i> / Å	9.6289(3)	22.4845(4)
<i>c</i> / Å	10.8161(3)	26.7287(4)
α / °	81.120(2)	76.8040(10)
β / °	76.281(2)	80.2820(10)
γ / °	84.486(2)	76.7200(10)
Volume/ Å ³	920.29(4)	7018.4(2)
Z	4	34
Density (calc)/ g cm ⁻³	1.910	2.016
Absorption coefficient/ mm ⁻¹	4.367	2.016
F(000)	520	4148
Crystal size/ mm ³	0.230 x 0.070 x 0.020	0.140 x 0.050 x 0.020
θ range/ °	3.655 to 27.058	3.519 to 27.500
Index ranges	-11 ≤ <i>h</i> ≤ 11 -11 ≤ <i>k</i> ≤ 12 -12 ≤ <i>l</i> ≤ 13	-16 ≤ <i>h</i> ≤ 16 -29 ≤ <i>k</i> ≤ 29 -34 ≤ <i>l</i> ≤ 34
Reflections collected	8175	104496
Independent reflections	3932	32107
R(int)	0.0388	0.1240
Absorption Correction	Gaussian	Gaussian
Data / restraints / parameters	3932 / 0 / 201	32107 / 3638 / 923
Goodness of fit, S	1.031	1.010
Final R indices [<i>I</i> > 2 σ (<i>I</i>)]	R ₁ = 0.0311 wR ₂ = 0.0765	R ₁ = 0.0788 wR ₂ = 0.1261
R indices (all data)	R ₁ = 0.0412 wR ₂ = 0.0804	R ₁ = 0.2720 wR ₂ = 0.1884
Max/min residual electron density/ e ⁻ Å ⁻³	+0.428 -0.683	+0.645 -0.683

Table 6.8: X-ray refinement data for compounds **6a** and **7**.

Compound	6a	7
Empirical formula	C ₁₂ H ₁₈ ClN ₂ P	C ₁₂ H ₁₈ AsClN ₂
Formula Weight	256.70	300.65
Temperature/ K	150(2)	150(2)
Wavelength/ Å	0.71073	0.71073
Crystal System	Triclinic	Monoclinic
Space Group	<i>P</i> -1	<i>Cc</i>
<i>a</i> / Å	9.8879(4)	8.8410(6)
<i>b</i> / Å	10.3627(4)	16.4442(8)
<i>c</i> / Å	13.4327(5)	10.2872(7)
α / °	85.789(3)	90
β / °	85.789(3)	115.180(8)
γ / °	85.789(3)	90
Volume/ Å ³	1342.34(10)	1353.47(17)
Z	4	4
Density (calc)/ g cm ⁻³	1.270	1.475
Absorption coefficient/ mm ⁻¹	0.380	2.685
F(000)	544	616
Crystal size/ mm ³	0.430 x 0.287 x 0.135	0.546 x 0.209 x 0.127
θ range/ °	2.895 to 27.485	2.840 to 27.483
Index ranges	-12 ≤ <i>h</i> ≤ 12 -13 ≤ <i>k</i> ≤ 12 -17 ≤ <i>l</i> ≤ 16	-7 ≤ <i>h</i> ≤ 11 -21 ≤ <i>k</i> ≤ 19 -13 ≤ <i>l</i> ≤ 10
Reflections collected	11520	3070
Independent reflections	5941	2031
R(int)	0.0252	0.0238
Absorption Correction	Gaussian	Gaussian
Data / restraints / parameters	5941 / 0 / 289	2031 / 2 / 145
Goodness of fit, S	1.013	1.052
Final R indices [<i>I</i> > 2 σ (<i>I</i>)]	R ₁ = 0.0393 wR ₂ = 0.0875	R ₁ = 0.0232 wR ₂ = 0.0567
R indices (all data)	R ₁ = 0.0580 wR ₂ = 0.1006	R ₁ = 0.0242 wR ₂ = 0.0577
Max/min residual electron density/ e ⁻ Å ⁻³	+0.289 -0.249	+0.710 -0.449

Table 6.9: X-ray refinement data for compounds **10** and **12**.

Compound	10	12
Empirical formula	C ₂₁ H ₁₈ NP ₃ S ₆	C ₂₁ H ₁₈ As ₃ NS ₆
Formula Weight	569.63	701.48
Temperature/ K	150(2)	150(2)
Wavelength/ Å	0.71073	0.71073
Crystal System	Trigonal	Triclinic
Space Group	<i>P</i> -3	<i>P</i> -3
<i>a</i> / Å	12.134(2)	11.277(7)
<i>b</i> / Å	12.134(2)	11.671(7)
<i>c</i> / Å	11.246(2)	12.023(7)
α / °	90	76.122(9)
β / °	90	67.953(7)
γ / °	120	87.177(8)
Volume/ Å ³	1434.0(5)	1422.4(15)
Z	2	2
Density (calc)/ g cm ⁻³	1.319	1.638
Absorption coefficient/ mm ⁻¹	0.655	3.954
F(000)	584	692
Crystal size/ mm ³	0.14 x 0.13 x 0.04	0.13 x 0.05 x 0.02
θ range/ °	1.81 to 27.53	1.95 to 27.49
Index ranges	-15 ≤ <i>h</i> ≤ 15 -15 ≤ <i>k</i> ≤ 15 0 ≤ <i>l</i> ≤ 14	-13 ≤ <i>h</i> ≤ 14 -14 ≤ <i>k</i> ≤ 15 0 ≤ <i>l</i> ≤ 15
Reflections collected	6447	6382
Independent reflections	2214	6382
R(int)	0.0353	0.0000
Absorption Correction	Sadabs	Gaussian
Data / restraints / parameters	2214/0/96	6382 / 0 / 273
Goodness of fit, S	1.093	1.136
Final R indices [<i>I</i> > 2 σ (<i>I</i>)]	R ₁ = 0.0984 wR ₂ = 0.2682	R ₁ = 0.0836 wR ₂ = 0.1573
R indices (all data)	R ₁ = 0.1047 wR ₂ = 0.2838	R ₁ = 0.1184 wR ₂ = 0.1676
Max/min residual electron density/ e ⁻ Å ⁻³	+1.38 -0.48	+1.066 -1.808

Table 6.10: X-ray refinement data for compounds **13b**, **14a** and **14b**.

Compound	13b	14a	14b
Empirical formula	C ₇ H ₆ Cl ₄ GaPS ₂	C ₇ H ₆ AlAsCl ₄ S ₂	C ₇ H ₆ AsCl ₄ GaS ₂
Formula Weight	396.73	397.94	440.68
Temperature/ K	150(2)	180(2)	150(2)
Wavelength/ Å	0.71073	0.71073	0.71073
Crystal System	Monoclinic	Monoclinic	Monoclinic
Space Group	<i>P2₁/c</i>	<i>P2₁/m</i>	<i>P2₁/m</i>
<i>a</i> / Å	7.9548(7)	11.4720(7)	11.409(4)
<i>b</i> / Å	18.2765(15)	7.0562(5)	7.015(2)
<i>c</i> / Å	9.3014(7)	17.819(2)	17.742(6)
α / °	90	90	90
β / °	90.812(7)	102.135(3)	102.483(3)
γ / °	90	90	90
Volume/ Å ³	1359.55(19)	1410.2(2)	1386.4(8)
Z	4	4	4
Density (calc)/ g cm ⁻³	1.938	1.874	2.111
Absorption coefficient/ mm ⁻¹	3.198	3.492	5.390
F(000)	776	776	848
Crystal size/ mm ³	0.496 x 0.148 x 0.115	0.14 x 0.02 x 0.01	0.30 x 0.03 x 0.02
θ range/ °	3.347 to 27.866	3.58 to 22.39	1.95 to 27.54
Index ranges	-6 ≤ <i>h</i> ≤ 10 -24 ≤ <i>k</i> ≤ 21 -12 ≤ <i>l</i> ≤ 10	-12 ≤ <i>h</i> ≤ 11 -7 ≤ <i>k</i> ≤ 7 -18 ≤ <i>l</i> ≤ 17	-14 ≤ <i>h</i> ≤ 14 -9 ≤ <i>k</i> ≤ 9 -22 ≤ <i>l</i> ≤ 22
Reflections collected	6994	7859	15899
Independent reflections	3079	1959	3426
R(int)	0.0492	0.1501	0.0385
Absorption Correction	Gaussian	Gaussian	Gaussian
Data / restraints / parameters	3079/0/138	1959 / 16 / 132	3426 / 0 / 177
Goodness of fit, S	1.109	1.203	1.019
Final R indices [<i>I</i> > 2 σ (<i>I</i>)]	R ₁ = 0.0748 wR2 = 0.1977	R1 = 0.0879 wR2 = 0.2281	R1 = 0.0221 wR2 = 0.0605
R indices (all data)	R ₁ = 0.0967 wR2 = 0.2145	R1 = 0.1095 wR2 = 0.2366	R1 = 0.0252 wR2 = 0.0625
Max/min residual electron density/ e ⁻ Å ⁻³	+2.418 -1.032	+2.393 -0.641	+0.537 -0.423

Table 6.11: X-ray refinement data for compounds **15a–15c**.

Compound	15a	15b	15c
Empirical formula	C ₁₂ H ₁₈ AlCl ₄ N ₂ P	C ₁₂ H ₁₈ Cl ₄ GaN ₂ P	C ₁₃ H ₁₈ F ₃ N ₂ O ₃ PS
Formula Weight	390.03	432.77	370.32
Temperature/ K	150(2)	150(2)	150(2)
Wavelength/ Å	1.54178	1.54178	0.71073
Crystal System	Orthorhombic	Orthorhombic	Monoclinic
Space Group	<i>Pbca</i>	<i>Pbca</i>	<i>P2₁/n</i>
<i>a</i> / Å	12.4817(2)	12.4840(3)	7.4354(4)
<i>b</i> / Å	12.4240(3)	12.4355(4)	13.7492(7)
<i>c</i> / Å	23.9322(6)	23.9697(7)	16.2737(13)
α / °	90	90	90
β / °	90	90	95.923(6)
γ / °	90	90	90
Volume/ Å ³	3711.23(15)	3721.17(18)	1654.81(18)
Z	8	8	4
Density (calc)/ g cm ⁻³	1.396	1.545	1.486
Absorption coefficient/ mm ⁻¹	7.005	8.055	0.337
F(000)	1600	1744	768
Crystal size/ mm ³	0.0471 x 0.296 x 0.207	0.433 x 0.088 x 0.054	0.563 x 0.247 x 0.185
θ range/ °	3.694 to 66.560	3.6888 to 73.741	2.908 to 27.874
Index ranges	-14 ≤ <i>h</i> ≤ 14 -13 ≤ <i>k</i> ≤ 8 -21 ≤ <i>l</i> ≤ 8	-15 ≤ <i>h</i> ≤ 14 -15 ≤ <i>k</i> ≤ 15 -20 ≤ <i>l</i> ≤ 29	-9 ≤ <i>h</i> ≤ 9 -17 ≤ <i>k</i> ≤ 18 -13 ≤ <i>l</i> ≤ 20
Reflections collected	7307	9043	9480
Independent reflections	2913	3660	3793
R(int)	0.0254	0.0292	0.0254
Absorption Correction	Gaussian	Gaussian	Gaussian
Data / restraints / parameters	2913 / 0 / 185	3660 / 0 / 185	3793 / 0 / 208
Goodness of fit, S	1.022	1.023	1.009
Final R indices [<i>I</i> > 2 σ (<i>I</i>)]	R ₁ = 0.0320 wR ₂ = 0.0837	R ₁ = 0.0289 wR ₂ = 0.0712	R ₁ = 0.0376 wR ₂ = 0.0869
R indices (all data)	R ₁ = 0.0353 wR ₂ = 0.0871	R ₁ = 0.0363 wR ₂ = 0.0772	R ₁ = 0.0548 wR ₂ = 0.0965
Max/min residual electron density/ e ⁻ Å ⁻³	+0.405 -0.401	+0.420 -0.476	+0.329 -0.360

Table 6.12: X-ray refinement data for compounds **16a–16c**.

Compound	16a	16b	16c
Empirical formula	C ₁₂ H ₁₈ AlAsCl ₄ N ₂	C ₁₂ H ₁₈ AsCl ₄ GaN ₂	C ₁₃ H ₁₈ AsF ₃ N ₂ O ₃ S
Formula Weight	433.98	476.72	414.27
Temperature/ K	150(2)	150(2)	150(2)
Wavelength/ Å	1.54178	1.54178	0.71073
Crystal System	Monoclinic	Monoclinic	Monoclinic
Space Group	<i>P2₁/n</i>	<i>P2₁/n</i>	<i>P2₁/n</i>
<i>a</i> / Å	7.2319(2)	7.2223(3)	9.3152(6)
<i>b</i> / Å	14.6027(5)	14.6495(5)	17.3419(9)
<i>c</i> / Å	17.8624(5)	17.8443(7)	11.1659(7)
α / °	90	90	90
β / °	94.910(3)	94.823(4)	111.586(7)
γ / °	90	90	90
Volume/ Å ³	1879.44(10)	1881.31(12)	1677.27(19)
Z	4	4	4
Density (calc)/ g cm ⁻³	1.534	1.683	1.641
Absorption coefficient/ mm ⁻¹	8.068	9.116	2.195
F(000)	872	944	840
Crystal size/ mm ³	0.259 x 0.108 x 0.079	0.310 x 0.051 x 0.043	0.257 x 0.201 x 0.143
θ range/ °	3.916 to 70.067	3.910 to 70.068	3.061 to 27.094
Index ranges	-8 ≤ <i>h</i> ≤ 8 -17 ≤ <i>k</i> ≤ 16 -15 ≤ <i>l</i> ≤ 21	-8 ≤ <i>h</i> ≤ 7 -17 ≤ <i>k</i> ≤ 10 -21 ≤ <i>l</i> ≤ 21	-11 ≤ <i>h</i> ≤ 9 -18 ≤ <i>k</i> ≤ 22 -14 ≤ <i>l</i> ≤ 13
Reflections collected	7146	7135	8059
Independent reflections	3547	3544	3636
R(int)	0.0238	0.0290	0.0327
Absorption Correction	Gaussian	Gaussian	Gaussian
Data / restraints / parameters	3547/ 0 / 181	3544 / 0 / 181	3636 / 0 / 208
Goodness of fit, S	1.017	1.036	1.074
Final R indices [<i>I</i> > 2 σ (<i>I</i>)]	R ₁ = 0.0277 wR ₂ = 0.0685	R ₁ = 0.0307 wR ₂ = 0.0754	R ₁ = 0.0398 wR ₂ = 0.0982
R indices (all data)	R ₁ = 0.0344 wR ₂ = 0.0729	R ₁ = 0.0383 wR ₂ = 0.0808	R ₁ = 0.0498 wR ₂ = 0.1078
Max/min residual electron density/ e ⁻ Å ⁻³	+0.544 -0.433	+0.512 -0.572	+0.624 -0.582

Table 6.13: X-ray refinement data for compounds **17** and **18**.

Compound	17	18
Empirical formula	C ₂₄ H ₃₆ N ₄ P ₂	C ₁₂ H ₁₈ AsIN ₂
Formula Weight	442.51	393.10
Temperature/ K	150(2)	150(2)
Wavelength/ Å	1.54178	0.71073
Crystal System	Monoclinic	Monoclinic
Space Group	<i>P</i> 2 ₁ / <i>c</i>	<i>Cc</i>
<i>a</i> / Å	9.1349(3)	9.2985(8)
<i>b</i> / Å	10.1970(3)	16.1525(9)
<i>c</i> / Å	14.2183(5)	10.3835(9)
α / °	90	90
β / °	107.085(4)	112.546(10)
γ / °	90	90
Volume/ Å ³	1265.97(8)	1440.3(2)
Z	2	4
Density (calc)/ g cm ⁻³	1.161	1.808
Absorption coefficient/ mm ⁻¹	1.680	4.482
F(000)	476	760
Crystal size/ mm ³	0.161 x 0.128 x 0.119	0.179 x 0.115 x 0.095
θ range/ °	5.065 to 70.069	3.298 to 26.372
Index ranges	-9 ≤ <i>h</i> ≤ 11 -11 ≤ <i>k</i> ≤ 12 -15 ≤ <i>l</i> ≤ 17	-11 ≤ <i>h</i> ≤ 9 -20 ≤ <i>k</i> ≤ 16 -10 ≤ <i>l</i> ≤ 12
Reflections collected	5003	3351
Independent reflections	2398	2199
R(int)	0.0258	0.0244
Absorption Correction	Gaussian	Gaussian
Data / restraints / parameters	2398 / 0 / 136	2199 / 2 / 147
Goodness of fit, S	1.013	1.063
Final R indices [<i>I</i> > 2 σ (<i>I</i>)]	R ₁ = 0.0389 wR ₂ = 0.1045	R ₁ = 0.0377 wR ₂ = 0.0932
R indices (all data)	R ₁ = 0.0458 wR ₂ = 0.1122	R ₁ = 0.0357 wR ₂ = 0.0972
Max/min residual electron density/ e ⁻ Å ⁻³	+0.347 -0.262	+1.410 -0.748

Table 6.14: X-ray refinement data for compounds **19**, **20** and **24a**.

Compound	19	20	24a
Empirical formula	C ₁₄ H ₁₃ AsOS ₂	C ₁₉ H ₂₅ AsN ₂ O	C ₁₄ H ₁₃ OPS ₂
Formula Weight	336.28	372.33	292.33
Temperature/ K	150(2)	150(2)	150(2)
Wavelength/ Å	0.71073	1.54178	0.71073
Crystal System	Monoclinic	Monoclinic	Monoclinic
Space Group	<i>P</i> 2 ₁ / <i>c</i>	<i>P</i> 2 ₁ / <i>c</i>	<i>P</i> 2 ₁ / <i>c</i>
<i>a</i> / Å	12.4575(8)	13.6908(3)	10.5734(6)
<i>b</i> / Å	6.1460(3)	9.18083(17)	6.1687(4)
<i>c</i> / Å	18.2764(12)	28.6493(6)	21.7415(17)
α / °	90	90	90
β / °	101.859(6)	94.418(2)	97.717(7)
γ / °	90	90	90
Volume/ Å ³	1369.45(15)	3590.30(13)	1405.24(16)
Z	4	8	4
Density (calc)/ g cm ⁻³	1.631	1.378	1.382
Absorption coefficient/ mm ⁻¹	2.771	2.599	0.477
F(000)	680	1552	608
Crystal size/ mm ³	0.233 x 0.167 x 0.139	0.191 x 0.155 x 0.073	0.399 x 0.228 x 0.083
θ range/ °	3.089 to 29.682	3.094 to 74.303	3.435 to 29.676
Index ranges	-16 ≤ <i>h</i> ≤ 14 -6 ≤ <i>k</i> ≤ 8 -25 ≤ <i>l</i> ≤ 18	-16 ≤ <i>h</i> ≤ 11 -11 ≤ <i>k</i> ≤ 6 -35 ≤ <i>l</i> ≤ 35	-10 ≤ <i>h</i> ≤ 14 -6 ≤ <i>k</i> ≤ 8 -27 ≤ <i>l</i> ≤ 28
Reflections collected	6339	13586	6336
Independent reflections	3230	7076	3294
R(int)	0.0255	0.0200	0.0213
Absorption Correction	Gaussian	Gaussian	Gaussian
Data / restraints / parameters	3230 / 0 / 163	7076 / 0 / 415	3294 / 0 / 152
Goodness of fit, S	1.062	1.028	1.099
Final R indices [<i>I</i> > 2 σ (<i>I</i>)]	R ₁ = 0.0394 wR ₂ = 0.0794	R ₁ = 0.0301 wR ₂ = 0.0774	R ₁ = 0.1086 wR ₂ = 0.2481
R indices (all data)	R ₁ = 0.0539 wR ₂ = 0.0878	R ₁ = 0.0355 wR ₂ = 0.0812	R ₁ = 0.1317 wR ₂ = 0.2625
Max/min residual electron density/ e ⁻ Å ⁻³	+0.688 -0.718	+0.513 -0.554	+1.512 -0.727

Chapter 6.7 General Computational Experimental

Density functional theory (DFT) calculations were performed using the graphical interface WebMO computational platform, which employed the Gaussian 09 package.⁶ Compounds **1a–1c**, **2a–2c**, **6a**, **6b**, **8a**, **8b**, **13+**, **15+**, **24'** and **25'** were initially geometry optimised using the meta-hybrid M06-2X functional³² and the Pople split valence basis set 6-311+G(2d,p)⁵ on all atoms, except iodine. In the case of iodine, M06-2X was again used, but the effective core potential (ECP) Def2TZVP was used as the basis set.⁸ For the arsenic containing compounds **3**, **4**, **7**, **14+**, **16+**, **19'** and **20'**, the meta-hybrid M06-2X functional and the Pople split valence basis set 6-311+G(2d,p) were still used, but for the arsenic heteroatom the ECP Los Alamos National Laboratory 2-double- ζ (LANL2DZ)^{33–35} was used as the basis set along with the M06-2X functional. After geometry optimisation a vibrational frequency calculation was undertaken to ensure each structure was a minimum on the potential energy landscape. Natural bond orbital (NBO) and molecular orbital analyses were then performed on the optimised geometries using the same functional and basis set described above.³⁶

Fluoride Ion Affinity (FIA) calculations were performed by calculating the enthalpy of the cation, fluoride and combined cation–fluoride complex from geometry optimised structures, using the M06-2X functional and 6-311+G(2d,p) basis set (LANL2DZ for As heteroatom). The change in enthalpy for the reaction was calculated. After this, a counterpoise correction was applied to the cation–fluoride complex, which generated a basis set superposition error (BSSE) value. The final FIA value was produced by the reaction enthalpy plus the BSSE value.

Chapter 6.8 References

- 1 W. H. Melhuish, *J. Phys. Chem.*, 1961, **65**, 229–235.
- 2 S. Stoll and A. Schweiger, *J. Magn. Reson.*, 2006, **178**, 42–55.
- 3 C. Adamo and V. Barone, *J. Chem. Phys.*, 1999, **110**, 6158–6170.
- 4 J. P. Perdew, M. Ernzerhof and K. Burke, *J. Chem. Phys.*, 1996, **105**, 9982–9985.
- 5 R. Ditchfield, W. J. Hehre and J. A. Pople, *J. Chem. Phys.*, 1971, **54**, 724–728.
- 6 Gaussian 09, M. J. Frisch, G. W. Trucks, H. B. Schlegel, G. E. Scuseria, M. A. Robb, J. R. Cheeseman, G. Scalmani, V. Barone, G. A. Petersson, H. Nakatsuji, X. Li, M. Caricato, A. Marenich, J. Bloino, B. G. Janesko, R. Gomperts, B. Mennucci, H. P. Hratchian, J. V. Ortiz, A. F. Izmaylov, J. L. Sonnenberg, D. Williams-Young, F. Ding, F. Lipparini, F. Egidi, J. Goings, B. Peng, A. Petrone, T. Henderson, D. Ranasinghe, V. G. Zakrzewski, J. Gao, N. Rega, G. Zheng, W. Liang, M. Hada, M. Ehara, K. Toyota, R. Fukuda, J. Hasegawa, M. Ishida, T. Nakajima, Y. Honda, O. Kitao, H. Nakai, T. Vreven, K. Throssell, J. A. Montgomery, Jr., J. E. Peralta, F. Ogliaro, M. Bearpark, J. J. Heyd, E. Brothers, K. N. Kudin, V. N. Staroverov, T. Keith, R. Kobayashi, J. Normand, K. Raghavachari, A. Rendell, J. C. Burant, S. S. Iyengar, J. Tomasi, M. Cossi, J. M. Millam, M. Klene, C. Adamo, R. Cammi, J. W. Ochterski, R. L. Martin, K. Morokuma, O. Farkas, J. B. Foresman, and D. J. Fox, Gaussian, Inc., Wallingford CT, 2016 .
- 7 F. Neese, Wiley Interdisciplinary Reviews. *Computational Molecular Science*, 2012, **2**, 73–78.
- 8 F. Weigend and R. Ahlrichs, *Phys. Chem. Chem. Phys.*, 2005, **7**, 3297–3305.
- 9 F. Neese, *J. Chem. Phys.*, 2005, **122**, 034107.
- 10 O. M. Demchuk, W. Świerczyńska, K. Dziuba, S. Frynas, A. Flis and K. M. Pietrusiewicz, *Phosphorus, Sulfur and Silicon*, 2017, **192**, 64–68.
- 11 M. A. Beckett, G. C. Strickland, J. R. Holland and K. S. Varma, *Polym. Commun.*, 1996, **37**, 4629–4631.
- 12 J. P. Green, S. J. Cryer, J. Marafie, A. J. P. White and M. Heeney, *Organometallics*, 2017, **36**, 2632–2636.
- 13 F. H. Allen, D. G. Watson, L. Brammer, A. G. Orpen and R. Taylor, *Typical interatomic distances: organic compounds*, International Tables for Crystallography, 2006, chapter 9.5, vol. C, pp. 790–811.
- 14 The Cambridge Structural Database. C. R. Groom, I. J. Bruno, M. P. Lightfoot and S. C. Ward, *Acta Cryst.*, **B72**, 2016, 171-179.
- 15 J. R. Lawson, L. C. Wilkins and R. L. Melen, *Chem. Eur. J.*, 2017, **23**, 10997–11000.
- 16 W. Wang, X. Shen, F. Zhao, H. Jiang, W. Yao, S. A. Pullarkat, L. Xu and M. Ma, *J. Org. Chem.*, 2018, **83**, 69–74.
- 17 Z. Zhu, P. Dai, Z. Wu, M. Xue, Y. Yao, Q. Shen and X. Bao, *Catal. Commun.*, 2018, **112**, 26–30.
- 18 K. Manna, Pengfei Ji, F. X. Greene and W. Lin, *J. Am. Chem. Soc.*, 2016, **138**, 7488–7491.

- 19 U. K. Das, C. S. Higman, B. Gabidullin, J. E. Hein and R. T. Baker, *ACS Catal.*, 2018, **8**, 1076–1081.
- 20 D. M. C. Ould and R. L. Melen, *Chem. Eur. J.*, 2018, **24**, 15201–15204.
- 21 M. K. Barman, K. Das and B. Maji, *J. Org. Chem.*, 2019, **84**, 1570–1579.
- 22 CrysAlisPro, Agilent Technologies, Version 1.171.37.33 (release 27-03-2014 CrysAlis171 .NET).
- 23 SHELXL-2013, G. M. Sheldrick, University of Göttingen, Germany (2013).
- 24 Nonius (1998). COLLECT. Nonius BV, Delft, The Netherlands.
- 25 Z. Otwinowski and W. Minor, *Methods in Enzymology*, Macromolecular Crystallography, Part A, (Eds. C. W. Carter Jr. and R. M. Sweet), 1997, **276**, 307–326. New York: Academic Press.
- 26 Bruker (2012). SAINT. Bruker AXS Inc., Madison, Wisconsin, USA.
- 27 MULTISCAN -Blessing, R. H. (1995) *Acta Cryst. A* **51**, 33–38.
- 28 Sadabs, Bruker AXS, Madison, WI, USA.
- 29 SHELXL-2013, G.M. Sheldrick, University of Göttingen, Germany (2013); SHELXL 2014: G.M. Sheldrick, *Acta Cryst.*, 2015, **C71**, 3–8.
- 30 G. M. Sheldrick, *Acta Cryst. C*, 2015, **71**, 3–8.
- 31 A. L. Spek, *Acta Cryst. D*, 2009, **65**, 148–155 .
- 32 Y. Zhao and D. G. Truhlar, *Theor. Chem. Account*, 2008, **120**, 215–241.
- 33 P. J. Hay and W. R. Wadt, *J. Chem. Phys.*, 1985, **82**, 270–283.
- 34 W. R. Wadt, and P. J. Hay, *J. Chem. Phys.*, 1985, **82**, 284–298.
- 35 P. J. Hay and W. R. Wadt, *J. Chem. Phys.*, 1985, **82**, 299–310.
- 36 NBO Version 3.1, E. D. Glendening, A. E. Reed, J. E. Carpenter and F. Weinhold.